Some properties of reaction: Bonded silicon nitride

T.G. Bushell

SOME PROPERTIES OF REACTION BONDED SILICON NITRIDE

by

T. G. Bushell, B.Sc.

(St. Cuthbert's)

A Thesis submitted to the University of Durham in candidature for the degree of Doctor of Philosophy

February, 1983.

To Anne

Our very business in life is not to get ahead of others, but to get ahead of ourselves.

Attributed to T.L.Monson.

'Well, I sort of made it up', said Pooh, ... it comes to me sometimes'.

A. A. Milne.

ABSTRACT

Electron Spin Resonance, Pulse Echo Ultrasonics and electrical conductivity measurements have been used to study the effect of the unreacted silicon which is present in Reaction Bonded Silicon Nitride (RBSN) as a result of the manufacturing process. One of the techniques (ESR) has been found to be very sensitive to the unreacted silicon, and the PEG Ultrasonic measurements have suggested that weight gain should not be the sole criterion by which to judge RBSN for mechanical applications.

ESR studies of unreacted silicon powder gave a signal similar to that reported for amorphous silicon with g = 2.0055 ; the line is attributed to dangling bonds. ESR spectra have been found for both RBSN and Hot Pressed Silicon Nitride (HPSN) with g values closer to the free electron value. Measurements on partially reacted materials showed a complex signal whose shape changed considerably over the temperature range 4 to 300 K. The behaviour of this line, presumed to be the sum of the silicon and RBSN signals is probably attributably to differences in the relaxation rates of the two species.

Determination of the elastic constants of the RBSN materials has shown that partially nitrided ceramics have lower strength than fully nitrided materials with similar densities, except in the region where the reaction is nearly complete (weight gain of 59% or more) when the effect of unreacted silicon is negligible, and the major factor governing strength is density.

A.C.electrical measurements on high weight gain materials have shown dielectric constant (ε') behaviour analagous to the mechanical strength in that the higher ε' has been found for the denser (less porous), but lower weight gain material. In contrast to this, however, the high weight gain material was found to have a lower $\tan\delta$ This is consistent with the lower levels of silicon in the fully reacted ceramic.

D.C. 'step response' measurements at room temperature gave results which fitted Jonscher's two stage relaxation theory

$$I_d(t) \alpha \frac{1}{(\omega_p t)^n + (\omega_p t)^k}$$

with n in the region 0.7 to 0.8 and k in the region 1.45 to 1.6.

D.C. and A.C. results over the temperature range 100°C to 900°C suggested that the predominant conductivity up to 750°C was hopping either in defect bands or localized states in the band tails.

ACKNOWLEDGEMENTS

I am most grateful to my supervisor, Dr.J.S. Thorp, for his unfailing guidance and assitance in the execution of this project and in the preparation of this thesis. I would also like to thank Steve Hodgskiss (of Dr. Thorp's research group) and Dick Dickens of United Glass PLC in St. Albans for many useful discussions.

My sincere thanks are also due to Professor G.G. Roberts for his generous provision of the departmental facilities and to the technical staff, especially Mr. R.T.Harcourt for his painstaking work in sample preparation, and Messrs. R.Waite, W.Mounsey, C.Savage and P. Richardson for their enthusiasm in the face of my (frequently) impossible demands.

I would also like to thank Advanced Materials Engineering Ltd. for the provision of samples and much useful technical information.

I am greatly indebted to Mrs. S.Mellanby and Mrs. P. Morrell for their careful typing of the script and to Mr.N.Thompson for the excellence of the Figures and Plates.

Finally, to Anne, without whom this thesis would not exist, thank you.

C O N T E N T S

LIST OF TABLES

CHAPTER 1

INTRODUCTION

Silicon nitride has for some years been established as a leading refractory ceramic. It possesses a range of properties not found in combination in other high temperature ceramics. Chief among these perhaps is its high strength at high temperatures which includes factors such as high surface hardness and good abrasion resistance, a high compressive strength both at room and high temperatures and good impact strength. Other desirable features are its low coefficient of thermal expansion, which leads to good thermal shock resistance, and the chemical stability of silicon nitride which renders the material very resistant to oxidation and to corrosion or attack by molten metals.

These properties have led to the application of silicon nitride in hostile environments where the metal alloys used conventionally are beginning to fail. Examples of such engineering applications are firstly in gas turbines and secondly in the smelting industry. In gas turbine manufacture, the use of metal alloys restricts the operating temperatures of turbine engines to just over 1050^{o}C. Their replacement by silicon nitride in key areas such as blade assemblies, heat exchangers, and combustion chambers might allow operating temperatures to be increased by 300^{o}C, with a consequent fuel saving of 40%. Corresponding advantages result in the smelting industry. Here it is found that silicon nitride is virtually unaffected by molten metals such as zinc and aluminium, where conventional stainless steel containers are rapidly degraded.

A third area of considerable importance lies in the field of electronics, particularly (for bulk material) at microwave frequencies. The dielectric properties of silicon nitride have been of interest for many years because of the potential applications of the material in electronic devices. The properties of thin films of silicon nitride were summarized some years

ago by Milek(1.1)but the dielectric properties of bulk silicon nitride did not receive much attention until recently. This interest has arisen from the potential application of silicon nitride for electromagnetic windows, in particular for use in missile radomes, because of the excellent thermal shock properties of the material. The first reference to the microwave permittivity (dielectric constant) of reaction bonded silicon nitride (RBSN) was made by Wells(1.2)in 1964. However it was not until the early 1970s that RBSN with sufficiently low dielectric loss ($\tan \delta < 0.01$) was reported by Westphal and Sils(1.3)on materials obtained from AML and the Raytheon Co. Walton(1.4)in 1972 reported the manufacture of low loss RBSN made by slip-casting silicon.

Perry and Moules(1.5),and Messier and Wong(1.6)have also reported the preparation of low loss RBSN suitable for radome applications. Table 1.1 summarises some of the early results.

The temperature coefficient of permittivity of silicon nitride is reported to be $\sim 10 \times 10^{-6}\ K^{-1}$ (1.3) but more lossy materials tend to show wide variations (+ 3 to +354) of temperature coefficient(1.5,1.6). Hence it was important for radome applications in particular, that manufacture of low loss silicon nitride, and the associated problems be resolved and this need remains at the present time. The permittivity of theoretically (or 100%) dense silicon nitride has been reported for thin films(1.1)but the results obtained ranged widely. Fully dense silicon nitride can be obtained by hot-pressing with and without additives and dielectric data have been reported for these materials.

Estimates of the permittivity can also be obtained from plots of ε against density and Table 1.2 collects some early microwave results. They show that there is a wide variation in ε' depending on the preparative technique.

The causes of poor dielectric properties and reproducibility have been under investigation by several workers(1.5,1.6)in the U.K. and U.S.A. but

progress has been slow. It is generally agreed that incomplete nitridation of commercial silicon is a major reason for poor dielectric properties. More recently, Thorp and Sharif (1.9, 1.10, 1.11) made a fairly extensive study of the electrical conductivity and dielectric properties of both hot-pressed silicon nitride and a range of "sialon" nitrogen ceramics. In their papers these authors reported that the a.c. and d.c. electrical conductivities of some hot-pressed polycrystalline nitrogen ceramics were measured between 400 and 1000°C. The materials examined were Si_3N_4, 5.0% MgO/Si_3N_4 and two sialons, $Si_{(6-z)}.Al_z.O_z.N_{(8-z)}$ having $Z \approx 3.2$ and $Z \approx 4.0$ respectively. The electrical behaviour of all the materials showed similar general features. The d.c. conductivities were about 10^{-10} Ω^{-1} cm^{-1} at 400°C and rose to between 10^{-6} and 10^{-5} Ω^{-1} cm^{-1} at 1000°C. The a.c. data, taken over the frequency range 15 Hz to 5 kHz showed that below about 500°C the a.c. conductivity ($\sigma_{a.c.}$) varied with frequency as $\sigma_{a.c.} \propto \omega^s$ where $0.7 < s < 1$ indicative of a hopping process ; in this temperature range the d.c. conductivity ($\sigma_{d.c.}$) agreed well with the relation $\sigma_{d.c.} = A \exp(-B/T^{1/4})$. Above 700°C both the a.c. and d.c. conductivities followed $\log \sigma \propto T^{-1}$. Hall effect and thermoelectric power measurements enabled the Hall mobility to be estimated as less than 10^{-4} cm^2 V^{-1} sec^{-1} at 400°C and showed that the materials were all p-type below 900°C and n-type above 900°C. The electrical properties of all four materials were consistent with the presence of a glassy phase. Subsequently the same authors extended their survey and measured the dielectric properties of some hot-pressed nitrogen ceramics at room temperature over the frequency range 200 Hz to 75 MHz and also at 9.3 GHz ; some low frequency measurements were also made at temperatures up to 500°C. The materials examined were again Si_3N_4, 5.0% MgO/Si_3N_4 and two sialons $Si_{(6-z)}.Al_z.O_z.N_{(8-z)}$ having $z = 4.0$ and $z = 3.2$ respectively. At room temperature the variation of the real part of the conductivity with frequency over the range 200 Hz to 9.3 GHz followed the $\sigma'(\omega) \propto \omega^n$ with $n = 0.9$. The dielectric constant (ε') and loss ($\tan \delta$) both fell slightly over this frequency range, the average values at 10^5 Hz being

about 9.5 and 5.5 x 10^{-3} respectively. The data fits well with the 'universal dielectric law', $\varepsilon'' \alpha \omega^{n-1}$ $(n < 1)$ and approximately fits the Kramers-Kronig relation $\varepsilon''(\omega)/\varepsilon'(\omega) - \varepsilon_\infty = \cot(\frac{n\pi}{2})$. This behaviour applies also at temperatures up to 500°C except that the value of n decreases as the temperature increases. The d.c. electrical properties were also measured between 18 and 500° C in applied electric fields up to 1.1 x 10^4 V cm^{-1}. The materials examined were Si_3N_4, 5 wt%, MgO/Si_3N_4 and two sialons having z = 3.2 and z = 4.0. The conduction in all the materials showed similar general features. The time dependent charging (I_C) and discharging currents (I_D) were observed which followed a $I(t) \alpha t^{-n}$ law at room temperature with n = 0.7 to 0.8. The exponent n for I_C decreased with increasing temperature. The current density-field (J_s-E) characteristics were onmic in applied fields of less than 3 x 10^3 V cm^{-1} ; conductivity increased with electric field above that range. Above about 280°C, σ was independent of E, its temperature dependence following $\log \sigma \propto T^{-1}$. Below about 230°C conductivity fitted a $\sigma \propto \exp(-B/T^{1/4})$ law in both low and high fields. There is a good correlation between the temperature and field variations of time dependent current and steady current. The conductivities were in the range of 10^{-15} to 10^{-16} $\Omega^{-1}cm^{-1}$ at 18°C and rose to 4 x 10^{-10} to 2 x 10^{-12} Ω^{-1} cm^{-1} at 500°C. The activation energies were in the range of 1.45 to 1.80 eV and 0.05 to 0.15 eV at above 300°C and near room temperature respectively.

This work emphasised the importance of making measurements on samples of controlled, or at least known-chemical composition and threw into a more general perspective the earlier comments made by Messier and Wong ; which referred specifically to the application of silicon nitride as a material for radomes. Messier and Wong pointed out that although it has been demonstrated that silicon nitride has outstanding potential for radome applications, practical difficulties in producing material with acceptable reproducible dielectric properties have hampered its development for such applications. Their work was undertaken to identify the causes of irreproducibility, and

to use these data to develop processing procedures for the fabrication of uniform material with acceptable dielectric properties. Silicon nitride is usually fabricated either by hot pressing or reaction sintering. The former process, which comprises consolidation under heat and pressure of silicon nitride powder with 1% to 5% MgO as a sintering aid, produces dense, extremely strong material. Forming complex shapes by hot pressing, however, is extremely difficult. Of greater interest for radome applications is reaction-sintered silicon nitride, formed by heating shapes comprised of compacted silicon powder in nitrogen at temperatures up to 1400°C. A major advantage of this process is that almost no volume change accompanies sintering ; machining costs are thus minimized and shrinkage effects can be ignored. In Messier and Wong's work three reaction-sintered Si_3N_4 specimens were fabricated in their laboratory and one was procured from a commercial supplier. The hot-pressed Si_3N_4 was obtained from three commercial sources. Dielectric property data were obtained at 10 GHz by use of the shortened waveguide technique (1.12).Their conclusions were that the difficulty of eliminating traces of unreacted silicon was a persistent problem in reaction sintering. Thus, although the dielectric properties of Si_3N_4 are controlled by second-phase impurities rather than by overall chemical impurities, any residual unreacted Si greatly increases both the dielectric constant and loss tangent. Any second-phases present such as, for example, SiC and $MoSi_2$ increase the dielectric loss, but the dielectric properties are unaffected by Fe silicide and Mg silicate phases.

Consequently, the central theme of the work described in this thesis was to establish and assess the role of unreacted silicon in determining the physical properties of reaction bonded silicon nitride. The choice of which properties were to be examined was mainly determined by which experimental facilities could be set up in the Department and these considerations led to concentration of effort in three directions, firstly on the determination of

elastic properties by ultrasonics methods, secondly attempts to quantify and examine the silicon proportion of unreacted silicon using electron spin resonance techniques and thirdly to examine the dielectric behaviour of samples characterised by use of the previous two techniques. In this thesis, Chapter 2 is devoted to a description of the preparation of reaction bonded silicon nitride and some comments on its structural characteristics. Chapters 3 and 4 give an account of experimental methods and techniques for ultrasonic measurements together with the results of an ultrasonic examination of the RBSN samples. Electron spin resonance techniques and theory are discussed in Chapter 5 and the e.s.r. results obtained from the RBSN samples are presented and discussed in Chapter 6, along with a brief review of the e.s.r. data available on amorphous and polycrystalline silicon : Chapter 7 gives a brief account of the electronic processes in disordered materials, in so far as they are relevant to low frequency conduction processes, and extends the discussion to consider non-electronic processes with relevance to a.c. conduction. In Chapter 8 d.c. and a.c. results on high weight gain RBSN are presented and discussed.

Reference	Density g/ml	Frequency GHz	ε	tan δ
1.2	∿ 2.3	9-12	6.17	0.017
1.3	2.449	8.52	5.54	0.0036
1.4	∿ 2.5	9.8	5.6	0.002
1.5	2.556	9.37	5.92	0.006
1.6	2.24	9.37	4.98	0.008
	2.49		6.15	0.004

TABLE 1.1: Dielectric Property Data for RBSN

Reference	Material	ε'	Frequency GHz
1.4	Slip-cast	9.2*	9.8
1.7	Isostatic	7.4	9.38
1.8	Hot-pressed	8.3	14.0
1.7	Hot-pressed with 5% MgO	7.6-7.9	10.0
1.7	CVD	7.5-8.8	9.38

* Calculated

TABLE 1.2 : Microwave Permittivity of Theoretically Dense Si_3N_4

CHAPTER 1

REFERENCES

1.1 J.T. Milek, Handbook of Electronic Materials, Vol.3 IFI/Plenum(1971).

1.2 W.M. Wells, Silicon Nitride as a High-temperature Radome Material. Reference UCRL 77 95, (1964).

1.3 W.B. Westphal and A. Sils, Dielectric Constant and Loss Data. Report AFML-TR-72-39, AD 746686, (1972).

1.4 J.D. Walton, Proceedings of 11th Electromagnetic Window Symposium. Atlanta, Ga 1972, p.103.
Amer Ceramic Soc, Bulletin 53 (3) 255 (1974).

1.5 G.S.Perry and T.R.Moules, Proceedings of 12th Electromagnetic Window Symposium, Atlanta Ga 67 (1974).

1.6 D.R. Messier and P.Wong, Proceedings of 13th Electromagnetic Window Symposium, Atlanta, Ga 3 (1976).

1.7 G.S. Perry, Private Communication.

1.8 K.S. Mazdiyasni and C.M.Cooke, J. Amer.Ceramic Soc, 56 (12) 628 (1973).

1.9 J.S.Thorp and R.I.Sharif, J.Mat.Sci. 11, 1494,(1976).

1.10 J.S.Thorp and R.I.Sharif, J.Mat.Sci. 12, 2274, (1977).

1.11 J.S.Thorp and R.I.Sharif, J.Mat.Sci. 13, 441, (1978).

1.12 T.W. Dakin and C.N.Works, J.Appl.Phys. 18, 789, (1947).

CHAPTER 2

REACTION BONDED SILICON NITRIDE - THE MATERIAL AND ITS PREPARATION

There are two industrial (dirty) methods of manufacturing silicon nitride ; namely hot pressing and reaction bonding. Although this thesis is concerned primarily with Reaction Bonded Silicon Nitride (RBSN), a comparison of the two methods is necessary to demonstrate the advantages to be gained from reaction bonding.

2.1 HOT PRESSED SILICON NITRIDE (HPSN)

Hot pressing yields full density high strength nitride with little or no porosity. Silicon powder is reacted with dry nitrogen at about 1400°C to produce a powder of nitride. This conversion to nitride is almost complete as the fine powder nature of the starting silicon allows nitrogen to react with all the available silicon. The nitride so produced has, predominantly, the α-structure (see section 2.4).

This RBSN powder is then hot pressed in air at 1700° C in a graphite die at between 1-2 tons per square inch to yield a fully dense nitride with the β structure. HPSN has, generally, greater strength than RBSN, due in the main to its pore free nature, however it is not possible to hot press complex shapes. The machining now required to produce a particular item in HPSN is a lengthy and costly operation.

2.2 REACTION BONDED SILICON NITRIDE (RBSN)

By contrast with hot pressing reaction bonding produces, at best, a material having only 80% of the theoretical density of silicon nitride, and about 20% porosity. Additionally the material contains an amount of unreacted silicon, dependent mainly upon the care taken in processing. The production is in two stages, the first being silicon sintering and machining which is followed by nitriding ; these are considered in more detail overleaf.

2.2.1 Silicon sintering and machining The starting material is again silicon powder. The particle size and impurity levels are given in Table 2.1. It will be noted that two different particle sizes are used. All the samples studied in the present work were manufactured from micronised powder. For most purposes the 'green' ceramic is produced by pressure sintering of the silicon powder, typical production parameters are:-

Pressure 185 $Mn.m^{-2}$

Temperature $1200^{o}C$

in an argon atmosphere. Other methods are injection moulding, (in which an organic binder is used, and burned off before nitriding) and slip casting. The green ceramic is relatively soft, and may be machined with ease. This allows complex patterns to be produced in a manner not available to the hot pressing process.

2.2.2 Nitriding of RBSN The green ceramic is nitrided in an electrically heated furnace employing silicon carbide electrodes. The development furnace used by AME to manufacture the samples used in this work is shown in Plate 1. The furnace was operated under a slight positive pressure of dry nitrogen, such that nitrogen was supplied according to reaction demand, rather than to change the atmosphere continually. A furnace temperature and pressure profile designed to produce complete nitridation is given in Figure 2.1. The degree of nitridation can be controlled by alteration of the furnace profile. Details of the profiles used for the current samples are given in section 2.5. The products of reaction bonding are dimensionally stable to about 0.1%. thus no more than a light dressing off operation is required on the patterns produced in the green ceramic. This is in stark contrast to the post manufacturing machining required for hot pressed materials. It is clear that if RBSN performs satisfactorily in other respects, it shows remarkable advantages over HPSN.

PLATE 2·1 FURNACE USED BY A.M.E. Ltd. FOR THE PRODUCTION OF RBSN USED IN THIS WORK

Impurity	AME powder (w%)	Commercial Powder (w%)
Fe	0.45	0.90
Al	0.25	0.20
Ca	0.052	0.30
Ti		0.10
Oxygen		1.0 (native oxide)
Particle size	Standard micronised 90% < 30μm	15μm (mean)

TABLE 2.1 Impurities in silicon powder used in RBSN manufacture

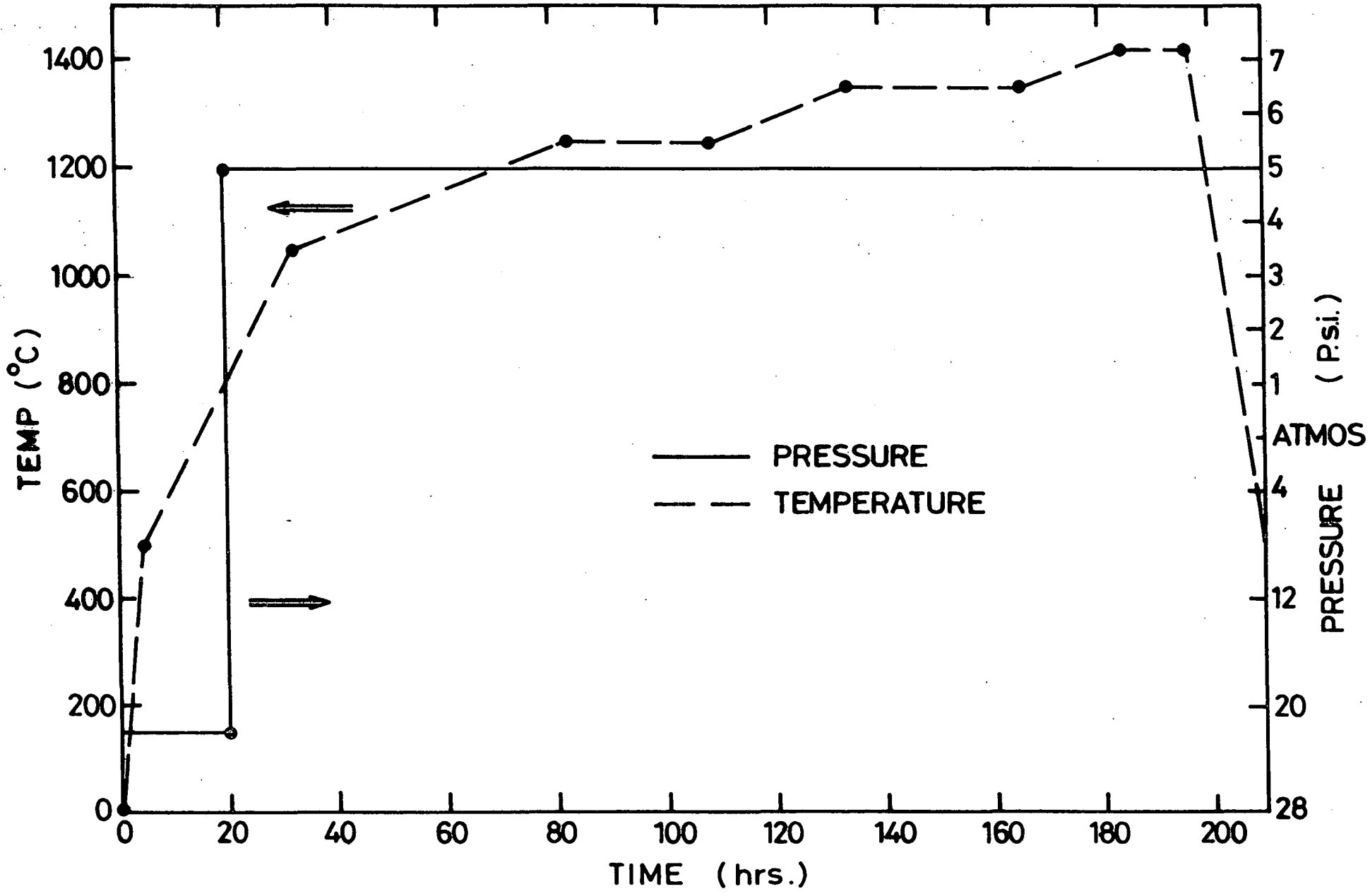

FIG. 2·1 TYPICAL NITRIDING RUN FOR "FULL WEIGHT GAIN" NITRIDE
(THIS SCHEDULE USED FOR RUNS 7 & 8 , TABLE 2·2)

The degree of nitridation referred to previously is conventionally called the 'weight gain' of the ceramic. This figure is an expression of the percentage by which the weight of the green ceramic has increased in the reaction. The maximum possible weight gain is 66.5%, which is calculated by assuming that all the available silicon is converted to silicon nitride. In practise the maximum weight gain which is achieved is about 64.5%, which implies that a small amount of free silicon remains in the reacted nitride, and that the reaction is limited not by silicon exhaustion, but by the inability of nitrogen to reach the remaining silicon.

2.3 FORMATION MECHANISM FOR RBSN

It is not proposed here to present an exhaustive survey of work done in an attempt to explain the formation of RBSN. Recently, however, Boyer & Moulson(2.1) and Moulson(2.2) have proposed a mechanism which accounts for the variations in the reaction caused by the presence of impurity iron in the starting silicon powder. An outline of this is presented here because, due to the relatively high levels of iron present in the AME materials used in this work, it is felt that this is the most likely model to consider.

Two steps have been proposed with this formation mechanism

(a) The dominant process is the volatilization of Si (via molten silicon alloys) and its subsequent vapour phase reaction with N_2, a CVD process leading to the formation of α-Si_3N_4

(b) Solution of nitrogen in liquid alloys occurs with formation of β-Si_3N_4; essentially a vapour, liquid, solid reaction process.

These two reactions are consistent with the dimensional stability of nitridation noted previously, as they allow reaction within, and unrestrained by, the bounds of the green ceramic, despite a 22% change in volume on conversion of Si to Si_3N_4. The iron impurity plays a major role in this

model. Figure 2.2 shows the behaviour of iron schematically. The iron, which is usually present as a result of steel ball mill grinding of the silicon powder, has three effects. Firstly to catalyse the removal, via SiO, of the native oxide covering the silicon particles, secondly to promote the growth of β-Si_3N_4 as a result of the solution of nitrogen in liquid FeS_2, and thirdly by the release of silicon vapour from the molten FeS_2 to allow the CVD reaction with nitrogen described above. The amount of Fe induced β growth is seen to be proportional to Fe concentration. The α growth does not exhibit such proportionally but is nevertheless the dominant process at Fe concentration levels above a few ppm. Figure 2.3 (after Boyer & Moulson (2.1)) shows this. This type of iron promoted growth predicts a nitride with α:β ratio between 1.5 and 8.0 according to iron concentration. This is consistent with the ratios found in commercial RBSN, and with those measured in the fully nitrided ceramics used here; see Table 2.2

2.4 STRUCTURE OF SILICON NITRIDE

Crystalline Si_3N_4 exists in the two forms referred to previously, those designated α and β. Both structures are hexagonal and both have a basic building unit of the silicon-nitrogen tetrahedron joined so that each nitrogen is shared by three tetrahedra. The most likely lattice parameters are, for α, a = 7.755 Å, c = 5.616 Å, and for β, a = 7.606 Å, and c = 2.907 Å. The theoretical densities calculated from these results are, for α, 3185 $Kg.m^{-3}$ and for β, 3196 $Kg.m^{-3}$. (2.3) Ruddleston and Popper (2.4) have suggested the structures shown in Figures 2.4 and 2.5 for the α and β structures respectively. Silicon atoms lie at the centre of tetrahedron with nitrogen atoms at each corner. The points in Figures 2.4 and 2.5 represent Si atoms and the numbers represent their heights, as fractions of the c spacing, above an

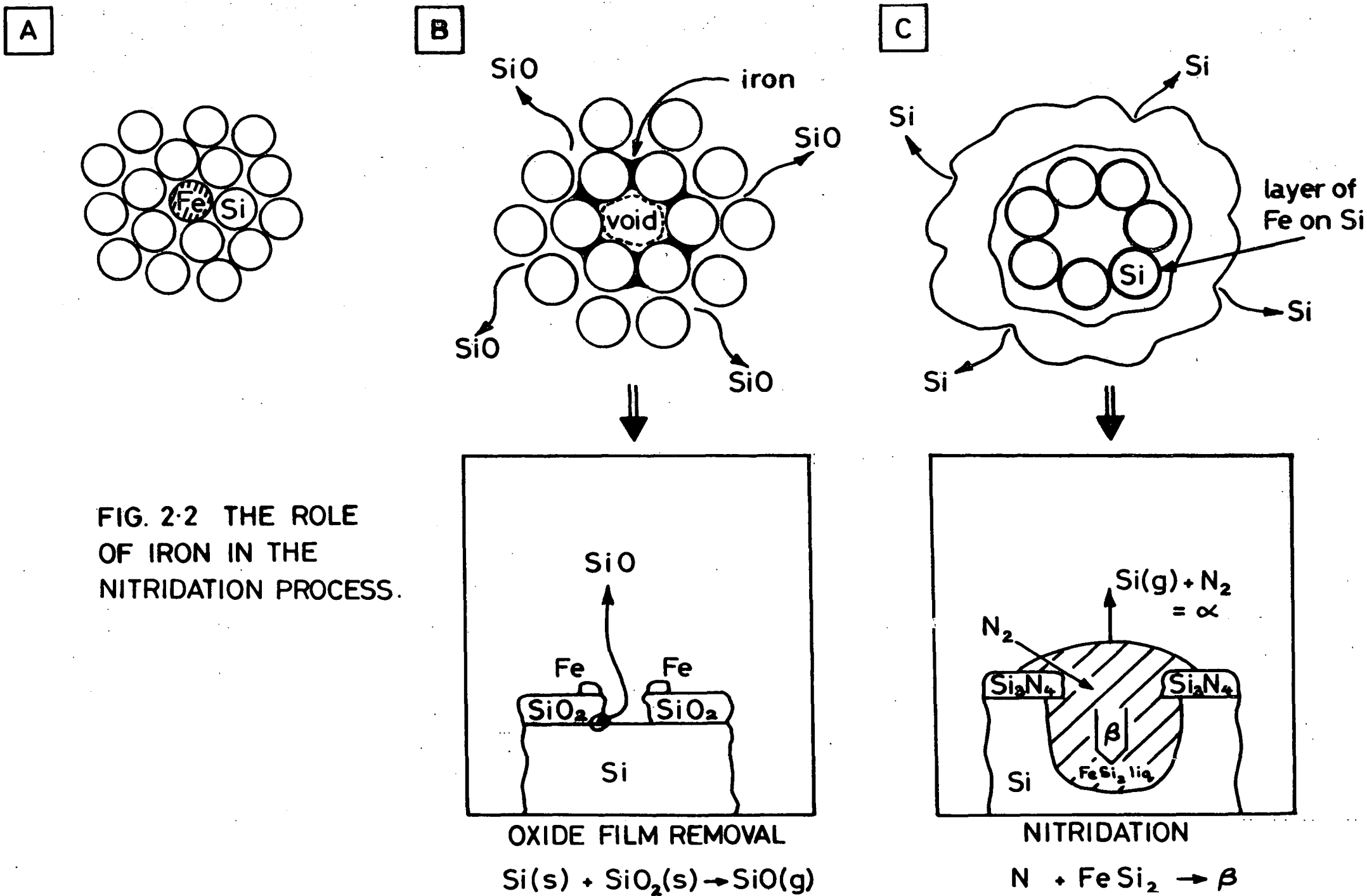

FIG. 2·2 THE ROLE OF IRON IN THE NITRIDATION PROCESS.

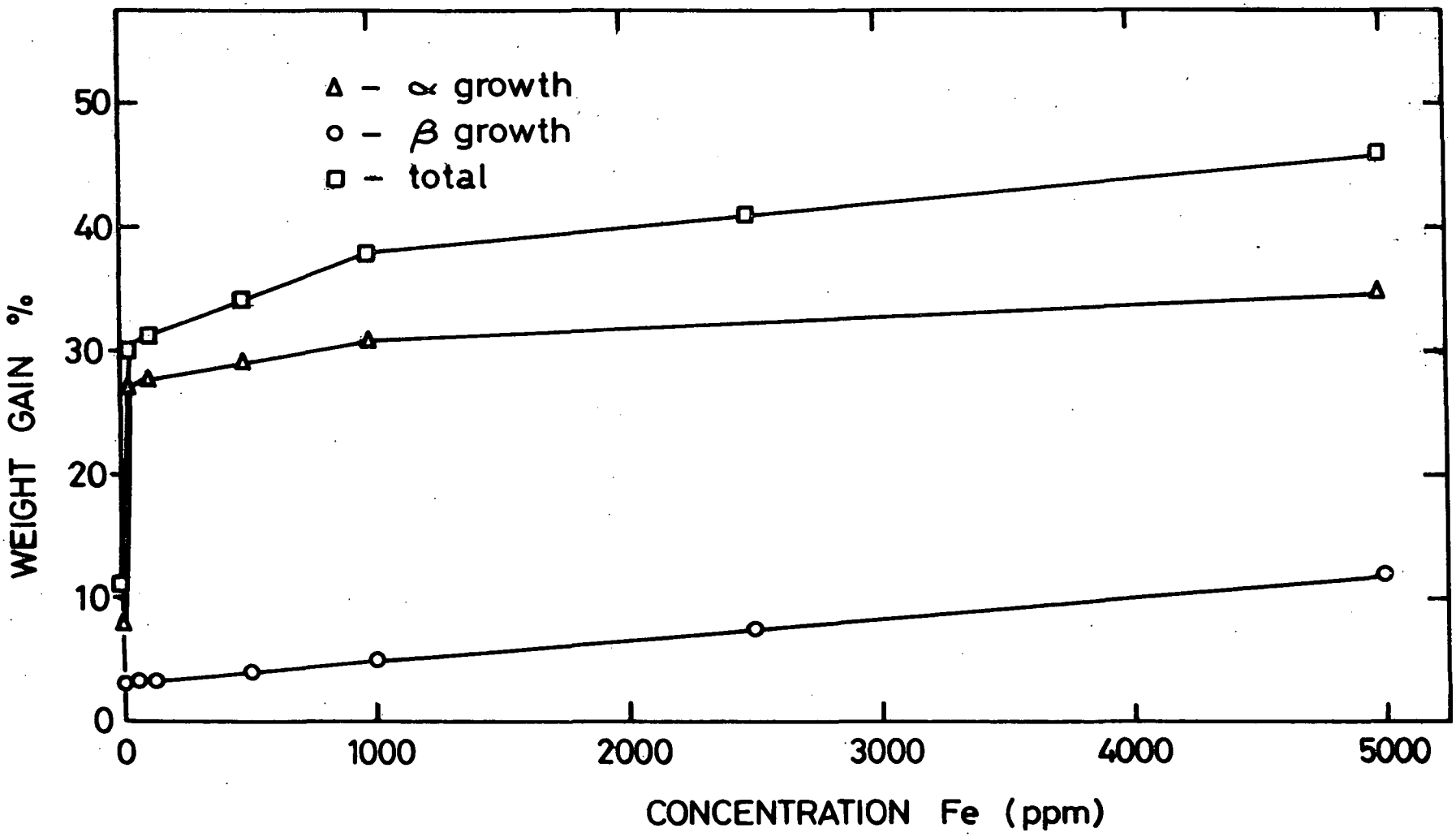

FIG. 2·3 DEPENDENCE OF α- AND β- Si_3N_4 YIELDS UPON Fe CONCENTRATION ; HIGH PURITY Si AND Fe ; 1350°C FOR 10 HRS. ; 760 TORR. N_2 (AFTER BOYER & MOULSON)

Firing Run	Figure Ref.	Range of weight gain (%)	Nitrided density ($Kg.m^{-3}$)	C_p	C_{si} (see text)	C_{sn}	Density 'green' ceramic	Approx. α : β ratio	Peak temp. (^oC)
1	2.6	18-22	1.95	0.281	0.391	0.327	1.60		1250
2	2.7	32-35	2.15	0.252	0.264	0.484	1.60		1240
3	2.8	34-42	2.24	0.238	0.206	0.555	1.60		1150
4	2.9	39-44	2.25	0.235	0.190	0.575	1.60		1340
5	2.10	44-49	2.35	0.221	0.132	0.646	1.60		1370
6	2.11	52-58	2.40	0.214	0.100	0.646	1.60		1440
7	2.1	55-59	2.54	0.195	0.015	0.790	1.60	1.5	1440
8	2.1	62-65	2.52	0.196	0.021	0.783	1.53	6.7	1440

TABLE 2.2 Preparation and composition data for the nitrides used in this work

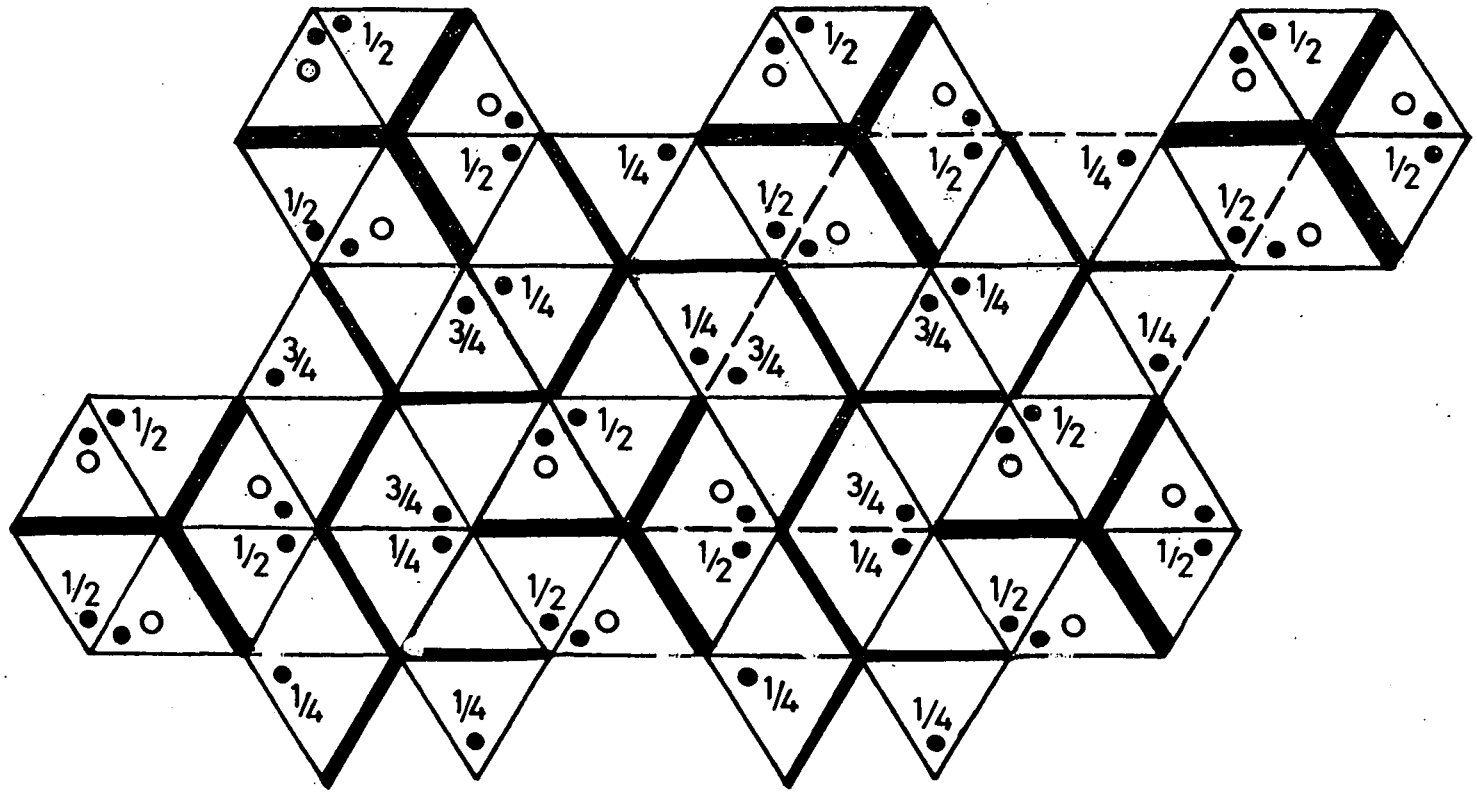

FIG. 2·4 SCHEMATIC CRYSTAL STRUCTURE OF αSi_3N_4

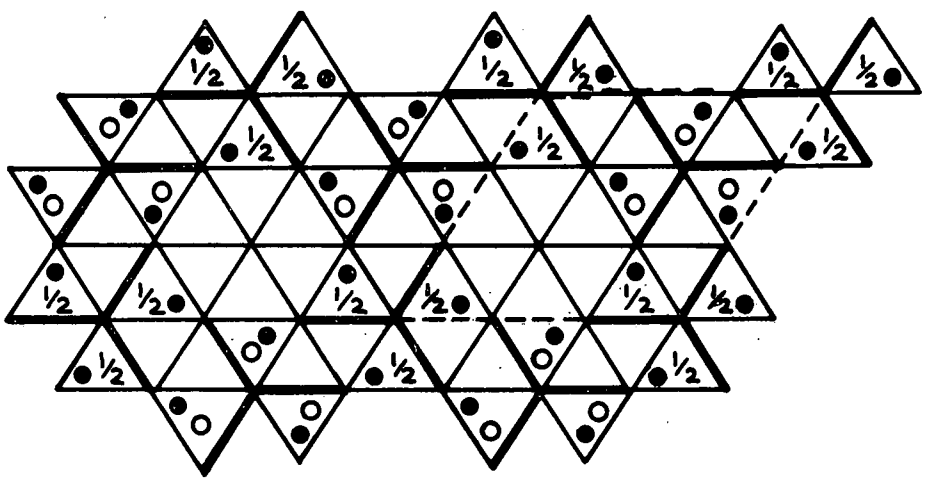

FIG. 2·5 SCHEMATIC CRYSTAL STRUCTURE OF β-Si_3N_4

arbitrary basal plane. The bold lines represent the edges of tetrahedra which lie in a plane parallel to the basal plane. The structure of α - Si_3N_4 is essentially similar to the β - structure but consists of alternate basal layers of β and a mirror image of β. Thus the c spacing of α - Si_3N_4 is approximately twice that of β-Si_3N_4.

A limited X-Ray study, using conventional powder methods has been carried out. Plate 2.2 shows the powder photographs taken:-

(a) Silicon powder supplied by AME as typical of the material used in the sample manufacture.

(b) Spectroscopically 'pure' silicon powder, for comparison.

(c) Si_3N_4 powder as supplied by AME, being 85% α - Si_3N_4

Comparison of (a) and (b), by inspection and analysis, show both to be silicon. Photograph (c) shows many more lines, as would be expected, as the hexagonal structure of Si_3N_4 has less symmetry than the cubic structure of Si. It has not been possible to analyse this plate, suggesting that the lines of both α - and β-Si_3N_4 are present.

2.5 RBSN PREPARED BY AME FOR THIS STUDY

It was stated earlier that interest has been shown in RBSN as a material for radomes, and that it must therefore behave as a radio window at microwave frequencies. A loss tangent of less than 0.01 is generally thought desirable (2.5,2.6). Further, several workers have demonstrated that the loss increases dramatically with the Si remaining unreacted, i.e. full nitridation is desirable for a low loss material (2.7,2.8)

The present work, which extended the study of partially nitrided RBSN into other areas, required samples with a range of weight gain from 0%, i.e. the green silicon compact, to 64.5% weight gain, the maximum achievable. These materials were manufactured by AME by varying the firing schedules in their development furnace. Table 2.2, shows the samples produced, with an indication of the peak firing temperatures, and

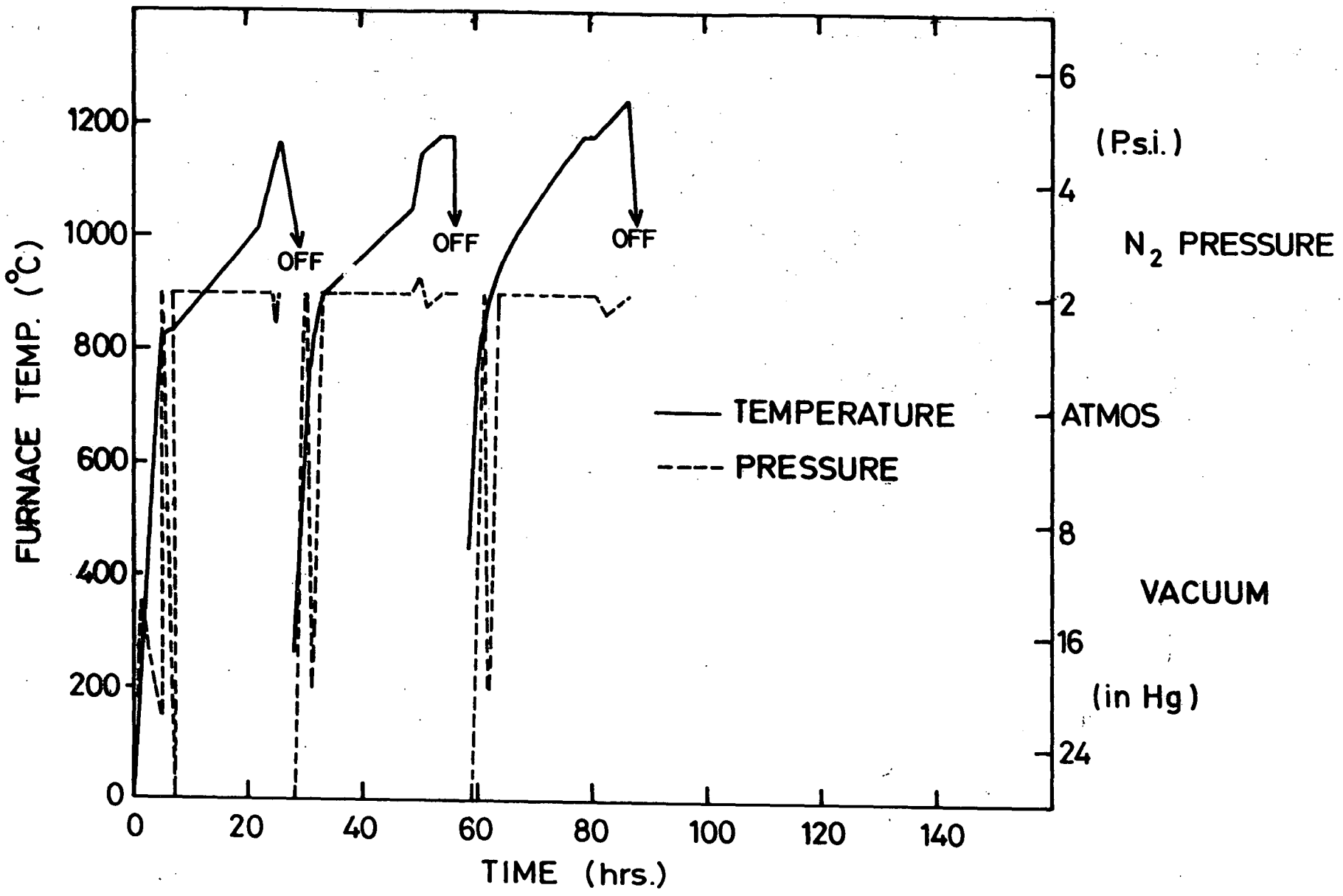

FIG. 2·6 FURNACE SCHEDULE MONITORED FOR RUN 1 , 18 - 22 % WT.GAIN

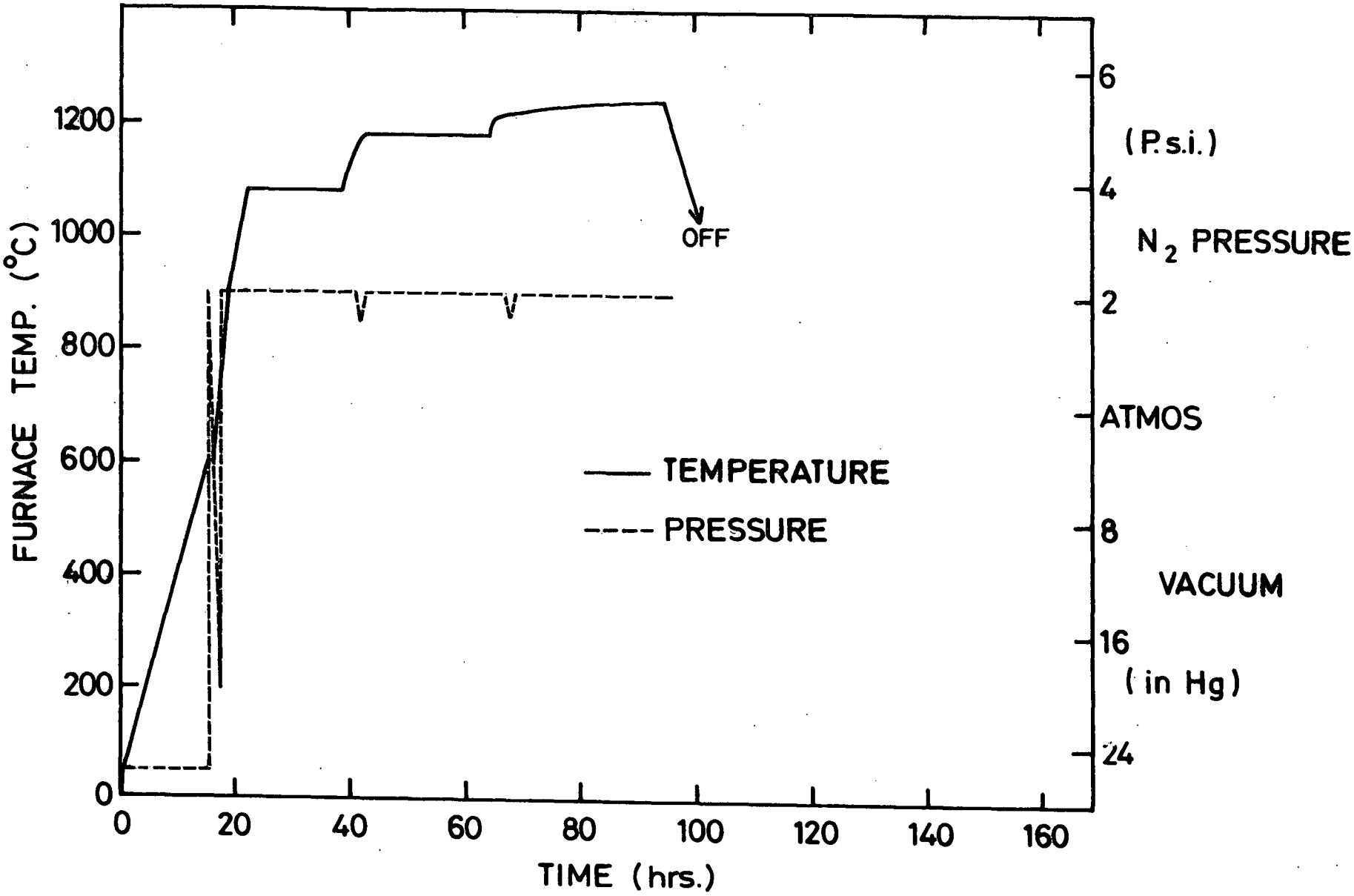

FIG. 2·7 FURNACE SCHEDULE MONITORED FOR RUN 2 , 32 - 35 % WT. GAIN

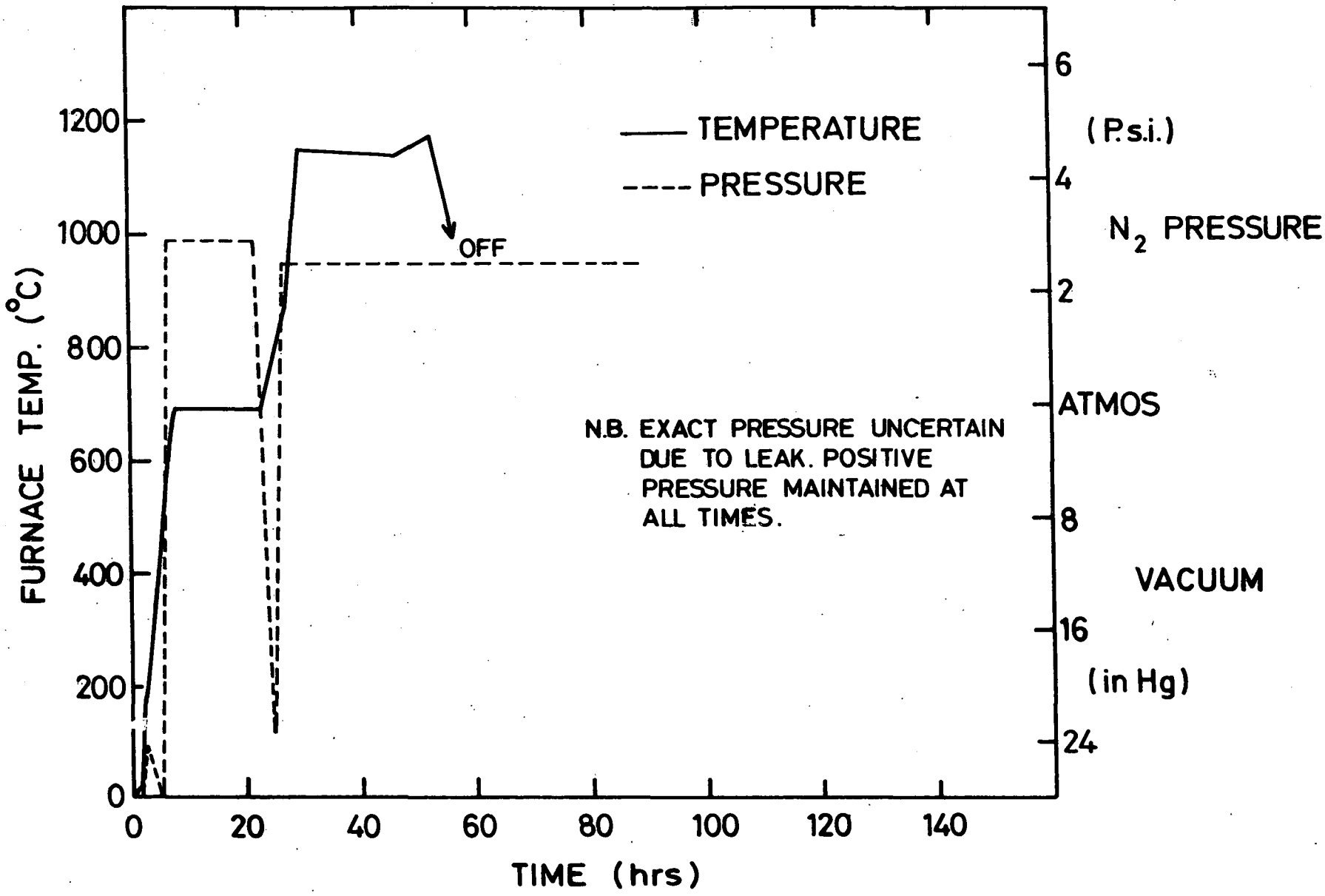

FIG. 2·8 FURNACE SCHEDULE MONITORED FOR RUN 3, 34 - 42% WT. GAIN

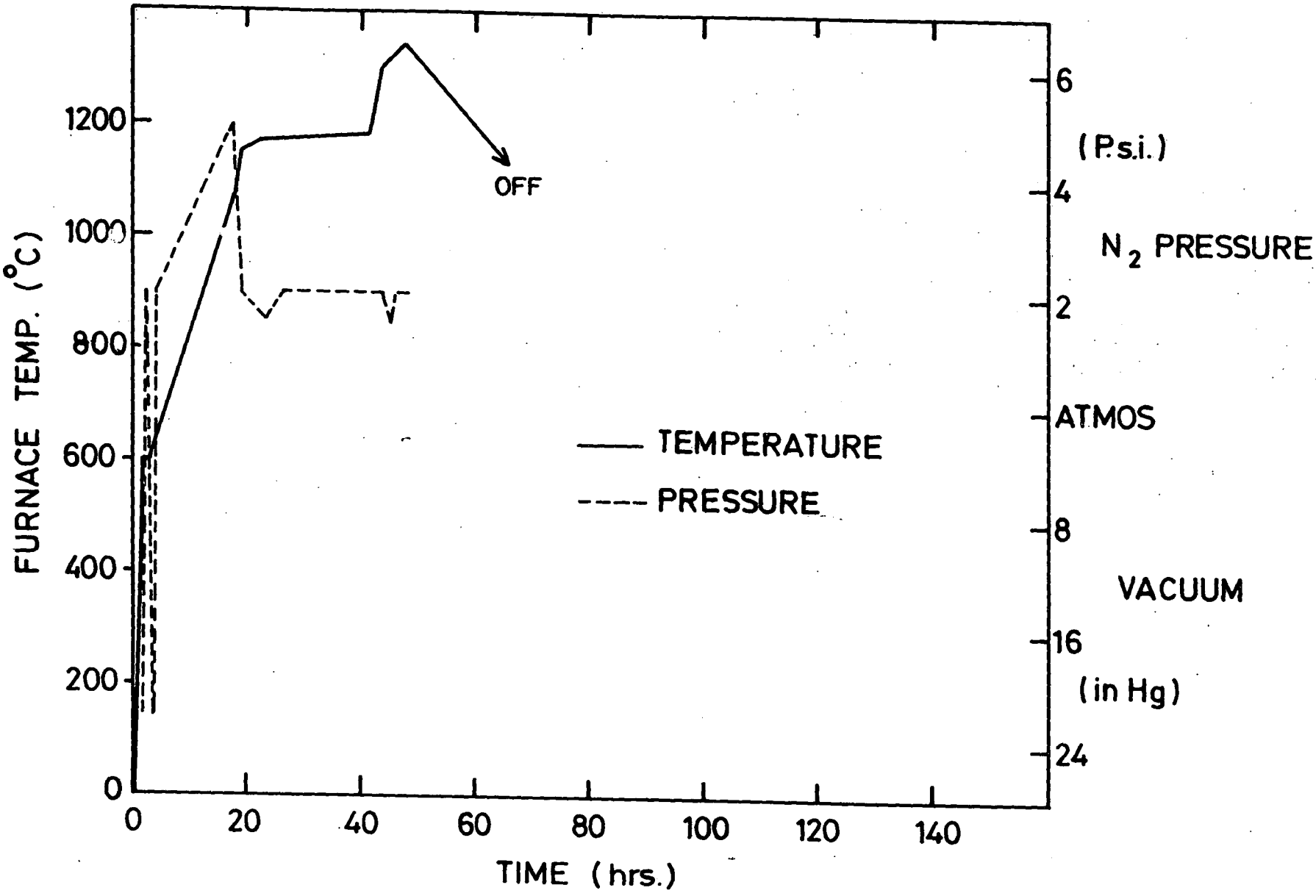

FIG. 2·9 FURNACE SCHEDULE MONITORED FOR RUN 4 , 39 - 44 % WT.GAIN

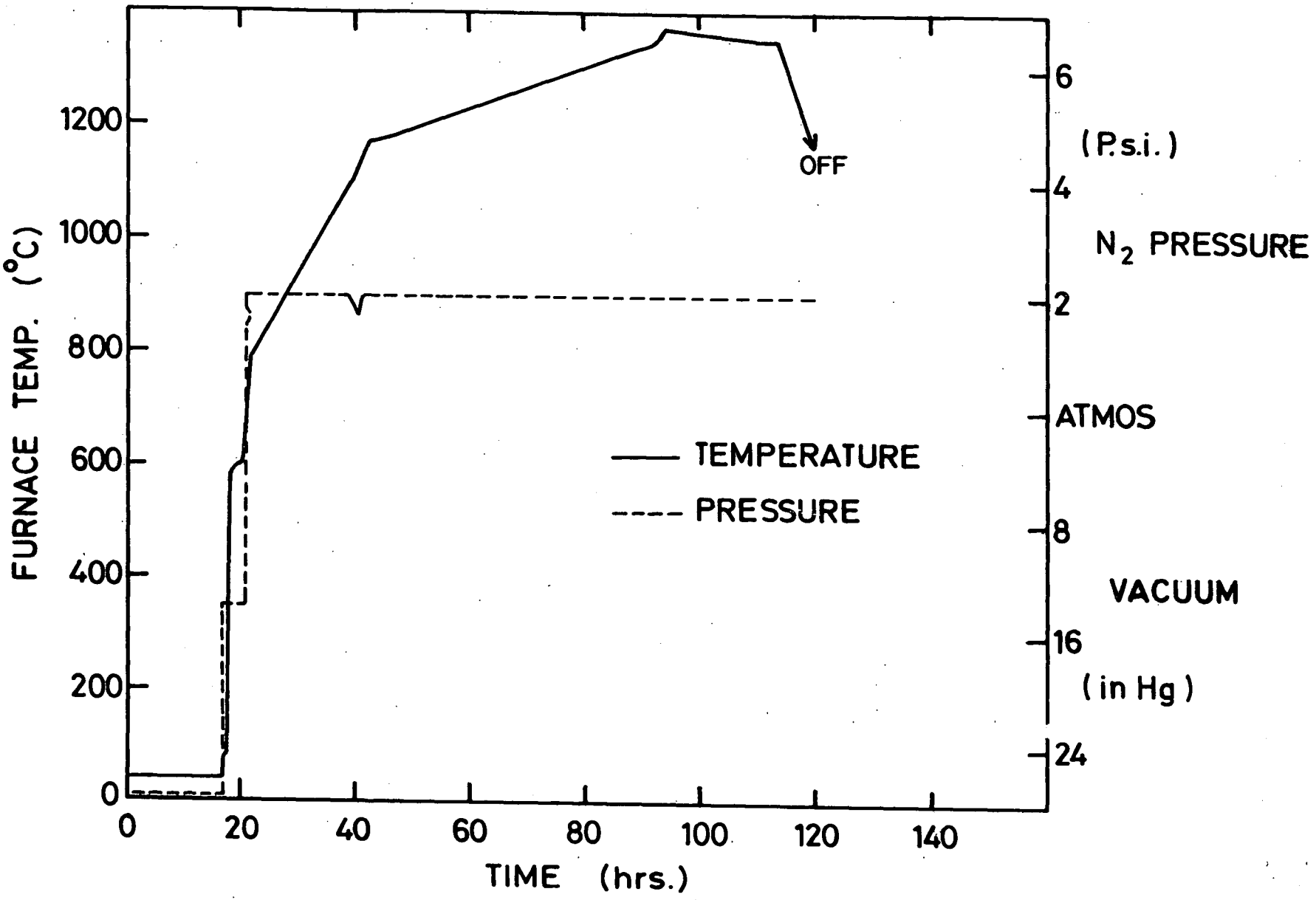

FIG. 2·10 FURNACE SCHEDULE MONITORED FOR RUN 5, 44 - 49 % WT. GAIN

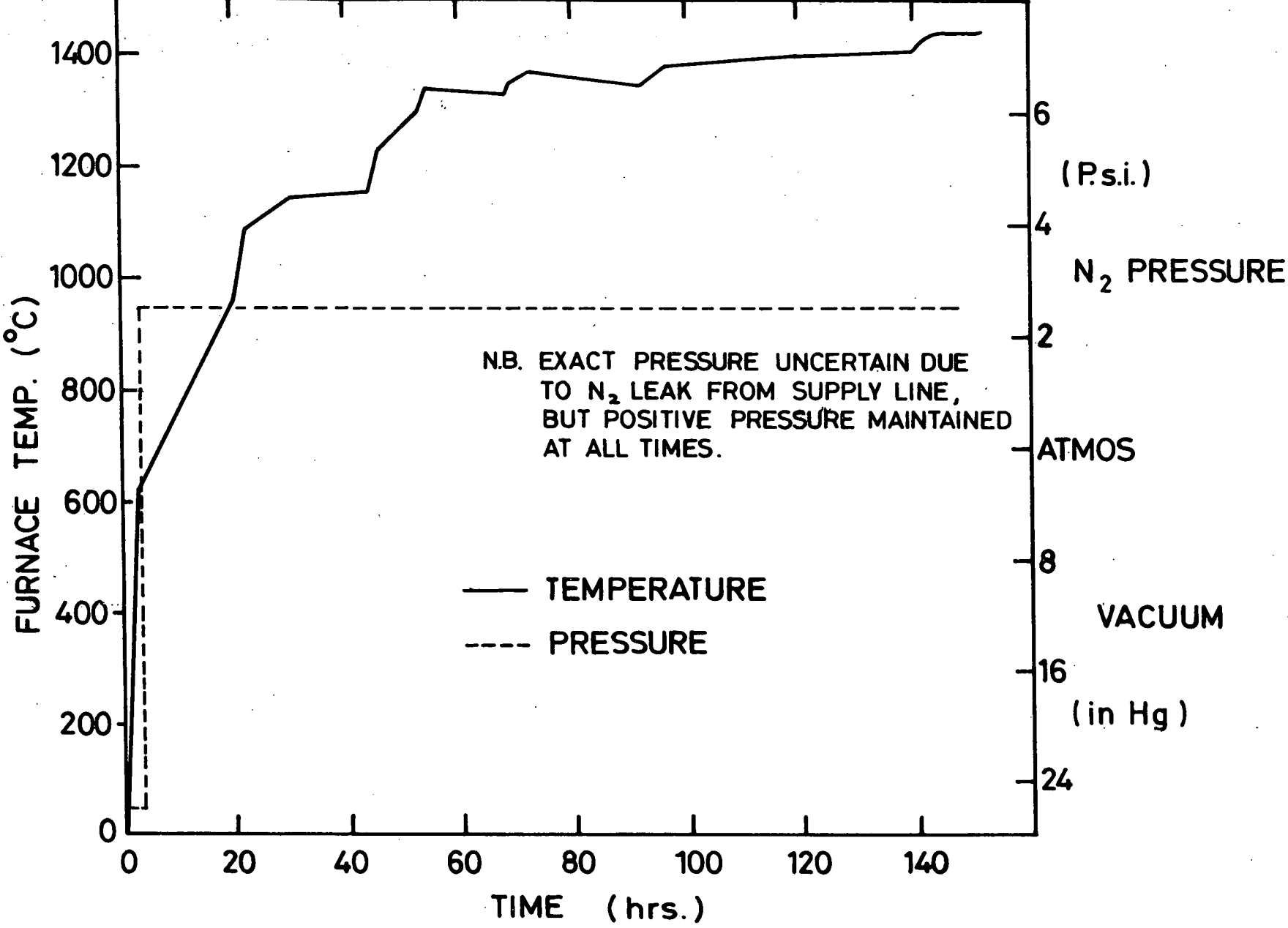

FIG. 2·11 FURNACE SCHEDULE MONITORED FOR RUN 6 , 52 - 58 % WT.GAIN

Figures 2.6 to 2.11 show the firing cycles graphically, along with the nitrogen pressure maintained in the furnace. The reasons for the apparent ambiguities in the nitriding runs are not clear; however, several points are worth making.

i. The exercise of manufacturing varying weight gain samples was an experimental one for AME, and involved the variation of temperatures and times when compared with a full nitridation schedule which itself can produce unpredictable materials.

ii. The temperature difference between Run 3, and Runs 2 and 4 which produced ceramics having very similar weight gains might be explained by reference to the uncertainty in the nitrogen supply in this run. Taking account of the chronology of the run, (it was the first following a full nitridation run) it is possible that a nitride of very low weight gain was being aimed for. The difficulty with which such a material was finally produced suggests that this is a non trivial procedure.

2.5.1 Fractional Composition The phase composition of the RBSN ceramics has a marked effect on their properties. It may readily be calculated using the relationships:-

$$C_p = 1 - 0.281\ \rho_g - 0.148\ \rho_n$$

$$C_{si} = 1.072\ \rho_g - 0.643\ \rho_n$$

$$C_{sn} = 0.791\ (\rho_n - \rho_g)$$

where C_p, C_{si} and C_{sn} are, respectively the volume fractions of porosity, Si, and Si_3N_4 in a nitrided compact. ρ_g is the density of the green ceramic, and ρ_n the density of the nitrided material. C_p, C_{si} and C_{sn} calculated for the materials used in this work are given in Table 2.2.

CHAPTER 2

REFERENCES

2.1 S. M. Boyer and A. J. Moulson, J. Mat. Sci. 13, 1637 (1978).

2.2 A. J. Moulson, J. Mat Sci. 14, 1017 (1979).

2.3 D. S. Thompson and P. L. Pratt, 'Science of Ceramics', Vol. 3, ed. G. H. Stewart (Academic Press, London, p.33 (1967).

2.4 S. N. Ruddlesden and P.Popper, Acta Cryst 11, 465 (1958).

2.5 S. J. Godfrey, J. Brit. Interplanet Soc. 22, 353 '1969).

2.6 G. S. Perry and T. R. Moules, Proceedings of 12th Symposium on Electromagnetic Windows' Ed. J. N. Harris (Georgia Institute of Technology, Atlanta, Georgia, p.67 (1974).

2.7 J. N. Harris, ibid p. 72.

2.8 D. R. Messier and P. Wong, AMMRC TR 74-21, September 1974.

CHAPTER 3

ULTRASONIC METHODS FOR THE STUDY OF SOLIDS

Ultrasonic methods are in widespread use for the study of the elastic and anelastic properties of solids, liquid and gases. For solids pulse echo methods are particularly important, and are employed both in the study of fundamental physical properties of materials and in non-destructive testing. Pulse techniques are particularly valuable for measurements at frequencies in the range 5 MHz to 50 GHz. At such frequencies plane bulk waves may be generated in samples of centimetre dimensions. In a typical solid (with longitudinal sound velocity equal to say 5×10^5 cm s^{-1}) these frequencies correspond to wavelengths of 10^{-1} to 10^{-5} cm and are many times greater than interatomic distances ($<10^{-7}$ cm). The solid can be considered to behave as an elastic continuum and the classical description of the propagation of plane waves in an elastically anisotropic medium is appropriate. In this chapter the principles of the pulsed ultrasonic methods used in the present work are described, beginning in Section 3.1 with the simple pulse echo method and continuing in Section 3.2 with pulse echo overlap, a modification of the pulse echo method used for more precise velocity measurements. The interpretation of results and the factors which can cause errors in the measurement of velocity and attenuation are discussed in Section 3.3. Details of equipment and its operation are given in Chapter 4.

3.1 PULSE ECHO TECHNIQUES

3.1.1 Basis of the pulse echo method In essence the pulse echo method is simple; it involves exciting a pulse of ultrasound in a sample with parallel end-faces and observing the multiple reflections which occur. In practice the precise measurement of ultra-sound velocity and attenuation

is not so simple and can involve many subleties of technique and interpretation.

A packet of high frequency stress waves of chosen polarisation may be introduced into the sample by use of a suitable transducer which is closely coupled to one of the end-faces of the specimen. A single transducer can be used as both the transmitter and receiver of ultrasound pulses (single-ended pulse echo method) or separate transmitting and receiving transducers can be used (double-ended method). A circular plate transducer greater than about 0.5 cm in diameter behaves as a near-ideal piston source at megahertz frequencies (>10MHz) and generates waves which are very nearly plane and have a wave-normal perpendicular to the end-faces of the specimen (and the plane of the transducer disc). The transducer may be activated by a burst of rf (rf pulse), or by a sharp rectangular pulse. Either piezoelectric (e.g. quartz crystal slices attached to the specimen with a suitable acoustic bond, or evaporated thin films of CdS or ZnO) or magnetostrictive (e.g. Ni film) transducers can be employed. In the case of a resonant transducer an rf pulse is tuned to either the resonant frequency or an odd harmonic of this.

The echo train resulting from a pulse of ultrasound may be observed by exciting the transducer with rf pulses short in duration compared to the transit time in the sample. The repetition rate of the rf pulses is kept low enough to ensure that the echoes arising from each pulse die away completely (due to losses in the sample) before the next is excited. Typically for a sample 1 cm in length, a pulse length of $\sim$1 μsec and a repetition rate of 1kHz are allowed. Each pulse is reflected back on its own path almost without loss when it is incident on the sample-vacuum (or sample-air) interface at the end of the sample (see Section 3.2). When the first echo arrives back at the transducer, a small amount of the ultrasound energy is converted back into an electrical signal, the rest is reflected at the acoustic impedance mismatch and traverses the sample again. The process repeats many

times to give a train of echoes which are amplified and displayed (often in a rectified and detected form) on an oscilloscope triggered at the same time as the pulsed rf generator. A block diagram of a typical system is given in Figure 3.1 and details of the equipment used here are given in Chapter 4.

3.1.2 Velocity and attenuation An advantage of pulsed ultrasonic techniques is that the velocity and attenuation of a mode can be measured simultaneously. The mode velocity is found from the sample length (ℓ) and the ultrasound transit time (t), the time for one complete round trip, which can be obtained by using a calibrated delay to move a time marker into coincidence with successive echoes. Corrections, which may need to be applied to the measurement, are discussed in Section 3.3.

The decay of the amplitude of successive echoes of a train is a measure of the ultrasound loses due to absorption and scattering in the material - so long as these losses are substantially greater than those due to reflection at the transducer end of the sample and other extraneous effects. Absorption and scattering processes each give an intensity loss (dI) per unit length (dx) which is proportional to the intensity (I(x)) of the beam, and thus

$$dI(x) \propto I(x)\, dx$$

so that

$$I(x) = i_o\, e^{-\alpha' x} \qquad (3.1)$$

where α' is a constant. The "attenuation" is generally defined by the relations

$$\alpha_{np/cm} = \frac{\alpha'}{2} = \frac{1}{(x_p - x_n)} \ln\left(\frac{u_p}{u_q}\right) \text{ nepers cm}^{-1} \qquad (3.2)$$

$$\alpha_{dB/cm} = \frac{20}{(x_p - x_q)} \log_{10}\left(\frac{u_p}{u_q}\right) \text{ dB cm}^{-1} \qquad (3.3)$$

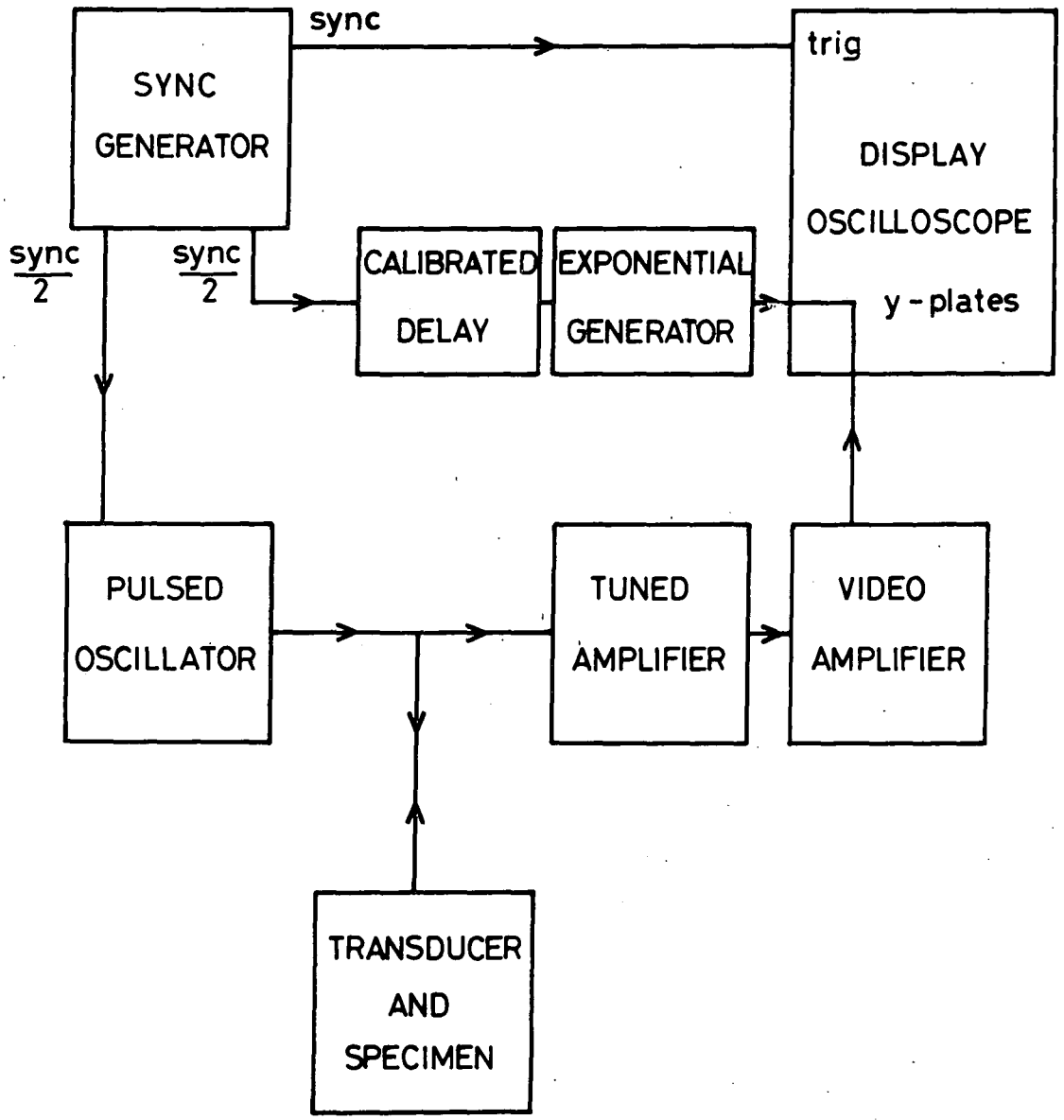

FIG. 3·1 BLOCK DIAGRAM OF THE MATEC INC. MODEL 9000 ATTENUATION COMPARATOR USED FOR SIMPLE SINGLE ENDED PULSE ECHO EXPERIMENTS

in units which measure respectively the decay of ultrasound amplitude (u) and of intensity (I) with distance (x). In units of dB μs^{-1} the attenuation is given by

$$\alpha_{dB/\mu s} = \frac{20}{(t_p - t_q)} \log_{10}\left(\frac{u_p}{u_q}\right) \text{ dB } \mu s^{-1} \qquad (3.4)$$

If the receiver is accurately linear, then the echo heights will be proportional to the ultrasound wave amplitude. The attenuation can be measured directly by fitting a calibrated exponential curve to the echo train.

3.1.3 Precision methods for measuring ultrasound velocity Although in many cases useful, valid measurements of velocity can be made directly from the echo train in the way described above, more sensitive techniques are needed if small changes in velocity are to be observed. Many such techniques have been reported. Pulse methods for precision velocity measurement include phase comparison (McSkimin (3.1) Williams and Lamb (3.2)), sing-around (Forgacs (3.3), Drabble and Brammer (3.4)), pulse superposition (McSkimin (3.5)), pulse echo overlap (May (3.6), Papadakis (3.7)) and a digital averaging technique (Lacy and Daniel (3.8)). Highly sensitive continuous wave methods including the sampled CW technique, are also used. These CW techniques have recently been reviewed by Bolef and Miller (3.9).

When the ultrasound velocities to be studied include those of impure modes with unknown polarisation and energy flux directions, pulse methods are advantageous. They allow a continuous and direct observation of the quality of the echo train, and it is possible to check that only the required mode is being excited and that spurious reflections are being avoided. In the present work on RBSN, the pulse echo overlap method has been used.

3.2 PULSE ECHO OVERLAP

The pulse echo overlap (PEO) method was introduced by May and Papadakis and improved by Chung, Chick and Silversmith (3.10), and Hellier, Palmer and Whitehead (3.11). It has since been widely used for ultrasonic velocity and attenuation measurements on thin and highly attenuating samples. This is because the PEO method requires only two good echoes for a velocity measurement, and compares with pulse superposition which, as it is essentially a summing operation, requires several more. Early pulse echo measurements had suggested that RBSN was highly attenuating, which led to the choice of the PEO method for this work.

The PEO method is a development of the basic pulse echo method, in which, by the use of electronic gating and delay circuits, echoes from different echo trains are displayed in coincidence on an oscilloscope, and a calibrated delay source is used to determine the transit time in the sample.

In principle, the method is as follows:

A frequency synthesiser is used to trigger the sweep of an oscilloscope, and also, after decade division, an RF generator which supplies megahertz pulses to a transducer attached to the sample. The received echoes are displayed on the oscilloscope. When the repetition rate of the frequency synthesiser is of the same order as the reciprocal of a multiple of the transit time, overlap (not summation) of the echo signals takes place on the oscilloscope. The exact overlap condition can now be found by concentrating on two of the echoes, which are selected by gating circuits, again driven from the synthesiser. The two chosen echoes are intensified on the oscilloscope display, and the synthesiser frequency is adjusted until all the RF oscillations in the echoes are in phase. Claims of measurements of changes in velocity of 1 part in 10^5 are made for the method and similar claims are made for the precision of velocity measurements themselves.

By this method the peaks in the observed echoes can be matched exactly and the difficulty of obtaining exact RF cycle to cycle matching experienced with the pulse superposition technique does not arise.

3.3 FACTORS AFFECTING VELOCITY MEASUREMENTS

3.3.1 The diffraction field of the transducer A finite area transducer does not behave as a perfect piston pressure source but has an associated diffraction field. Such a transducer does not generate a perfectly parallel beam of plane waves but excites a slightly divergent beam whose pressure profile varies in a complex way across the face of the transducer and into the specimen. The beam divergence can cause gross errors, or even prevent valid velocity and attenuation measurements if it causes the ultrasound beam to impinge on the sidewalls (the effect is additional to any energy flux deviation which may occur). In an isotropic medium the beam divergence angle (β) is given by

$$\beta = \sin^{-1} (1.22 \ \lambda/D) \qquad (3.5)$$

for a circular disc transducer of diameter D and a sound wavelength λ in the specimen. In the case of a small transducer with a diameter of say 2 mm, generating 15 MHz ultrasound waves in an isotropic medium with longitudinal velocity equal to 5×10^5 cm s^{-1}, the divergence is about 5° (see (Figure 3.2)).

For anisotropic media the beam is not conical and the full solution for arbitrary propagation directions is complex (Kharusi and Farnell 3.12). However a comparatively simple method for estimating the angular beam width due to diffraction spreading in anisotropic media has been suggested by Liu and Green (3.13). A finite acoustic source is considered to have associated with it a finite bundle of wave vectors, each with its own energy flux direction parallel to the appropriate gradient vector of the slowness surface.

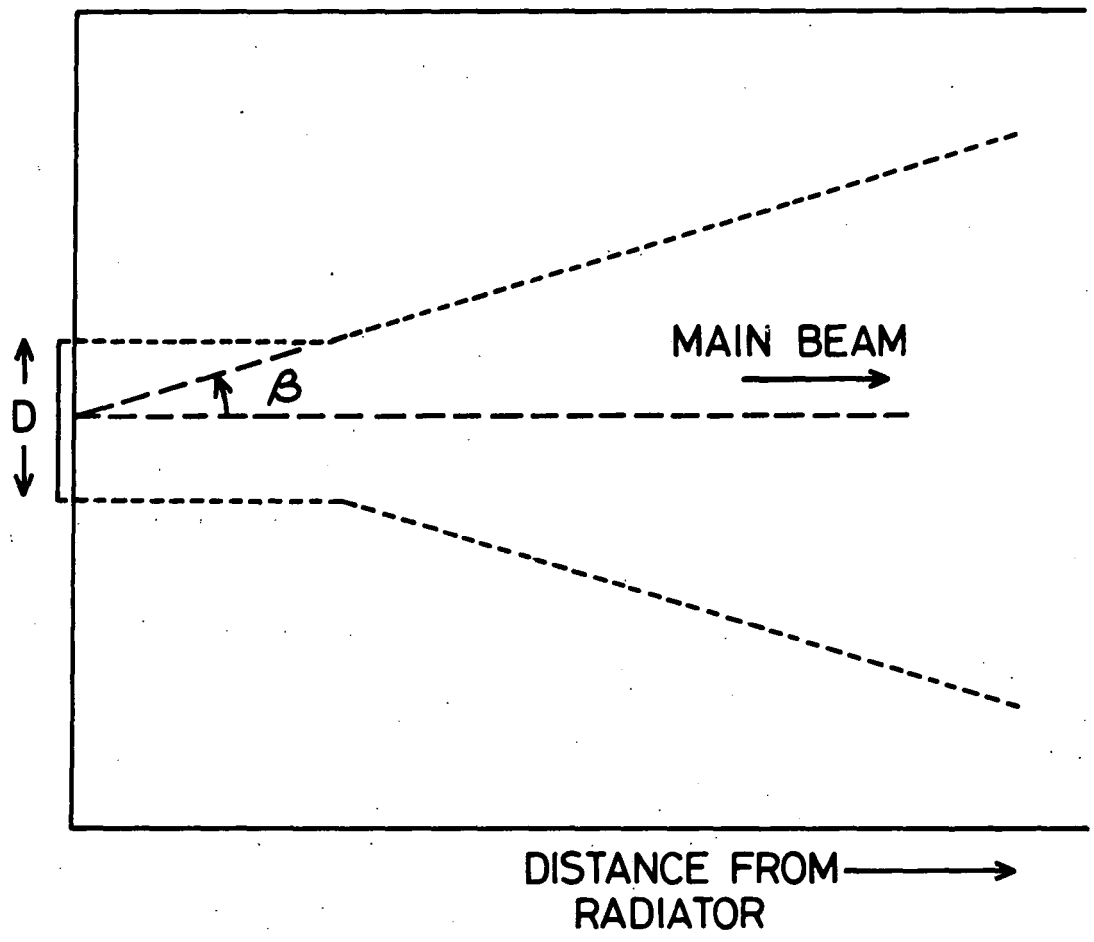

FIG. 3·2 BEAM DIVERGENCE DUE TO DIFFRACTION
(AFTER MASON 1958)

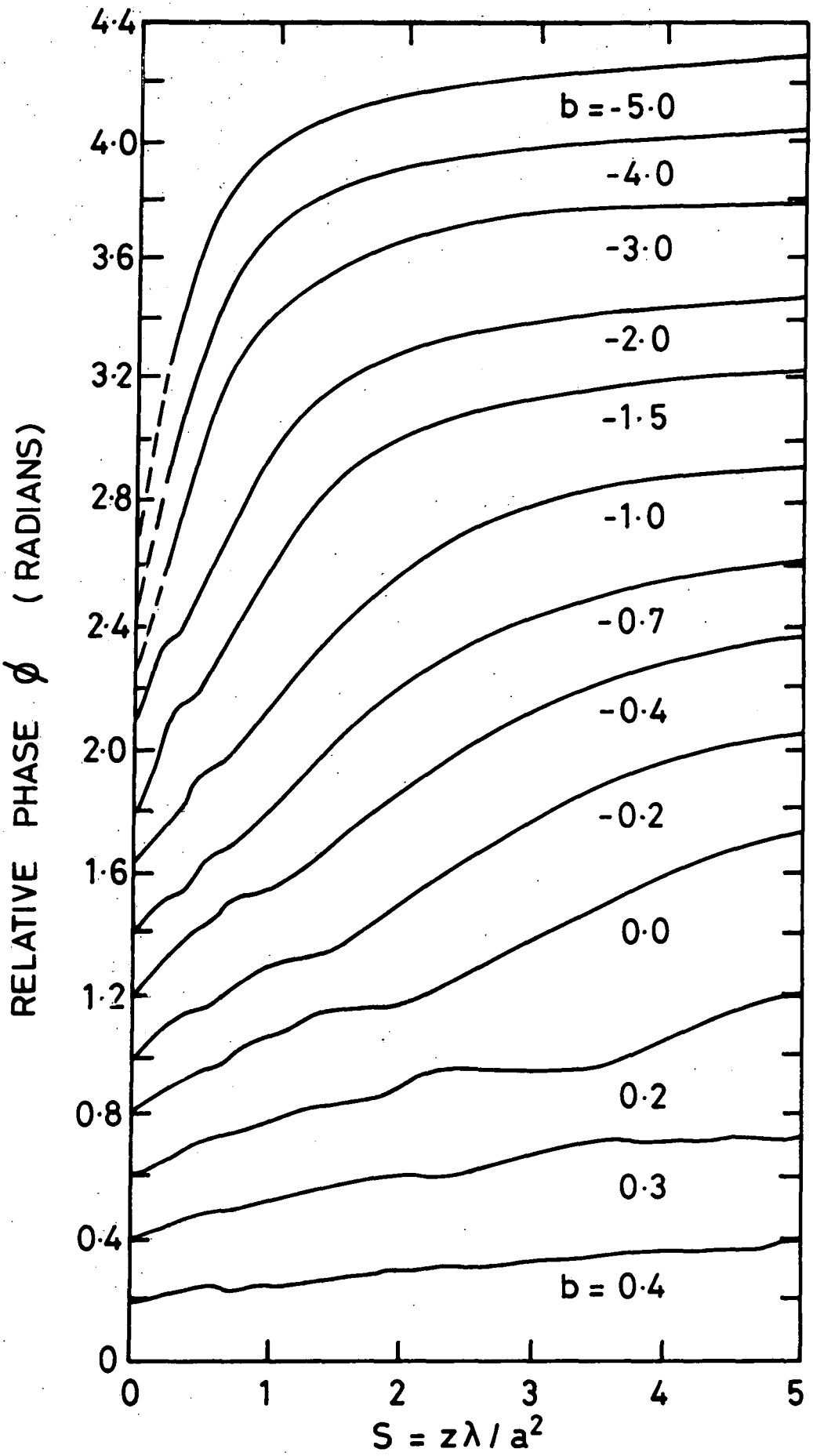

FIG. 3·3 RELATIVE PHASE ADVANCE OF PURE LONGITUDINA WAVES DUE TO DIFFRACTION AS A FUNCTION OF NORMALISED DISTANCE INTO SPECIMEN AND THE ANISOTROPY FACTOR b (after PAPADAKIS 1966

pure mode direction for which the velocity is v_o. For all values of b (see Figure 3.3) the change in relative phase shift from the source (S = 0) to infinity (S =∞) is $\pi/2$ radians. With increasing anistropy ϕ tends to approach $\pi/2$ more rapidly.

To estimate the effect of this phase advance on measurements of phase velocity, an isotropic medium can be considered. For a typical sample, say 7 mm thick, with a longitudinal velocity of 5×10^6 mm s^{-1} the diffraction effect due to the transudcer used predominently in this work (1 mm effective radius and 15 MHz) can be calculated.

The normalised distance S ($= z\lambda/a^2$) from the source for echo no's, 1, 2, 3 ... will be 4.66, 9.33, 13.99 ... etc, and from Figure 3.3, after the first echo, successive echoes will all have nearly the same relative phase, and be separated by the actual transit time in the sample. Thus, once the end error associated with the bond and transducer has been evaluated (see 3.3.3) the PEO method can be used with the second and successive echoes.

3.3.2 Non-parallelism of specimen faces In a pulse echo experiment a burst of ultrasound generated by a suitable ultrasonic transducer is reflected back and forth between opposite parallel faces of a specimen, and detected by the same or another transducer. The transducer is a phase sensitive device; any phase variations which occur over its area lead to interference and are a source of error. Such phase variations can arise if the opposite faces of a sample are not perfectly parallel. Then the reflected ultrasound wave meets the transducer at a small angle and different surface elements of the transducer detect different phases of the wave. Errors in attenuation and velocity measurement can result, and to prevent these, specimens must be prepared to high degrees of parallelism, especially for studies at higher megahertz frequencies.

For a wedged sample with wedge angle θ, it has been shown (Truell et al 3.17) that the echo pattern will be modulated by a factor

$$\frac{2 J_1 (2kna\theta)}{2kna\theta} \qquad (3.7)$$

where J_1 is a Bessel function, a is the transducer radius, n the echo number and $k = 2\pi f/v$. The form of this function is illustrated in Figure 3.4. Thus the echo train has nodes (known as the 1st, 2nd, ... zero points) at z (= $2kan\theta$) equal to 3.83, 7.01 ... and maxima at z equal to 5.1, 8.45 ... Each echo is reduced in amplitude compared with that it would have had if the sample had been parallel: the attenuation usually appears to be increased. In such a situation the measured attenuation - most conveniently obtained by fitting a calibrated exponential curve to the first echo and the maximum at $z = 5.1$ - can be corrected by use of Figure 3.4, using either the known wedge angle of a sample or an "effective" wedge angle determined by finding how the position of the first minimum depends upon the ultrasound frequency. As the ultrasound frequency is increased, this first zero moves nearer the source. (Because the values of z for each echo are proportional to frequency) and the correction required (usually in dB cm^{-1} or dB μs^{-1}) increases. However at high frequencies it is possible for the echoes to be so widely spaced in z-value that the apparent attenuation may be less than the real value and correction is then difficult. When measurements are made on samples with high intrinsic attenuation, echoes beyond the zero point at $z = 3.83$ may not be visible. In this case ($z < 1$) the modualating factor (3.7) can be simplified to $e^{-z^2/8}$ and the measured attenuation between the first and the n^{th} echo can be suitably corrected.

Although in principle the effects of non-parallelism on measured attenuation can be corrected, in practice there are several difficulties due to the limitations of the theory which (i) deals only with one-

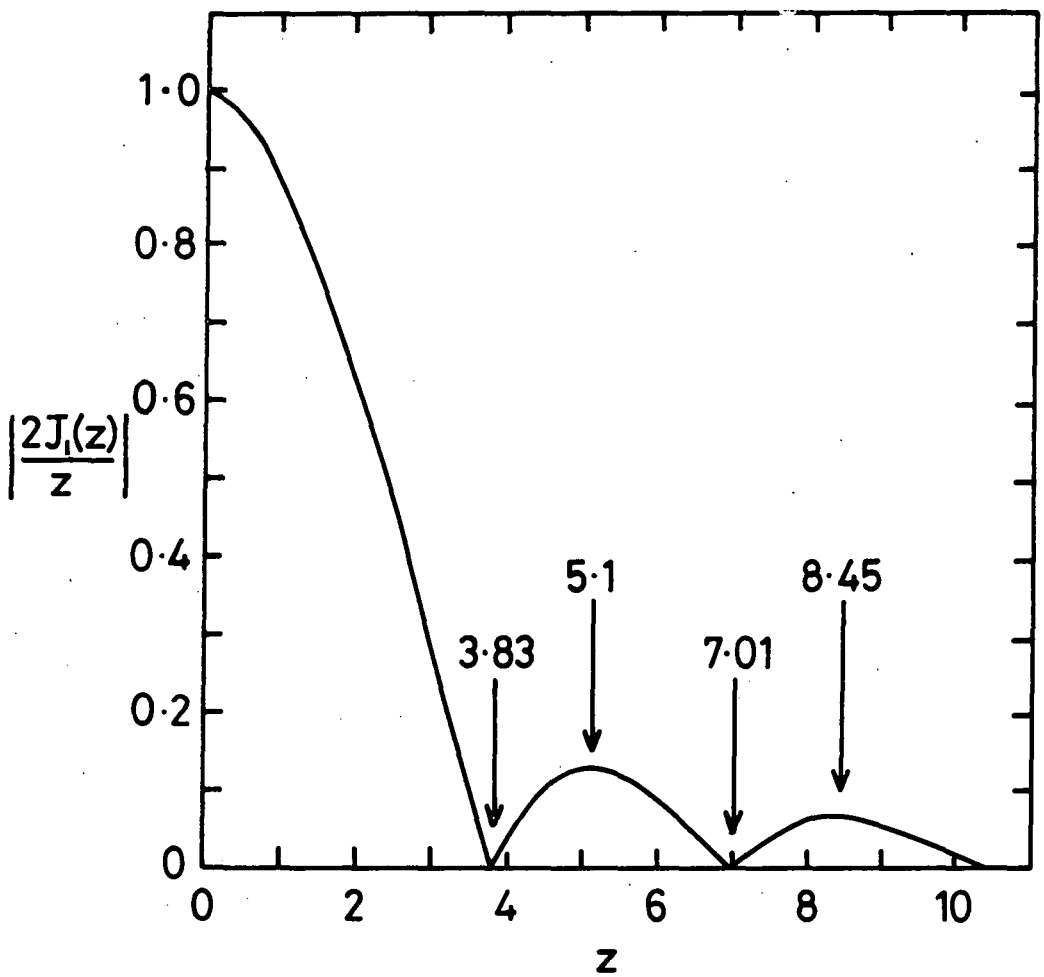

FIG. 3·4 THEORETICAL MODULATION OF ECHO PATTERN FOR A NON-PARALLEL SAMPLE

dimensional wedging in isotropic materials and (ii) cannot take account of interference which may occur if, after multiple reflections between the misoriented faces, the ultrasound beam is sufficiently deflected sideways to hit the specimen walls. Similar difficulties prevent the correction of the non-parallelism errors in measured velocities. The effects of non-parallelism, while not apparent when the simple pulse echo method is used, show up when more precise measuring techniques are employed. In the sampled-continuous wave technique, non-parallelism leads to spurious maxima which are often as large as the true resonance maxima (Miller and Bolef 1970) (3.18) Thus a prime requirement for accurate measurement of velocity as well as attenuation is an echo train with an exponetial decay. Parallelism of the opposite sample faces to better than 10^{-4} radians is required for studies at 10 MHz - or better than 10^{-7} radians at 1 GHz - and a similar parallelism of the transducer-sample bond is necessary.

3.3.3 Effect of bond length upon velocity measurements

The ultrasonic transducer and its bond to a specimen have an associated transit time. In order to obtain the full precision available from the PEO method it is necessary to evaluate this time, and deduct it from the measured transit times. The least complicated way of achieving this, as long as the samples are initially, sufficiently thick, is to measure transit times at two or three successively shorter propagation lengths. The transit times measured are plotted against sample length, and the intercept on the time axis, i.e. the transit time in the transducer and bond alone, gives the time to be deducted from the measured transit times.

CHAPTER 3

REFERENCES

3.1 H.J. McSkimin, IRE Trans on Ultrasonic Engineering PGUE-5, 25, (1957).

3.2 J. Williams and J. Lamb, J.Acoust.Soc.Am.30, 308, (1958).

3.3 R.L. Forgacs, J.Acoust.Soc.Am. 32, 1697, (1960).

3.4 J.R. Drabble and A.J.Brammer, Proc.Phys. Soc, 91,959 (1967).

3.5 H.J. McSkimin, J.Acoust.Soc.Am. 33, 12, (1961).

3.6 J.E.May, IRE Natl. Conv.Rec, 6, 132,(1958).

3.7 E.P. Papadakis, J.Acoust. Soc.Am. 42, 1045, (1967).

3.8 L.L. Lacy and A.C.Daniel, J.Acoust.Soc.Am. 52, 189, (1972).

3.9 D.I. Bolef and J.G.Miller, Physical Acoustics (eds. W.P.Mason and R.N. Thurston), 95, Academic Press, New York, (1971).

3.10 D.H. Chung, B.B. Chick and D.J. Silversmith, Rev.Sci.Inst. 40,718,(1969).

3.11 A.G.Hellier, S.B.Palmer and D.G.Whitehead, J.Phys. E, 8, 352, (1975).

3.12 M.S. Kharusi and G.W.Farnell, J.Acoust.Soc.Am, 48, 665, (1970).

3.13 J.M.Liu and R.E.Green, J.Appl.Phys. 43, 2010, (1972).

3.14 E.P. Papadakis, J.Acoust.Soc.Am. 40, 863, (1966).

3.15 H.J.McSkimin, J.Acoust.Soc.Am. 32, 1401, (1960).

3.16 H.J.McSkimin, Physical Acoustics, Vol.1A (ed.W.P.Mason) 271 Academic Press, New York (1964).

3.17 R. Truell, C.Elbaum and B.B.Chick, Ultrasonic Methods in Solid State Physics, Academic Press, New York, (1969).

3.18 J.G.Miller and D.I.Bolef, J.Appl.Phys 41, 2282 (1970).

CHAPTER 4

ULTRASONIC EXAMINATION OF REACTION BONDED SILICON NITRIDE

4.1 SPECIMEN PREPARATION

Preliminary pulse-echo measurements showed that in order to obtain good echo-trains with this material specimens having thicknesses of about a centimetre were required. Fortunately it was possible to obtain, via AME Ltd, bulk pieces of material of various degrees of nitridation which were sufficiently large for specimens to be cut from them with dimensions rather over 1 cm cube. This cutting, although rather a slow operation, was successfully completed using a diamond wheel saw. The subsequent specimen preparation is very important to the success of ultrasonic experiments. To support an echo-train it is vital that the reflecting faces be parallel to each other. If they are not, the path of the waves moves away from the original propagation direction after repeated reflections. This causes gross distortion of the echo-train as a result of the transducers receiving different phases of wave across its diameter. Each specimen had opposite cube faces carefully polished flat and parallel using a "Logitech" precision lapping machine with successively finer grades of diamond paste (down to 8 micron). The surface finish of the faces is very important since a good bond can only be made to a smooth flat surface. In general, at 15 MHz, the operating frequency used here, degrees of parallelism and flatness of 1 part in 10^4 (and a surface smoothness achieved using an 8μ diamond paste) were required. Precision micrometer dial gauges and interferometric methods were used to check the flatness and parallelism of the faces.

Quartz piezoelectric transducers have been used to generate and detect ultrasound in the specimens of reaction bonded silicon nitride. Quartz crystal

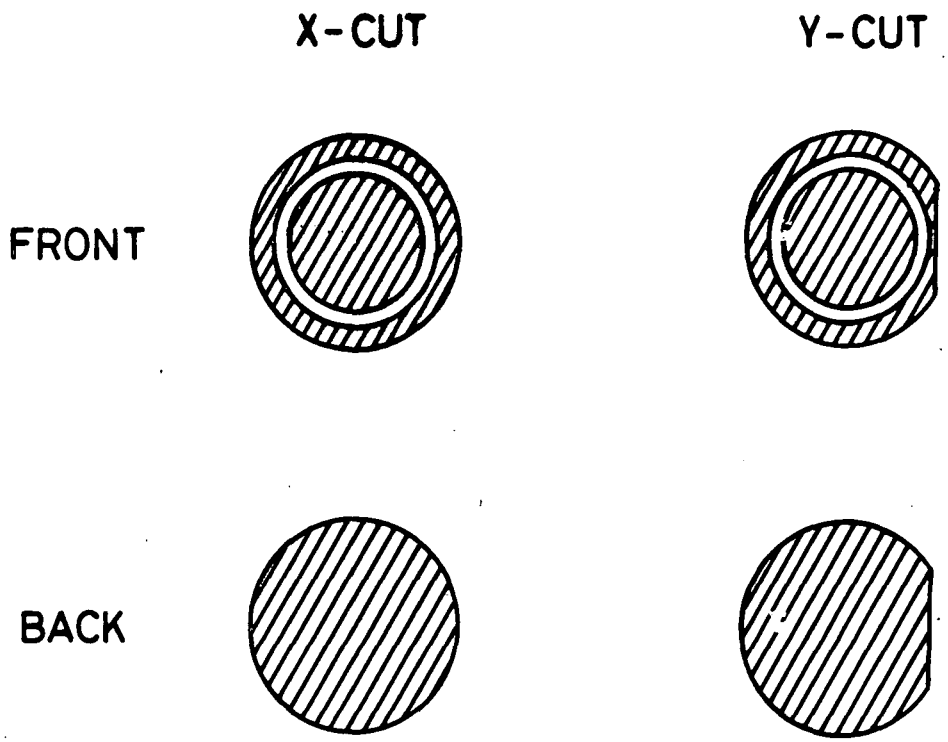

FIG. 4·1 QUARTZ CRYSTAL TRANSDUCERS SHOWING THE COAXIAL GOLD PLATING

plate transducers have some valuable advantages over evaporated film transducers ; plate transducers can be moved to different places on a sample face and the polarization direction can be rotated if required, whereas evaporated film transducers cannot be moved without being destroyed and take several hours to fabricate. Standard "X-cut" and "Y-cut" transducers were used. These transducers are cut as discs with faces normal to the X and Y axes respectively. An alternating electric field parallel to the axis produces vibration in the direction parallel to the X-axis in the first case (longitudinal transducer) and normal to the Y-axis in the second case (shear transducer). The shear transducers used were marked with a flat parallel to the vibration direction. The resonant frequency of a transducer is determined by its thickness and the appropriate velocity of sound in the quartz ; for megahertz operation, transducers need to be thin and are fragile. Two sizes of transducer (1cm or 6mm in diameter) were used. They had coaxial gold plating as shown in Figure 4.1. This form of plating allows contact to be made to both electrodes from one side, and gives an active area approximately equal to that of the centre electrode. In the course of this work transducers with resonant frequencies 15 MHz (Brooke's Crystal Co.Ltd), have been employed.

Crystal plate transducers must be attached to the specimens under test by use of a suitable bonding agent. The bond formed must be thin, parallel and must provide good acoustic coupling for longitudinal and shear waves. Many different bonding agents are in use. Permanent bonds can be obtained by applying pressure to a Au-In-Au sandwich (Sittig and Cook (4.1)), or by use of epoxy resin ; solid bonds can be obtained by use of low melting point organic solids including salol, phenyl salicylate, phenyl benzoate, benzoic acid (see Pace (4.2) for details) ; or liquid bonds may be made by use of viscoelastic liquids, oils and greases (e.g. Dow Resin 276-V9, silicone oil 250,000 c.s., Nonaq stopcock grease). The specific mechanical impedances of some of these bonding materials are given in Table 4.1.

TABLE 4.1

Mechanical properties of bonds and transducers

	Longitudinal	Shear	Ref.
Nonaq stopcock grease 25°C, 20MHz	$Z_L = 2.7 \times 10^5$	-	4.4
Dow resin 276-V9	$Z_L = 2.25 \times 10^5$	$Z_S = 0.9 \times 10^5$	4.4
	$V_L = 2.4 \times 10^5$	$v_S = 1.1 \times 10^5$	4.5
Silicon oil DC703	$Z_L = 1.37 \times 10^5$	-	4.6
Silicon oil DC200	$Z_L = 1.20 \times 10^5$	-	4.6
Quartz	$Z_L = 15.3 \times 10^5$	$Z_S = 10.4 \times 10^5$	4.4

Z_L, Z_S specific acoustic impedances in mechanical ohms cm^{-2}

v_L, v_S sound velocities in cm s^{-1}

Here the most suitable bonding materials have been found to be Dow resin 276-V9 (Dow Chemical Co., U.K., agents : R.W.Greef Co.Ltd), Nonaq stopcock grease (Fisher Scientific Co., U.K.agents: Kodak Ltd., Research Chemicals Sales) and phenyl salicylate. Dow resin is very useful at room temperatures; it is a highly viscous liquid which will form satisfactory bonds with almost any solid. To form a bond, a little resin is spread over the face of a sample with a razor blade to give a uniform thin layer, and the transducer is pressed into position with light pressure. The extremely viscous nature of the resin permits the transducer to be moved about the face of the sample as required (an important advantage of liquid bonds over solid ones). On cooling below ice temperature Dow resin freezes and the bond crumbles and fails. Nonaq stopcock grease is less viscous. Bonds are formed by placing a blob of grease on the sample face, putting the transducer in position on top of the grease and then moving it with a circular motion to expel excess bonding material. Bond preparation using phenyl salicylate is only slightly more complicated. At room temperature the material is a solid and its melting point is 42^{o}C. To form a bond the sample is placed on a hot plate at about 55^{o}C and allowed to warm. When up to temperature a few crystals of phenyl salicylate are placed on the sample surface. When these have melted, a transducer is placed on the liquid, and moved around in the same way as for Nonaq grease. When all the excess liquid has been expelled, the sample is removed from the hot plate, and allowed to cool. Great care has to be taken with all these bonding techniques to avoid transducer breakage as the transducers are very fragile.

In ultrasonic work on single crystals it may be important that transducers, especially those producing shear waves, are carefully aligned with the crystal axes. In this case a bonding material such as the Dow resin is particularly suitable, allowing, as it does, transducer movement. In the present work, the polycrystalline nature of the RBSN samples meant that this freedom was not required, so phenyl salicylate bonds were used predominantly.

4.1.1 Determination of Correction for Bond Delay

As described in section 3.3.3 the sample bond transducer system has associated with it a transit time due to the bond, and the acoustic mismatch between the sample and the transducer. This time was evaluated graphically for RBSN samples with weight gains of approximately 22.5%, and 59%, and found to be of the order of 0.03 μs in both cases. These samples had weight gains at the top and bottom of the available range, and the results suggested that 0.03 μs was a reasonable correction figure to use throughout. Figure 4.2 shows the graph obtained for the 59% weight gain sample.

4.2 PULSE ECHO OVERLAP TECHNIQUE

The pulse echo overlap system used in this work is shown in block diagram form in Figure 4.3.

The pulse modulator and receiver used was a Matec 6600 with an RF plug-in module covering the frequency range 10-100 MHz. The unit is applicable to both single and double ended experiments, and here it was configured for single ended operation. Figure 4.4 shows the single ended operation in terms of the transducer configuration, and the echoes received from the transducer. The receiver in the Matec 6600 both amplified and rectified the echoes, producing a series of echo envelopes. This meant that overlap had to be achieved using the oscilloscope Y amplifier alone. The 6600 allowed individual adjustment of pulse width, amplitude and RF frequency so that fine tuning could be carried out to obtain the most useful signal on the oscilloscope.

The whole system was triggered by a Bradley 235 frequency synthesiser with a stability of 1 part in 10^6. This was fed to the Decade Divider and Dual Delay Generator (an 'in-house' copy of a similar Matec unit). This generated Sync. pulses at the synthesiser CW frequency, and Sync.pulses at this frequency divided by 10, 100, or 1000, these latter going to the Mater Synchroniser and Exponential Generator (a Matec 1204A). The Decade

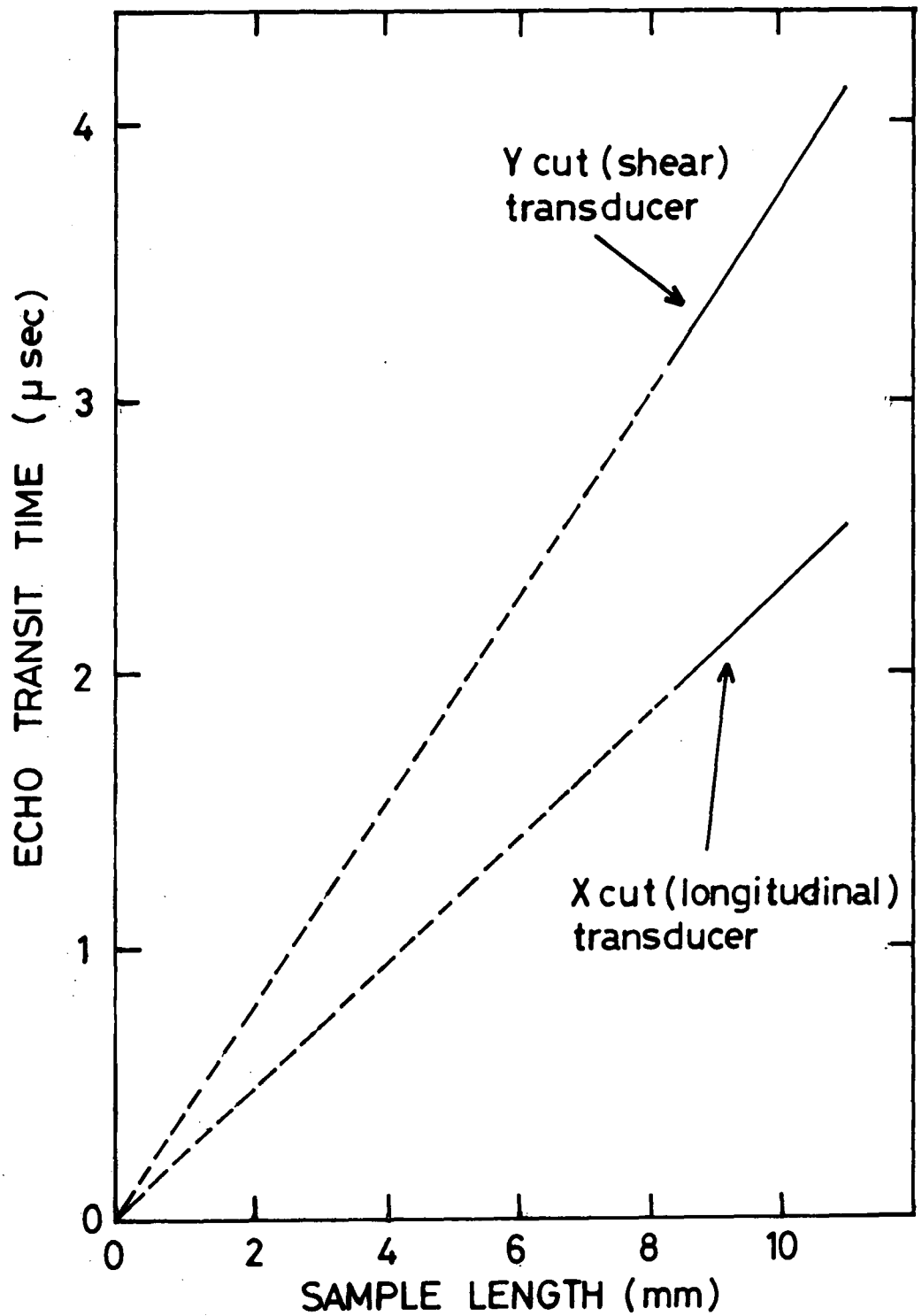

FIG. 4·2 TRANSDUCER / BOND TRANSIT TIME CORRECTION FOR A 59% WEIGHT GAIN RBSN SAMPLE

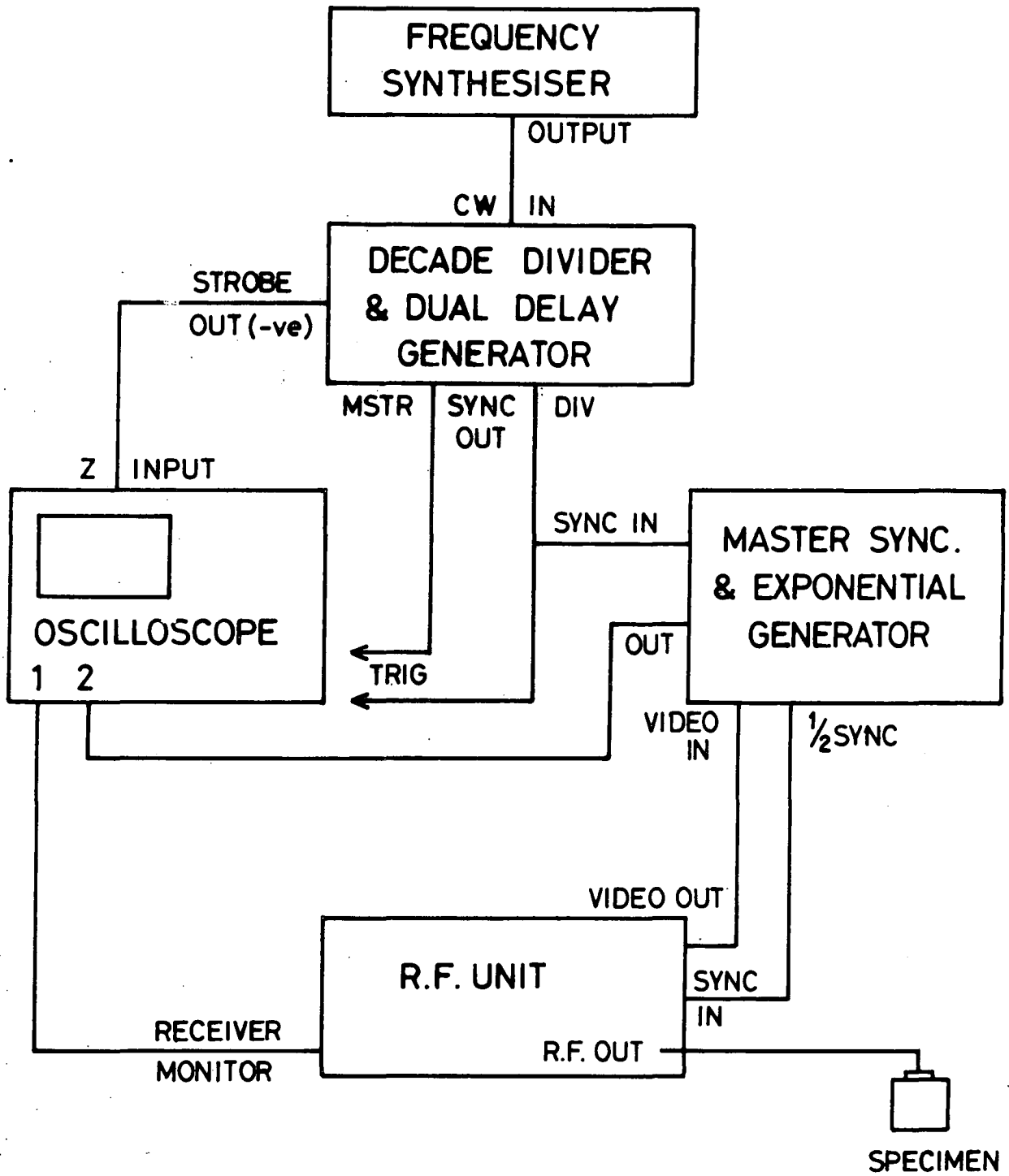

FIG. 4·3 BLOCK DIAGRAM OF THE PULSE ECHO OVERLAP SYSTEM

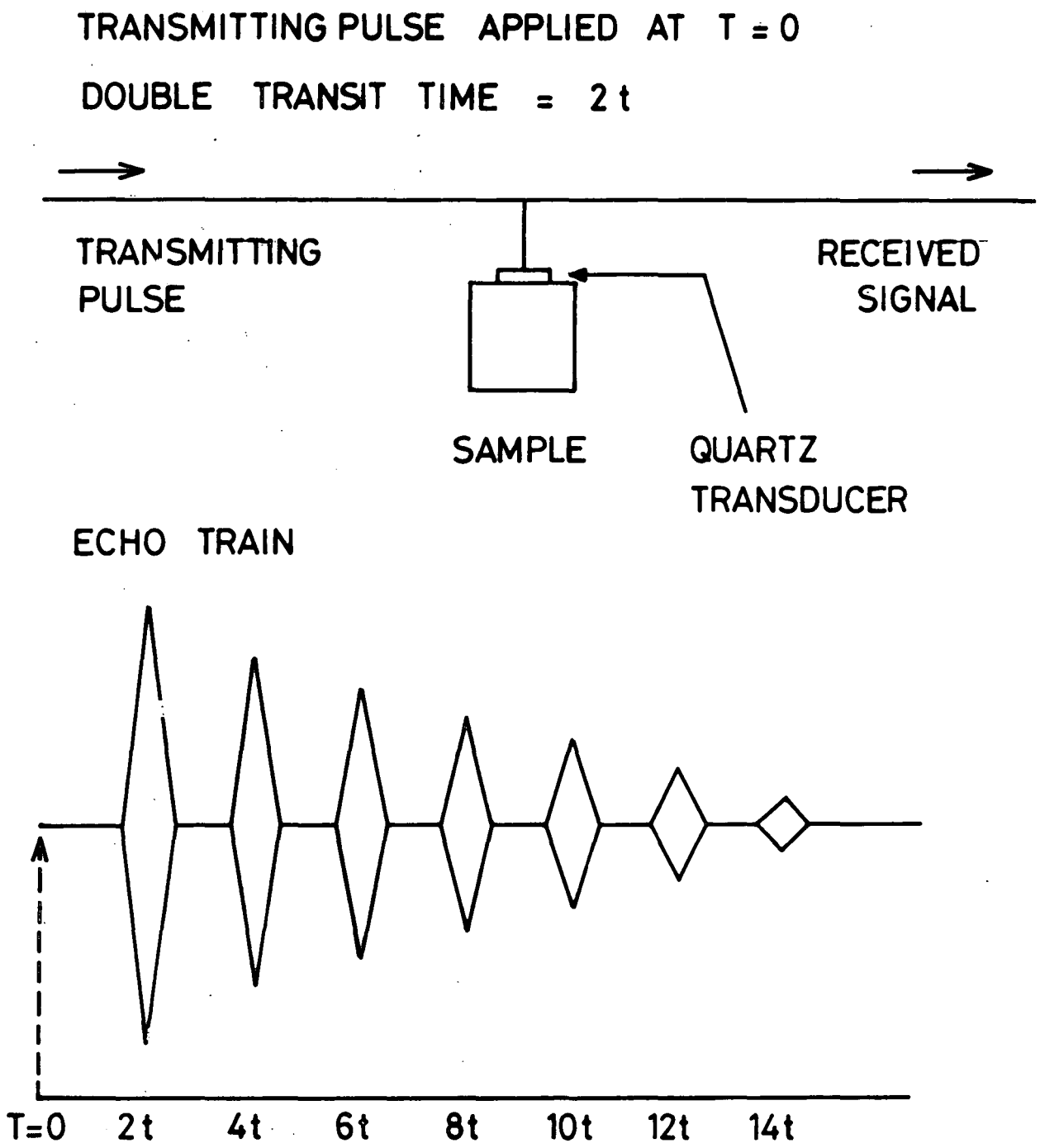

FIG. 4·4 SINGLE ENDED PULSE ECHO METHOD

Divider also provided the electronic gating necessary to observe just two overlapped echoes on the oscilloscope. The gating signal was fed to the Z input of the oscilloscope. The Master Synchroniser generated, on alternate Sync. pulses, a trigger pulse for the RF generator, and an exponential. It also received the rectified echo train and made this, and the exponential available to the oscilloscope. These could be displayed separately, successively or superimposed by choice of suitable trigger input and timebase.

4.2.1 Experimental Procedure

Initially the frequency synthesiser, set arbitrarily, was used to trigger the oscilloscope via the Decade Divider and the basic echo train (either RF or video) was displayed. A rough measurement of the transit time in the sample was made using the oscilloscope timebase. This was done to facilitate reasonably accurate setting of the synthesiser near to the expected result. Overlap may occur at multiples or submultiples of the correct frequency, and it was necessary to recognise and, at times avoid these frequencies, although they can be used intentionally. Plate 4.1 shows the RF and video echo trains.

The two echoes to be overlapped were chosen, and then intensified using the Delay, Strobe Width and Strobe Amp. controls of the Decade Divider. The rest of the echo train was suppressed on the oscilloscope by use of the 'scope Y amplifier, (Plate 4.2 (a)). By changing from divided to CW trigger for the oscilloscope, and by digit by digit adjustment of the frequency synthesiser, along with careful oscilloscope setting, exact overlap was obtained (Plate 4.2(b)).

In this condition the ultrasonic velocity for the RF pulse in the sample was given by

$$V_{us} = \frac{2\ell}{T_t}$$

where ℓ is the sample length and T_t the transit time. This initial transit

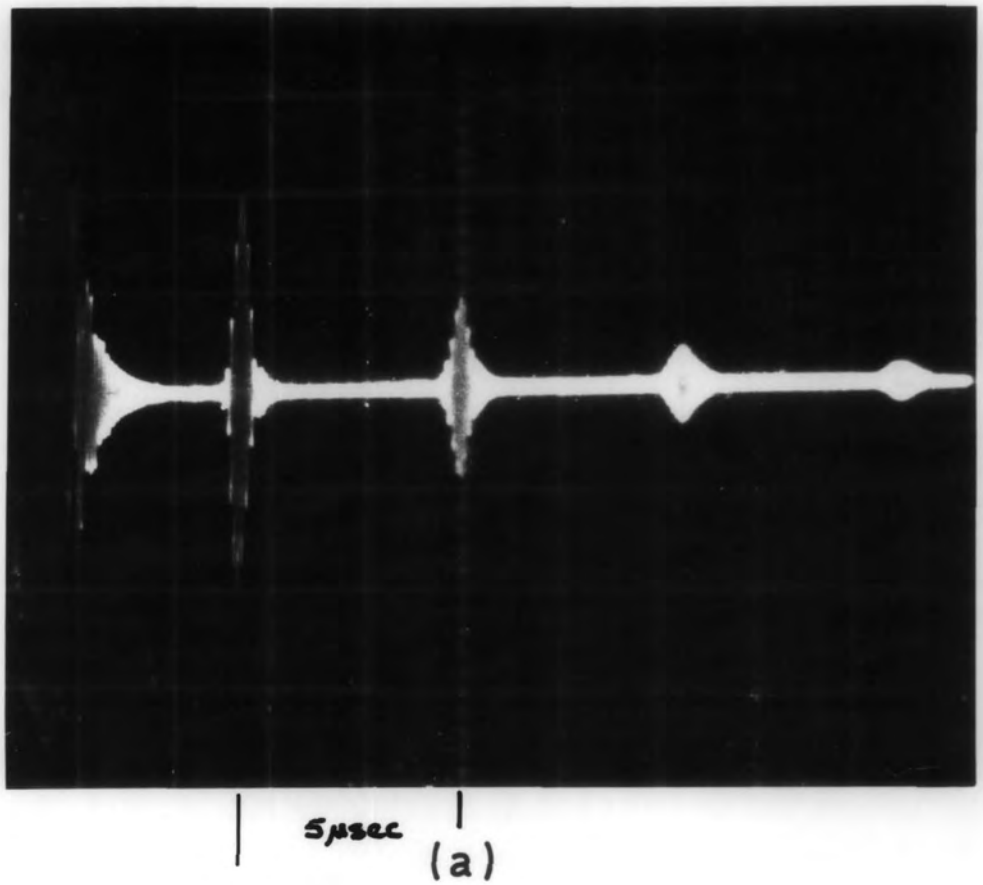

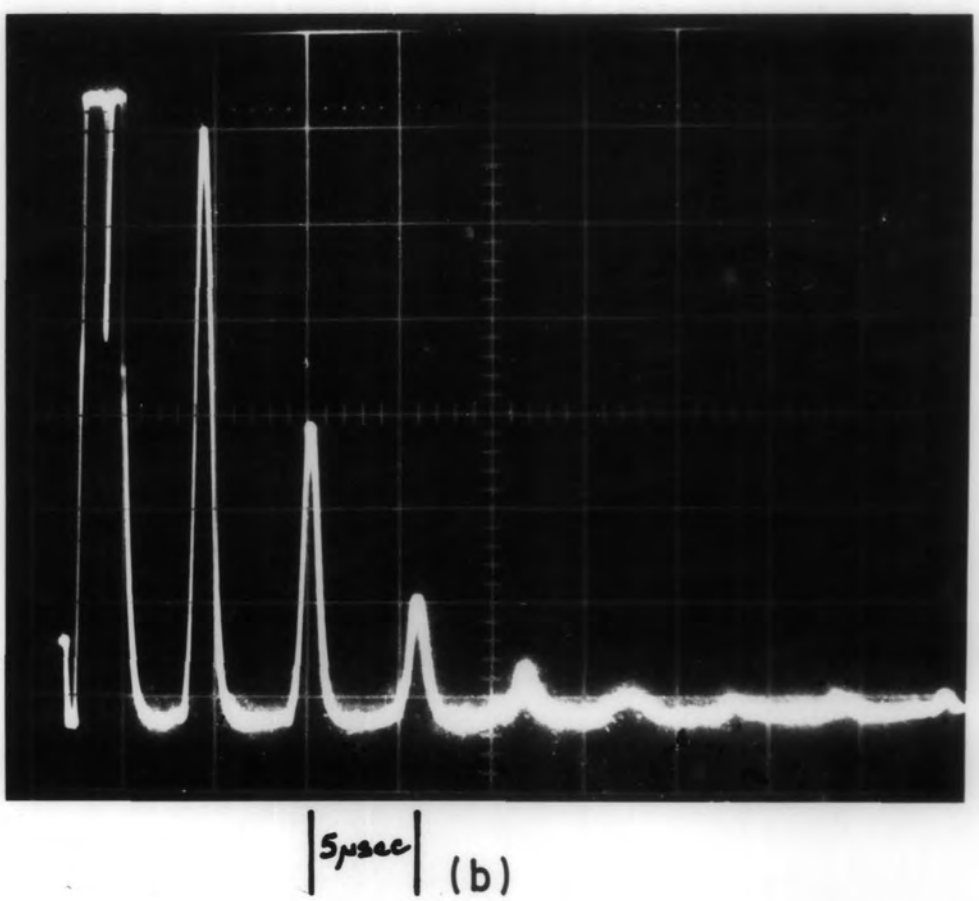

PLATE 4·1 (a) R.F. ECHO TRAIN
(b) VIDEO ECHO TRAIN

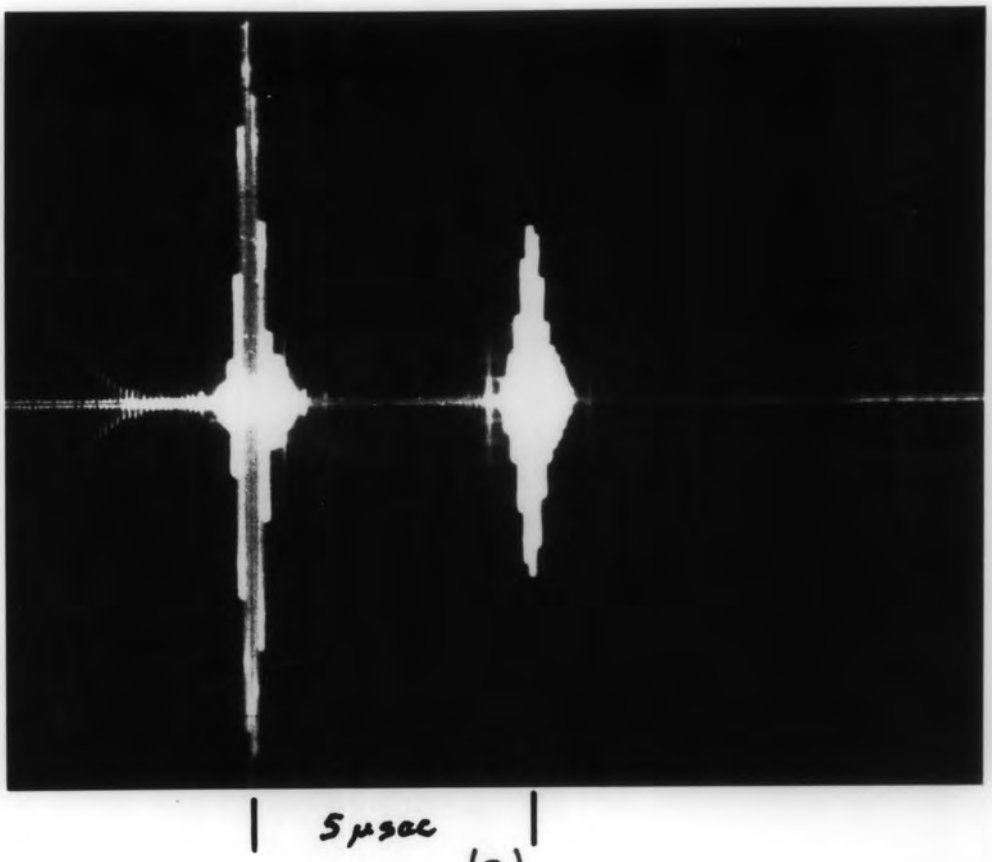

(a)

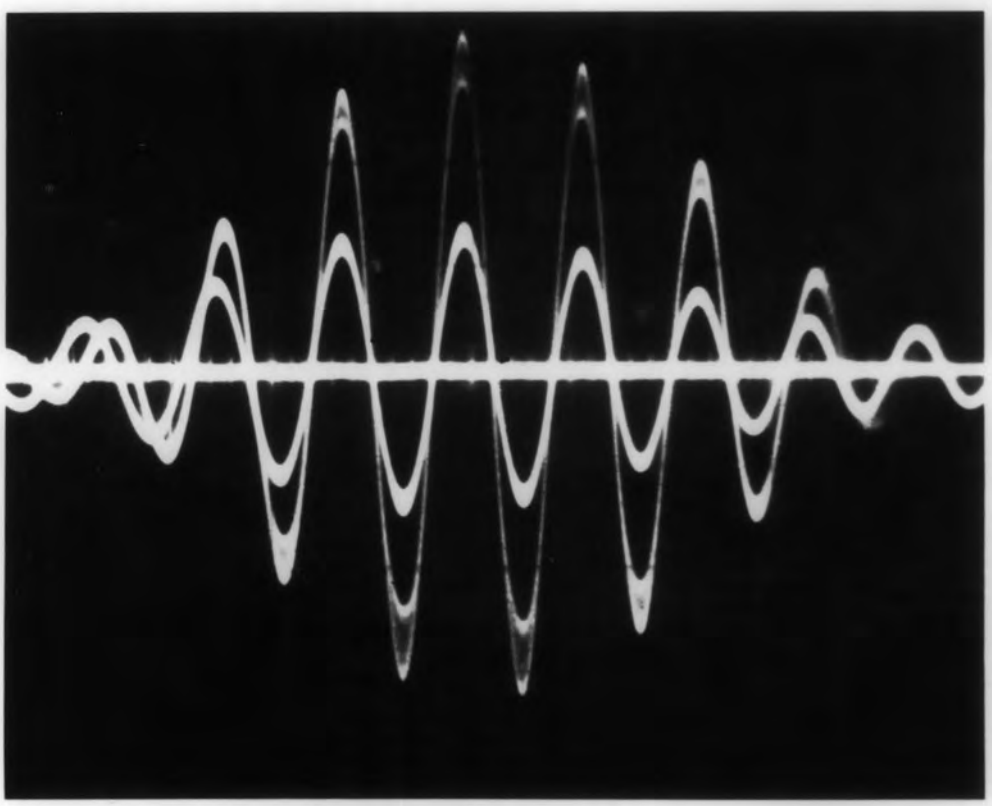

(b)

PLATE 4·2 (a) TWO ECHOES INTENSIFIED PRIOR TO OVERLAP

(b) THE SAME TWO ECHOES OVERLAPPED EXACTLY

time was then confirmed by overlap of different pairs of echoes, both adjacent, and non-adjacent.

4.3 EXAMINATION OF SPECIMENS

4.3.1 Derivation of Elastic Moduli

Using the pulse echo overlap technique outlined above the longitudinal and shear velocities have been measured RBSN samples with weight gains varying from 22% to 64.5% and with densities from 1950 kg/m^3 to 2540 kg/m^3.

The velocities thus measured are related directly to the elastic constants of material, assuming that we are dealing with linear elastic i.e. Hookeian solid. The elastic constants form a fourth rank tensor, and in principal there are eighty one of them, however, as crystal symmetry increases the number of non-zero elastic constants decreases until for a cubic crystal, for example, there are only three independent elastic constants C_{11}, C_{12}, and C_{44}.

A polycrystalline solid however can in many instances be considered to be elastically isotropic or nearly so. This is because the individual anisotropics of the randomly oriented crystallites cancel out, and an average value of elastic constants is obtained. (Exceptions to this would be if, for example, the material were fibrous e.g. wood or had a preferred orientation of crystallites; as far as is known neither consideration applies to RBSN). There are thus only two independent elastic constants, namely C_{11}, and C_{12} since $2C_{44} = C_{11}-C_{12}$ for an elastically isotropic solid. In practice results are often expressed in terms of some other elastic constants (for convenience and ease of comparison), the more common

being Young's modulus E, the bulk modulus K, the shear mobulus μ, Poisson's ratio γ, and Lame's constants λ, and μ_L. The latter are defined by the relationships

$$\lambda = C_{12} \tag{4.1}$$

$$\mu_L = C_{44} \tag{4.2}$$

$$\text{and } \lambda + 2\mu = C_{11} \tag{4.3}$$

In terms of C_{11} and C_{44} the longitudinal and shear ultrasonic velocities (V_L and V_s respectively) are given by

$$V_L = \left(\frac{C_{11}}{\rho} \right)^{\frac{1}{2}} \tag{4.4}$$

$$\text{and } V_s = \left(\frac{C_{44}}{\rho} \right)^{\frac{1}{2}} \tag{4.5}$$

where ρ is the density of the material. Thus Lame's constants are related to the ultrasonic velocities by

$$\mu_L = \rho V_s^2 \tag{4.6}$$

$$\text{and } \lambda \quad \rho \left(V_L^2 - 2V_s^2 \right) \tag{4.7}$$

It is useful also to note that

$$C_{44} = \mu_L = \mu \tag{4.8}$$

and that the shear modulus μ is given by

$$\mu = \rho V_s^2 \tag{4.9}$$

The experimental measurements enabled the values of the longitudinal and shear ultrasonic velocities to be determined. These are related to the elastic constants E, K and γ by following three relationships

(a) Young's Modulus, E.

$$E = \frac{\mu_L(3\lambda + 2\mu_L)}{(\lambda + \mu_L)} = \frac{\rho V_s^2(3V_L^2 - 4V_s^2)}{V_L^2 - V_s^2} \qquad (4.10)$$

(b) the bulk modulus, K

$$K = \lambda + \tfrac{2}{3}\mu_L = \frac{\rho(3V_L^2 - 4V_s^2)}{3} \qquad (4.11)$$

(c) Poissons ratio,

$$\gamma = \frac{\lambda}{2(\lambda + \mu_L)} = \frac{(V_L^2 - 2V_s^2)}{2(V_L^2 - V_s^2)} \qquad (4.12)$$

4.3.2 Results and Discussion Both the longitudinal and shear ultrasonic velocities were found to depend on the degree of nitriding which had been given to the sample during preparation. In the first instance the percentage weight gain was taken as a measure of the degree of nitriding and Figure 4.5 shows the results obtained. The general trend of the variations of both longitudinal and shear velocities is to increase as the percentage weight gain increases. The effect is quite marked, the change in V_L for example being from about 6000 ms^{-1} for 20% weight gain to around 8000 ms^{-1} for fully nitrided material, (63% weight gain). However, closer examination of the data, particularly in the high weight gain region reveals an apparent discrepancy in the results, in that

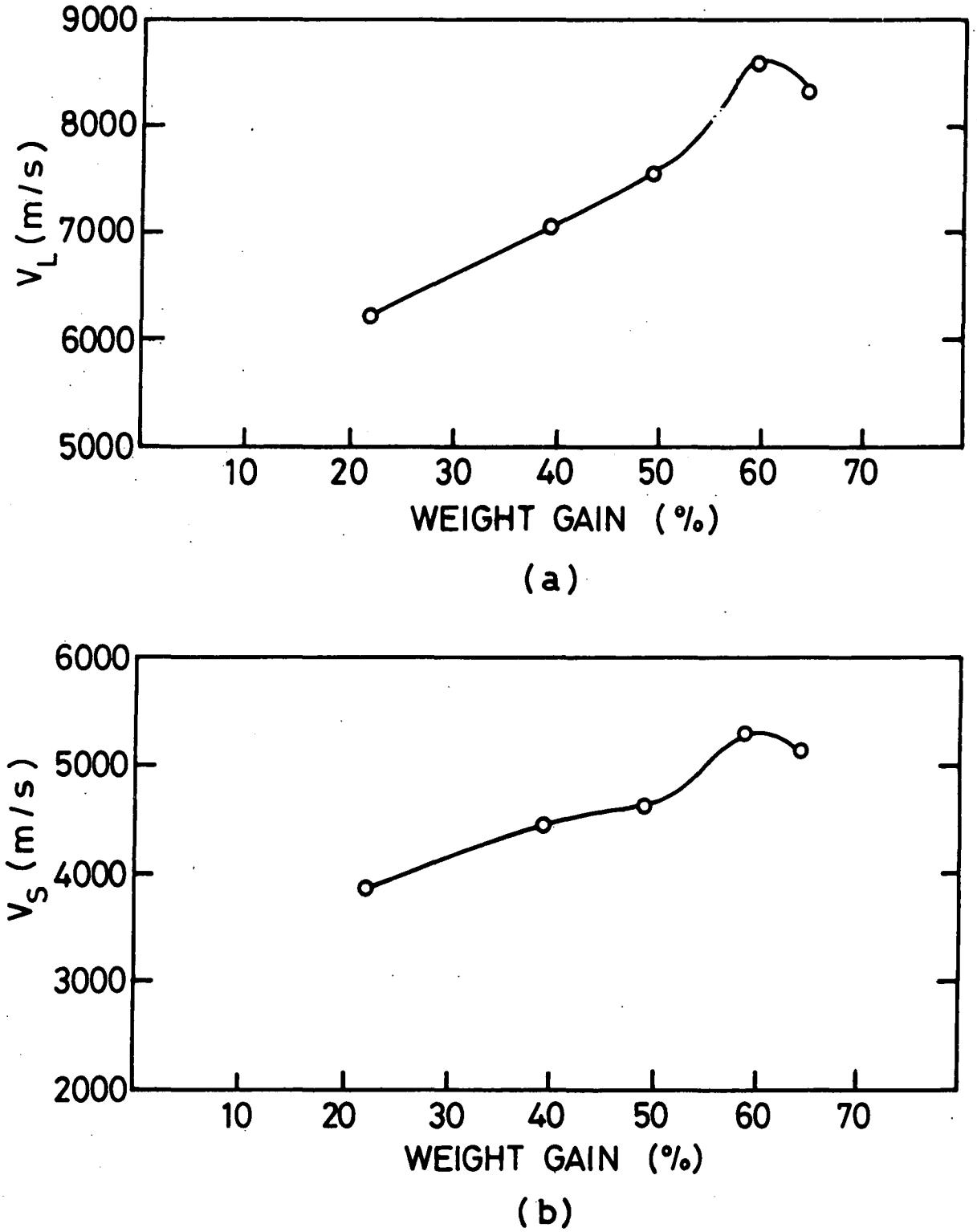

FIG. 4·5 VARIATION OF ULTRASONIC VELOCITY WITH DEGREE OF NITRIDING ; (a) LONGITUDINAL VELOCITY V_L, (b) SHEAR VELOCITY V_S.

the highest velocities were recorded for 59% weight gain material. This suggested that a better approach would be to analyse the data in terms of density, or porosity. This approach reveals a rather different situation and indicates that the important factor in determining strength is not the weight gain in itself but the porosity and density of the nitride. This in turn must be related to the density of the 'green' compact, so that a denser compact will produce a stronger product for a given weight gain.

Figures 4.6 and 4.7 show the variations of ultrasonic velocity expressed in these terms. In Figure 4.6 the longitudinal and shear ultrasonic velocities are plotted as functions of density; the graphs now show a steady rise in velocity as full nitridation is achieved. The corresponding converse effect is illustrated by Figure 4.7 which shows that samples with the highest porosity give the lowest ultrasonic velocities. Here the fractional porosity, P, is given by

$$P = 1 - 0.281\ \rho_{green} - .148\ \rho_{Nitride} \qquad (4.13)$$

where ρ_{green} is the density of the 'green' compact and $\rho_{Nitride}$ is the density of the nitride.

Similar trends are apparent in the variations of the elastic moduli derived from the longitudinal and shear ultrasonic velocities. The plots of Young's Modulus (a measure of the resistance to extension) and the bulk modulus (the resistance to hydrostatic pressure) are given in Figure 4.8a and 4.8b respectively. These bear out the conclusion that the porosity and density of the nitride are the main factors controlling its strength.

Some further comments can be made regarding the values of Young's Modulus obtained for the range of RBSN samples examined. The porosity of a ceramic can be related to the Young's modulus by the expression, (Moulson,4.3)

$$E_p = E_o \exp(-3P) \quad GN.m^{-2} \qquad (4.14)$$

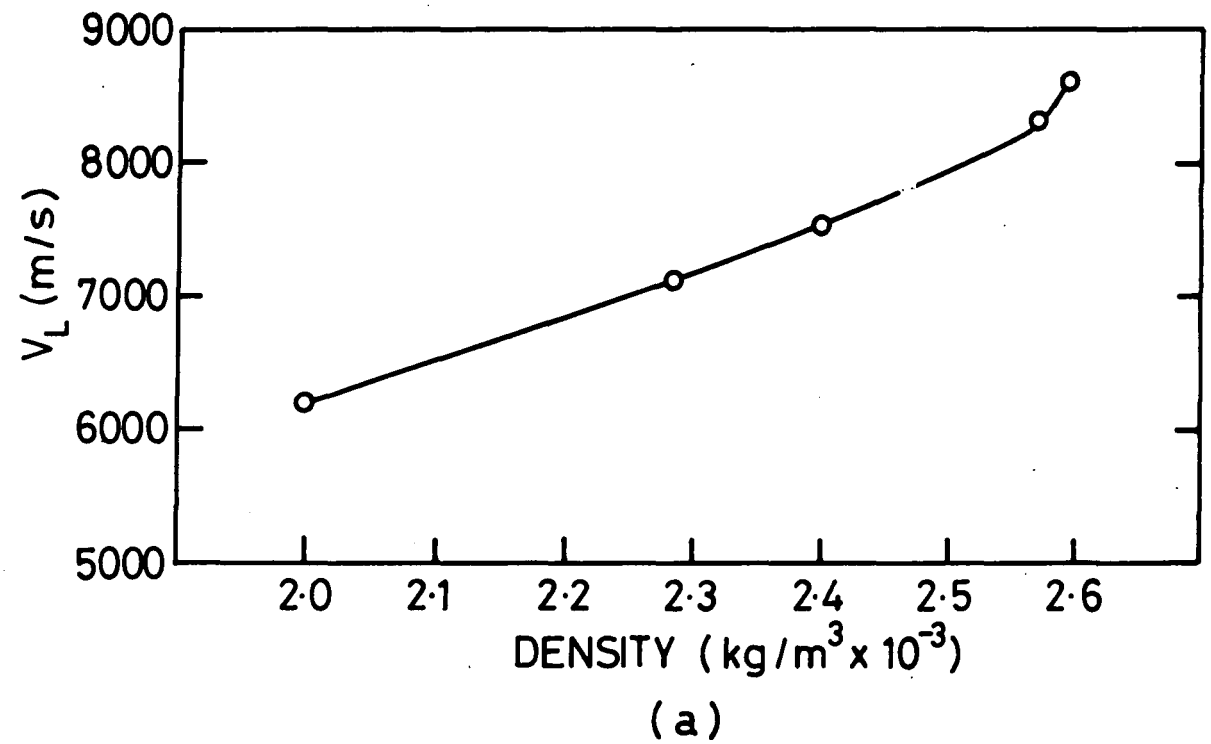

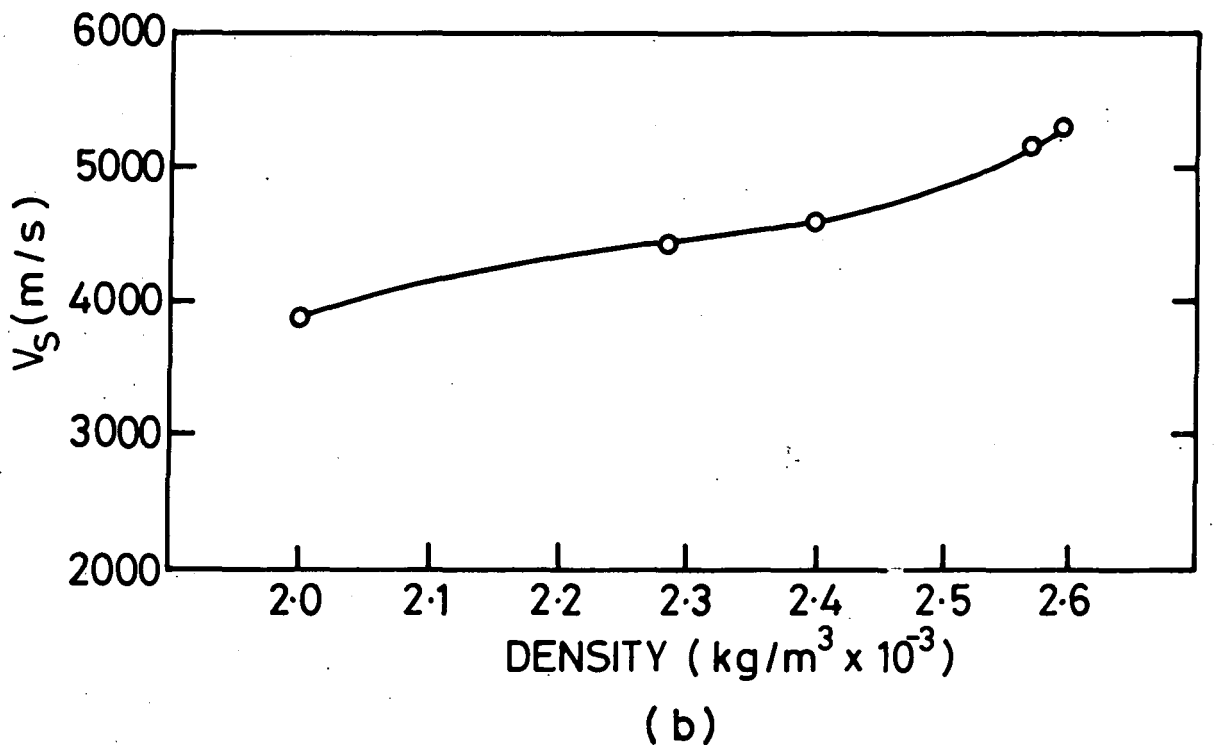

FIG. 4·6 VARIATION OF ULTRASONIC VELOCITY WITH DENSITY AT VARIOUS STAGES OF NITRIDATION ;
(a) LONGITUDINAL VELOCITY V_L , (b) SHEAR VELOCITY V_S

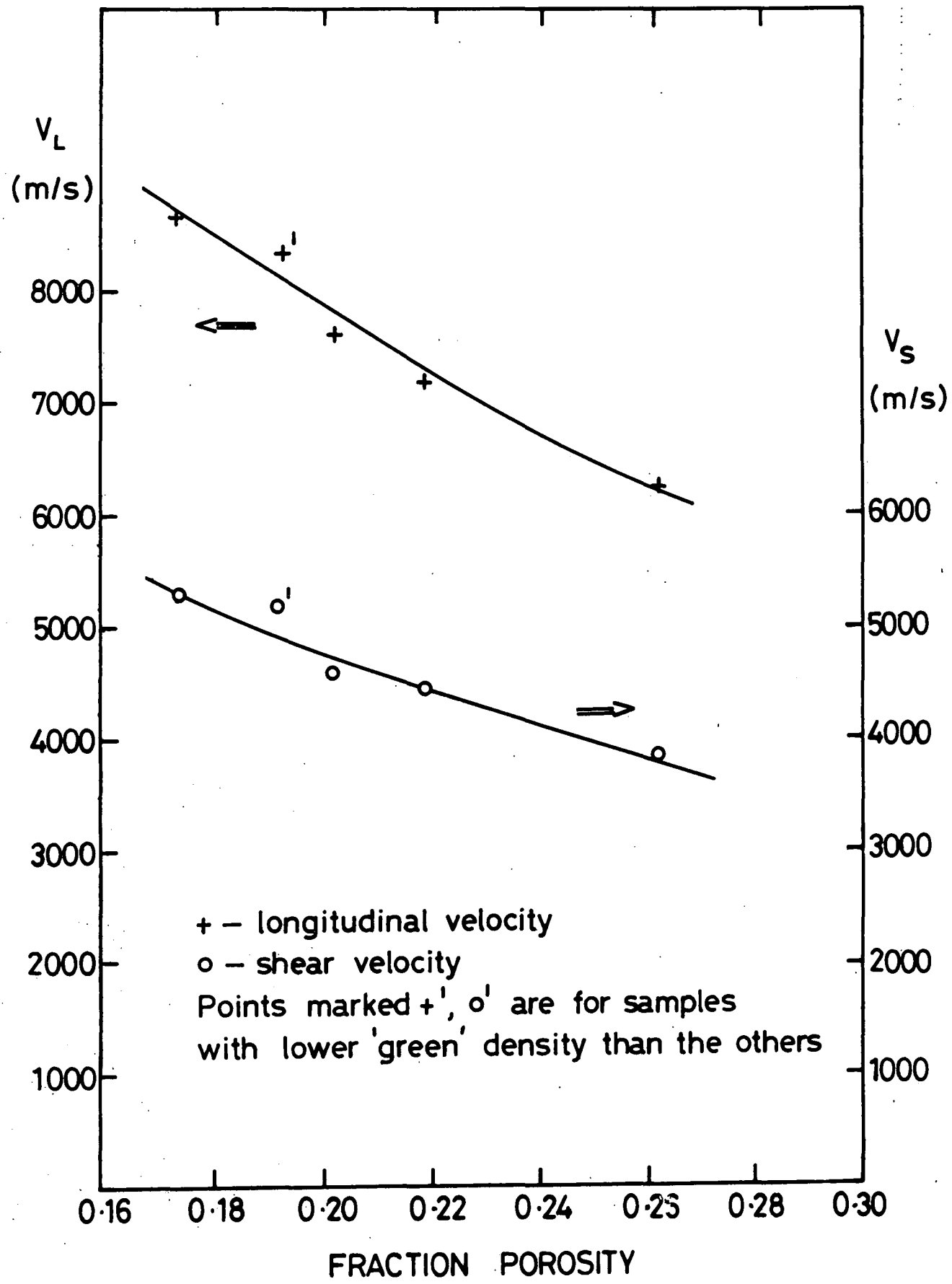

FIG. 4·7 POROSITY vs ULTRASONIC VELOCITY FOR REACTION BONDED SILICON NITRIDE

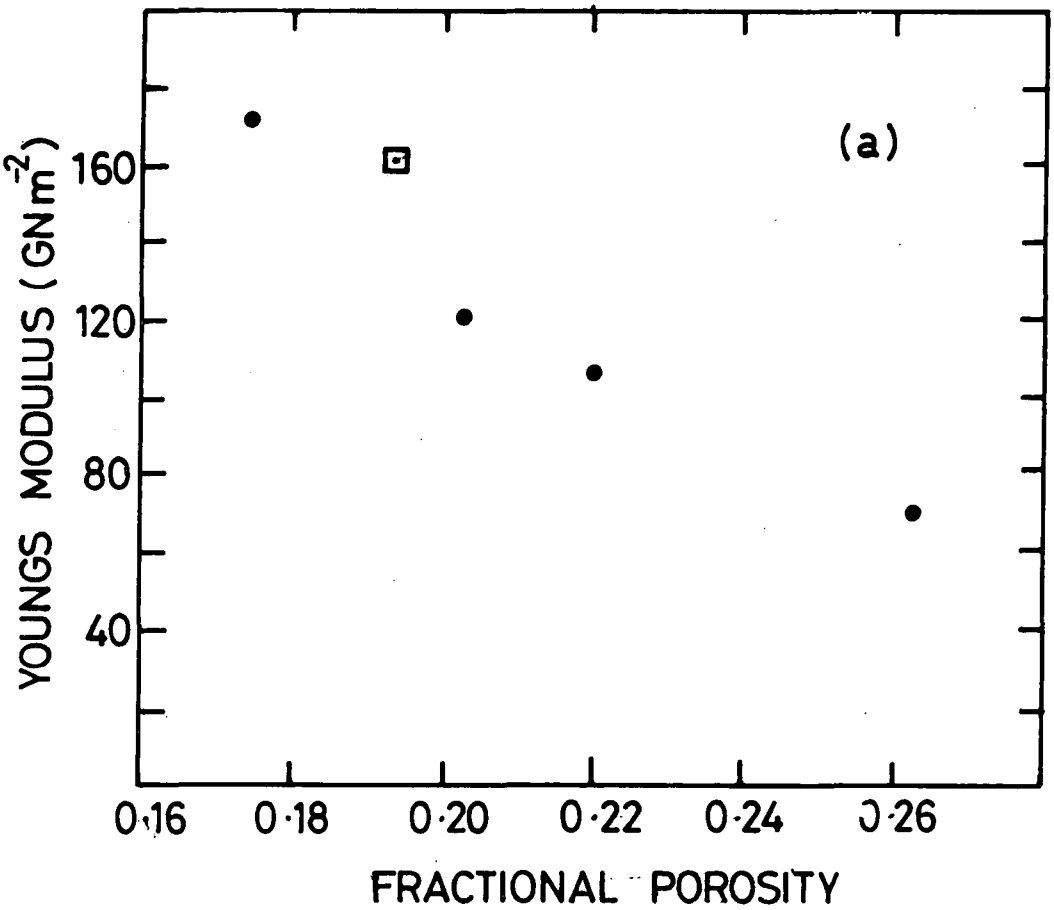

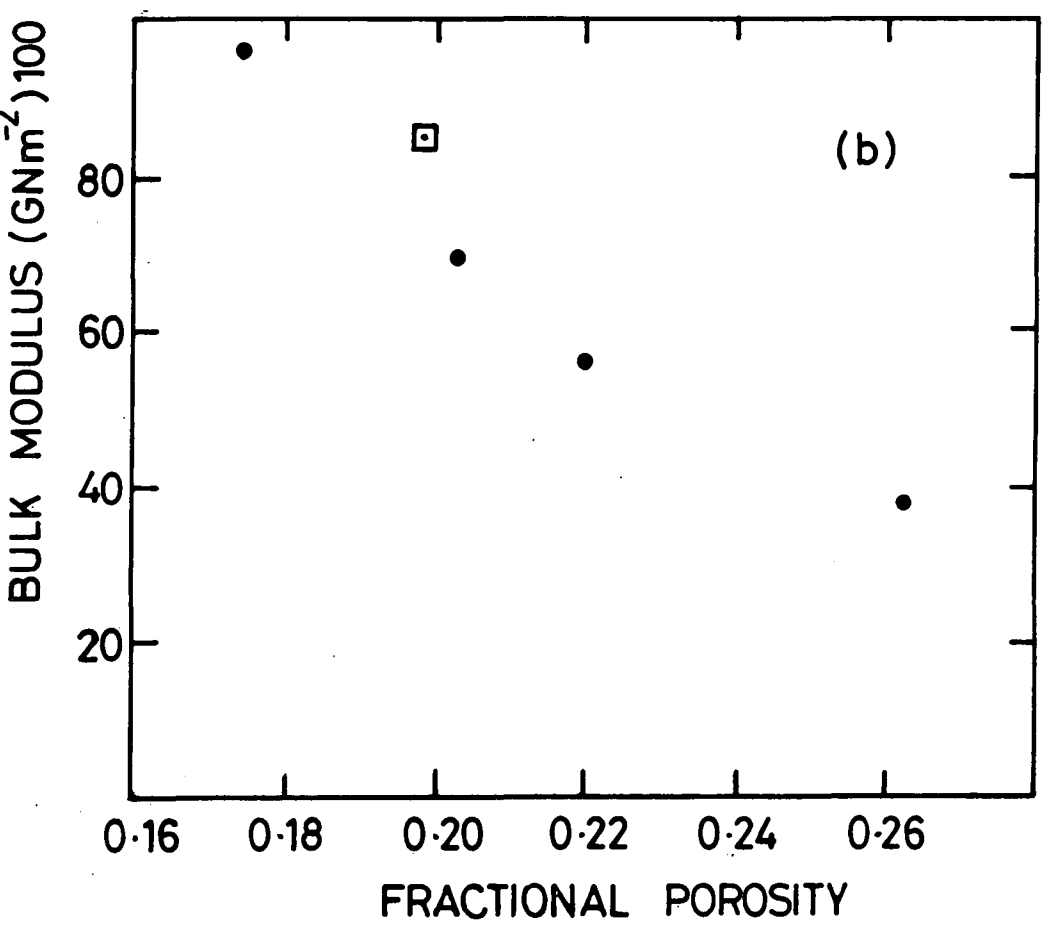

FIG. 4·8 a) YOUNGS MODULUS vs FRACTIONAL POROSITY
b) BULK MODULUS vs FRACTIONAL POROSITY
• -- ρ_g = 1·6 kg.m^{-3} : ⊡ -- ρ_g = 1·53 kg.m^{-3}

where P is the fractional porosity, and E_o the Youngs modulus value for a non-porous material. E_p is the Young's modulus for a given porosity. Strictly speaking such a relation can only be applied to fully nitrided materials, i.e. to those with no unreacted silicon since E_o must be different for a non-porous material consisting of silicon nitride and silicon. However, since this difference is likely to be small (at least for small amounts of free silicon) it is reasonable to assume that high weight gain materials would have Young's Modulus close to the line $E_p = E_o \exp(-3P)$ $GN.m^{-2}$. On this basis it would be expected that Young's Modulus for low weight gain materials should fall below the same line. If a value of 300 $GN.m^{-2}$, being the mean of some 25 published values of Young's Modulus for hot pressed silicon nitride is taken for E_o in equation (4.14) and the RBSN results plotted and compared with (4.14) (Figure 4.9), this is shown to be the case.

To summarise, ultrasonic determination of the basic elastic constants of the range of RBSN samples available, has shown that weight gain, i.e. the degree of nitridation, has a major effect upon the strength of RBSN. This however, is not the whole story for considering two materials with similar weight gains, both nearly fully reacted, it has been found that the stronger material is the one with the lower porosity and highest density, and not necessarily the highest weight gain.

By implication, therefore, the strength of an RBSN compact will depend upon the density of the 'green' ceramic, as well as the weight gain as long as the weight gain is sufficiently high for the free silicon to have a negligible effect upon the strength.

An excessively dense silicon compact will, as noted previously, inhibit the final stages of nitridation ; it may be, however, that to obtain high strength in RBSN a high 'green' density should be used at the expense of incomplete nitridation.

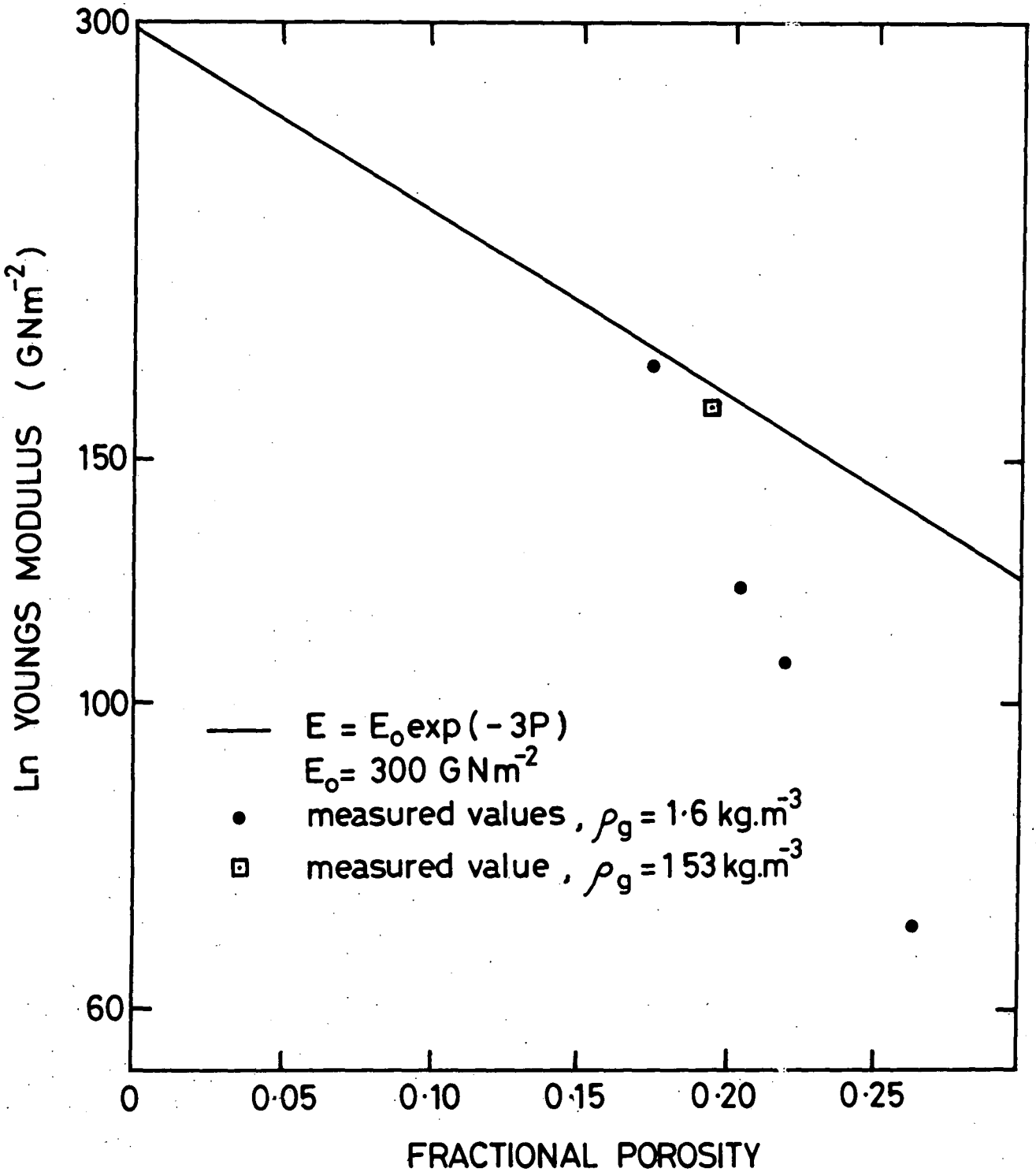

FIG. 4·9 YOUNGS MODULUS OF REACTION BONDED SILICON NITRIDE vs FRACTIONAL POROSITY : MEASUREMENT AND PREDICTION

CHAPTER 4

REFERENCES

4.1 E.K.Sittig and H.D. Cook, Proc IEEE 56, 1375, (1968).

4.2 N.G. Pace, Ph.D.Thesis, University of Durham, (1970).

4.3 A. J.Moulson, J.Mat.Sci.14, 1017, (1979).

4.4 H.J.McSkimin and P.Andreatch J.Acoust.Soc.Am.34,609,(1962).

4.5 H.J.McSkimin, J.Acoust.Soc. Am.22, 413 (1950).

4.6 H.J.McSkimin, IRE Trans on Ultrasonic Engineering PGUE-5,25,(1957).

CHAPTER 5

MICROWAVE SPECTROSCOPY

5.1 GENERAL FEATURES

Microwave spectroscopy consists of the observation of the interaction with atomic systems of electromagnetic radiation in the microwave region of the spectrum, this broadly being from 1GHz. to 300GHz., the high frequency limit between microwaves and the far infrared being rather ill defined. As in many other branches of spectroscopy this involves the determination of energy level separations by exciting transitions between the levels with incident radiation of known wavelength and then detecting the resulting changes in the intensity of the output radiation. The particular case of electron spin resonance (e.s.r.) spectroscopy concerns transitions between the energy splittings which are caused by an unpaired electron's interaction with an external magnetic field, with nuclear spins and with surrounding atoms. Since materials which contain these unpaired electrons are paramagnetic, e.s.r. is also referred to as paramagnetic resonance. The nature of the interaction is essentially magnetic, and takes place, at these frequencies, between the magnetic component of the electromagnetic wave, and the magnetic dipoles of the electrons of the atoms or ions being observed. In the case of paramagnetism, certain ions possess unpaired electrons in unfilled orbital shells, and it is these electrons which give rise to a residual magnetic dipole moment. In the case of solids, if paramagnetic ions are distributed in a diamagnetic host lattice, the magnetic properties of the material will be dominated by those of the paramagnetic ions, although these will be modified by the influence of the crystalline electric field of the host lattice at the paramagnetic ion site.

The first experimental observation of the interaction of microwaves with matter was that performed by Cleeton & Williams (5.1) who observed

the absorption spectrum of ammonia at frequencies between 7 and 30GHz, although severly hampered by the lack of any commercial microwave equipment available at that time. The rapid acceleration of research into microwave apparatus, caused by the requirements of radar during the last war, made the ready availability of microwave generators and circuit elements an inducement to continue research in the subject, and resonant magnetic absorption was first reported by Zavoisky (5.2), and Cummerow & Halliday (5.3). For the magnitude of homogeneous magnetic fields that may easily be obtained in the laboratory ($\sim$ 1 tesla) the induced energy level splittings are typically about 1 cm^{-1}, and hence the appropriate radiation which is required to promote transitions between the levels is in the microwave region of the electromagnetic spectrum. The basic aim of an e.s.r. measurement, therefore, is to detect the absorption of power from a microwave beam by a paramagnetic sample during resonance. Unlike most forms of spectroscopy, in which the energy of the radiation is varied to match the relevant energy level splittings, it is experimentally more convenient to keep the microwave frequency fixed and to vary the energy level separations by sweeping the external magnetic field through the resonance condition.

The Chapter presents an introduction to the fundamental principles of e.s.r. The detailed theory has been discussed in several standard texts, e.g. Assenheim (5.4), Ayscough (5.5). In the present context the essential points are firstly that electron spin resonance techniques can enable a detailed assessment to be made of the positions, local environments and interactions of individual atomic species in solids and secondly that the methods may be applied to materials in single crystal, sintered polycrystalline or powder form, although the two latter groups may involve considerable complexity both in experiment and interpretation.

Electrons in all materials may be considered as possessing two types of motion, giving rise to (a) orbital angular momentum, due to motion around

the nucleus of an atom and (b) an intrinsic spin angular momentum corresponding to the electron spinning about its own axis. Since electrons possess charge both types of motion produce magnetic moments and hence, in an external magnetic field, the electrons behave as magnetic dipoles with a tendency to align themselves to the direction of the field. In most materials the electrons are arranged in pairs of opposing spins so that there is no net magnetic moment and hence the materials are classified as diamagnetic. There are several classes of materials, however, in which unpaired electrons can exist, causing an overall magnetic moment which gives rise to paramagnetism. Some examples of transition metal and rare earth compounds, where incomplete d or f orbitals may leave one or more electrons unpaired; free radicals, where a bonding electron is left associated with only one atom; F-centres, in which electrons or holes are trapped at point defects; atoms or molecules which possess an odd number of electrons; metals and semiconductors, in which the conduction electrons can cause paramagnetism.

Thus successful interpretation of e.s.r. spectra can lead to fairly detailed models for the relevant paramagnetic centres, by providing information on the charge state, the type of binding, the amount of interaction with surrounding nuclei and the symmetry of the environment. The value of the g-parameter and the magnitude of its departure from the free electron value gives an indication of the strength of the crystal field and the degree of spin-orbit coupling. The anisotropy of the g-value reflects variations in crystal field and hence can be used to deduce information concerning the defect site and the crystal structure. The identification of a defect or its surrounding nuclei can be particularly precise if there are electron-nuclear interactions, giving hyperfine structure to the spectra. The magnitude of the hyperfine splitting is proportional to both the nuclear magnetic moment and the probability of finding the electron at the nucleus.

Since the area under an absorption line is proportional to the number of unpaired spins, e.s.r. can be used as a sensitive, non-destructive method of determing defect concentrations, providing care is taken with calibration procedures and the signal is not saturated by excessive power.

Overall, e.s.r. is one of the most powerful tools available for the study of defects in insulators, because it can only detect the presence of paramagnetic centres and therefore obtains results independently of surrounding diamagnetic material, which would swamp signals from low concentration centres in less selective techniques. E.s.r. has been used to study defects which are introduced into a crystal lattice by irradiation or dislocation. The charge state of trapping centres can often be deduced from the sign of Δg, the difference from the free electron g-value, which is negative for an electron trap but positive for a hole trap. The technique has been widely applied to the characterisation of impurity centres, such as those deliberately doped into single crystals to produce maser materials. (e.g. Thorp, 5.6) and laser rods (Thorp, Brown and Buckley 5.7) or to characterise doped insulators, (Thorp, Vasquez and Hutton 5.8, Thorp and Hossain, 5.9).

5.2 THE SINGLE FREE ELECTRON

Quantum theory states that the angular momentum, and hence also the magnetic moment, of the electron may only hold certain discrete values. With the simplest case of a single free electron, with no orbital angular momentum, the spin-only angular momentum is given by:-

$$P_s = \frac{1}{2} \frac{h}{2\pi} \tag{5.1}$$

and the magnetic moment is:-

$$\mu_s = \beta = \frac{eh}{4\pi mc} \tag{5.2}$$

In the presence of an external magnetic field the electron experiences a torque which tries to align its magnetic moment vector with the direction of the field, but quantisation restricts the number of possible orientations, so that the magnetic moment can never be completely parallel to the field, but instead it precesses around the field direction at an angular frequency, ω_o, where:-

$$\omega_o = \gamma \, Ho \tag{5.3}$$

Ho is the magnetic field value and γ is the magnetogyric ratio and is 17.6×10^6 sec^{-1} $Gauss^{-1}$ for a free electron. The energy of a magnetic dipole of moment μ in the presence of a magnetic field Ho is given by:-

$$E = \mu \, Ho \cos \theta \tag{5.4}$$

where θ is the angle between the magnetic field and the axis of the dipole. In the case of a free electron there are only two allowed orientations of magnetic moment, corresponding to magnetic quantum numbers, Ms, of $\pm\frac{1}{2}$, and there are consequently only two permitted energy levels, E, described by:

$$E = 2 \, \beta \, M_s \, Ho \tag{5.5}$$

Thus the application of a magnetic field splits the previously-degenerate electron energy level into two different levels, separated by energy $2 \, \beta \, Ho$.

In real systems, where the magnetically-induced energy splittings may be affected by additional interactions, the relation of energy to magnetic field is given by:-

$$E = g \, \beta \, Ho \tag{5.6}$$

where g is a numerical factor which is determined experimentally. (Due to relativistic corrections, g = 2.0023 for a free electron).

5.3 THE PARAMAGNETIC ION IN A CRYSTALLINE ENVIRONMENT

A free ion has associated quantum numbers J, L and S, corresponding to the total, orbital and spin angular momenta respectively; J being the vector sum of L and S, and a result of quantum theory is that the ground state of such an ion has degeneracy (2J+1) in the absence of any applied magnetic field.

The strong electric fields present in a crystal lattice can modify this quantum state in several ways. The first is the breaking of the coupling between L and S, resulting in the orbital ground state degeneracy being due to S alone, and therefore (2D+1) in value, the higher orbital states being usually far removed in energy from the ground state: this condition is known as 'quenching'. The second effect can be a partial lifting of the degeneracy of the ground state, subject to the limitation of Kramers' Theorem (Kramers 5.10) which states that an ion with an odd number of unpaired electrons must retain twofold degeneracy of those levels. The energy splitting caused by this lifting of the ground state degeneracy is called the zero field splitting, and frequently corresponds to quanta of microwave radiation. This situation applies in the case of ions of the iron group of transition elements, only the lowest orbital energy level normally being populated, and the energy splitting of the higher orbital states corresponding to quanta of energy of optical frequencies.

In a crystalline environment, if the spin-orbit coupling is incompletely quenched, the degeneracy of the ground state may not correspond to the true spin quantum number of the free ion, S, and therefore an effective spin, S', is assigned to the ion, such that the observed degeneracy is (2S'+1). In the case of complete quenching S' is equal to S. The application of a magnetic field, H, causes further lifting of the degeneracy of the ground state, splitting the levels into discrete spin energy states, with an energy separation E, where, as stated earlier

$$E = g\beta H M \qquad (5.7)$$

where β is the Bohr magneton, the unit of magnetic moment, g is the spectroscopic splitting factor, equal to 2.0023 for a free electron spin, and otherwise giving an indication of the degree of orbital quenching, and analagous to the Lande g-factor for a free ion; M is the magnetic quantum number, having values in the range +S' to -S'. A quantum mechanical selection rule dictates that transitions may only be observed between spin states for which $\Delta M = 1$. This only applies however for pure spin states, and a further effect of the crystalline field is to cause mixing of the pure spin states. Thus, in an ion having $S' = 3/2$ (e.g. Cr^{3+}), an energy level $|i\rangle$ may be described, using the notation of Dirac 5.11, by,

$$|i\rangle = a_i|3/2\rangle + b_i|1/2\rangle + c_i|-1/2\rangle + d_i|-3/2\rangle \qquad (5.8)$$

the eigenvectors a_i, ... being normalised by,

$$|a_i|^2 + |b_i|^2 + |c_i|^2 + |d_i|^2 = 1 \qquad (5.9)$$

The consequence of this is that the selection rule $\Delta M = 1$ breaks down, and the so called 'forbidden' transitions may be observed.

The spin Hamiltonian (Abraham & Pryce, B.11) is a convenient description of the ground state levels of an ion. The precise form is a function of the particular symmetry of the host lattice, but generally it can be expressed as:

$$s = g\,\underline{H}.\underline{S}' + D(S_z'^2) + S'(S'+1) + E(S_x'^2) + \text{HFS terms} \qquad (5.10)$$

The first term represents the energy of the spin magnetic moment due to its orientation with respect to the applied magnetic field. The second term possesses axial symmetry, and is proportional to the transverse component of S', and may be interpreted as a quadrupole interaction between ion and lattice. The third term is a non-axially symmetric anistropy in

the x - y plane due to an electric moment of high order. The energy separation of the ground state levels in zero magnetic field is due to the D & E terms in the Hamiltonian; in an axially symmetric system, such as ruby, with S' = 3/2 the term E is approximately zero, and hence the zero field spliting is 2D.

If the nucleus of the ion has a nuclear magnetic moment, then additional hyperfine splitting (HFS) terms must be added to $\mathcal{H}_s$.

Using the spin Hamiltonian, the solutions of

$$\mathcal{H}_s |i\rangle = E_i |i\rangle \qquad (5.11)$$

are derived in terms of E_i, the eigenvalues (energies) of the states $|i\rangle$.

5.4 MICROWAVE POWER ABSORPTION

In order to detect splittings in the electron energy levels it is necessary to excite a transition between two levels with e.m. radiation of frequency ν, such that:-

$$h \nu = g \beta H_o \qquad (5.12)$$

The mechanism by which the radiation induces a transition is also of a magnetic nature and may be thought of as being due to the oscillating magnetic field component of the e.m. radiation exerting an additional torque on the electron's magnetic moment, causing it to change direction and hence its energy when the microwave frequency is equal to the magnetic moment's precession frequency. In practice, the excitation of transitions by the microwave beam will take place over a range of frequencies on either side of the resonant value or, in the normal experimental set-up with a fixed microwave frequency, interaction occurs over a range of magnetic field values, so that when the field is slowly swept through the resonance condition, while the amount of reflected power is measured, an absorption

line of finite width is produced. Since there is an equal probability of an interaction between the microwave beam and an electron causing either an absorption or emission of power, the ability to detect such transitions relies on there being an excess population of electrons in the lower energy state. The relative populations of the energy levels is given by a Boltzmann distribution:

$$\frac{n_1}{n_2} = \exp\left[\frac{-g\,\beta\,H_o}{kT}\right] \tag{5.13}$$

where n_1 and n_2 are the populations of the upper and lower energy states respectively. The net power absorption, therefore, increases as the temperature is lowered, causing an increase in e.s.r. signal-to-noise ratio.

To a first approximation, the population difference, $\Delta n = n_2 - n_1$, between the two energy levels may be expressed as:-

$$\Delta n = \frac{Ng\,\beta\,H_o}{2kT} \tag{5.14}$$

where N is the total concentration of unpaired electrons. Integration of the detected absorption line gives a measure of the total net power absorbed, P, which is given by

$$P = \frac{2\,\pi^2\,\nu^2\,H_o^2\,S(S+1)\,Ng^2\,\beta}{3kT} \tag{5.15}$$

where S is the total spin angular momentum. Hence the total amount of power absorbed is proportional to the total number of unpaired electrons in the sample.

5.5 PARAMAGNETIC RELAXATION

In order to describe the mechanism whereby a spin system achieves thermal equilibrium within itself and with its surroundings three processes

must be considered. These are spin-spin relaxation, cross relaxation and spin-lattice relaxation, which is the main concern of this thesis. Spin-spin relaxation is the process by means of which the spin system achieves thermal equilibrium within itself, cross relaxation is the attainment of equilibrium between spins of different species, while spin-lattice relaxation describes the way in which the spin system transfers energy to the lattice.

Dipolar interactions within a spin system have the effect of broadening the Zeeman levels of the system (this is a contribution to the homogeneous broadening of the resonance line), and they also effect the transitions between the broadened levels by means of which excited spins transfer their energy to non-excited spins and hence establish equilibrium within the system. Waller (5.13) performed the first calculation of the spin-spin relaxation time, T_2, considering a simple $S = \frac{1}{2}$ system in low magnetic field, such that the Zeeman energy was less than the internal field due to the surrounding nearest neighbour ions, and obtained the result

$$T_2 \cong \frac{6g^2 \beta^2 N^{\frac{1}{2}}}{hr^3} \qquad (5.16)$$

N being the number of nearest neighbour ions at distance r from the centre being considered. For pure paramagnetic salts with typical inter-atomic spacings of a few angstroms this results in $T_2 \cong 10^{-9}$ secs, and even in magnetically dilute systems, T_2 is very short in comparison with the spin lattice relaxation time.

Kronig & Bouwkamp (5.14) considered the case, usual under E.S.R. conditions, of the Zeeman energy being much greater than the dipolar energy

$$g \beta H >> \frac{g^2 \beta^2}{r^3} \qquad (5.17)$$

and in this situation found that

$$T_2 = \frac{6g^2 \beta^2 N^{\frac{1}{2}}}{h} \exp (H/H_i)^2 \qquad (5.18)$$

where H_i is the average internal field due to the other spins acting at the spin in question. In order of magnitude $1/T_2$ is equal to half the homogenous resonance linewidth, and since it does not involve the lattice energy, it is essentially temperature independent.

For more complicated spin systems, either with $S > \frac{1}{2}$ or containing more than one type of spin centre, the process of cross-relaxation, discussed by Bloembergen et al. (5.15), and further by Grant (5.16), must be considered. Where the levels of a single multilevel spin system are exactly, or to a close approximation, equispaced, or where the energy spacings of the levels are in simple whole number ratios, or where these relationships apertain between the energy levels of two different spin systems in the same sample, then spin energy may be transferred by the transition of one or more excited ions to their ground state, with the simultaneous transition of a non-excited ion to an excited state, the total spin energy being conserved.

If the energy spacings of the levels involved, say $h\nu_a$ and $h\nu_b$, are not exactly equal, so that, say

$$2h\nu_a \cong h\nu_b \qquad (5.19)$$

implying that the simultaneous downward transition of two 'a' spin results in the upward transition of one 'b' spin, then the dipole - dipole coupling will take up or supply the energy difference necessary for energy conversion. Measurements of cross-relaxation times, and harmonic cross relaxation are in fairly good agreement with the theories of Bloembergen and Grant.

The time that it takes for a spin system to return from an initial perturbed state to a state in thermal equilibrium with its surroundings (the lattice in the case of a solid) is known as the spin-lattice relaxation time, T_1. Considering a simple two level system, with energy levels E_1 and E_2, $E_1 < E_2$, and respective spin populations n_1 and n_2 ($n_1 + n_2 = N$ the total spin population), the rates at which relaxation transitions occur

between the levels may be defined by relaxation transition probabilities, w_{12} and w_{21} for upward and downward transitions respectively, (these are not the same as the stimulated transition probabilities w_{12} etc.). It is the calculation of these transition probabilities from consideration of the properties of the paramagnetic ions and the host lattice, and external experimental conditions, that theories of relaxation have attempted.

Waller (5.13) made a calculation of T_1 in which he considered that the spin and orbital angular momenta of a paramagnetic ion were completely decoupled, and that the spin was influenced by the lattice vibrations (phonons) only by their modulation of the dipolar coupling. This led to results which were serveral orders of magnitude larger than the experimental results obtained from studies of r.f. susceptibilities by Gorter (5.17) at Leiden University, although the two main processes (direct and Raman relaxation) were shown to agree in form with Waller's predictions. Later work by Heitler and Teller (5.18) postulated that the modulation of the crystalline Stark effect by the phonons would provide a stronger relaxation mechanism, but still led to relaxation times that were too long when compared to experiment. Subsequently, Van Vleck (5.19) refined the theory of the mechanism which is largely accepted now, that the lattice vibrations modulate the crystalline field at the paramagnetic ion due to their displacement (strain) of the surrounding ions of the host lattice, and hence couple the phonons to the orbital momentum of the paramagnetic ion, and residual spin-orbit coupling then results in an overall coupling between the phons and the spin, this being the mechanism whereby each individual spin transfers its energy to the lattice, with no co-operative effects from the other spins to which it is coupled. The theory was amplified by Mattuck and Strandberg (5.20), using a modification of Van Vleck's approach to derive a spin-Hamiltonian formalism for the transition group ions, and Orbach (5.21) proposed a third process involving real excited states of the ion, which is especially relevantin describing the relaxation of the rare earth ions.

In dealing with the relaxation of a single ion to the lattice, three processes may be involved. These are the direct process, the Raman process and the Orbach, or resonance relaxation, process. These processes do not involve any co-operative processes such as cross-relaxation, or exchange interactions between clusters of ions, and are usually applicable only to salts of low paramagnetic concentration.

In the direct process the spin relaxes from state $|b\rangle$ to state $|a\rangle$ and in so doing emits a single phonon of energy ε_{ab}, where σ_{ab} is the splitting in energy between the two states. Calculation of the transition probability for this process for a Kramers doublet (one in which the two spin states are time conjugates of each other of half integral quantum number) leads to the dependance of T_1 on temperature and applied magnetic field being

$$T_1 = aH^{-4}T^{-1} \tag{5.20}$$

while for a non-Kramers salt, the dependence is

$$T_1 = a' (\sigma_{ab})^{-2}T^{-1} \tag{5.21}$$

Where σ_{ab} is proportional to the applied magnetic field, then T_1 is inversely proportional to H^2.

The Raman process involves the scattering of a phonon of energy $h\nu_p'$ to energy $h\nu_p'' - h\nu_p' = \sigma_{ab}$. This is equivalent to the absorption of the phonon of $h\nu_p'$ by the spin in state $|b\rangle$, causing a transition to a virtual state $|c\rangle$, followed by the emission of the $h\nu_p''$ phonon, and relaxation of the spin to state $|a\rangle$. The calculated dependences for T_1 for this process are, for a Kramers salt,

$$T_1 = bH^{o}T^{-9} + b_1H^{-2}T^{-7} \tag{5.22}$$

the dependence of $H^{-2}T^{-7}$ only being relevant under certain circumstances,

as discussed by Orbach (1961a). For a non-Kramers salt the dependence is

$$T_1 = b' H^{o} T^{-7} \qquad (5.23)$$

The third relaxation process, the Orback, or resonance relaxation, discovered by Finn, Orbach & Wolf (5.22) is also a two phonon process, involving the absorption of a phonon $h\nu_p'$ by the spin in state $|b\rangle$, and its transition to a close lying excited level $|c\rangle$, with a splitting Δ above the ground levels, and then subsequent relaxation of the spin to state $|a\rangle$, with emission of a phonon $h\nu_p''$, where, as for the Raman process, $h\nu_p'' - h\nu_p' = \sigma_{ab}$, but the state $|c\rangle$ is a real state, not a virtual one. This process is only important if the splitting Δ is less than the Debye energy, $k\varepsilon_D$, which is that of the highest energy phonon in the lattice phonon spectrum. In this case,the dependence of T_1 on temperature is exponential;

$$T_1 = c \exp(-\Delta / kT) \qquad (5.24)$$

for both Kramers and non-Kramers salts, and the megnetic field depends on both internal hyperfine and dipolar fields, as well as applied field (Orbach, 5.23).

CHAPTER 5

REFERENCES

5.1 G.E.Cleeton and N.H.Williams, Phys. Rev. 45, 234 (1934).

5.2 E. Zavoisky, J.Phys. USSR 9, 211, (1945).

5.3 R.L. Cumerow and D. Halliday, Phys. Rev 70, 433, (1946).

5.4 H. Assenheim "Introduction to E.S.R" Hilger (1966).

5.5 P.B. Ayscough "Electron Spin Resonance in Chemistry" Methuen (1967).

5.6 J.S. Thorp, H.P.Buckley, J'Mat.Sci. 9, 1499, (1974).

5.7 G.Brown, C.J.Kirkby, and J.S.Thorp, J.Mat.Sci 9, 1337 (1974).

5.8 J.S. Thorp, R.A. Vasquez, C.Adcock and W.Hutton, J.Mat.Sci 11,(1976).

5.9 J.S.Thorp, M.D.Hossain, J.Mat.Sci. 15, 2647, (1980).

5.10 H.A.Kramers, Proc.Acad.Sci. Amsterdam 33, 959, (1930).

5.11 P.A.M.Dirac, Quantum Mechanics, OUP, (1947).

5.12 A. Abragam and M.H.L.Pryce, Proc. Roy.Soc. A 205, 135 (1951).

5.13 I. Waller, Z.Phys. 79, 370, (1932).

5.14 R de L Kronig and C.J.Bouwkamp, Physica 5, 521, (1938).

5.15 N. Bloembergen, Phys.Rev 104, 324, (1956).

5.16 W.J.C.Grant, Phys. Rev. 134, A 1554, (1964).

5.17 C.J. Gorter, Paramagnetic Relaxation, Elsevier Pub.Co.(1947).

5.18 W.Heitler and E.Teller, Proc.Roy.Soc. A155, 629 (1936).

5.19 J.H.Van Vleck, Phys.Rev. 57, 426, (1940).

5.20 R.Mattuck and M.W.P. Strandberg, Phys.Rev. 119, 1204, (1960).

5.21 R. Orbach, Proc.Roy.Soc.A 264, 458, (1961).

5.22 C.B.P. Finn, R.Orbach and W.P.Wolf, Proc.Phys.Soc.77, 261, (1961).

5.23 R.Orbach, Proc. Roy. Soc. 264, 485, (1961).

CHAPTER 6

ESR: EXPERIMENTAL METHODS AND RESULTS

6.1 APPARATUS

All the ESR measurements were made using the Department's Varian V-4502-15 X-Band spectrometer fitted with an Oxford Instruments ESR 9 liquid helium cryostat. This allowed 9 GHz ESR measurements over a temperature range of 3.8 → 300°K

6.1.1 The Varian V4502-15 Spectrometer

This section is intended to give a summary of the basic features and operation of the V4502-15, a block diagram of which is presented in Figure 6.1. More detailed information regarding the techniques of ESR spectroscopy may be found in the books by Poole (1972) (6.1) and Wilmhurst (1967) (6.2).

The microwave source, a X-Band Klystron, could be tuned to adjust the output frequency over a range of $\sim 9.5 \pm 0.5$ GHz. The klystron supplied microwave power via an isolator, a variable attenuator and a length waveguide to the first arm of a magic tee or microwave bridge (Figure 6.2). The magic tee is a device which will not permit the direct passage of power into an opposite arm. Thus in the figure power incident on arm 1 would be split equally between arms 2 and 3 with no power going to arm 4. In the spectrometer power was fed to arm 1, arm 2 was terminated in a matched load, while arm 3 was terminated in the microwave cavity located between the poles of the electromagnet. The detector was located in arm 4, seeing microwave power only when the bridge was unbalanced by absorption in the cavity. In fact the start of any change in reflected power would be missed under these conditions because a small amount of power is needed to bias the crystal detector 'on'. Therefore, in practice a nylon coupling screw in the cavity was adjusted (in the off resonance condition) to give a null output from the detector and then the detector was biased 'on' using a slide-screw tuner in arm 2.

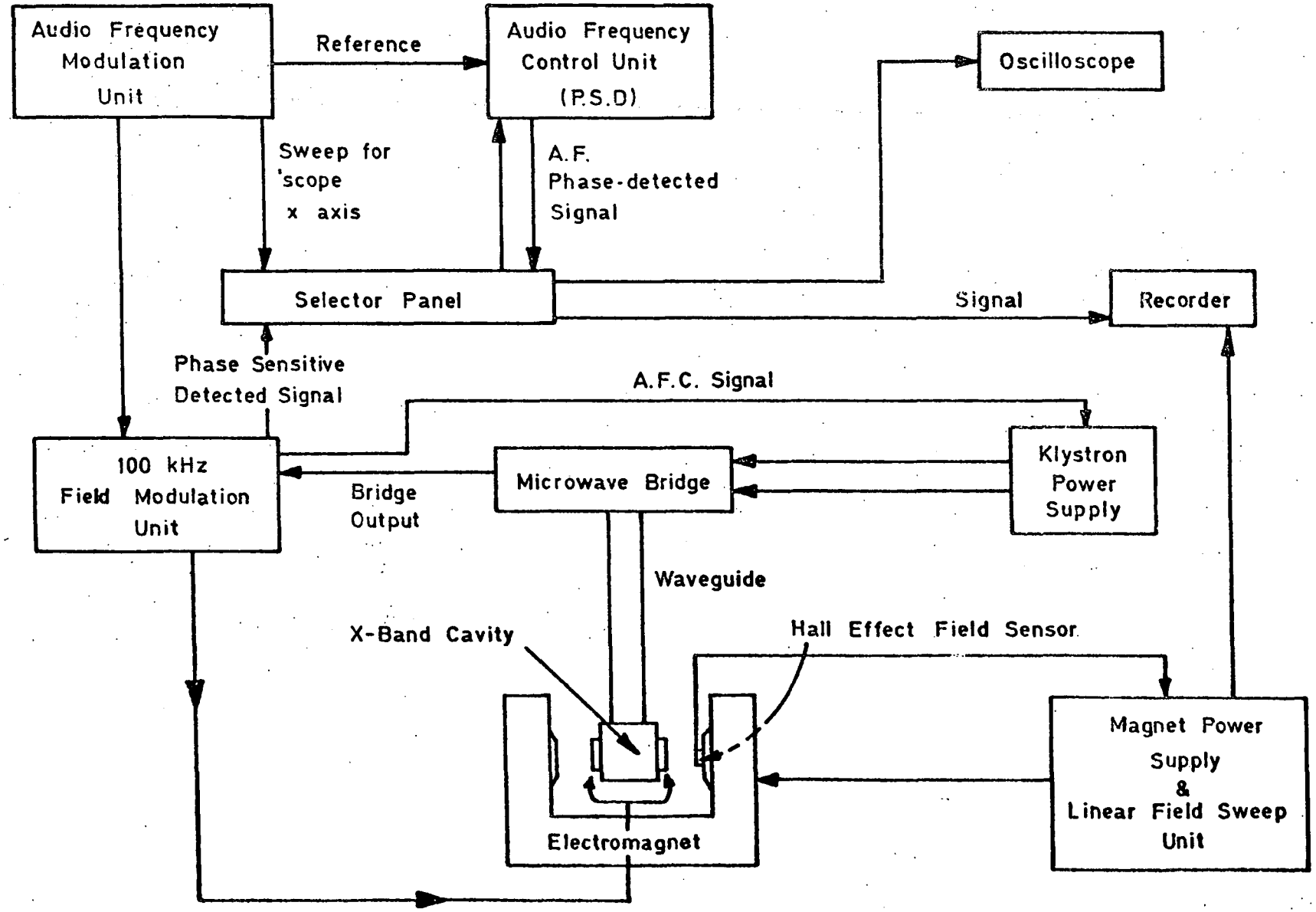

FIG.6·1 BLOCK DIAGRAM OF E.S.R. SPECTROMETER

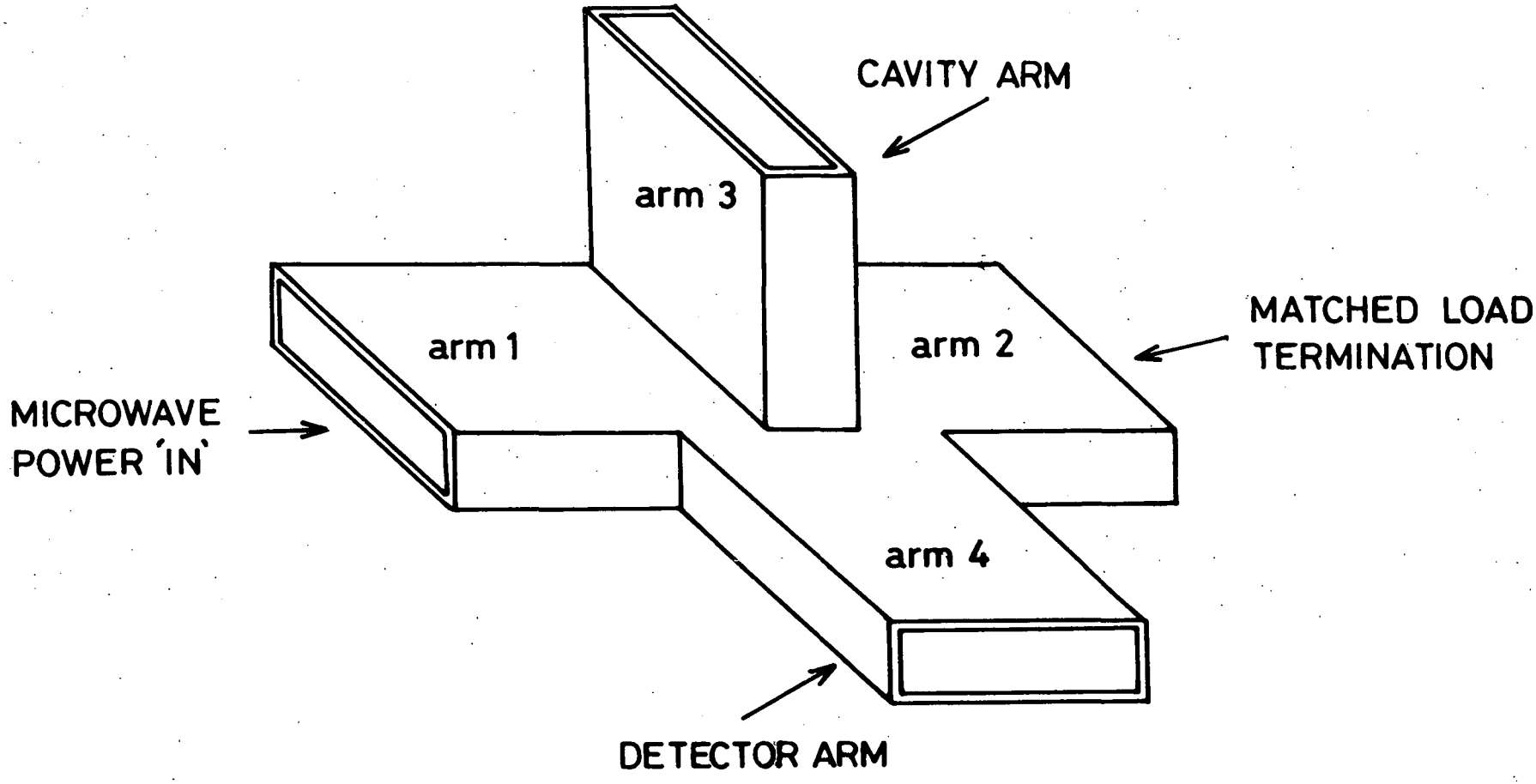

FIG. 6·2 MICROWAVE FOUR ARM BRIDGE (ARMS MARKED AS USED IN THE VARIAN SPECTROMETER)

A microwave cavity consists of a resonant section of waveguide, usually gold plated, in which the microwave power builds up standing waves of high electric and magnetic fields. For ESR spectroscopy, the sample is placed in a region of high r.f. magnetic field.

The Varian spectrometer used a V4531 cavity operating in the E_{102} mode so that the sample could be placed in the centre of the cavity. Holes in the electrically neutral top or bottom faces of the cavity allowed the insertion of samples and the cryostat glassware. Provision for sample irradiation was made by slots in the front face of the cavity, although the facility was not used in the present work.

The klystron frequency had to be adjusted to the resonant frequency of the combination of the cavity and any sample holder and sample within it. This was achieved by applying a sawtooth modulation signal to the klystron reflector voltage, and displaying the output from the detector (arm 4 of the magic tee) on an oscilloscope. With the klystron frequency close to the resonance of the cavity a dip in the display was observed corresponding to the frequency being swept through the cavity resonant frequency. Once the dip had been found the modulation was turned off and the klystron frequency was adjusted to give the minimum power output (corresponding to the cavity resonant frequency) using the DC reflector voltage.

To maintain the condition over the periods required, the spectrometer employed an Automatic Frequency Control (AFC) system. This involved low amplitude 10 kHz modulation being applied to the klystron reflector voltage with consequent modulations in frequency and detected power output. The modulated power output was fed, via a lock-in amplifier, to a phase-sensitive detector, together with a 10 kHz reference signal. When the klystron frequency was identical to the cavity resonant frequency the reflected modulation frequency was double the original frequency, i.e. 20 kHz, but under other conditions the 10 kHz component could be detected. This 10 kHz component was then used to generate the appropriate DC correction to the klystron reflector

voltage to reset the klystron frequency.

The external swept DC magnetic field was provided by a V3605 12" electromagnet controlled by a VFR 5203 field regulated power supply. A linear sweep of field with respect to time and long term magnetic field stability was ensured by the use of a Hall effect field sensor attached to one of the magnet pole faces. A reference voltage, proportional to the required field was compared to the output Hall voltage, itself proportional to the actual field. If these two voltages were not equal an error signal was generated which caused the magnet current to be adjusted until the required field was reached. The system was claimed to be capable of setting the desired field to 1 Gauss with a 1 part in 10^5 repeatability and a resolution of 0.02 Gauss.

Absorption of power by the sample as the field is swept through the magnetic resonance condition in turn changes the impedance of the cavity, and causes a change in the power level reflected to the magic tee. This unbalances the bridge and the change in power level, corresponding to the absorption is detected in arm 4. It is possible to detect these changes under DC conditions but, as the noise generated by the crystal detector is inversely proportional to frequency, high frequency modulation of the ESR signal is introduced to increase the signal-to-noise ratio. To facilitate this a pair of field modulation coils are built into the walls of the cavity and a 100 kHz signal is applied to them. Thus the sample experiences the (large) swept DC magnetic field with a low amplitude (0.1 to 1 gauss) 100 kHz modulation field.

Thus, when the DC magnetic field is swept through a resonance line, the DC power level is detected along with the 100 kHz modulation, the phase and magnitude of which are determined by the slope of the resonance absorption line (Figure 6.3a). Then, by using a lock-in amplifier and phase sensitive detector with a 100 kHz, reference signal, a DC output which approximates to the first derivative of the absorption line is produced and displayed on a chart recorder. The conditions under which this is not so, are detailed in section 6.1.2.

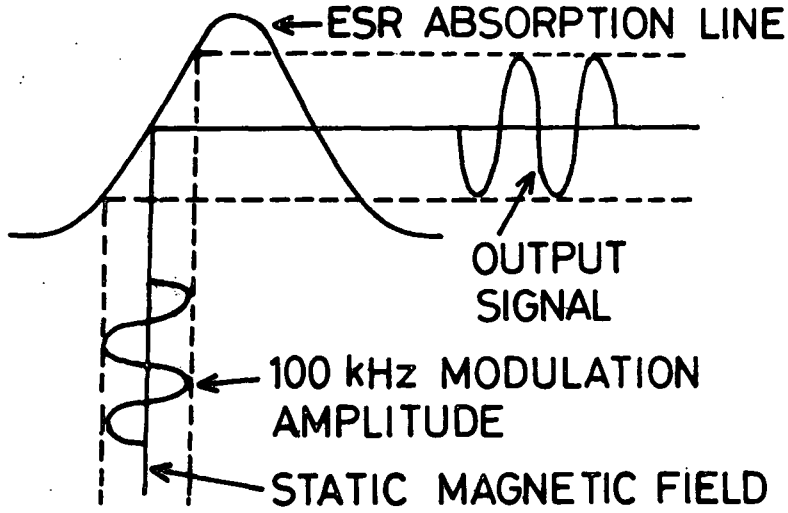

(a)

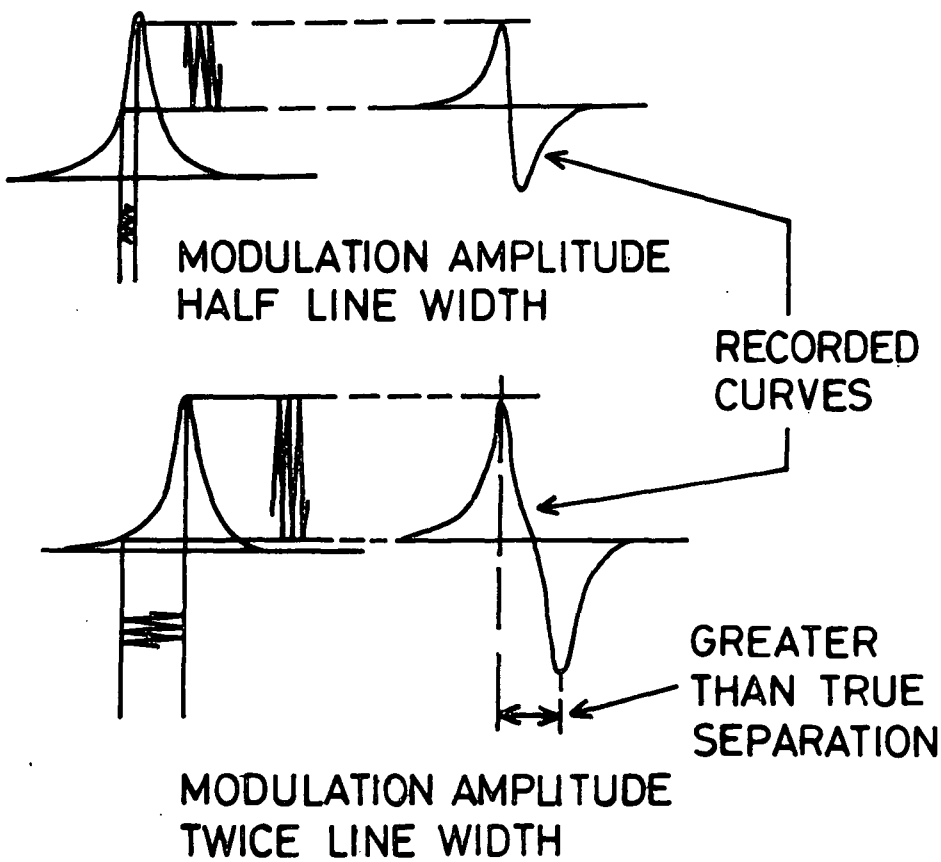

(b)

FIG. 6·3 (a) E.S.R. OUPUT SIGNAL RESULTING FROM FIELD MODULATION
(b) EFFECT OF EXCESSIVE FIELD MODULATION

In order that the signal to noise (S.T.N.) ratio be maximised, the sample must be accurately placed in the high magnetic field region of the cavity. Two 11 mm holes are provided in the cavity (top and bottom) and sample, either power or solid fragments were placed in spectrosil quartz tubes and inserted into the cavity. Spectrosil quartz was used as its high purity guards against spurious ESR signals.

6.1.2 Possible Sources of Error in ESR Measurements

There are two major sources of error in ESR measurements, one of which is prevalent at low temperatures, and the other at high temperatures, or in samples with a low spin concentration.

Firstly, if too much rf power is used the signal may saturate, i.e. the rate of excitation may be greater than the rate of relaxation. This is most likely to occur at low temperatures, where a spin system may have a long relaxation time. Power saturation manifests itself in a reduction of the first derivative peak amplitude, and an apparent line broadening.

In practice, power saturation is detected by observing the peak height of the absorption trace with an increase of power until a reduction in height is noted. The power is then reduced slightly. This method ensures that the maximum signal-to-noise ratio is obtained without distortion.

The second source of error is modulation broadening, which occurs if the magnitude of the field modulation is of the same order as the linewidth of the absorption under observation. This might be the case at room temperature in a system with a low spin concentration, or, as in the present work when the conducting nature of the low weight gain RBSN samples resulted in a damped cavity Q if too large a sample was used. A high modulation field improves the signal-to-noise performance of the spectrometer so at higher temperatures the level of modulation is usually a compromise between increasing the STN ratio and the risk of modulation broadening. Figure 6.3 (b) shows the effect on the ESR derivative signal.

6.1.3 Cryogenic Facilities

The Varian spectrometer used in this work was fitted with an Oxford Instruments ESR 9 liquid helium continuous flow cryostat which incorporated temperature control between 3.8 K and 300 K. The cryostat consists essentially of a stainless steel capillary tube which directs helium, supplied by a transfer tube from a storage dewar, into a quartz dewar placed in the high magnetic field region of the microwave cavity. The basic items of the system are shown in Figure 6.4. Within the cryostat, the whole liquid helium path is isolated from ambient temperature by, firstly the return flow of helium to the gas recovery system and secondly a vacuum jacket. Liquid helium is pumped continuously to the cryostat via the transfer tube, which is insulated in the same way as the cryostat itself. The helium then emerges from the capillary in the cryostat just below the cavity and passes the gold/iron thermocouple to strike a 3 mm bore quartz tube containing the sample. The tube is introduced into the cavity and held in place by a gas-tight O-ring seal at the top of the quartz cavity insert. After striking the sample tube the helium is pumped, via the transfer tube, a needle valve and flow meter to a recovery system by a diaphragm pump. The pressure in the cryostat was maintainedat $\sim 6 \times 10^{-5}$ torr to provide insulation for the helium capilliary. When operating below $\sim$ 60 K cryopumping of the residual gases in the cryostat took place so the valve connecting the vacuum system to the vacuum pump was closed under these conditions, reducing the cryostat pressure still further.

Two means of temperature control were provided on the cryostat. For coarse control the helium flow rate could be adjusted with the needle valve in the gas return line. Fine adjustment and closed loop control was achieved by the ESR 9 control unit using the input from the thermocouple and the heating element wound just below the tip of the helium capillary tube.

Some precautions had to be taken to ensure smooth running of the cryostat.

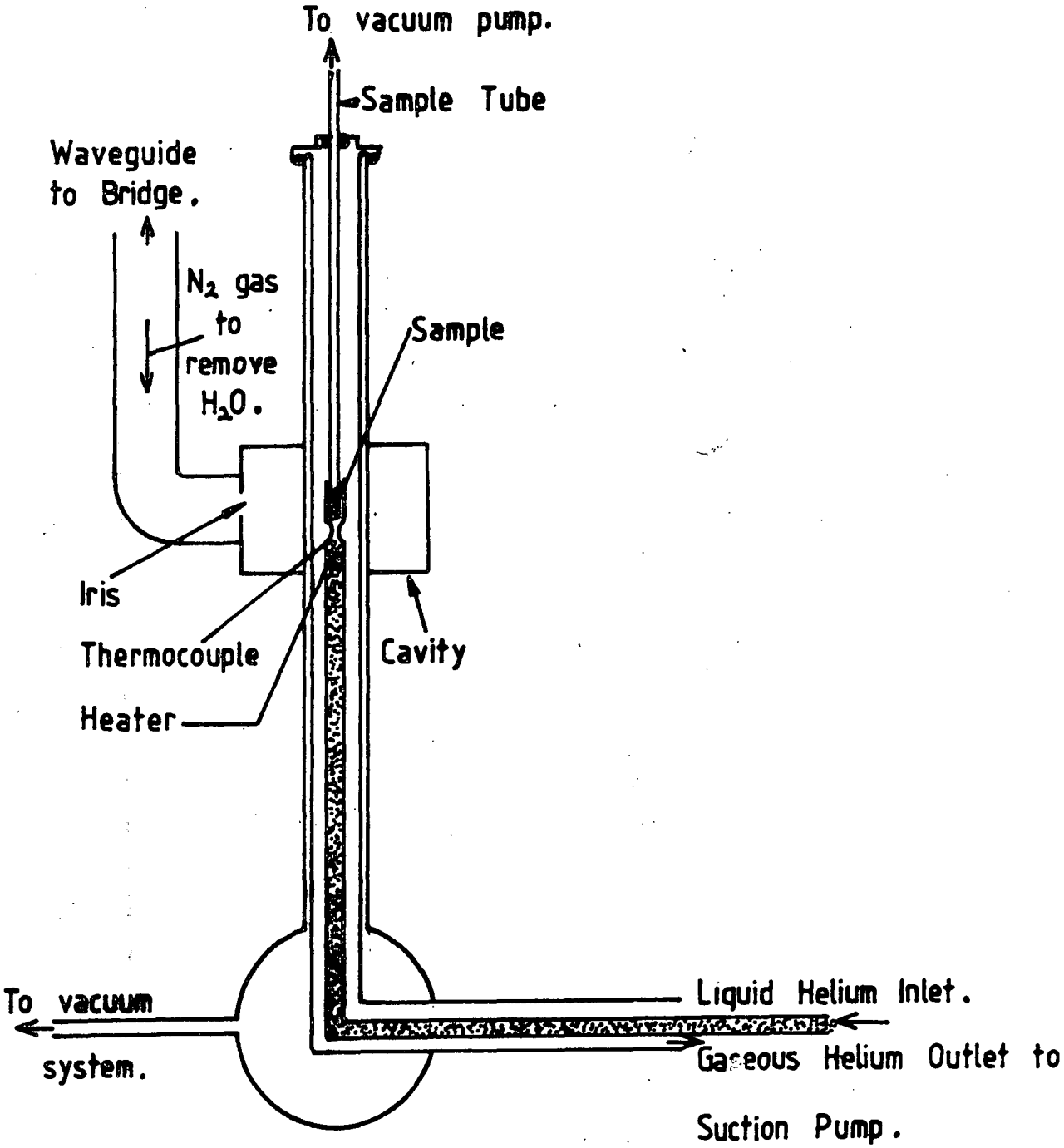

FIG. 6·4 CRYOSTAT FACILITIES

(a) It was necessary to provide a dry nitrogen purge to the cavity, especially if the vacuum level in the cryostat was poor. This was because, at very low temperatures with a poor vacuum the quartz dewar had a tendency to ice-up externally. Then, upon warming, the cavity Q was damped by the melting ice. The use of a dry atmosphere prevented this happening.

(b) When working with powders in the sample, the condensation and subsequent boiling of residual gases in the sample tube would smear the power up the tube walls. This was overcome either by ensuring that the rise in temperature was slow, or, as shown in Figure 6.6 by evacuating the sample tube.

6.2 COMPUTER ANALYSIS OF ESR DATA

As noted earlier, the phase sensitive detection system used to increase the S.T.N. ratio of the recorded absorption spectra results in the production of a first derivative of the line actually being recorded. In order to assess the shape of the absorption distribution, it is necessary to integrate the data. A FORTRAN computer program has been developed to integrate the data (using Simpson's Rule) and to calculate, via the moments of the absorption line, the skewness and kurtosis of the line. The program also takes account of the variations in working spectrometer frequency and normalizes the data such that the field values calculated are those which would have observed with a spectrometer frequency of 9.3 GHz. This has allowed easy comparison of data taken at several different frequencies and has permitted plotting of all data on similar field axes. Appendix 1 contains the details of the algorithms used, and the code developed.

6.3 ELECTRON SPIN RESONANCE IN AMORPHOUS AND POLYCRYSTALLINE SILICON

ESR in amorphous silicon was first reported, for sputtered material, by Brodsky and Title in 1969 (6.3). The result was confirmed on evaporated silicon by Voget-Grote, Stuke and Wagner (6.4). Both these results were very similar to the observed resonance signals from crushed crystalline samples.

In 1961 Walters and Estle (6.5) showed that the spin signal in such crystalline samples stems from defect states in the bulk of the damaged material rather than from surface states. This is in agreement with Kaplan et al (6.6) who observed that clean cleaved silicon surfaces exhibit no spin signal and Stuke (6.7) who reported an increase in spin density following sample bombardment with rare gas ions. It is, therefore, commonly accepted that E.S.R. signals in amorphous and polycrystalline silicon exhibit the properties of paramagnetic electrons localized at defects in the bulk.

The following features are observed in the reported experimental work.

(a) There is a single, predominantly symmetric and inhomogeneously broadened line.

(b) Hyperfine structure, if present, is unresolved.

(c) There is, of course, no angular anisotropy.

(d) The linewidth ΔH_{pp} is temperature dependent if the sample shows hopping-type d.c. conductivity.

The published data on amorphous silicon (for example Stuke (6.8) shows ΔH_{pp} at about 5 gauss at 100 K and rising to 7 gauss at 350 K. The line is basically Lorentzian in shape with the wings broadening more than the centre at higher temperatures. Movaghar and Schweitzer (6.9) have shown that a distribution of relaxation times leads to this behaviour. Figure 6.5 (after Stuke (6.8)) shows the calculated (solid) lines and experimental points. Voget-Grote et al (6.4) have shown that the linewidth can be described by the superposition of a temperature independent part $\Delta H_{pp}(0)$ and a temperature dependent part $\delta H_{pp}(T)$ and Movaghar and Schweitzer (6.10) have estimated the value of $\Delta H_{pp}(0)$ to be between 1 and 10 gauss.

Brodsky & Title reported a g value of 2.0055 ($\pm$ .0005) for amorphous silicon in 1969 (6.3) and this value has been confirmed since. The same authors reported a g value of 2.003 $\pm$ .001 and a ΔH_{pp} of 6 for thin film silicon carbide at the same time.

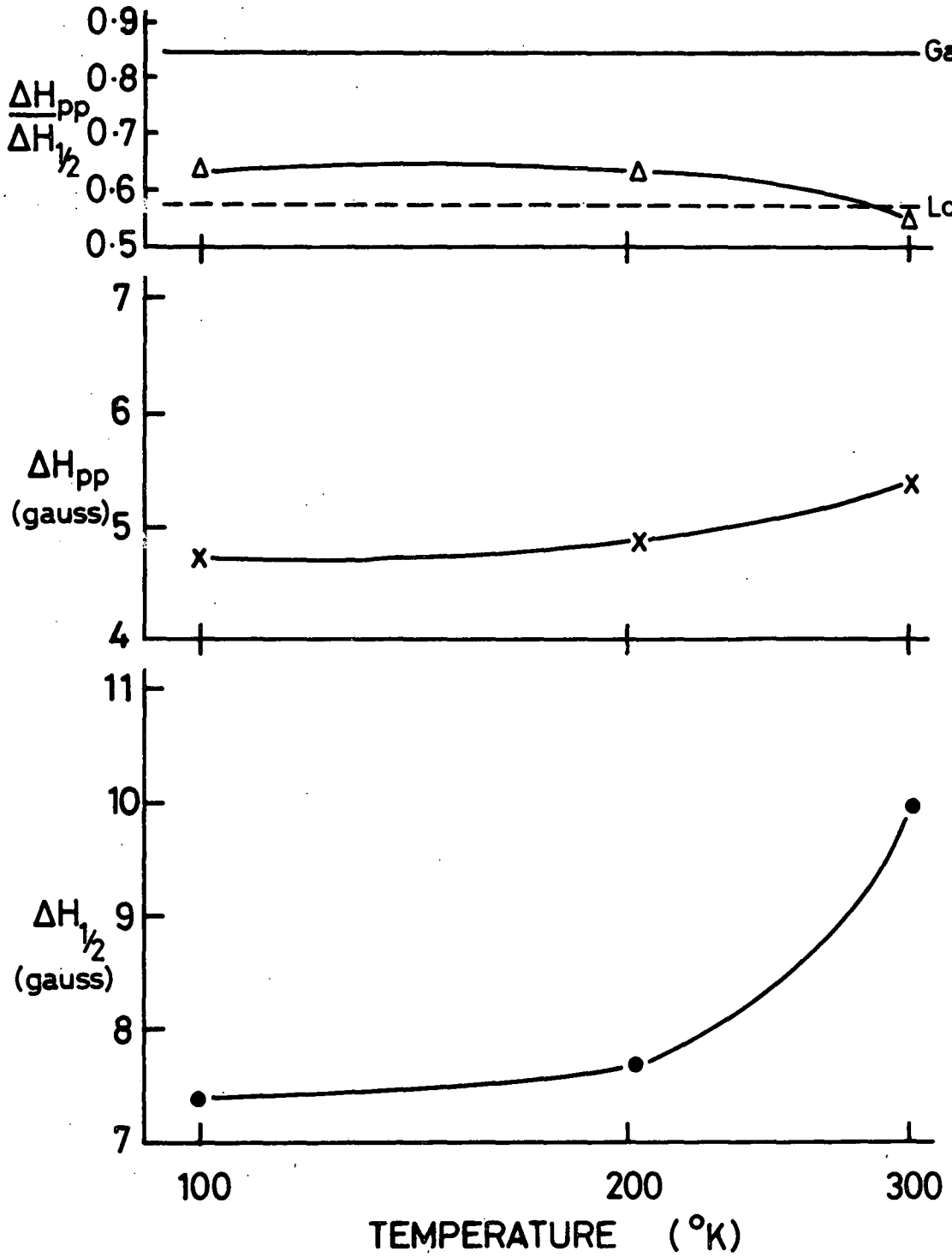

FIG. 6·5 ESR IN AMORPHOUS SILICON AFTER STUKE (6·8)
=== THEORY, Δ x • EXPERIMENTAL.

To sum up then, high spin densities are observed by ESR ($\sim 10^{19}$ spins/cm^3) in evaporated and sputtered amorphous silicon ; such results strongly indicate that of a high density of dangling bonds is produced by these preparative techniques. By contrast preparation of a-Si by the glow discharge deposition of silane produces a material with no (or a very small) ESR signal and it seems that hydrogen incorporated in to the structure during preparation saturates most of the dangling bonds (6.7).

6.4 RESULTS

ESR measurements have been made in the temperature range 3.8 K to 300 K on the following materials :-

(i) Silicon powder from AME Ltd, used in the preparation of RBSN

(ii) RBSN powder of 64.5% weight gain from the same source

(iii) Hot pressed silicon nitride from Newcastle University

(iv) Partially nitrided RBSN samples having weight gains in the region 22.5 to 59.5%.

6.4.1 Silicon Powder

Figure 6.6 shows the ESR derivative signal measured on the silicon powder used by AME Ltd. as starting material for the manufacture of RBSN. Such data taken at temperatures from 3.8 to 300^{o}K has been integrated so as to evaluate the lineshape. Figure 6.7 shows ΔH_{pp} (from the derivative data) $\Delta H_{\frac{1}{2}}$ height (from the integrated line) and the ratio of the two by which the lineshape can be gauged. Figure 6.8 shows ratios for Lorentzian and Gaussian Lineshapes. It can be seen that the ... level of ΔH_{pp} reported earlier has been observed along with the increase in linewidth with increasing temperature. In the $\Delta H(o)$ region the lineshape is predominantly Lorentzian and tends to Gaussian at higher and lower temperatures. The results obtained here are comparable with those reported earlier on amorphous silicon (6.3, 6.4, 6.7).

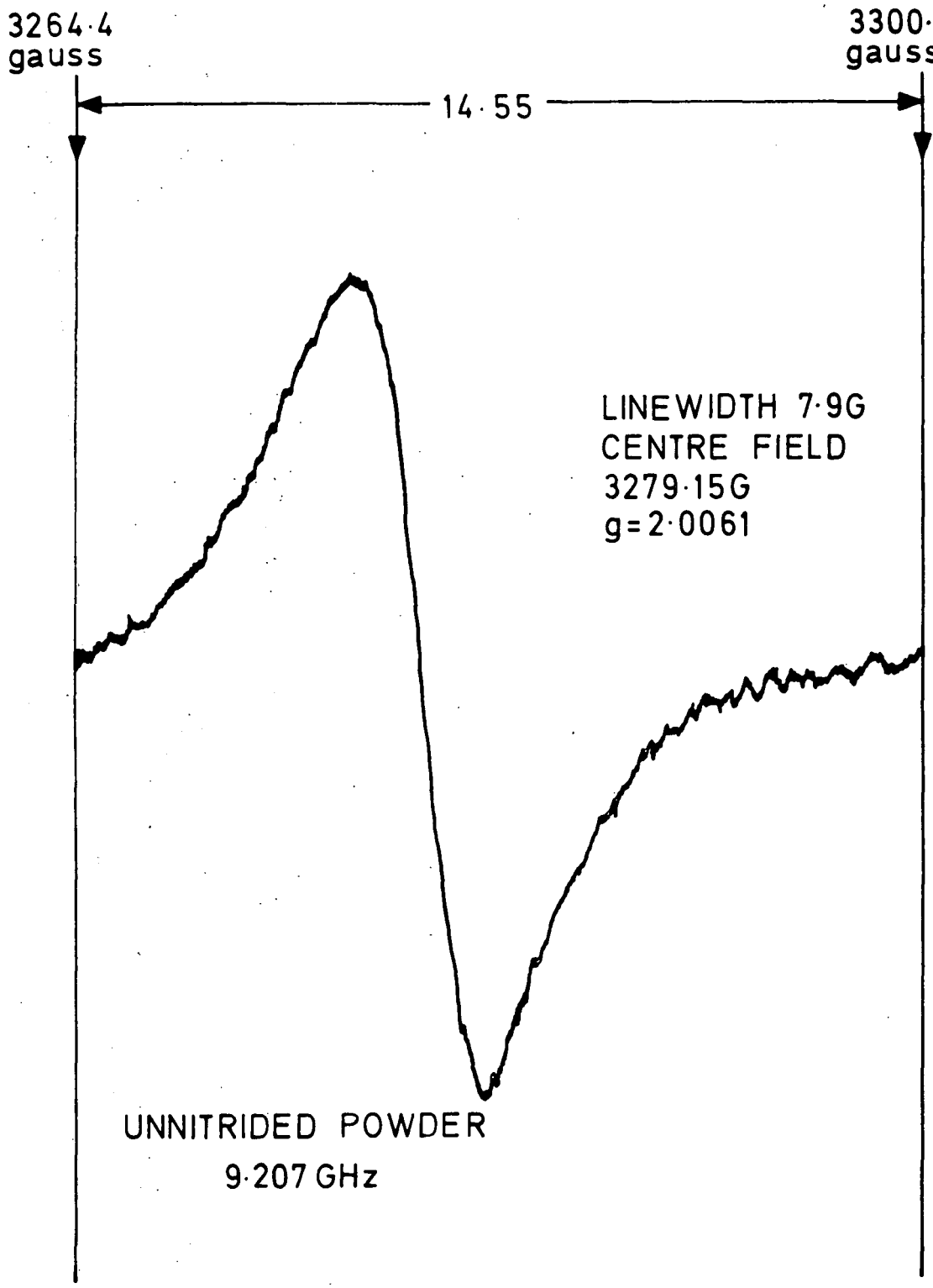

FIG.6·6 FIRST DERIVATIVE ESR SPECTRUM OF OF UNNITRIDED SILICON

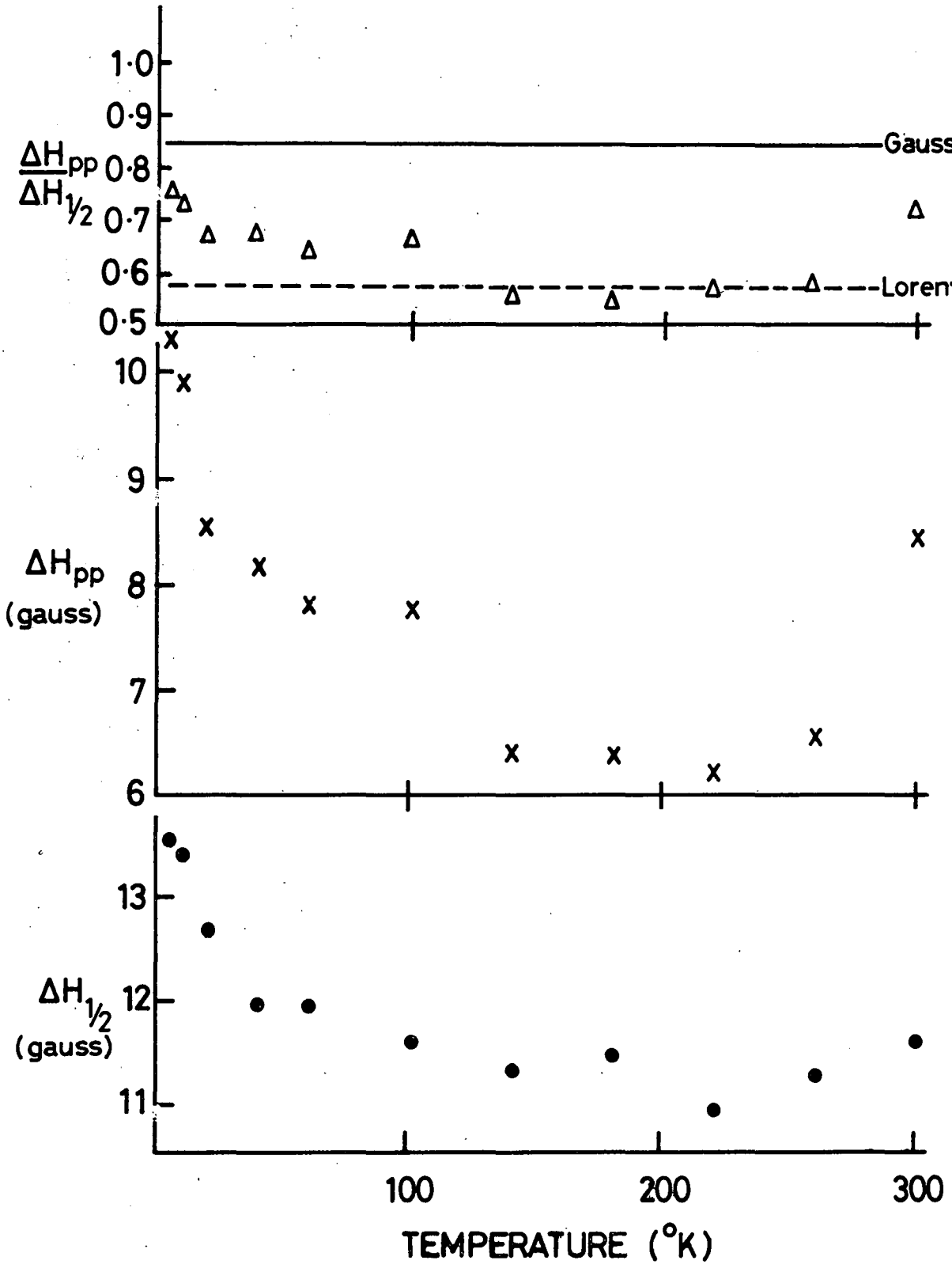

FIG. 6·7 COMPOSITE PLOT OF ΔH_{pp}, $\Delta H_{1/2}$ AND THE RATIO $\frac{\Delta H_{pp}}{\Delta H_{1/2}}$ FOR UNREACTED A.M.E. Ltd. SILICON POWDER.

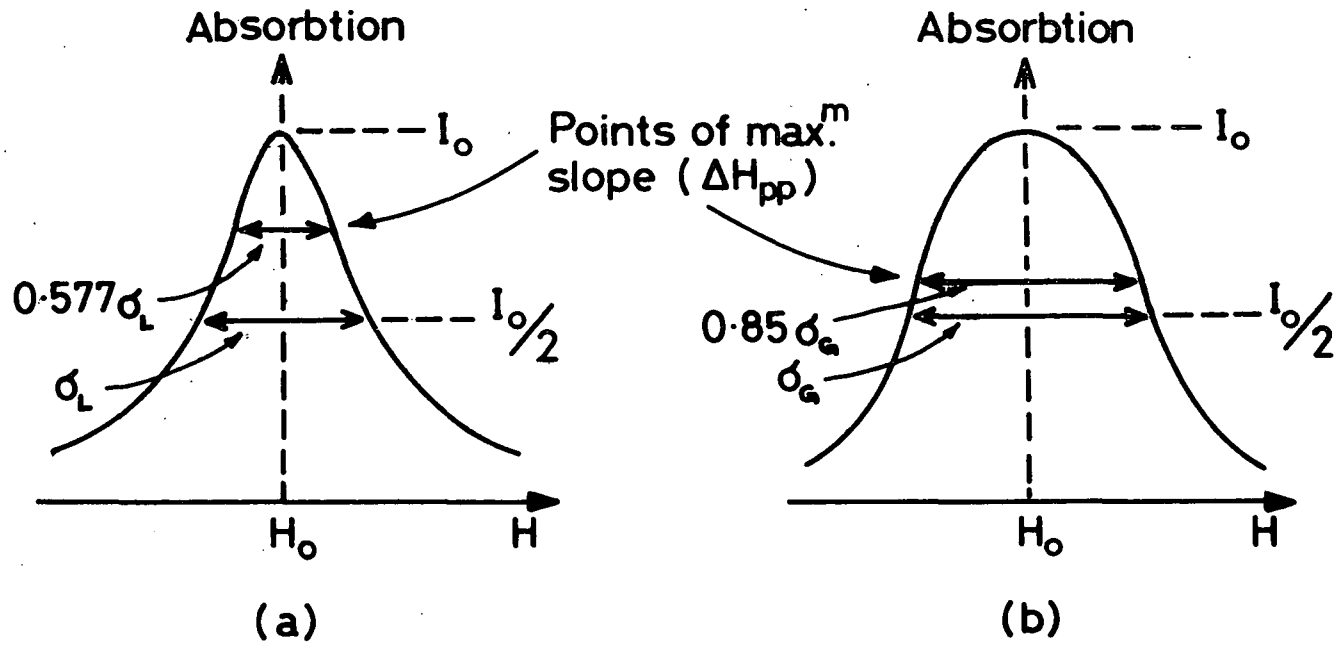

FIG. 6·8 CHARACTERISTICS OF (a) LORENTZIAN AND (b) GAUSSIAN LINESHAPES

6.4.2 64.5% weight gain RBSN

Figure 6.9 shows a single derivative line observed for 64.5% weight gain RBSN powder, having a g value of 2.002, and Figure 6.10 shows a composite plot for this material similar to 6.7 for unreacted silicon. The essential features of the nitride line are similar to those of the silicon line, with the exception that the g value is shifted slightly closer to the free electron value.

6.4.3 Hot Pressed Silicon Nitride (HPSN)

Figure 6.11 shows a single derivative line observed at room temperature for HPSN, and Figure 6.12 shows the composite for the same material. The features here are rather different, in that the lineshape is more nearly Gaussian, and that the rise in ΔH_{pp} and $\Delta H_{\frac{1}{2}}$ observed at the temperature approached 300°K with the unreacted silicon, and RBSN, is absent here.

6.4.4 ESR of Partially Nitrided RBSN

Figures 6.13, 6.14, and 6.15 show the ESR spectra obtained from nitrides having weight gains of 22.5%, 49% and 59.3% respectively over a temperature range from 4°K to 300°K. In all cases a double line can be seen which is presumed to be a combination of the silicon and RBSN lines reported earlier. The change in lineshape with temperature is not yet understood, but as the g value of the 'pure' lines does not change with temperature, an explanation is most likely to be found by examination of the relative relaxation rates of the two species.

One striking feature is that both the silicon and the nitride line are well observed in the 59% weight gain sample, and it is noticeable that the 64.5% weight gain material signal shows a slight 'silicon bump'.

Thus ESR appears very sensitive to the presence of silicon in RBSN.

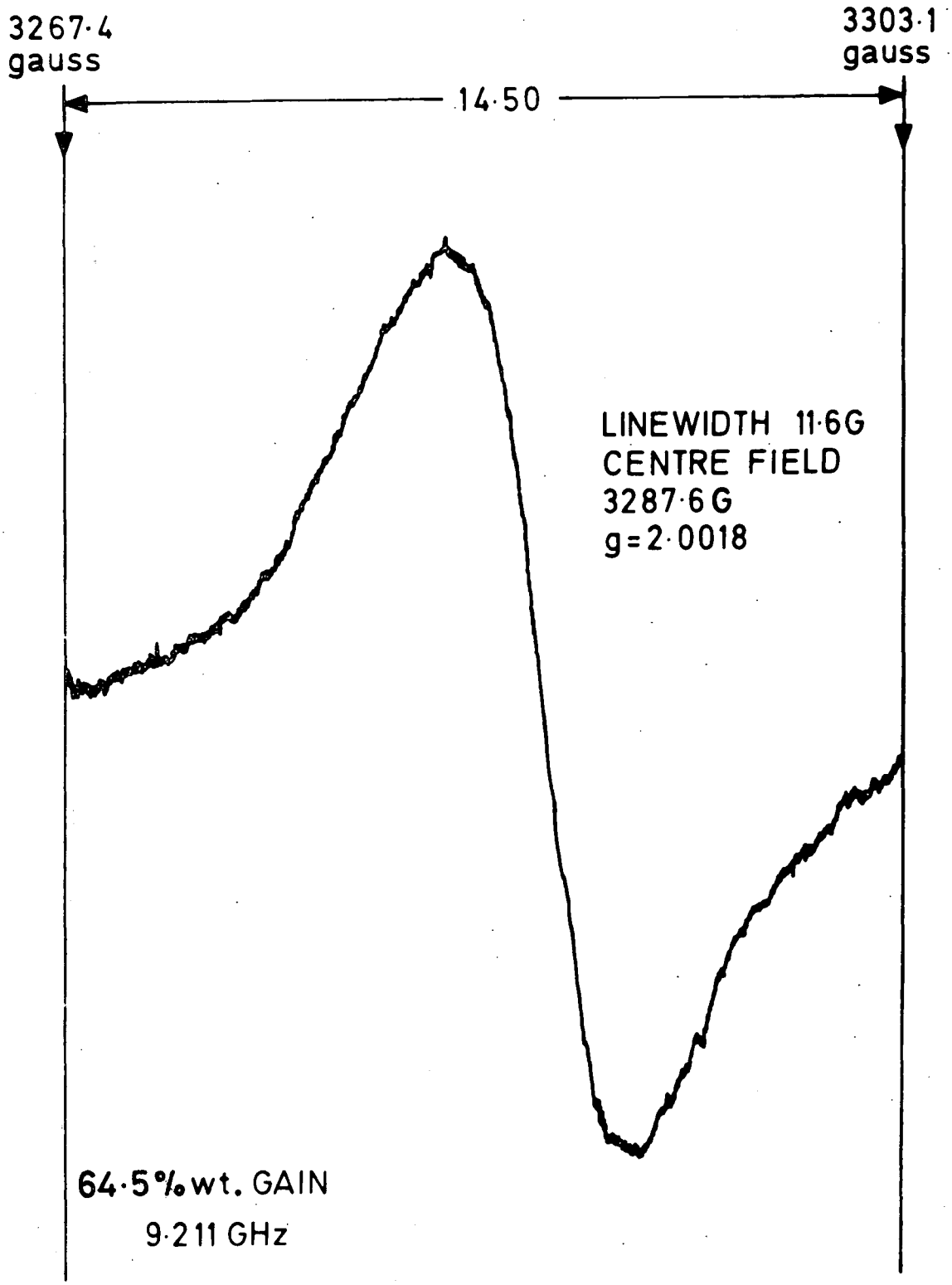

FIG.6·9 FIRST DERIVATIVE ESR SPECTRUM OF 64·5% WEIGHT GAIN RBSN

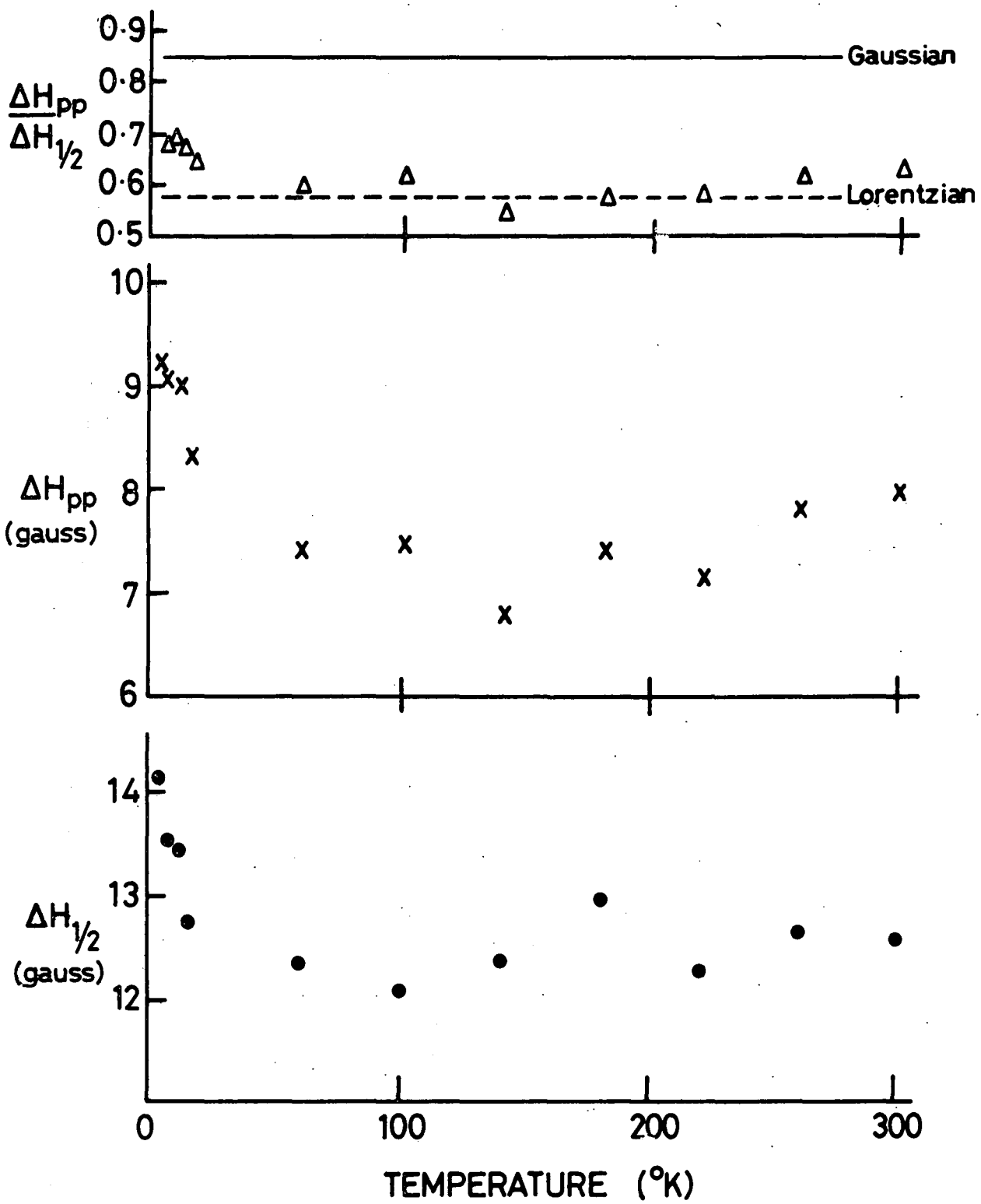

FIG. 6·10 COMPOSITE PLOT OF ΔH_{pp}, $\Delta H_{1/2}$ AND THE RATIO $\Delta H_{pp}/\Delta H_{1/2}$ FOR TOTALLY REACTED RBSN POWDER

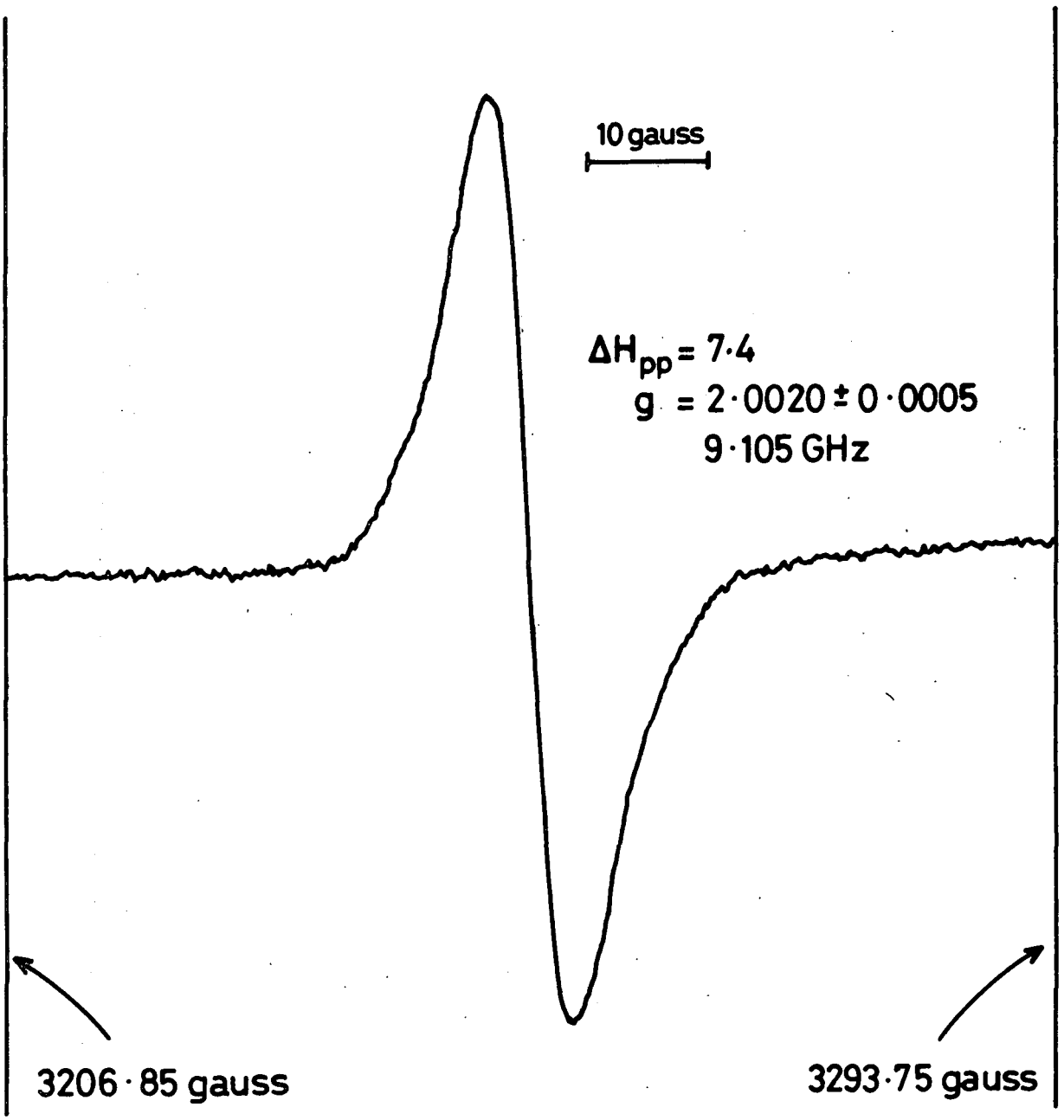

FIG. 6·11 DERIVATIVE ESR SPECTRUM OF HOT PRESSED SILICON NITRIDE AT 20°C

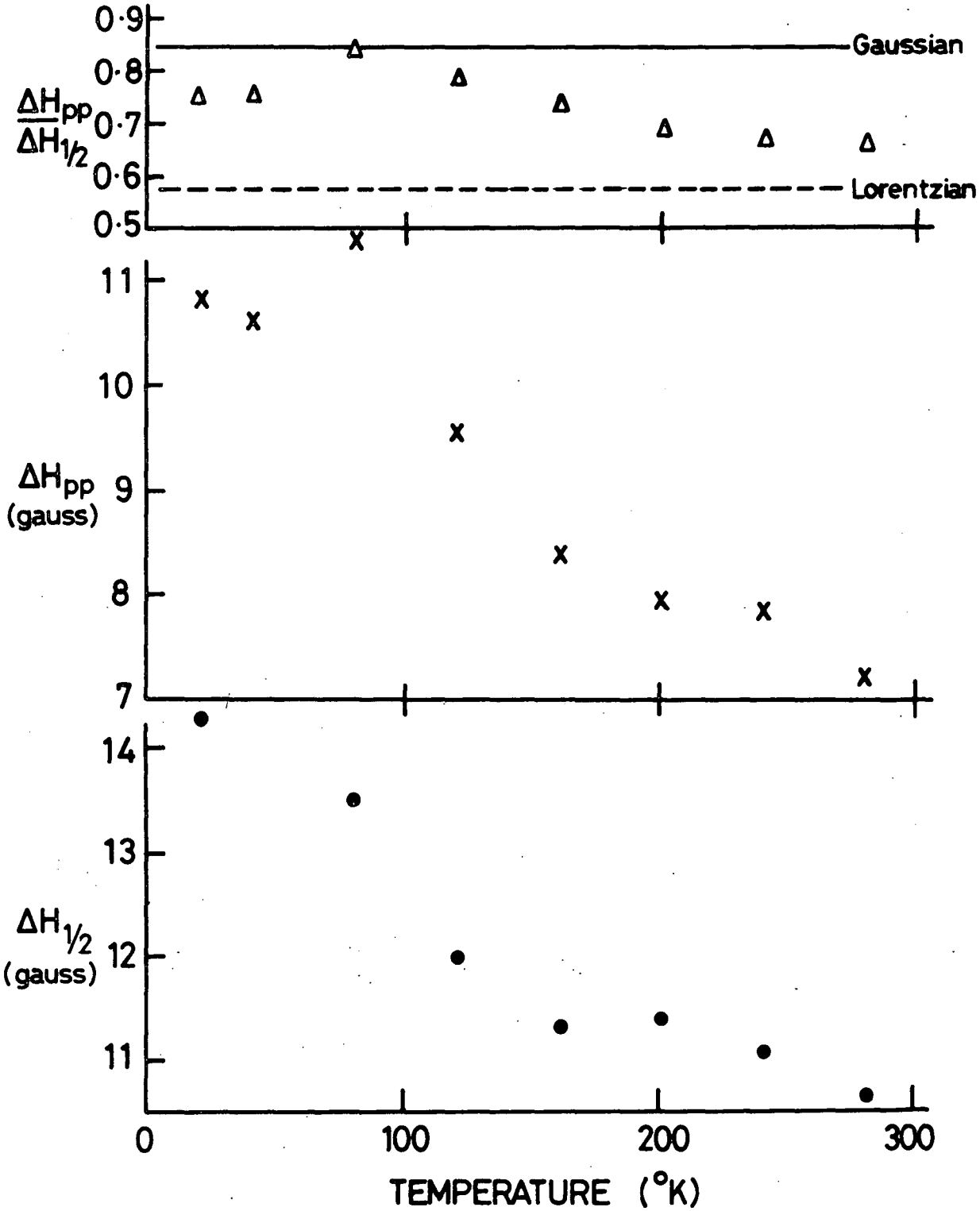

FIG. 6·12 COMPOSITE PLOT OF ΔH_{pp}, $\Delta H_{1/2}$ AND THE RATIO $\Delta H_{pp}/\Delta H_{1/2}$ FOR HOT PRESSED SILICON NITRIDE

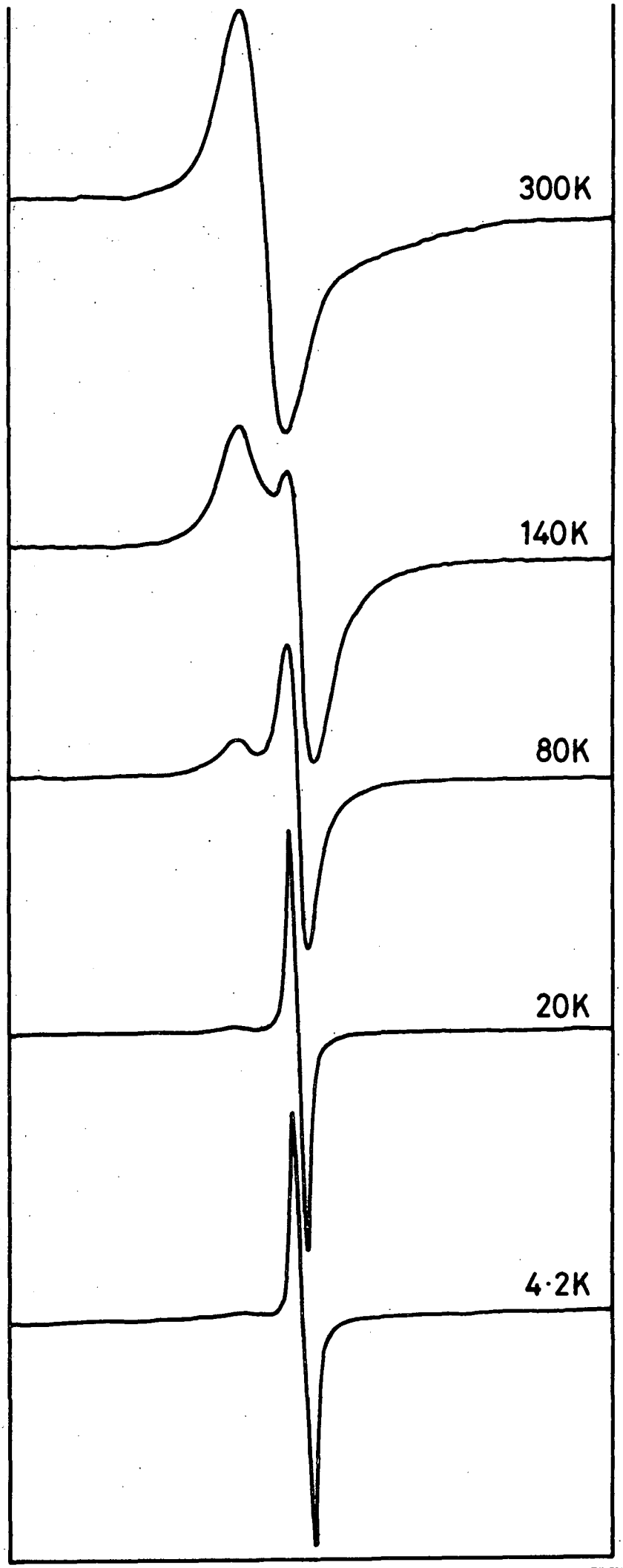

FIG.6·13 VARIATION OF ESR SPECTRUM WITH TEMPERATURE
22% WEIGHT GAIN Si_3N_4, 9·110 GHz

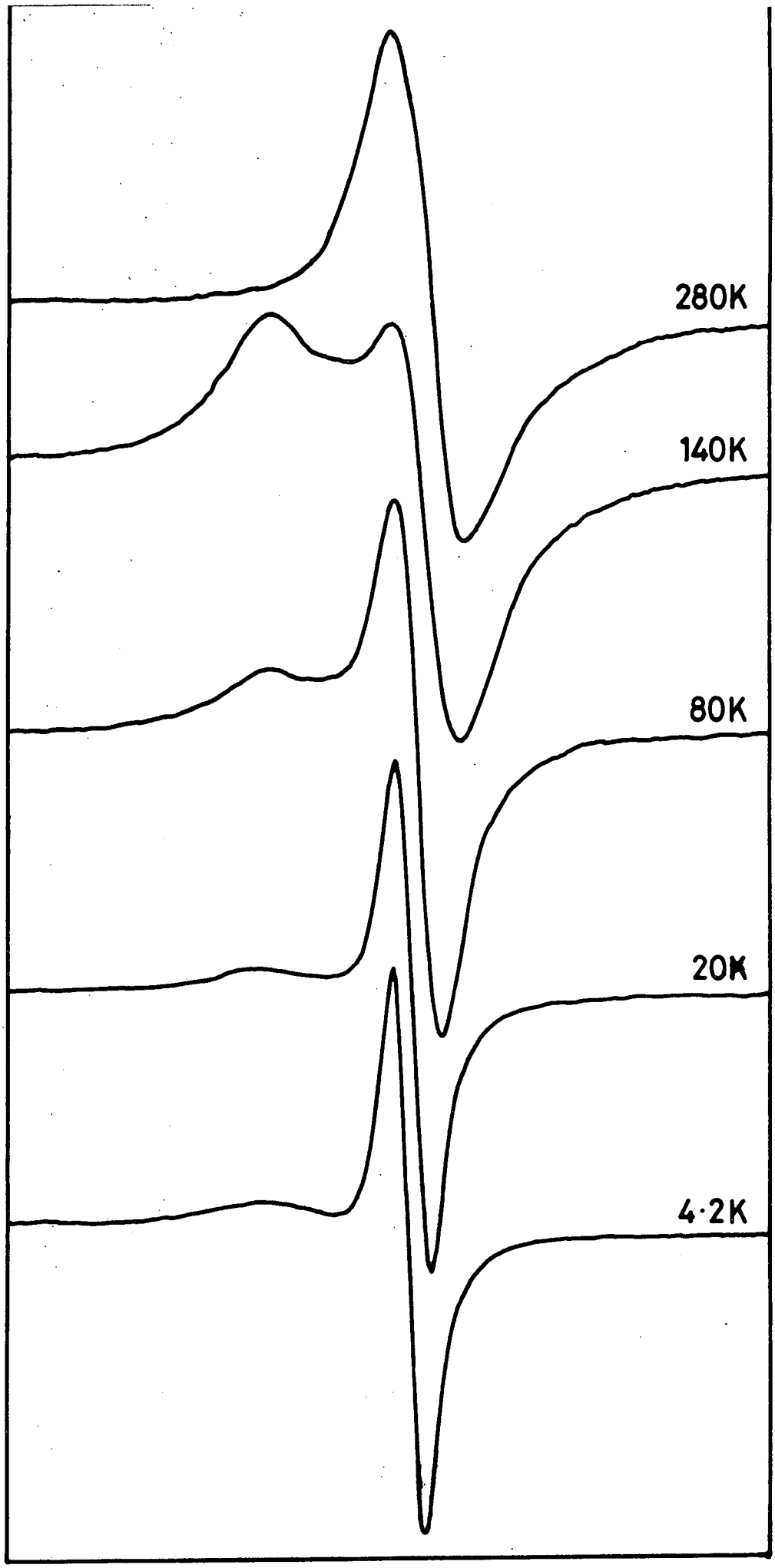

FIG. 6·14 VARIATION OF ESR SPECTRUM WITH TEMPERATURE
49% WEIGHT GAIN Si_3N_4, 9·107 GHz

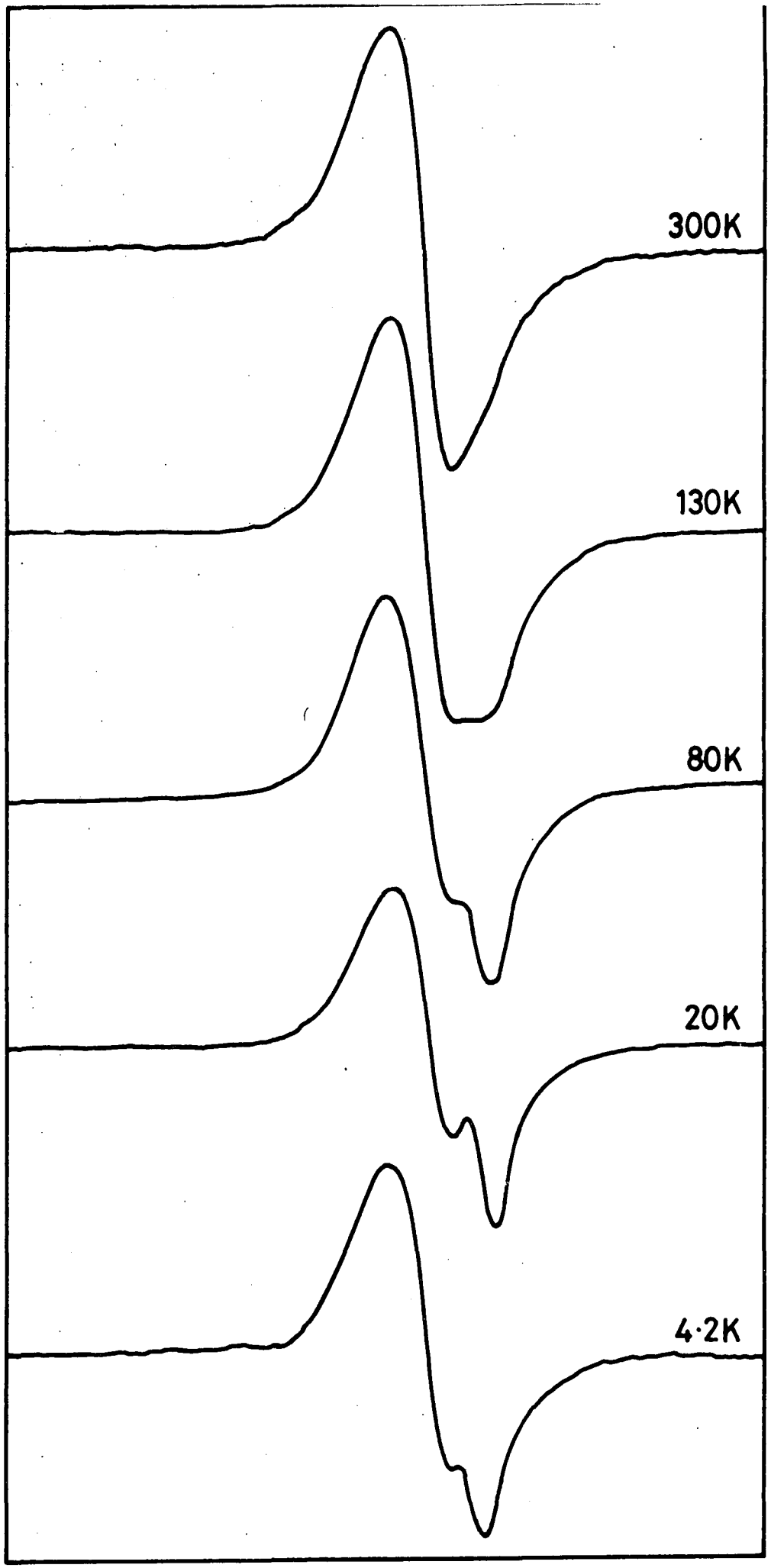

FIG. 6·15 VARIATION OF ESR SPECTRUM WITH TEMPERATURE, 59% WEIGHT GAIN Si_3N_4 , 9·102 GHz

CHAPTER 6 - REFERENCES

6.1 C.P. Poole and H.A.Farach, The Theory of Magnetic Resonance Academic Press, Wiley Interscience, New York, 1972.

6.2 T.H.Wilmshurst, Electron Spin Resonance Spectrometers- Hilger, 1967.

6.3 M.H.Brodsky and R.S.Title, Phys.Rev. Lett. 23, 581 (1969).

6.4 U.Voget-Grote,J.Stuke and H.Wagner in 'Structure and Excitation of Amorphous Solids' (New York; American Institute of Physics) p.91 (1976).

6.5 G.K.Walters and T.L.Estle, J.Appl.Phys., 32, 1854 (1961).

6.6. D.Kaplan, D.Lepine, Y.Petroff and P.Thirry, Phys.Rev.Lett., 35, 1376 (1975).

6.7 J.Stuke, in 'Electronic Phenomena in Non-crystalline Semiconductors' (Leningrad; Nanka) p.193 (1976).

6.8 J. Stuke, in 'Amorphous and Liquid Semiconductors' (Edinburgh ; University Press), p.406 (1977).

6.9 B. Movaghar and L. Schweitzer, Phys. Stat. Solidi (b), 80, 491 (1977).

6.10 B. Movaghar and L. Schweitzer, Phil.Mag. B 37, 683 (1978).

CHAPTER 7

CONDUCTIVITY THEORY

7.1 Justification

A decision regarding the theory to apply to the conductivity behaviour of a material such as reaction bonded silicon nitridie (RBSN) is not easy. This is due to the essentially dirty nature of the material which means that it does not fit into any clearly defined categories. It is possible, however, by considering the manufacturing process, and the limited structural information available to make a reasonable guess about where to look.

As noted previously, the starting material for RBSN manufacture is commercial silicon powder. This has two implications. Firstly, as the silicon powder is polycrystalline, it is reasonable to assume that the ceramic is also, and X-Ray powder photography bears this out. Secondly, the silicon powder contains impurities, which implies that the ceramic will contain defects due to impurity as well as those due to bonding between individual crystallites of nitride. Clearly, then, single crystal theory is not going to provide the answers. Moving to the other end of the spectrum of order in materials, amorphous solids, and comparing the situation in amorphous materials with the ceramic outlined above, there are several similarities:-

1. Absence of long range order, in the single crystal sense.
2. Bond distortion providing the links between areas of short range order, and,
3. In 'practical' or doped materials, a defect structure.

According to Mott and Davis (7.1) and several other workers, the electronic properties of non-crystalline and disordered solids are due to short range order, which maintains the essential features of the bandgap, and to defects in the structure present either as a result of fabrication, or deliberate or impurity doping, which gives rise to states in the bandgap. It seems

reasonable, therefore, to look to non-crystalline and disordered materials when seeking to explain the electrical and dielectric behaviour of RBSN. In view, however, of the wide range of classes of materials which exhibit similar dielectric properties, the review of AC and dielectric properties will not be limited to electronic processes.

7.2 Localization, and band structure models

In 1930 Wilson explained the difference between metallic conductors and non-metals by suggesting that each electron be described by a Bloch wavefunction

$$\psi = v(x, y, z) \exp(i.\underline{k}.\underline{r}) \qquad (7.1)$$

associated with a wavenumber $\underline{k}$. The allowed energy states then fall into bands which may be separated by energy gaps. The material is a non-metal if, at zero temperature all bands are either empty or full. Further, if an energy gap ΔE separates empty from occupied bands the material is an intrinsic semiconductor with the number of carriers proportional to $\exp(-\Delta E/2kT)$. Extrinsic semiconductors have levels of shallow donors or acceptors provided by impurities. The material is metallic if, at zero temperature, one or more bands are partially occupied, and the conductivity tends to a finite value as $T \rightarrow 0$.

In disordered materials the wavefunction corresponding to the eigenstates are not Bloch functions, as $\underline{k}$ is not a good quantum number. This, it might be thought, would lead to the absence of an energy gap in such materials. However, the most striking fact about many disordered materials is that they are transparent, either in the IR or visible spectrum. Glasses are probably the best examples of this. It is certain then that an energy gap must exist. The band theory of solids has depended since 1930 upon the concept of a periodic lattice, and there was some surprise, in the early days of the theory of disordered materials that a bandgap could exist there too. However, Anderson (7.2) showed, in 1958, that, by using the tight binding approximation,

which in crystalline materials gives rise to a narrow band of levels, bandgaps can exist in disordered lattices, (Figure 7.1). He went on to show that under certain conditions all the wavefucntions for a given energy E would be localized. A localized state, in the context of crystals, was not new, it is merely a trap below the conduction band. What was new about Anderson's approach was the idea that a finite and continuous density of states could exist in which all the states are localized. Figure 7.2 shows the Anderson model of the density of states.

The density of states, then, remains a valid concept for disordered and non-crystalline materials, and, as for crystals, states in the gap are a consequence of defects. Further, as long as the essential short range features of the crystal state remain in disordered materials (i.e. similar bond angles, local co-ordination, and bond lengths) the gross features of the crystalline band structure and density of states will remain.

The 'states in the gap', whether intrinsic or extrinsic, are of considerable importance. The first major influence on the subject was made by the paper of Cohen, Fritzche and Ovshinsky (7.3), CFO, which supposed that disorder would lead to overlapping band tails of localized states, Figure 7.3(a). In the model, those states derived from the conduction band would be neutral when empty, and those derived from the valence band would be neutral when full. The states in the overlap region would be charged, leading to centres with unpaired spins, and pinning the Fermi level. This model, with strongly overlapping tails is thought unlikely to apply to amorphous semiconductors and insulators, which exhibit a bandgap evidenced by transparency in the IR or visible. It is thought more likely that a true bandgap exists in such materials, where all the bonds are saturated, and there are no long range fluctuations. Figure 7.3(b) shows this structure. Gross bond distortions might give rise to a finite density of deep tail states. Considering now, 'real' disordered materials, these are thought to contain imperfections (i.e. defects) such as impurities , or

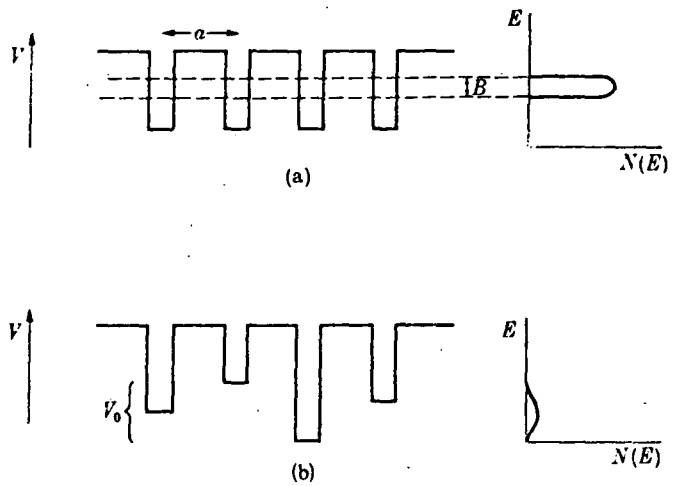

FIG 7·1 (a) Potential wells for a crystalline lattice. (b) Potential wells for the Anderson lattice. The density of states $N(E)$ is also shown.

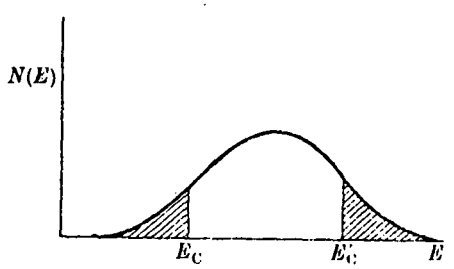

FIG 7·2 Density of states in the Anderson model when states are non-localized in the centre of the band. Localized states are shown shaded. E_C, E'_C separate the ranges of energy where states are localized and non-localized.

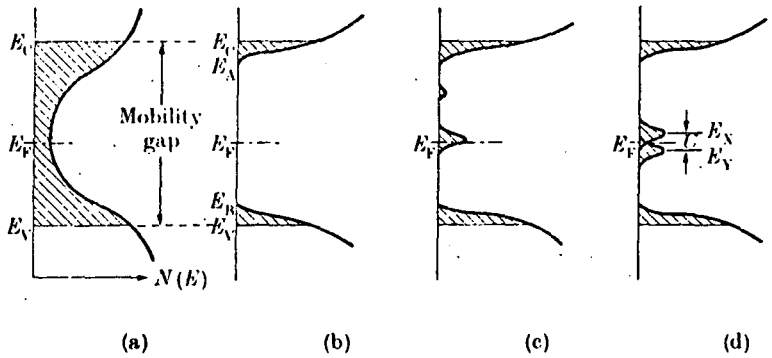

FIG 7·3 Various forms proposed for the density of states in amorphous semiconductors. Localized states are shown shaded. (a) Overlapping conduction and valence band tails as proposed by Cohen *et al.* (1969), the CFO model; (b) a real gap in the density of states, suggested here as being appropriate for a continuous random network without defects; (c) the same as (b) but with a partially compensated band of defect levels; (d) the same as (b) but with overlapping bands of donor (E_Y) and acceptor (E_X) levels arising from the same defect.

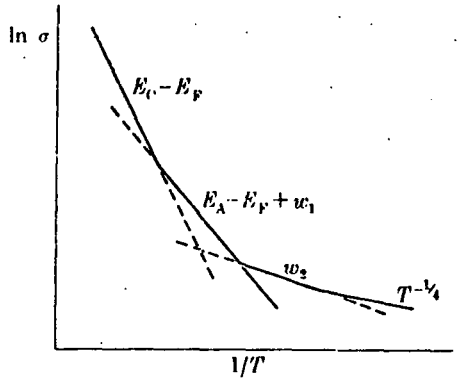

FIG 7·4 Illustration of the temperature dependence of conductivity expected

dangling bonds at the surface of internal microvoids, and it is reasonable to expect these, just as in crystals to produce states in the bandgap. One particularly interesting feature of amorphous semiconductors, which is said by some to be their most surprising and yet characteristic feature, is that the Fermi level is located near mid-gap, and appears to be pinned there over a wide range of temperatures. Spear (7.4, 7.5) and his co-workers at Aberdeen have shown that this is not a universal property with their work on doped glow discharge amorphous silicon, however, it appears that, in general, amorphous semiconductors are not normally 'intrinsic', in the sense that the conduction and valence bands control the position of the Fermi level.

Several alternative suggestions have been made for the distribution of states in the bandgap of disordered materials, as alternatives to the CFO model. Two of these are shown in Figures 7.3 (c) and (d). In Figure 7.3(c) electrons from a band of donors partially occupy a stronger band of deep acceptors. This model, proposed by Davis and Mott (7.6) was based on experimental evidence suggesting the existence of a finite density of states at the Fermi energy. The role of donors and acceptors could, of course, be reversed. This model allowed optical transparency, but offered no explanation as to why the controlling states should lie near mid-gap. In 1977, however, Mott (7.7) extended the idea, suggesting that if defect states (e.g. dangling bonds) were responsible for the states, then they could act as both deep donors and acceptors, with single and double occupancy conditions leading to two bands. This is illustrated in Figure 7.3(d).

Adopting this model for amorphous silicon and germanium, an electron spin resonance signal is expected, along with variable range hopping (see section 7.3) predominating the current transport at low temperatures. There exists a mass of experimental data confirming this on amorphous silicon and germanium films, and ESR signals for polycrystalline silicon powder and also RBSN are reported here. The one common feature of all the models presented above, is the presence of some sort of dividing line between localized and

extended states, indeed it is intrinsic to Anderson's model of localization. This dividing line is usually referred to as a mobility edge. In some systems, known as 'Fermi Glasses', in which the Fermi level of a degenerate electron gas can be moved through this critical energy, very clear evidence of existence of the mobility edge has been obtained. As far as amorphous and disordered materials are concerned, it is not possible to explore mobility edges in this way because of the pinning of the Fermi level discussed previously, although the work on doped glow discharge silicon must be close to achieving this. There is however much indirect evidence for their existence and it is using the concept of a mobility edge, along with the band models described above, that the d.c. conduction processes which might be found, are considered.

7.3 Temperature Dependence of d.c. conductivity

Conduction in three regions, as defined by the band structure models must be considered. These correspond to transport by carriers,

(a) excited beyond the mobility edge into non-localized states in the conduction or valence bands.

(b) Transport by carriers excited into localized states at the band edge, and then hopping at energies close to E_A or E_B.

(c) Transport by carriers close to E_F if there is a finite density of states at that level.

Now, considering each of these cases in order:-

(a) In this case, considering electrons as the carriers, the conductivity is given by

$$\sigma = \sigma_{min} \exp\left(-\frac{E_c - E_F}{kT}\right) \qquad (7.2)$$

where σ_{min} is the minimum metallic conductivity, and arises from a discussion of mobility edges. A plot of $\ln\sigma$ against $1/T$ should give a straight line of slope $E(0)/k$ where $E_C - E_F = E(0) - \gamma T$, and the intercept on the $\ln\sigma$ axis

will be $\sigma_{min}\exp(\gamma/k)$. Davis and Mott (7.6) examining high temperature conductivity data, expressed it in the form $C\exp(-E/kT)$, and plotting C against E found values of C clustered around $10^3\ \Omega^{-1}\ cm^{-1}$ for most materials. It was thought that this could correspond to the pre-exponential factor $\sigma_{min}\exp(\gamma/k)$, although, owing to the uncertainty in the term (γ/k) it is not felt to be a good test for conduction at a mobility edge. Estimates of the value of σ_{min} range from 100 to 600 $\Omega^{-1}\ cm^{-1}$.

(b) Here, considering electrons in the localized states just below the conduction band, the conductivity will be given by

$$\sigma = \sigma_1 \exp\left(\frac{E_A - E_F + W_1}{kT}\right) \qquad (7.3)$$

where w_1 is the activation energy for hopping. Although this term will decrease with decreasing temperature, an approximately linear ln σ against 1/T plot is again expected as the major temperature dependence is through the carriers excited into the band tail. σ_1 is expected to be several orders of magnitude lower than σ_{min} because of the lower mobility below the mobility edge, and because of the lower concentration of carriers in the band tail.

(c) If there is a finite density of states at E_F then carriers hopping between localized states will make a contribution. For this

$$\sigma = \sigma_2 \exp\ (-w_2/kT) \qquad (7.4)$$

may be written, where $\sigma_2 \leq \sigma_1$, and w_2, the hopping energy is of the order of half the width of the band of states responsible, if the band diagram is of the form shown in Figure 7.3(c). This is the result of nearest neighbour hopping. If the band structure is as shown in Figures 7.3(a) or (d) or the temperature is such that kT is less than

the bandwidth, variable range hopping is expected. The conductivity here will have the form

$$\sigma = \sigma_2^{1} \exp(-B/T^{\frac{1}{4}}) \qquad (7.5)$$

as shown by Mott in 1968 and 1969 (7.8, 7.9), where $B = 2(\alpha^3/kN(E_F))^{\frac{1}{4}}$. The terms σ_2 and σ_2^{1} are not easy to evaluate because of uncertainity in the α term, which in turn depends on ν_{ph}, a function of the phonon spectrum.

Figure 7.4 shows the four possible regions of conductivity expected, with their associated activation energies.

7.4 AC Conductivity; Dielectric Theory

In considering ac conductivity it is not sufficient to look only at the 'electronic' mechanisms proposed for dc conduction, for, as Jonscher argues (7.10, 7.11) the relationship developed to describe electronic ac behaviour ($\sigma_{ac} \alpha \omega^s$ with s between 0.4 and 0.8; section 7.6) is observed, albeit with a wider range of values of s, in a very wide range of materials, including, not only disordered, (electronic) glassy and amorphous solids, but also in ordered molecular solids where the carriers may be electrons, polarons, protons or ions. All that is required is a mechanism with an extremely wide distribution of relaxations times.

A more general approach is therefore made to a.c. conductivity theory here, starting with the basic dielectric concepts and including both the expected a.c. behaviour of the electronic hopping model and Jonscher's broader relaxation approach.

7.4.1. COMPLEX DIELECTRIC CONSTANT

There is a complex parameter for any dielectric material which determines its behaviour in the presence of an electric field. This parameter is usually called the complex dielectric constant or permittivity represented by ε^*. For free space or vacuum $\varepsilon^* = \varepsilon_o$ and ε^* is usually used in the form of a normalized complex dielectric constant (ε_r) or relative permittivity, i.e.

$$\varepsilon_r = \frac{\varepsilon^*}{\varepsilon_o} = \varepsilon' - j\,\varepsilon'' \tag{7.6}$$

Separating real and imaginary parts of both sides gives,

$$\varepsilon' = R_e \left\{ \frac{\varepsilon^*}{\varepsilon_o} \right\} \tag{7.7}$$

and

$$\varepsilon'' = I_m \left\{ \frac{\varepsilon^*}{\varepsilon_o} \right\} \tag{7.8}$$

The real part ε', directly represents the amount of energy which can be stored by the applied electric field in a dielectric material. On the other hand, the imaginary part, ε'' is a direct measure of how much energy is dissipated in the form of heat. The relative permittivity, then can be written as,

$$\varepsilon_r = \varepsilon' (1 - j \operatorname{Tan} \delta) \tag{7.9}$$

where

$$\operatorname{Tan} \delta = \frac{\varepsilon''}{\varepsilon'} \tag{7.10}$$

Tan δ is proportional to the ratio of the power lost in heat, to the energy stored per cycle in the dielectric material. It is called the loss tangent and is a useful factor in electronic engineering and material science for determining the power loss. The complex relative permittivity and its real (ε') and imaginary (ε'') components with their associated loss angle are illustrated vectorially in Figure 7.5. The quentities ε' and ε'' are both dimensionless, because it is assumed that all values are relative to free space; therefore they preserve their values irrespective of the selected system of units.

7.4.2 Polarization

The application of an electric field to a dielectric results in the positive and negative charged particles of each atom being displaced from their equilibrium positions in opposite directions. These displacements, however, are usually limited, to very small fractions of an atomic diameter. From the macroscopic point of view, this represents a displacement of the entire positive charges relative to the negative charges throughout the dielectric. This condition is called polarization. The polarization of a particular dipole (its dipole moment), depends on the electric field E_{loc} at the dipole, i.e.

$$P = \alpha E_{loc} \tag{7.11}$$

where α is the polarizability factor. The polarization of the dielectric can also be defined as the electric dipole moment per unit volume (7.12).

$$P = \sum r_n \, q_n \tag{7.12}$$

where r_n is the position vector for the charge q_n.

In isotropic materials the polarization has the same direction as the electric field causing it and here α, is a scalar quantity. In anisotropic materials polarization has different values in each direction, so α will be a tensor

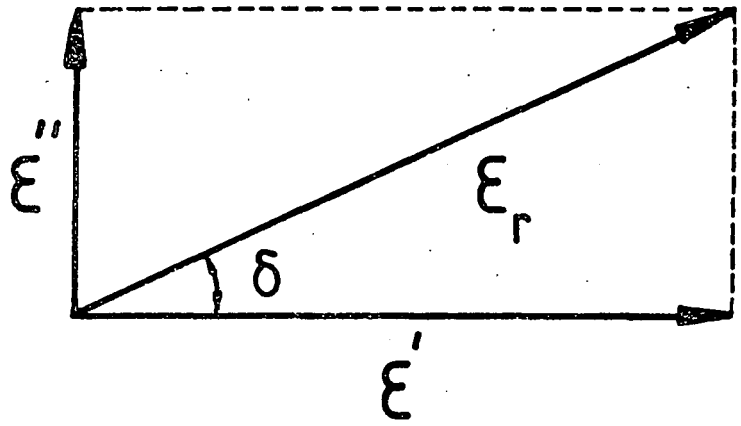

FIG.7·5 COMPONENTS OF RELATIVE DIELECTRIC CONSTANT.

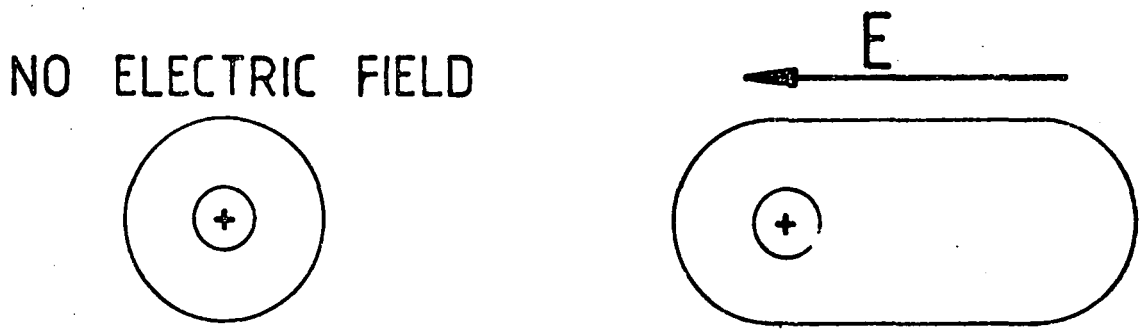

FIG.7·6 ELECTRONIC POLARIZATION.

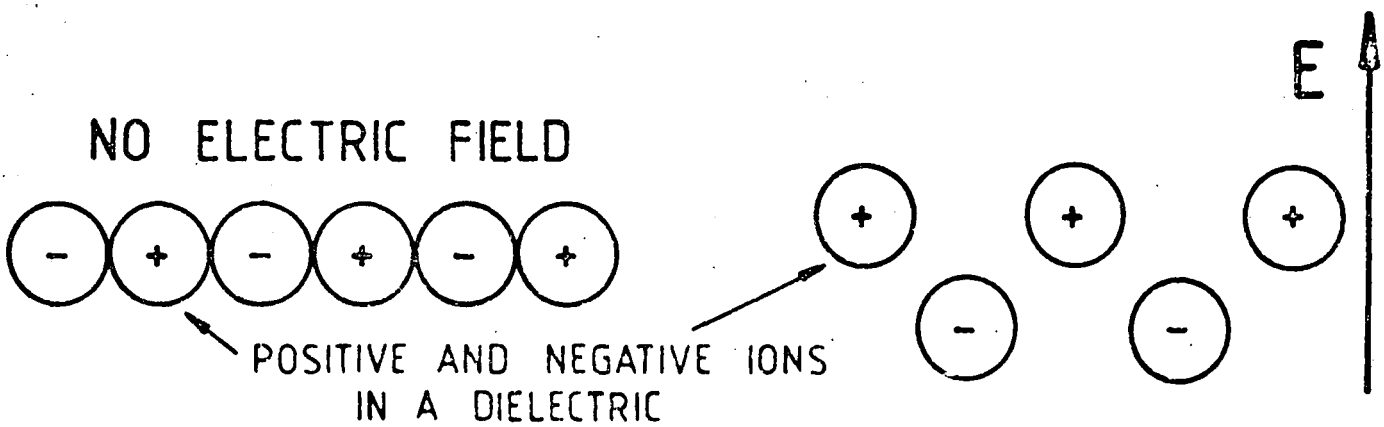

FIG.7·7 IONIC POLARIZATION.

quantity. The polarization, P electric displacement, D and electric field E are related to each other (7.13, 7.14) by

$$D = P + \varepsilon_o E \qquad (7.13)$$

and

$$D = \varepsilon_o \varepsilon_r E \qquad (7.14)$$

From Eqns. 7.13 and 7.14 a relation between polarization and complex relative dielectric constant may be obtained as,

$$P = \varepsilon_o E (\varepsilon_r - 1) \qquad (7.15)$$

from which, it is seen that ε_r must be greater than unity.

There are three mechanisms of polarization, namely Electronic Polarization, Ionic Polarization and Dipole Orientation. Electronic Polarization is illustrated in Fig. 7.6. It is known that in any dielectric material the positive atomic nucleus is surrounded by a cloud of negative electrons. By applying an external electric field to the material, the electrons are slightly displaced relative to the nucleus and an electric dipole moment is created; electronic polarization has occurred in the system. This polarization is established during a very brief interval of time (10^{-15}s) which corresponds to the ultraviolet range of wavelength. Since this mechanism of polarization occurs in all atoms or ions, it can be observed in all dielectrics irrespective of whether other types of polarization are displayed. This polarization satisfies Maxwell's theory, i.e.

$$\varepsilon = \mu^2 \qquad (7.16)$$

where μ is the refractive index at optical wavelengths.

Ionic Polarization arises in a different way. In this polarization, the positive and negative

ions in a partially ionic solid are displaced relatively from their equilibrium positins when an external electric field is applied. This is shown in Fig. 7.7. The charge displacement polarizes the ions and produces an induced electric moment. This polarization also arises from the displacement of the nuclei and it is frequency dependent in the infra-red region, when the applied frequency approaches that of the molecular vibration. The time required for this process is longer than for electronic polarization (about 10^{-13} to 10^{-12}s). In the presence of ionic polarization Maxwell's equation does not hold and $\varepsilon > \mu^2$. Dipole Orientation arises in a straightforward manner when an external electric field is applied to a dielectric material, atoms with displaced positive and negative charges tend to orient themselves in a direction opposite to that of the applied electric field, Fig. 7.8. This results in a reduced internal electric field compared with the applied field. Assuming that all the molecules are oriented with their dipole axes in the direction of the field, a permanent moment will be added to the induced moment. The orientation of the molecules is however opposed by their thermal motion, which varies with temperature. As a result at high temperatures the thermal motion practically prevents the orientation of the molecules and hence the polarization is reduced. Debye has derived the polarization for polar molecules and showed that molecules with zero rotational energy contribute to orientation polarizability and that the number of this kind of molecule decreases with increasing temperature. Dipole polarization can appear in pure form only in gases, liquids and amorphous bodies. In crystalline bodies at temperatures below the melting point, the dipoles are frozen and so they can not be oriented and dipole polarization cannot occur in them.

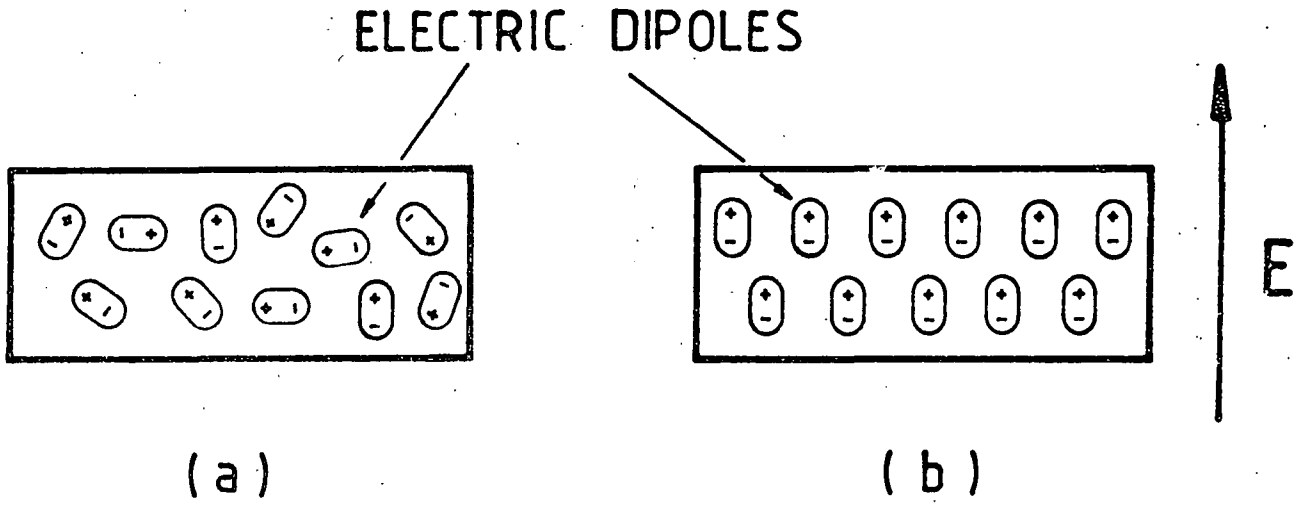

FIG. 7·8 DIPOLE ORIENTATION; (a) RANDOM DIPOLES IN AN UNCHARGED DIELECTRIC. (b) ORIENTATION POLARIZATION BY AN ELECTRIC FIELD.

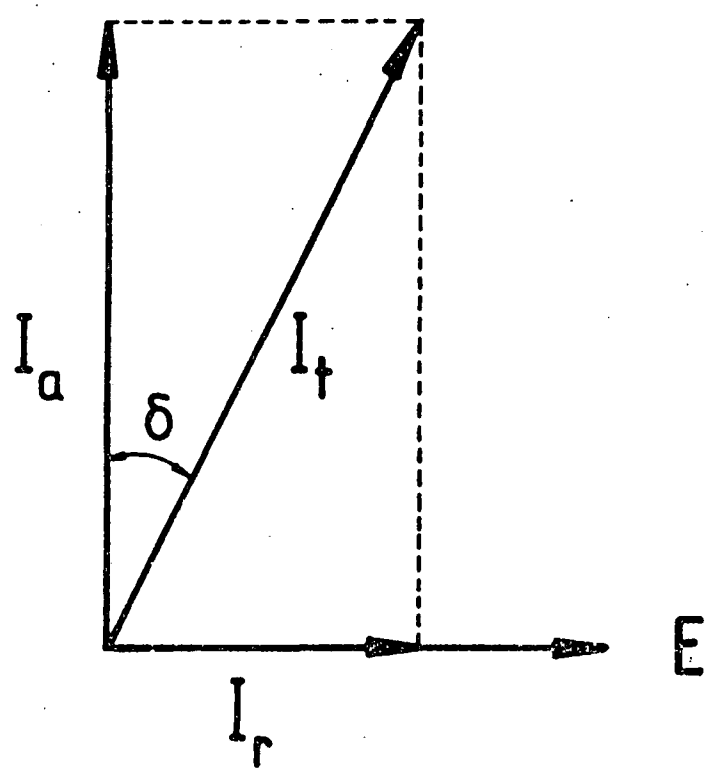

FIG. 7·9 VOLTAGE - CURRENT DIAGRAM OF A DIELECTRIC WITH LOSS.

7.4.3 Dielectric Loss Angle

In an ideal dielectric of the capacitor, the phasor of current would be ahead of the phasor of electric field, E, by 90^{o} and the current would be purely reactive, as shown in Fig. 7.9.

In practice the phase angle, ϕ, is slightly less than 90^{o}, and

$$I_t = I_a + I_r \tag{7.17}$$

where I_t = total current, I_a = active component = $E\,\omega\,\varepsilon' C$, I_r = reactive component = $E\,\omega\,\varepsilon''\,C$.

The phase angle, ϕ , is very close to 90^{o} in a high quality dielectric capacitor. An angle δ can be defined by

$$\delta = 90^{o} - \phi \tag{7.18}$$

This angle, δ , is called the dielectric loss angle; and

$$\text{Tan}\,\delta = \frac{I_r}{I_a} = \frac{E\,\omega\varepsilon''\,C}{E\,\omega\varepsilon'\,C} = \frac{\varepsilon''}{\varepsilon'} \tag{7.19}$$

This parameter is very important for a dielectric material and it is called the loss tangent (Tanδ). Sometimes the quality factor of a dielectric is specified and this is given by $Q = \frac{1}{\text{Tan}\,\delta}$.

7.4.4 Frequency Dependence of ε' and ε''; Debye Model.

The time required for electronic or ionic polarization to be established is very small compared with the period of the applied field and there is no reason to expect that any frequency dependence should appear in such dielectrics. This is not so in the case of dipole polarization; the value of ε' of a polar dielectric begins to drop when the frequency begins to increase.

By removing the applied electric field all the dipoles in the material relax to a new equilibrium position and the polarization decays exponentially. the relaxation time is defined as the time in which the polarization is reduced to $\frac{1}{e}$ times its original value. The relaxation time, τ, depends on various factors such as, the viscosity of the medium, the size of the polar molecules, the frequency and the temperature of the material. If the polar molecules are large, or the viscosity of the medium is high, or the frequency of the applied field is high, the rotary motion of molecules becomes out of step with the field and the polarization will acquire an out-of-phase component. Thus the displacement current acquires a conductance component in phase with the field which results in a thermal dissipation of energy (Fig. 7.9).

The dependence of ε' and ε'' on frequency are shown in Fig. 7.10. As the frequency increases the total polarization will decrease and hence ε' decreases. All of the energy applied to the material by the electric field is not used to orient the dipoles, but some is lost to the material by increasing the random thermal motion that exists in every substance. Therefore as ε' decreases, ε'' should increase. This phenomenon is shown in Fig. 7.10. The reduction in ε' in the frequency region near 10^6 Hz is due to dipolar polarization, whereas near 10^{12} and 10^{15} Hz, atomic and electronic polarizations are responsible. As the frequency increases above 10^{16} Hz the contribution of the dipole orientation eventually disappears, and the permittivity levels off at a lower value ε_∞. At zero frequency (d.c. field), $\varepsilon = \varepsilon_s$, where ε_s is the static value of dielectric constant.

There is a relation between ε_∞ ε_s and frequency which is known as the Debye equation (7.13, 7.15, 7.16). It can be derived from the relation,

$$\varepsilon^* = \varepsilon_\infty + \frac{\varepsilon_s - \varepsilon_\infty}{1 + j\,\omega\,\tau} \qquad (7.20)$$

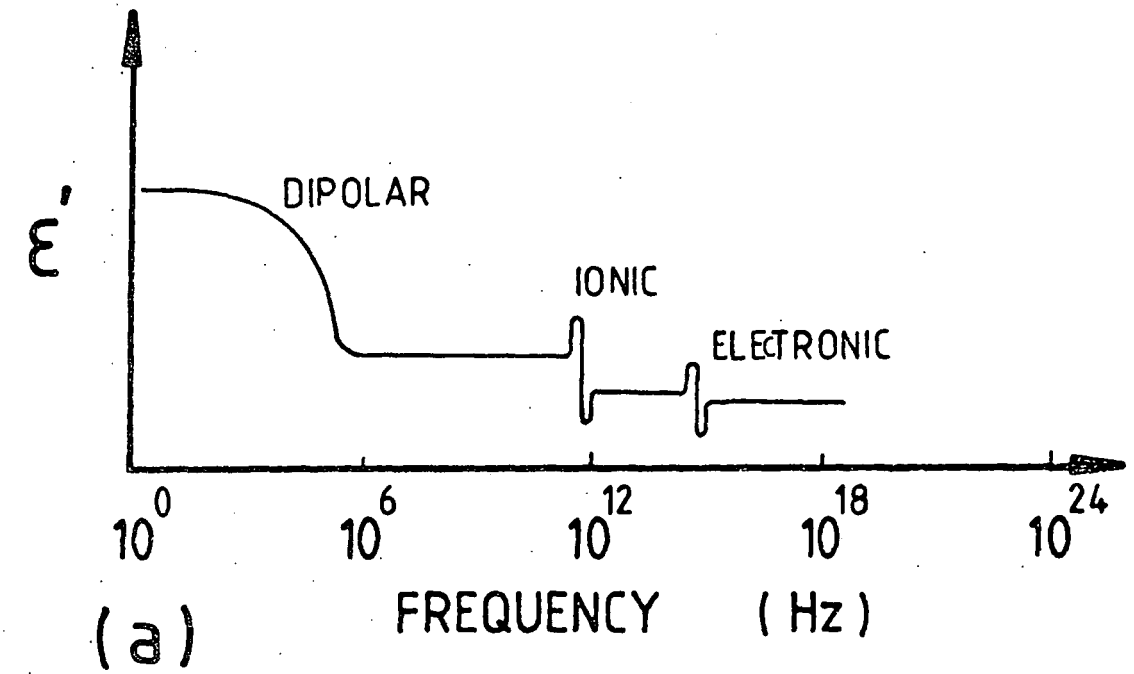

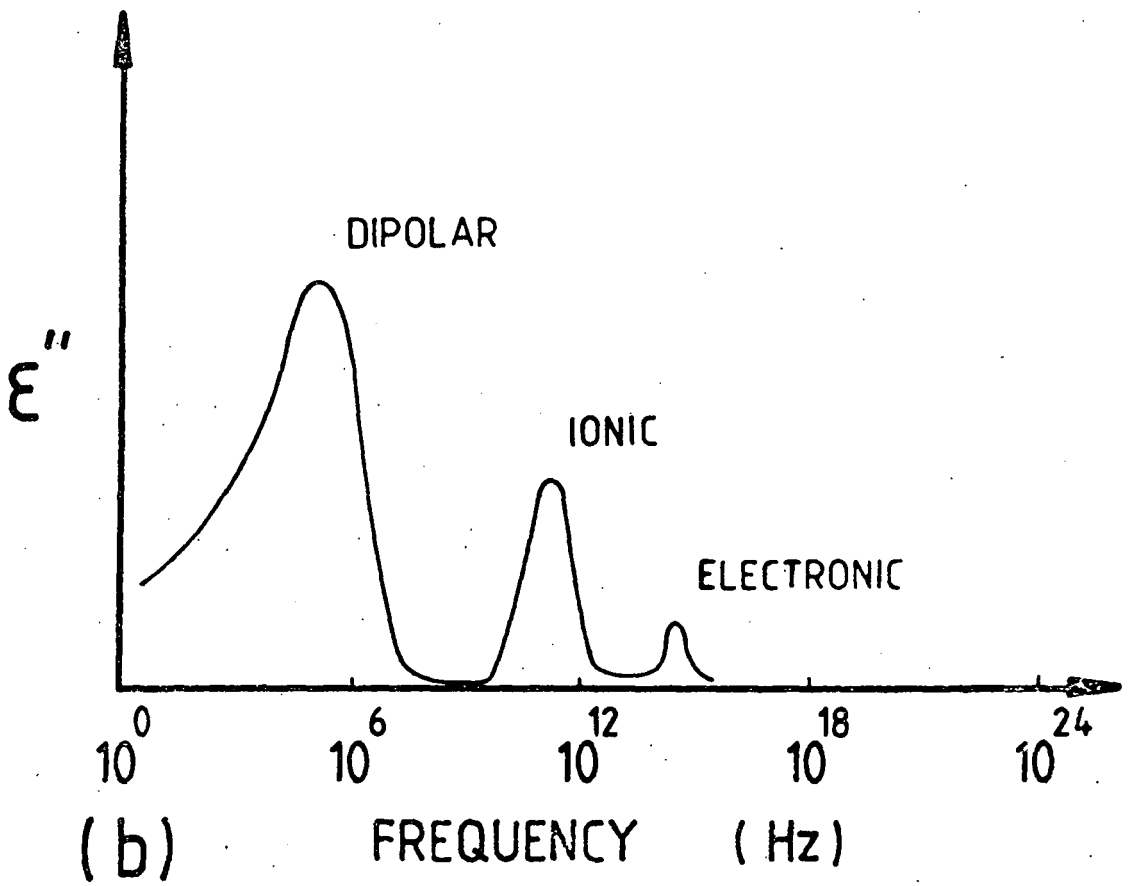

FIG. 7·10 FREQUENCY BEHAVIOUR OF (a) DIELECTRIC CONSTANT AND (b) LOSS FACTOR.

Introducing $\varepsilon^* = \varepsilon' - j\varepsilon''$ and comparing real and imaginary parts yields,

$$\varepsilon'(\omega) = \varepsilon_\infty + \frac{\varepsilon_s - \varepsilon_\infty}{1 + \omega^2\tau^2} \tag{7.21}$$

and

$$\varepsilon''(\omega) = \frac{(\varepsilon_s - \varepsilon_\infty)\omega\tau}{1 + \omega^2\tau^2} \tag{7.22}$$

where τ = relaxation time and ε_∞ and ε_s are as defined before. Equations 7.21 and 7.22 are called the Debye equations. Their ratio is

$$\frac{\varepsilon''(\omega)}{\varepsilon'(\omega) - \varepsilon_\infty} = \omega\tau \tag{7.23}$$

These equations are plotted in Fig. 7.11. Eliminating $\omega\tau$ between eqns. 7.21 and 7.22 gives

$$\left[\varepsilon' - \frac{\varepsilon_s - \varepsilon_\infty}{2}\right]^2 + \varepsilon''^2 = \left[\frac{\varepsilon_s - \varepsilon_\infty}{2}\right]^2 \tag{7.24}$$

which is the equation of a circle. Since $\varepsilon'' > 0$ a semicircle will be physically meaningful. The Debye semicircle has the advantage of giving a representation of a simple relaxation process when the relative permittivities ε', ε'' are plotted on a complex plane. The a.c. electrical conductivity can be represented by,

$$\sigma_{ac}(\omega) \propto \frac{\omega^2}{1 + \omega^2\tau^2} \tag{7.25}$$

This applies only for dipolar processes; at frequencies $f < \frac{1}{\tau}$, σ_{ac} is proportional to ω^2. This result differs from that obtained on the hopping model, which is described later.

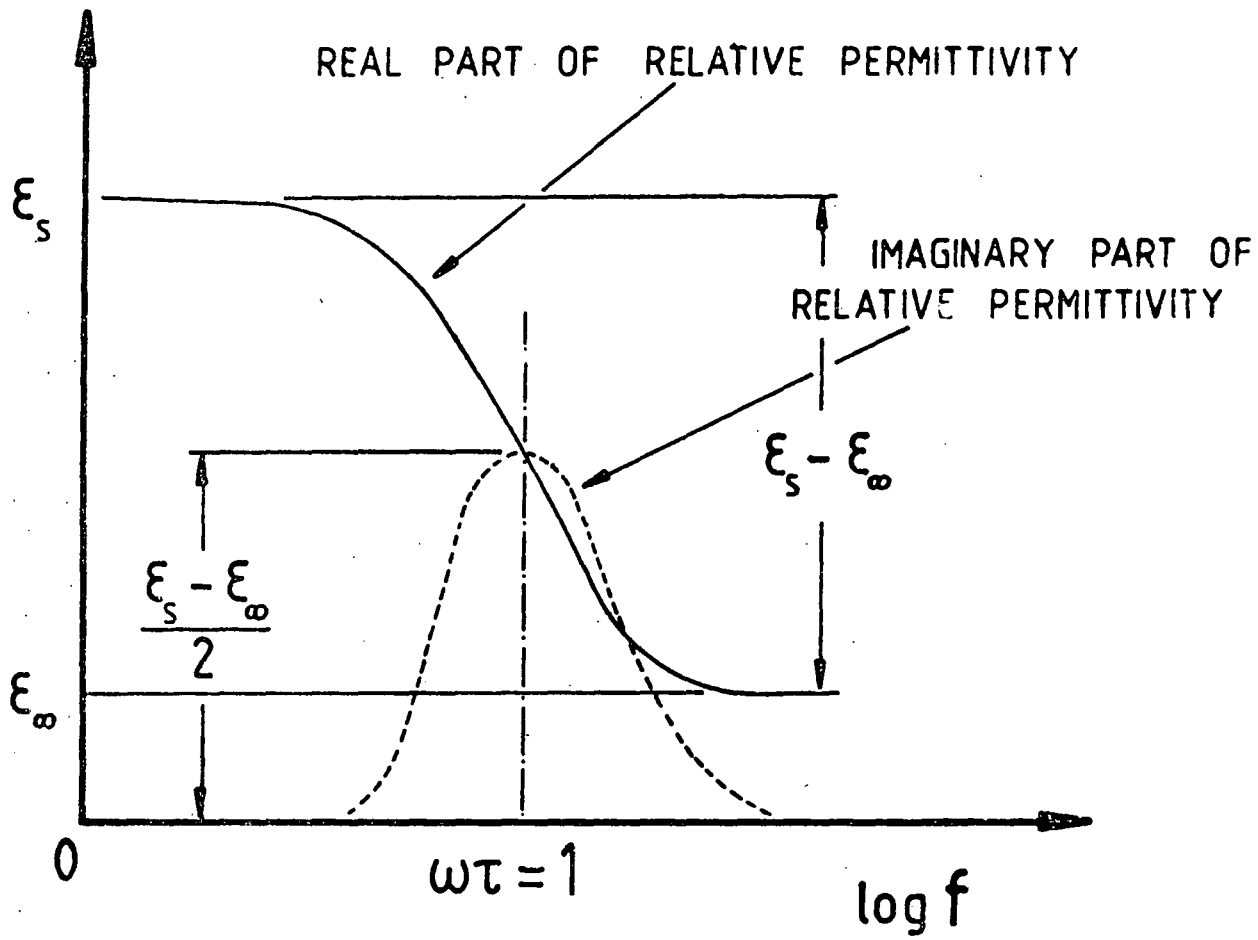

FIG. 7·11 THE VARIATION OF ε' AND ε'' WITH FREQUENCY FOR DEBYE RELAXATION.

7.4.5 Temperature dependence of Permittivity

In solid dielectric materials the nature of the dependence of dielectric constant on temperature may be determined by various factors. In most cases when the temperature increases, the ionic polarization increases and hence the magnitude of ε' will be increased. In contrast, the increase of temperatures does not affect the electronic polarization. The dipole orientation contribution is also directly proportional to the temperature, which facilitates the rotation of dipoles in an applied electric field. The cases of isotropic and cubic dielectrics, have been studied by Havinga (7.17) whose approach is based on the Clausius-Mosotti equation,

$$\frac{\varepsilon'-1}{\varepsilon'+2} = \frac{N\alpha}{3\varepsilon_o} \qquad (7.26)$$

in which N = the number of molecules per unit volume, ε_o = permittivity of free space, and α = polarizability of molecules, and ε' = dielectric constant. In eqn. 7.26, N can be replaced by,

$$N = \frac{N_A \rho}{M} \qquad (7.27)$$

where N_A = Avogadro's number (6.022169×10^{23} mol^{-1}), M = molecular weight (kg), ρ = density (kg m^{-3})

$$\frac{\varepsilon'-1}{\varepsilon'+2} = \left\{\frac{4\pi}{3}\right\}\left\{\frac{\alpha}{V}\right\} \qquad (7.28)$$

where V is equal to the volume of a small sphere of material, and other quantities are as have been defined before; the volume of the sphere must be large relative to the lattice dimensions.

The Clausius-Mosotti equation is applicable to all cubic and isotropic materials and the derivation is based on this assumption. From eqn. 7.26 Havinga derived the relation

$$\frac{1}{(\varepsilon'-1)\ (\varepsilon'+2)} \left\{\frac{\partial \varepsilon'}{\partial \varepsilon T}\right\}_p = A + B + C \qquad (7.29)$$

which introduces three parameters A, B and C whose significance is as follows. The parameter A arises from volume expansion. As a result of expansion the number of polarizable particles per unit volume is reduced (since the number of particles is constant); by increasing temperature ε' decreases. The quantity B relates to the increase of polarizability of the particles when volume expansion occurs and the parameter C arises from the dependence of polarizability of the particles on temperature (in a constant volume). A, B, and C can be evaluated from dielectric constant versus temperature data, the magnitudes of A, B and C are invariable for each specific material. Bosman and Havinga (7.18) have found that the sum of A and B is always positive and hence, (A + B) contributes in the increasing of ε'. The factor C is negative for those types of material with $\varepsilon' > 10$ and it is positive for those which have $\varepsilon' < 10$. They also state that the temperature dependence of a dielectric constant (eqn. 7.29) is always postive for $\varepsilon' < 20$ and is negative for $\varepsilon' > 20$.

7.5 CONDUCTION MECHANISMS

The phenomenon of electrical conduction shows appreciable variations depending on the nature of the charge carrier in the given material. It is an electrical property of matter that has an enormous range of values and it should be noted that both the magnitude of conductivity and the nature of conduction can completely change according to the temperature and the structure of the material. The type of conductivity can be determined from measurements of transport numbers, which are related to the Hall constant or the thermoelectric coefficient. The basic theoretical expression for all mechanisms of conductivity is given (7.19)as,

$$\sigma = \sum_i z_i e \; n_i \; \mu_i \qquad (7.30)$$

Where	σ	= conductivity	$(ohm^{-1}\ m^{-1})$
	z_i	= charge of the current carrier	(e)
	e	= modulus of the electronic charge	$(1.602 \times 10^{-19}\ C)$
	n_i	= carrier density	(m^{-3})
	μ_i	= mobility	$(m^2\ v^{-1}\ s^{-1})$

The total conductivity is usually found by summing i for all the various mechanisms. In equation 7.30 the magnitude of z is unity for electrons and holes but for ions it depends on the valence state.

The basic types of conduction are:

1. Electron Conduction: In this conduction the carriers are elementary negatively charged particles, i.e. electrons or positively charged particles, i.e. holes (metallic or semiconductor type n or p).

2. Ionic Conduction: Here, the carriers are ions, and the flow of the current through the material is accompanied by electrolysis. It takes place by passing ions from one unit cell into another. The ion must overcome a certain energy barrier each time it penetrates and passes a structural element of the solid.

The conductivity formula

$$\sigma = \sigma_o \exp \left\{ \frac{-E_o}{kT} \right\} \qquad (7.31)$$

covers all the conduction mechanisms which are being considered.

The electronic and ionic conduction mechanisms are divided into four fundamentally different classes as follows: (a) intrinsic ionic, (b) extrinsic ionic, (c) instrinsic electronic, and (d) extrinsic electronic.

The calculation of carrier density, n, varies from one mechanism to another. In the intrinsic ionic mechanism the carrier density will be equal to the density of ions in the lattice, while in the extrinsic ionic mechanism it may be determined by chemical analysis. The intrinsic electronic carrier density may be calculated using standard equations. In the case of a dielectric, the material is assumed to be a wide bandgap semiconductor. In intrinsic behaviour the number of electrons, n_e, is equal to the number of holes, n_h. Initially, it is assumed that the effective masses of electrons and holes are equal to their rest mass; then the concentration of electrons or holes may be written as:

$$n_e = n_h - 2 \left[\frac{2 M \pi k T}{h^2} \right]^{3/2} \exp \left(- \frac{E_g}{2kT} \right) \qquad (7.32)$$

where n_e = concentration of electrons in the conduction band (m^{-3})

n_h = concentration of holes in the valence band (m^{-3})

M = rest mass of the electron (9.108×10^{-31} kg)

k = Boltzmann's constant (1.38×10^{-3} J k^{-1})

T = absolute temperature (k)

h = Planck's constant (6.625×10^{-34} Js)

E_g = energy gap (eV)

This can be simplified to

$$n_e = n_h = 5 \times 10^{21} \; (T)^{3/2} \exp \left(- \frac{E_g}{2kT} \right) \; m^{-3} \qquad (7.33)$$

and the conductivity also is given by,

$$\sigma_{in} = \left\{ \text{const.} \right\} \exp \left[\frac{- (E_c - E_v)}{kT} \right] \qquad (7.34)$$

vacancies, n is given by,

$$n = N \exp\left\{ - \frac{E}{2kT} \right\} \qquad (7.36)$$

where N = total number of atoms in unit volume of crystal, E = energy of formation of vacancy. The presence of Schottky defects increases the volume of the crystal. For Frenkel defects, in which an atom is transferred from a lattice site to an interstitial position in the lattice, the number of atoms left in position, n is given by,

$$n = \sqrt{NN'} \exp\left\{ \frac{-E}{wkT} \right\} \qquad (7.37)$$

where N = total number of atoms in unit volume of crystal, N' = total number of possible interstitial positions, E = energy required to take an atom from its position. These defects can occur in any part of the crystal and are mobile representing another type of conduction mechanism.

7.5.2 Impurity Conduction

Impurity conduction has been studied by Mott and Twose (7.23) and Mott (7.24). It is assumed that electrons occupy the donor levels and holes occupy acceptor levels. Mott and Twose pointed out that charge transport can occur by tunnelling from an occupied donor level to an adjacent vacant donor level. Alternatively, charge transport may proceed by excitation of the localized electron over the potential barrier which separates it from an adjacent vacant site. This process can be called impurity conduction. Impurities have a double effect on the conductivity of crystals. Firstly, they represent a source of highly mobile ions with low activation energy and therefore increase by many times the conductivity of such crystal and secondly they weaken the crystal lattice and facilitate the movement of lattice ions.

7.6 A.C. Conductivity; Electronic Model

The band structure models described earlier, and used in Section 7.3 to explain the d.c. conduction behaviour of electronic materials must also be applicable to the a.c. case.

Considering the three mechanisms again:-

(a) For carriers excited to the extended states near E_C or E_V a dependence of conductivity of the Drude type might be expected,

$$\sigma\ \omega \quad = \quad \frac{\sigma(o)}{1 + \omega^2\ \tau^2} \tag{7.38}$$

The relaxation time τ will be very short ($\sim 10^{-15}$ secs). Bearing this in mind, it is clear that, for the electrical range of frequencies (say up to 10^7Hz), no frequency dependence of the conductivity associated with carriers in the extended states is expected.

(b) for carriers in the localized states just below the band edge a dependence of conductivity upon frequency of the type $\omega(\ln(\nu_{ph}/\omega))^4$ is expected, i.e. as ω^s, where $s<1$, when $\omega<\nu_{ph}$. A temperature dependence similar to that expected in the d.c. case might be expected here, so that for the conduction band σ_{ac} would increase as $\exp(-(E_A-E_F)/kT)$.

(c) Thermally activated hopping for a.c. conductivity in a high density of localized defect states has been examined by Mott (7.25) and Mott and Davis (7.1). The concepts have also been explored by Pollak (7.26) and Pollak and Geballe (7.27). As in the d.c. case they proposed that the transport of electric charge occurs by hopping of electrons between localized states, i.e. the a.c. conductivity of a hopping system has been based on a pair approximation, in which successive hops are independent of either other The hopping probability is given by,

$$\frac{\omega\ \tau}{1 + \omega^2\ \tau} \tag{7.39}$$

where τ is the mean time which is taken to jump (jumping time). It is also suggested that in order to compensate the impurity (which produces the defect band) it is necessary for some of the localized stated to be vacant. The coulombic potential between states may be altered by thermal energy. However, it can be changed by an applied electric field, which establishes a new equilibrium, and then polarization has occurred. The rate of polarization can be considered as a current in a a.c. measurement. The polarization is related to the hopping time and also to the distance of separation of two sites.

Hopping conduction cannot produce a large conductivity but the introduction of impurities can give a major contribution to the a.c. conductivity at lower temperatures. In 1969 Austin and Mott (7.28) gave

$$\sigma(\omega) = \frac{\pi}{3} e^2 kT \left[N(E_F)\right]^2 \alpha^{-5} \left[\ell n\left(\frac{\nu ph}{\omega}\right)\right]^4 \omega \qquad (7.40)$$

for the frequency dependence of σ and Davis and Mott (7.6) used the formula to analyse some early experimental results. More recently further theoretical treatments have given essentially similar results. Pollak (7.29) replaced the factor $\pi/3$ with $\pi^3/96$ and Butcher and Hayden (7.30) gave the factor a value of $3.66\pi^2/6$. Therefore for conduction in defect states close to E_F $\sigma(\omega)$ against $\ln\omega$ is approximately linear with a slope s given by

$$s = 1 - \frac{4}{\ell n\ (\nu ph/\omega)} \qquad (7.41)$$

where ν_{ph} is a characteristic phonon frequency. With ν_{ph} in the range 10^7 to 10^{13} Hz and $\omega = 10^4\ s^{-1}$, s varies from 0,4 to 0,8. Values outside this range are considered unlikely. Figure 7.12 shows this graphically.

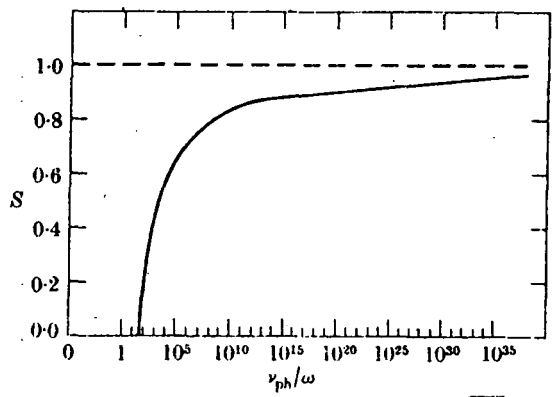

FIG 7·12 Plot of $s = 1 - \{4/\ln(\nu_{ph}/\omega)\}$ against ν_{ph}/ω.

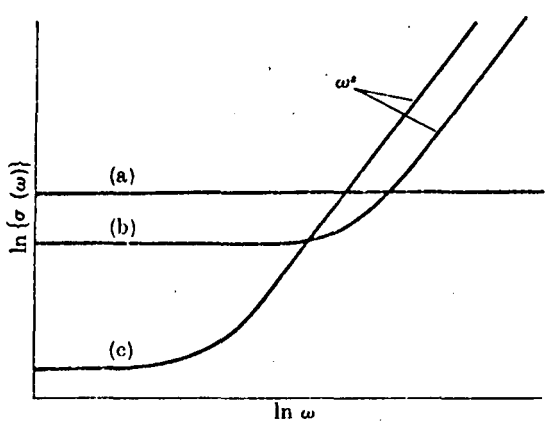

FIG 7·13 Schematic illustration of the frequency dependence of conductivity for the three modes of conduction described in the text.

Figure 7.13 shows the frequency dependence expected for the three mechanisms described above. To distinguish between the two ω^s regions, reference must be made to their frequency variation with temperature. Conduction in the localized states at the band edge will, as stated earlier, show a temperature dependence similar to that expected in the d.c. case while defect band hopping should show $\sigma(\omega)$ proportional to temperature if kT is small compared with the energy range over which $N(E_F)$ may be taken as constant, and independent of T if kT is larger than the width of some well defined defect band in which E_F lies. These two criteria correspond to those under which, for d.c. conduction, variable range and nearest neighbour hopping respectively are expected.

7.7 AC(ω^s) CONDUCTIVITY : THE JONSCHER 'UNIVERSAL' LAW

The electronic model of a.c. conductivity limits the value of s in the equation

$$\sigma(\omega) \alpha \omega^s \qquad (7.42)$$

to the range $0.4 < s < 0.8$ by placing sensible limits on the value of ν_{ph}. Jonscher, as stated earlier, argues that a similar relationship is observed not only in electronic materials, but in a much wider range where the conduction mechanisms are demonstrably not electronic. The observed range of values of s, is , however wider, with $0.1 < s < 1.0$.

The hopping mechanism was suggested first by Pollak and Geballe (7.27). They measured the conductivity of n-type silicon containing various impurities and observed that the magnitude of the measured a.c. conductivity was larger than the measured d.c. conductivity; they attributed this to polarization caused by hopping processes. These polarization mechanisms may be considered in terms of the Debye susceptibility $X(\omega)$, which is due to rotating dipoles or localized ionic charges and is a function of frequency. The susceptibility is complex and can be expressed as

$$X(\omega) = \left[X'(\omega) - j\, X''(\omega) \right] \propto \frac{1}{1 + j\,\omega\,\tau} \qquad (7.43)$$

where τ is the relaxation time and is the reciprocal of the natural hopping frequency in the absence of any external electric field; (τ may be temperature dependent); ω is the angular frequency; $X'(\omega)$ and $X''(\omega)$ are the real and imaginary parts of the Debye susceptibility.

The right-hand side of eqn. 7.43 can be divided into real and imaginary parts as follows:

$$\left[X'(\omega) - j\, X''(\omega) \right] \propto \left[\frac{1}{1 + \omega^2 \tau^2} - j \frac{\omega \tau}{1 + \omega^2 \tau^2} \right] \qquad (7.44)$$

Ideally the imaginary part of the susceptibility, i.e. the dielectric loss is equal to

$$X''(\omega) = \frac{\omega \tau}{1 + \omega^2 \tau^2} \qquad (7.45)$$

Examination of eqn. 7.45 shows that there will be a maximum when $\omega\tau = 1$ which corresponds to a peak loss whose width at half-height is equal to $1/\sqrt{2}$ times the peak height. In real dielectric materials, however, the

majority show much broader peaks. This type of loss can be represented in empirical form (7.31)

$$\frac{1}{X''(\omega)} = \left(\frac{\omega}{\omega_1} \right)^{-m} + \left(\frac{\omega}{\omega_2} \right)^{1-n} \qquad (7.46)$$

In this equation ω_1 and ω_2 are dependent on temperature and both exponents m, and 1-n, are smaller than unity. It is found that the behaviour of many dielectric materials in which the polarization is due to hopping conduction of ions or electrons, the loss in the material, (and consequently the conduction), is described by the second term of eqn. 7.46.

The dielectric response of a wide range of materials shows that the observed behaviour departs strongly from the Debye response and it follows a "Universal dielectric response law", in which the dielectric loss follows the emprical law.

$$x''(\omega) \propto \omega^{n-1} \qquad (7.47)$$

where the exponent n, lies in the range $o< n< 1$ with typical values between 0.6 and 0.95. It has been shown that both the Debye and the "Universal Response" may be caused by either dipolar or by hopping charge mechanisms. The relationship of $X''(\omega)$ with frequency implies that the real part of $X(\omega)$ must have the same frequency dependence, i.e.

$$X'(\omega) \propto \omega^{n-1} \qquad (7.48)$$

There is an important relationship between $X''(\omega)$ and $X'(\omega)$. The ratio of the imaginary to real parts of the susceptibility, is independent of frequency (7.16) i.e.

$$\frac{X''(\omega)}{X'(\omega)} = \cot\left(\frac{n\pi}{2}\right) \tag{7.49}$$

This relationship is known as the Kramers-Kronig equation and represents the"Univeral Law" of dielectric behaviour. It has a very simple significance, namely that

$$\frac{\text{Energy lost per cycle}}{\text{Energy stored per cycle}} = \text{const} = \cot\left\{\frac{n\pi}{2}\right\} \tag{7.50}$$

This behaviour should be compared with the Debye relations which show that the ratio obtained by dividing the imaginary and real part of Eqn. 7.44 is equal to $\omega\tau$. In contrast Eqn. 7.49 has its basis in the non-Debye polarization, and this kind of polarization has been found experimentally to be applicable to all kinds of materials.

The interpretation of the complex dielectric permittivity by considering the "Universal Law" may be expressed by $\varepsilon^*(\omega)$, which is a function of frequency, by writing it in real and imaginary parts:

$$\varepsilon^*(\omega) = \varepsilon'(\omega) - j\,\varepsilon''(\omega) \tag{7.51}$$

$$= \varepsilon_\infty + a(j\ \omega)^{n-1} \tag{7.52}$$

$$= \varepsilon_\infty + a\left[\sin\left\{\frac{n\pi}{2}\right\} - j\ \cos\left\{\frac{n\pi}{2}\right\}\right]\omega^{n-1} \tag{7.53}$$

where ε_∞ is the limiting permittivity, i.e. the permittivity at high frequency, and $o < n < 1$; the constant (a) determines the strength of the polarization. The characteristic feature of this "non-Debye" or universal relationship is that the ratio of the imaginary to the real part of the dielectric susceptibility is independent of frequency. That is,

$$\frac{\varepsilon''(\omega)}{\varepsilon'(\omega) - \varepsilon_\infty} = \cot\left\{\frac{n\pi}{2}\right\} \tag{7.54}$$

This is in contrast with the Debye dipolar behaviour of Eqn. 7.23 where this ratio is equal to $\omega\tau$.

In most materials the conductivity has usually been found to be also a function of frequency and its general form is,

$$\sigma(\omega) = \sigma_o + \sigma_{ac}(\omega) \tag{7.55}$$

where σ_o is the d.c. conductivity and $\sigma_{ac}(\omega)$ is the true a.c. conductivity. There is no evident correlation between the magnitudes of d.c. and a.c. components of conductivity, although $\sigma_{ac}(\omega)$ has a weaker temperature dependence that σ_o. The Eqn. 7.55 can be written in the form of

$$\sigma(\omega) = \sigma_o + \omega \varepsilon_o \varepsilon''(\omega) \tag{7.56}$$

where the dispersion obeys the relation

$$\varepsilon''(\omega) \propto \varepsilon'(\omega) \propto \omega^{n-1} \tag{7.57}$$

and consequently only $\sigma_{ac}(\omega)$ follows the relationship

$$\sigma_{ac}(\omega) \propto \omega^{n} \tag{7.58}$$

This dependence of conductivity with frequency is not only found in disordered, glassy and amorphous solids but also in ordered molecular solids in which the carriers involved can be electrons, polarons, protons or ions. The exponent n is found to be close to unity but is temperature dependent, decreasing as the temperature increases. It is also possible to study the frequency dependence of conductivity at very low frequencies by considering d.c. step discharge currents in the time domain.

The time-domain response of a dielectric material to a step-function electric field $E(t) = 0$ for $t < 0$ and $E(t) = E_o$ for $t > 0$, may be described in terms of the resulting charging current

$$i_c(t) = \varepsilon_o E_o(\delta(t) + f(t)) + i_o \tag{7.59}$$

where the δ-function represents the response of the 'free space component' while the function $f(t)$ describes the dynamic response of the polarisation $P(t)$, due to the dielectric medium filling the space in question. The current i_o represents the d.c. limit due to whatever conduction processes may be operating under the steady applied field E_o. A sudden removal of the steady field results in a discharge current $i_d(t)$, which in a linear system should be given by the polarization component of (7.59), i.e.

$$i_d(t) = i_c(t) - i_o \tag{7.60}$$

The time-domain response and the complex frequency-domain response $\chi(\omega)$, are related by the complex Fourier transformation,

$$\chi(\omega) = \int_o^\infty f(f) \exp(-i\omega t)\, dt \tag{7.61}$$

This can give considerable experimental advantages, if in a certain spectral region measurement of $\chi(\omega)$ is difficult, as for example at low frequencies where the d.c. contribution i_o swamps the measured part of loss (7.32). It has been noted previously that the electrical conductivity of dielectric materials is well represented by the empirical formula

$$\sigma(\omega) = \sigma_o + \Lambda(T)\, \omega^{n(T)} \tag{7.62}$$

which implies that the dielectric loss is a function

$$\chi''(\omega) \alpha \omega^{n(T)-1} \tag{7.63}$$

Closely related to these two relationships is the corresponding time-domain response, which is well known to follow in many materials, the power law

$$i_d(t) \alpha t^{-n} \tag{7.64}$$

which is the Fourier transform of (7.63). Here, clearly, this power law corresponding to the universal dielectric behaviour cannot be valid over the infinite the range since the total charge in the system would become infinite. This means that there must be a time when the slope of the discharge current must become steeper than - 1, as shown in Figure 7.14, and it can be shown that the complete time-domain response corresponding to the relation 7.46 may be written in the form

$$l_d(t) \alpha \frac{1}{(\omega_p t)^n + (\omega_p t)^k} \tag{7.65}$$

where the exponent k is greater than unity, and n is the same as in the universal relation 7.63. At times in excess of the reciprocal peak frequency, $t > 1/\omega_p$, the second term in the denominator of equation 7.65 dominates, and the logarithmic slope goes through the value - 1. Figure 7.15 shows the frequency domain response corresponding to the time-domain behaviour described above.

In Jonscher's interpretation of the observed experimental data a two state time domain-response is proposed, the 'primary' high frequency stage representing the initial many bodied reaction to a step function, and the 'secondary' being a final smaller scale adjustment after the primary process has run its course. This approach suggests that the frequency-domain loss peaks are the results, therefore, of two separate processes, and is in complete contrast to the classical Debye process in which one physical cause generates the whole loss peak.

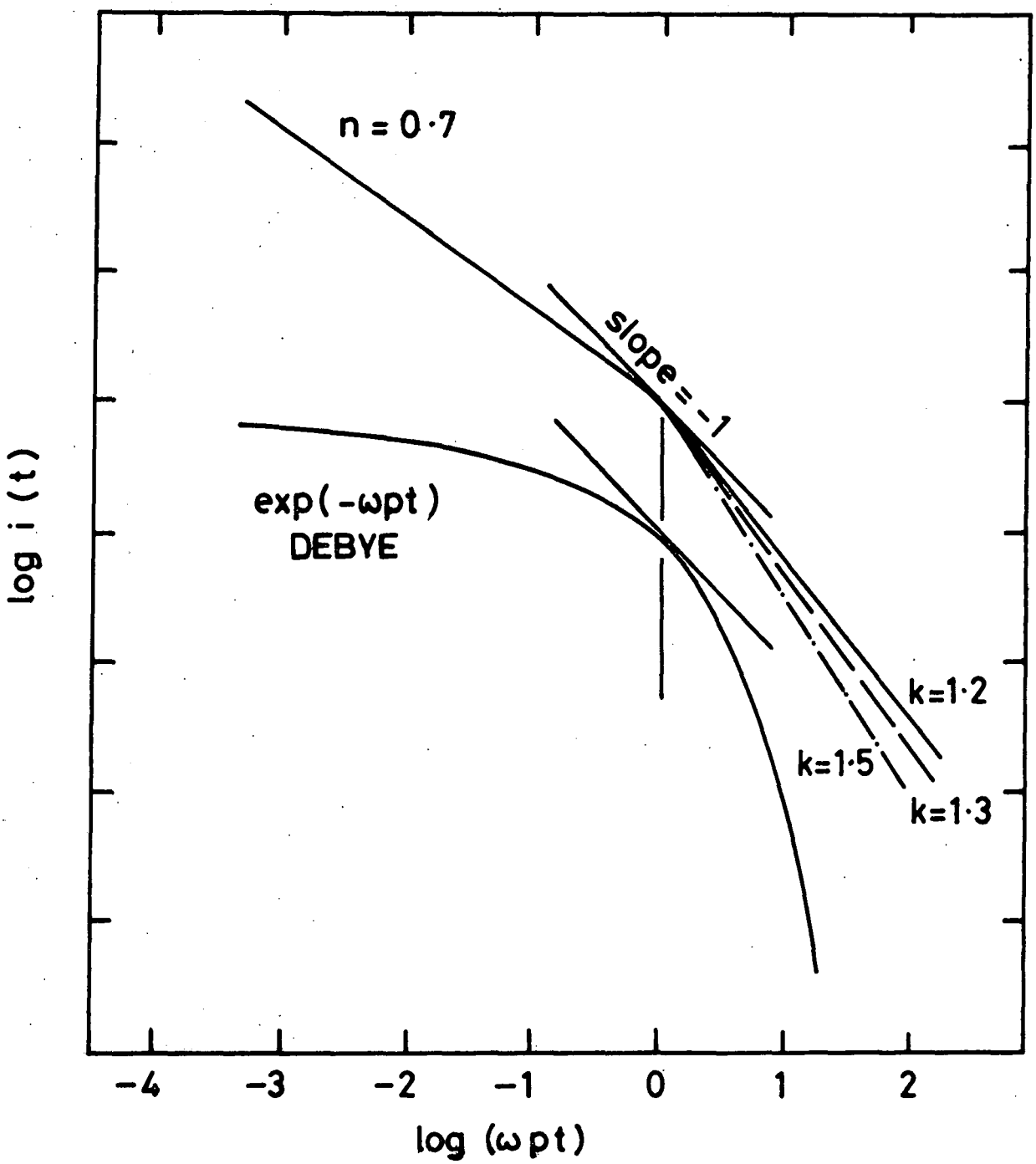

FIG. 7·14 THE TIME-DOMAIN RESPONSE OF A DIELECTRIC FROM EQUATION (7·) WITH n = 0·7 AND k = 1·2, 1·3 & 1·5. THE SLOPE -1 IS SHOWN AT TIME t = $1/\omega p$. THE CURVE FOR AN 'IDEAL' DEBYE SYSTEM IS SHOWN FOR COMPARISON

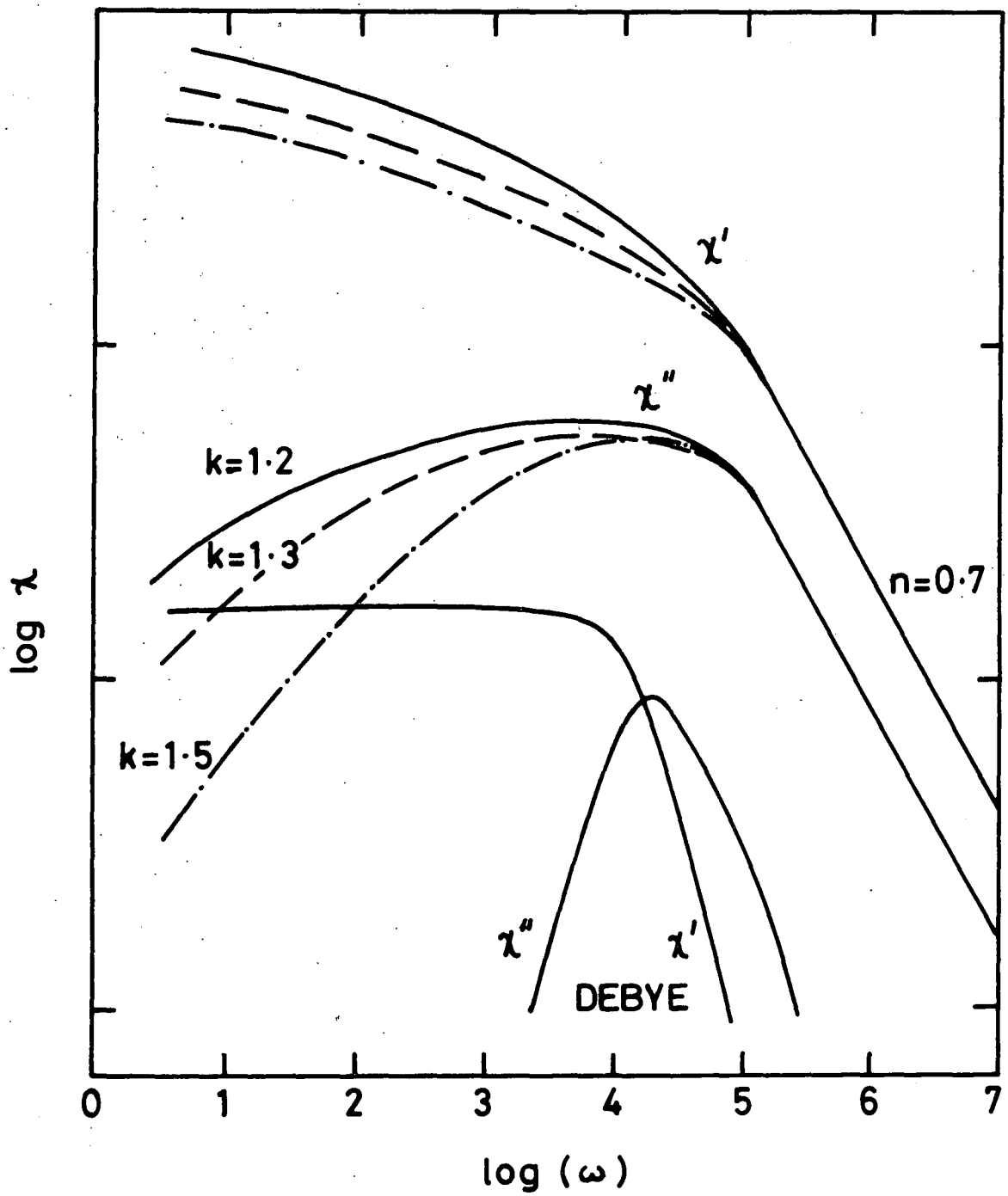

FIG. 7·15 THE FOURIER TRANSFORMED (FREQUENCY-DOMAIN) DATA OF FIG. 7·14. THE 'IDEAL' DEBYE RESPONSE IS AGAIN SHOWN.

CHAPTER 7

REFERENCES

7.1 N. F. Mott and E. A. Davis, 'Electronic Processes in Non-Crystalline Materials', 2nd edition, Oxford University Press (1979).

7.2 P. W. Anderson, Phys. Rev. 109, 1492 (1958).

7.3 M. H. Cohen, M. Fritzsche, and S. R. Ovshinsky, Phys. Rev. Lett, 22, 1065 (1969).

7.4 W. E. Spear and P. G. LeComber, Phil. Mag. 33, 935 (1976).

7.5 P. G. LeComber and W. E. Spear in 'Structure and Excitations of Amorphous Solids' (AIP Conference Proceedings No. 31) p.284 (1976).

7.6 E. A. Davis and N. F. Mott, Phil. Mag. 22, 903 (1970).

7.7 N. F. Mott, Phil. Mag. 26, 505 (1972).

7.8 N. F. Mott, J. Non-Cryst. Solids 1.1 (1968).

7.9 N. F. Mott, Phil. Mag. 19, 835 (1969).

7.10 A. K. Jonscher, Nature, 267, 673 (1977).

7.11 A. K. Jonscher, Phil. Mag. B, 6, 587 (1978).

7.12 C. Kittel in 'Introduction to Solid State Physics' Wiley & Sons Inc., New York, 4th Edition. (1971)

7.13 A. Von Hipple in 'Dieletrics and Waves', John Willey and Sons Inc., London, (1962).

7.14 J. B. Blakemore in 'Solid State Physics', 2nd Edition, Saunders Company, London (1974).

7.15 P. J. Harrop in 'Dielectrics', Butterworth, London (1972).

7.16 A. K. Jonscher Coll. and Poly. Sci. 253, 231 (1975).

7.17 E. E. Havinga, J. Phys. Chem. of Solids 18, 253 (1961)

7.18 A. J. Bosman and E. E. Havinga, Phys. Rev., 129, 1593 (1963).

7.19 G. A. Samara, J. Phys. Chem. of Solids, 40, 509 (1979).

7.20 F. A. Kroger and H. J. Vink, Solid State Physics 3, 307, (1956).

7.21 A. B. Lidiard, Handbuck der Physik 20, 246 (1957).

7.22 N. F. Mott and R. W. Gurney in 'Electronic Processes in Ionic Crystals', 2nd Edition, Oxford University Press, (1957).

7.23 N. F. Mott and W. D. Twose, Adv. in Physics 10, 107 (1961).

7.24 N. F.Mott, Adv. in Physics 16, 49 (1967).

7.25 N. F. Mott in 'Metal Insulator Transitions', Taylor and Francis, London (1974).

7.26 M. Pollak, Phys. Rev. 138,A1822 (1965).

7.27 M. Pollak and T. H. Geballe, Phys. Rev, 122, 1742 (1961).

7.28 I. G. Austin and N. F. Mott, Adv. in Phys. 18, 41 (1969).

7.29 M. Pollak, Phil. Mag. 23, 519 (1971).

7.30 P. N. Butcher and K. J. Hayden in 'Amorphous and Liquid Semiconductors' (Edinburgh, University Press) p.234 (1977).

7.31 A. K. Jonscher, Nature 253, 717 (1975).

7.32 R. Lovell, J. Phys. C; Solid State Phys. 7, 4378 (1974).

CHAPTER 8

CONDUCTIVITY ; TECHNIQUES AND RESULTS

Measurement of the conductivity of RBSN had two aims ; firstly to determine the effect of unreacted silicon upon the conductivity, dielectric constant and dielectric loss of completely and partially nitrided RBSN, and secondly, to attempt to identify the conductivity mechanism (s) involved. This Chapter describes the methods used for d.c. and a.c. conductivity measurements, and the results obtained on samples of 59 and 64.5% weight gain samples of RBSN. Meaningful measurements on materials with lower weight gains were not possible either because of difficulties fabricating contacts or, in the case of dielectric measurements because of the high dielectric loss encountered in the samples.

8.1 EXPERIMENTAL METHODS

8.1.1 D.C. Measurements at Room Temperature

At room temperature RBSN is a good insulator and therefore measurement involves the detection of low current levels ($\sim 10^{-12}$ A). The major problem in measurements at this level is to ensure that the current detected is that which actually passes through the sample rather than that which flows over the surface of the sample, or through the apparatus used to support the sample during measurement, the leakage current. There are two approaches which can be made to eliminate, or at least reduce, the effect of leakage currents. The first is to attempt to reduce leakage to the level at which it is insignificant when compared with the bulk current flow in the sample, and the second is to accept that leakage will occur and then ensure that the leakage current is routed round the measuring instrument in the circuit. The latter approach is the one which has been adopted here.

As stated earlier there are two sources of leakage to be considered. The first, the leakage over the surface of the sample can be dealt with by use of a 'guard ring' electrode on the sample which is held at the same potential as the non-sample side of the detector. The electrode arrangement is shown in Figure 8.1. The apparatus leakage is catered for in much the same way in that the metallic poles contacting the sample are mounted in insulators which in turn are connected electrically. This centre connection is held at the same potential as the guard ring. The three terminal jig used in the present work is illustrated in Figure 8.2.

Figure 8.3 shows the circuit used in room temperature d.c. measurements. The metal enclosure round the sample was used to shield it from electrostatic interference. The electrodes were gold, evaporated onto the sample surface.

This apparatus was used to measure the response of high weight gain RBSN samples to step changes in voltage (see Section 7.7) at room temperature.

8.1.2 D.C. Measurements Above Room Temperature

At elevated temperatures the need for elaborate leakage precautions was not so great as at room temperature as the resistance of the samples was reduced with increasing temperature. However, it was still necessary to shield the sample within its heating furnace by placing it within a metal tube. The furnace and sample arrangement is shown in Figure 8.4. In this case contact was made to the sample using 'fired on' platinum paste.

The upper and lower limits of usable temperatures for d.c. measurements were as follows :-

The upper limit (at 900^{o}C) was governed by the platinum contact to the ceramic. This was fired in an argon atmosphere at 950^{o}C as at temperatures above 1000^{o}C platinum is known to form intermetallic compounds with the silicon in RBSN. The inert atmosphere was used in both sample pareparation and measurement, to guard against oxidation of the residual silicon in the ceramic.

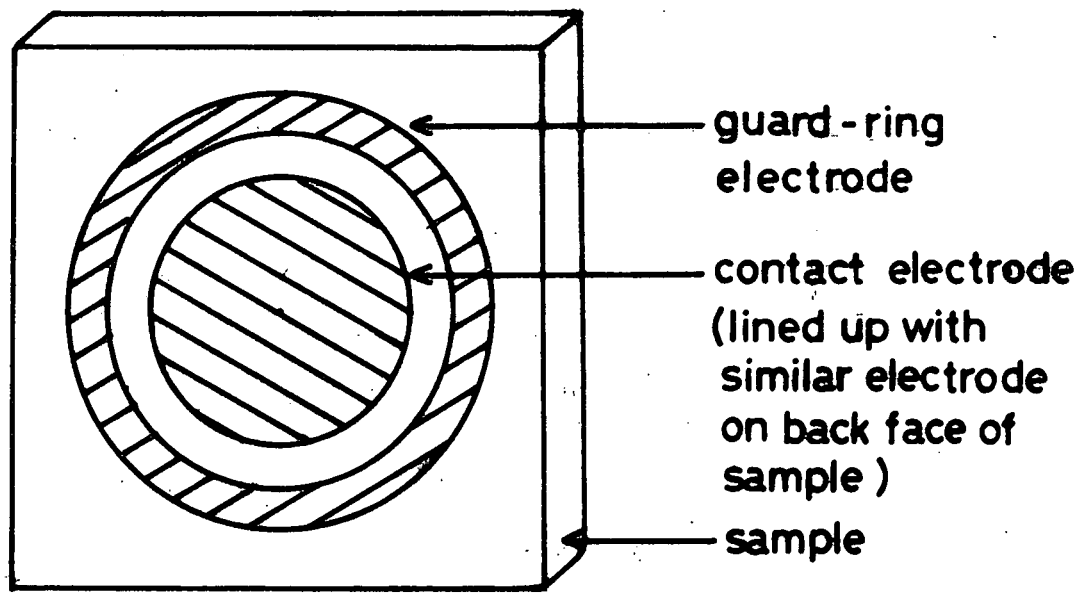

FIG. 8·1 GUARD-RING ELECTRODE ARRANGEMENT USED FOR DISCHARGE CURRENT MEASUREMENTS

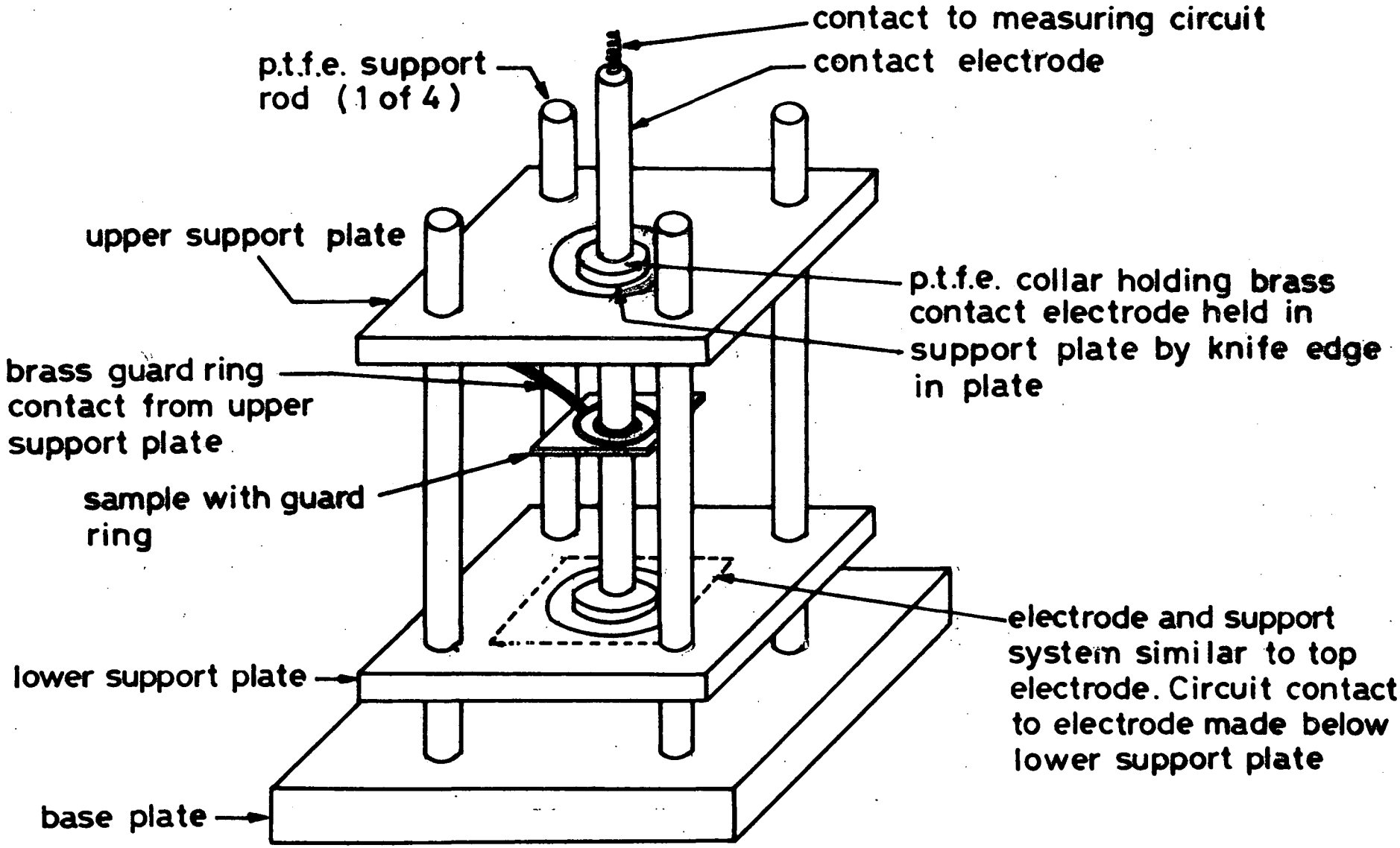

FIG. 8·2 APPARATUS USED FOR DISCHARGE CURRENT MEASURMENTS AT ROOM TEMPERAT

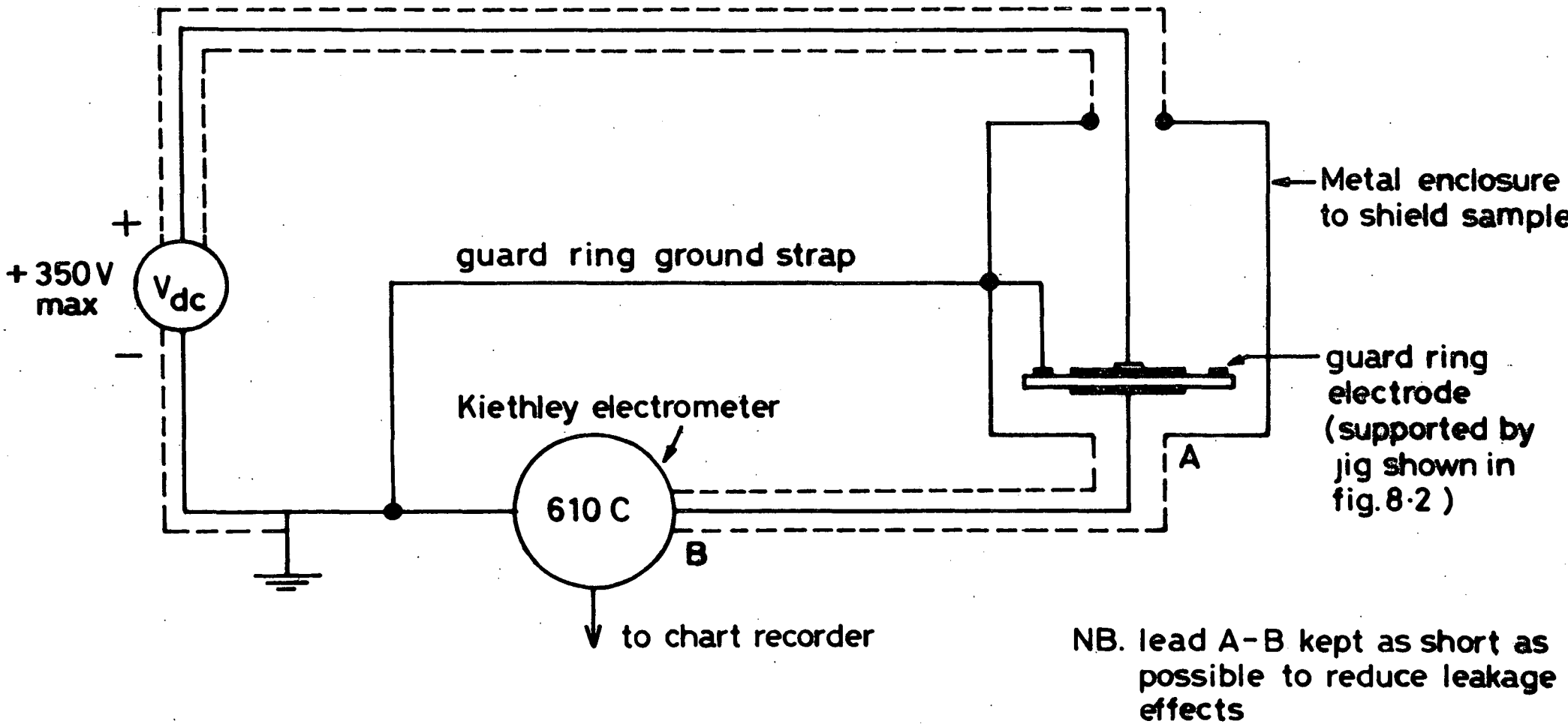

FIG. 8·3 CIRCUIT FOR D.C. DISCHARGE CURRENT MEASUREMENTS

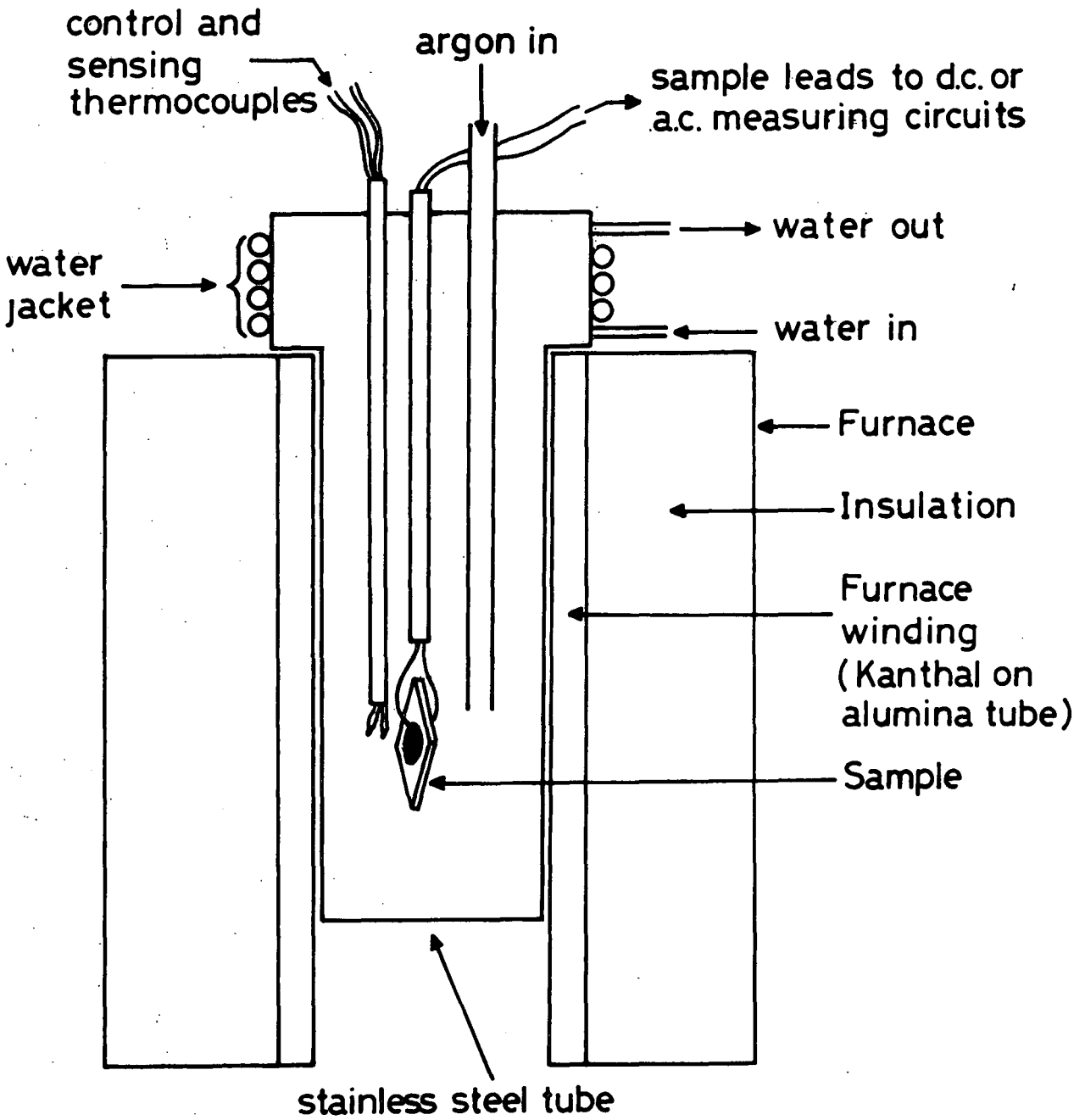

FIG.8·4 FURNACE USED FOR ELEVATED TEMPERATURE D.C. AND A.C. MEASUREMENTS

The lower limit was set at about 300°C as below this the noise generated in the measurement circuit by the furnace winding was high in comparison with the sample current.

The measuring circuit used was basically as shown in Figure 8.3 with the furnace detail of Figure 8.4 replacing the shielded enclosure, and the sample having only two terminals, and no guard-ring.

The apparatus was used for measurement of the variation of conductivity with temperature of high weight gain samples.

8.1.3 A.C. Measurements

A.C. measurements were made over the frequency range 3 Hz to 300 kHz from room temperature to 900°C, again on high weight gain samples, using the furnace described above, and shown in Figure 8.4. However, in this case, the sample was connected to a phase sensitive detector circuit which measured the two quadrature components of the signal from the sample. This is shown in Figure 8.5.

Considering the circuit :-

An a.c. voltage V_1, is applied to the test capacitance C_x in series with a standard capacitor C_o. The voltage measured across C_o is :

$$V_o = V_1 \cdot \frac{C_x}{(C_o + C_x)} \tag{8.1}$$

and if $C_o >> C_x$, $V_o = V_1 \frac{C_x}{C_o}$ (8.2)

and if C_o has a fixed value

$$\frac{V_o}{V_1} = A\,C_x, \text{ where A is constant.} \tag{8.3}$$

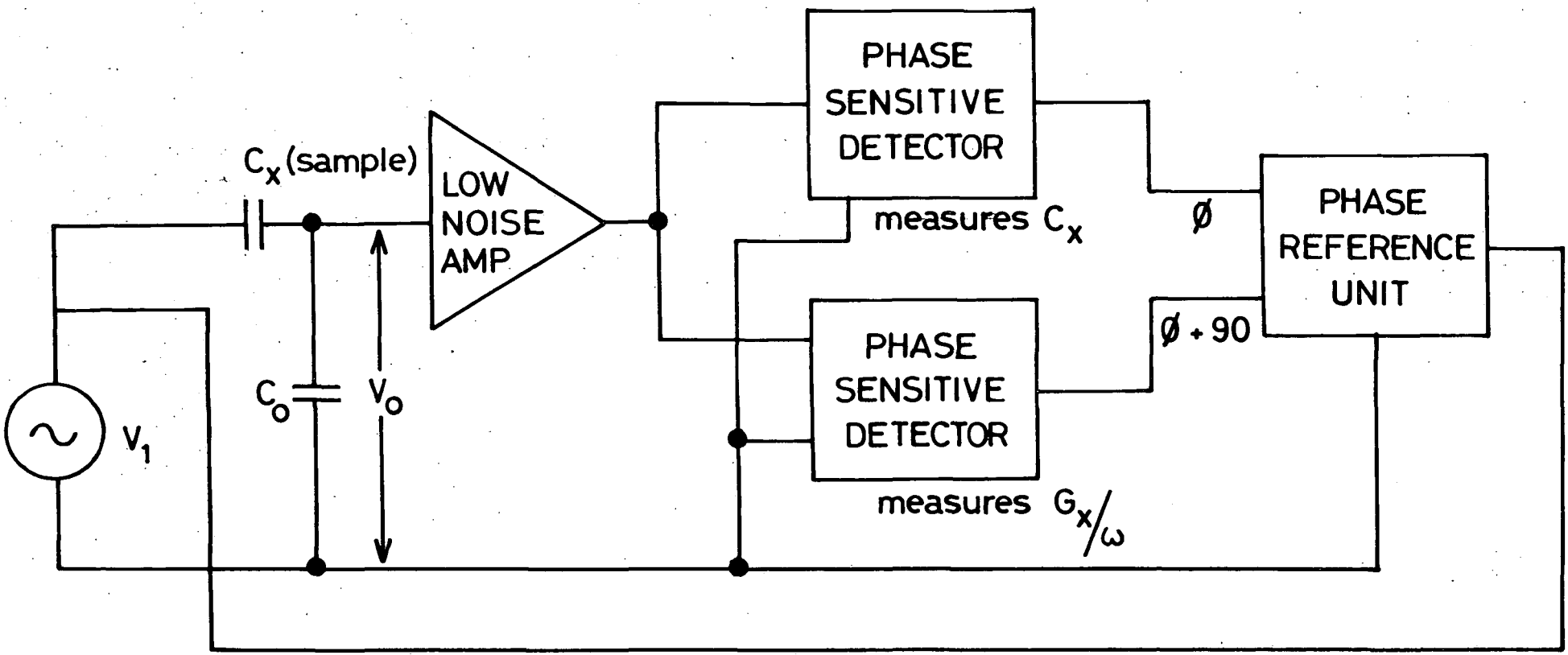

FIG. 8·5 PHASE SENSITIVE DETECTION CIRCUIT FOR CAPACITANCE AND CONDUCTANCE MEASUREMENTS IN THE FREQUENCY RANGE 3 Hz. TO 300 kHz.

Considering now the conductance in parallel with C_x, and if $G_x << \omega C_o$.

$$V_o = V_1 \cdot \frac{-j G_x/\omega + C_x}{C_o} \qquad (8.4)$$

which can be represented by two voltages, one in phase with V_1 ; $V_1 C_x/C_o$, and one in quadrature with V_1 ; $V_1 G_x/\omega C_o$.

These two voltages are measured, after amplification of V_o, by the phase sensitive detector which for the capacitive voltage is referenced by an voltage in phase with V_1 and for the conductive voltage is referenced by a voltage in quadrature with V_1.

From the measured voltages the following can be derived :-

Sample capacitance and dielectric constant (ε')

$$C_x = \frac{V_o C_o}{V_1} \qquad (8.2a)$$

and then $$\varepsilon' = \frac{C_x d}{\varepsilon_o A} \qquad (8.5)$$

where d = sample thickness

A = area of electrodes

Sample conductance and conductivity (Re (σ))

$$G_x = \frac{\omega V_o C_o}{V_1} \qquad (8.6)$$

and then $$\mathrm{Re}(\sigma) = \frac{G_x d}{A} \qquad (8.7)$$

Tan δ and ε''

$$\text{Tan } \delta = \frac{V_{G_x}}{V_{C_x}} \tag{8.8}$$

where V_{G_x} and V_{C_x} are the measured conductive and capacitive voltages respectively.

and therefore $\varepsilon'' = \tan \delta \, \varepsilon'$ (8.9)

The phase sensitive detectors set a lower limit of 0.0005 on the detectable value of tan δ.

8.2 RESULTS

8.2.1 D.C. Measurements at Room Temperature

As stated above the measurements done here were to study the time domain response of the ceramic to step changes in voltage. Figure 8.6 and 8.7 show the discharge current from RBSN samples with weight gains of 59.3% and 64.5% respectively, following charging to 350 V. Both curves clearly have a 'knee' at a time of approximately 2×10^4 seconds and appear to fit the relationship (7.65).

$$I_d(t) \alpha \frac{1}{(\omega_p t)^n + (\omega_p t)^k}$$

where n = 0.71 (59.3%) and 0.82 (64.5%)

and k = 1.46 (59.3%) and 1.6 (64.5%)

It should be noted that the Y-axis on these plots is of current and not conductivity.

For comparison of RBSN with Hot Pressed Si_3N_4, Figure 8.8 shows the current discharge for HPSN from 100 Volts and gives n = 0.69 and k = 1.7.

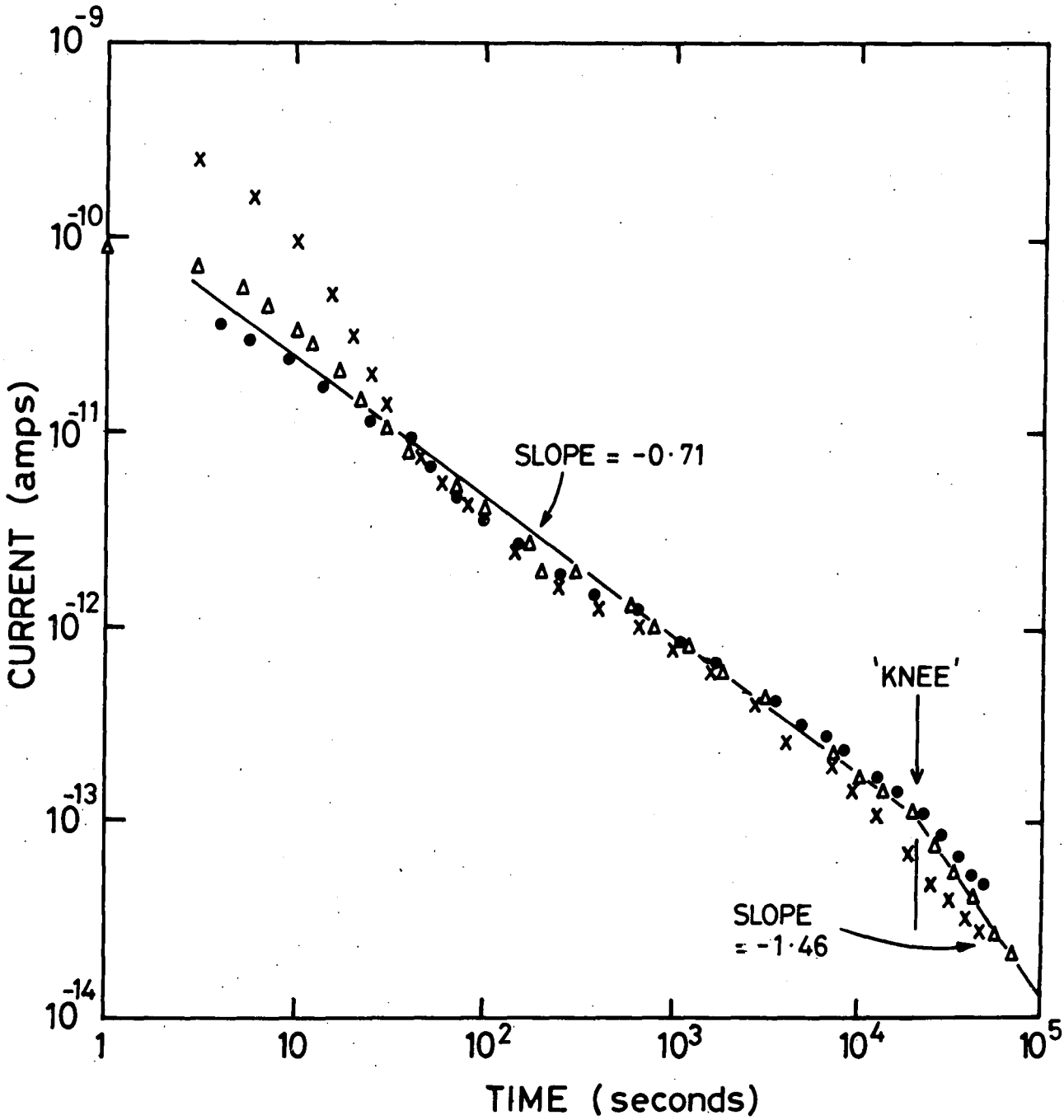

FIG. 8·6 DISCHARGE CHARACTERISTIC FOR 59·3 % WEIGHT GAIN RBSN ; ROOM TEMPERATURE (SYMBOLS CORRESPOND TO DIFFERENT SAMPLES OF NOMINALLY IDENTICAL COMPOSITION)

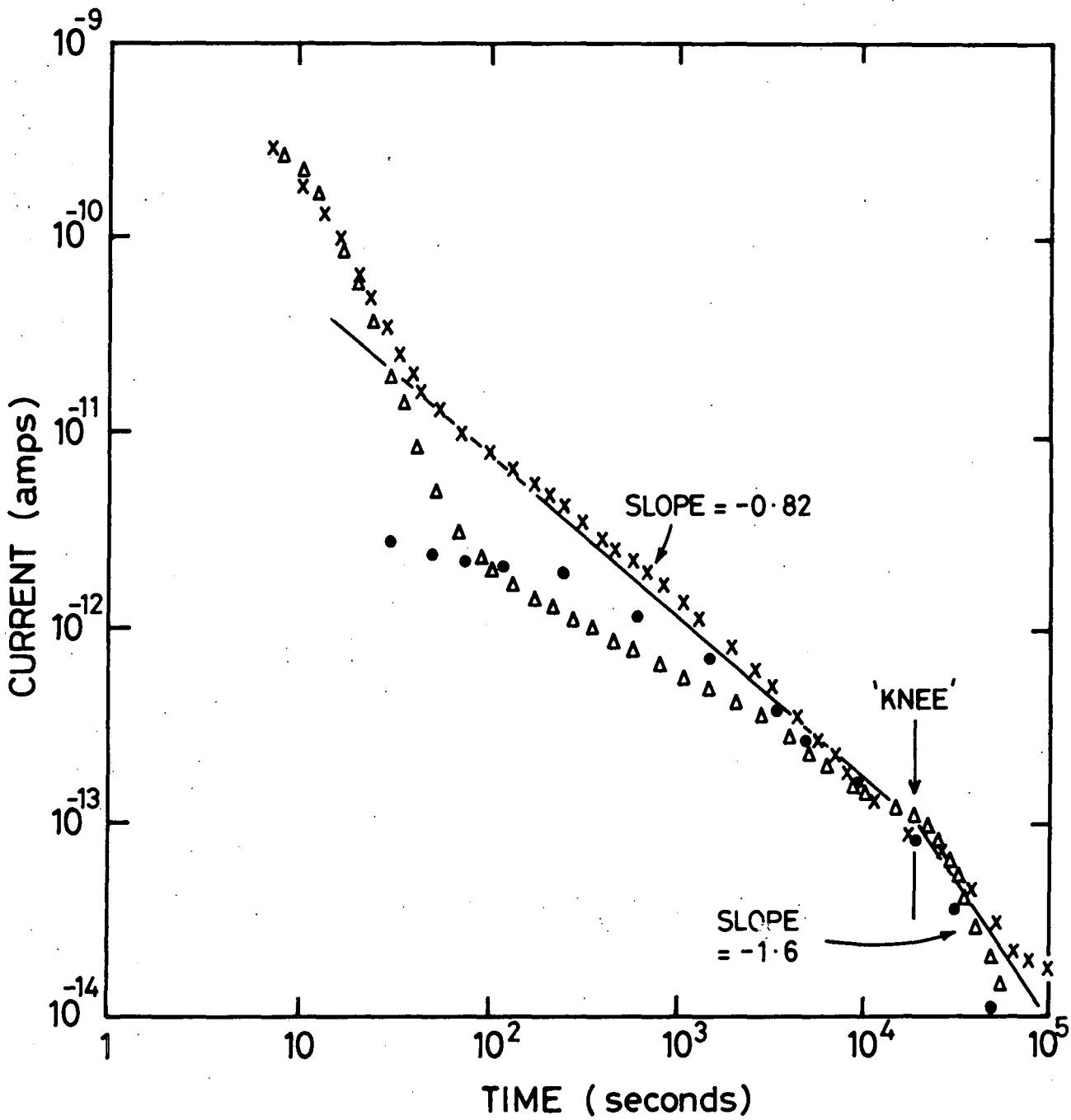

FIG. 8·7 DISCHARGE CHARACTERISTIC FOR 64·5% WEIGHT GAIN RBSN ; ROOM TEMPERATURE (SYMBOLS CORRESPOND TO DIFFERENT SAMPLES OF NOMINALLY IDENTICAL COMPOSITION)

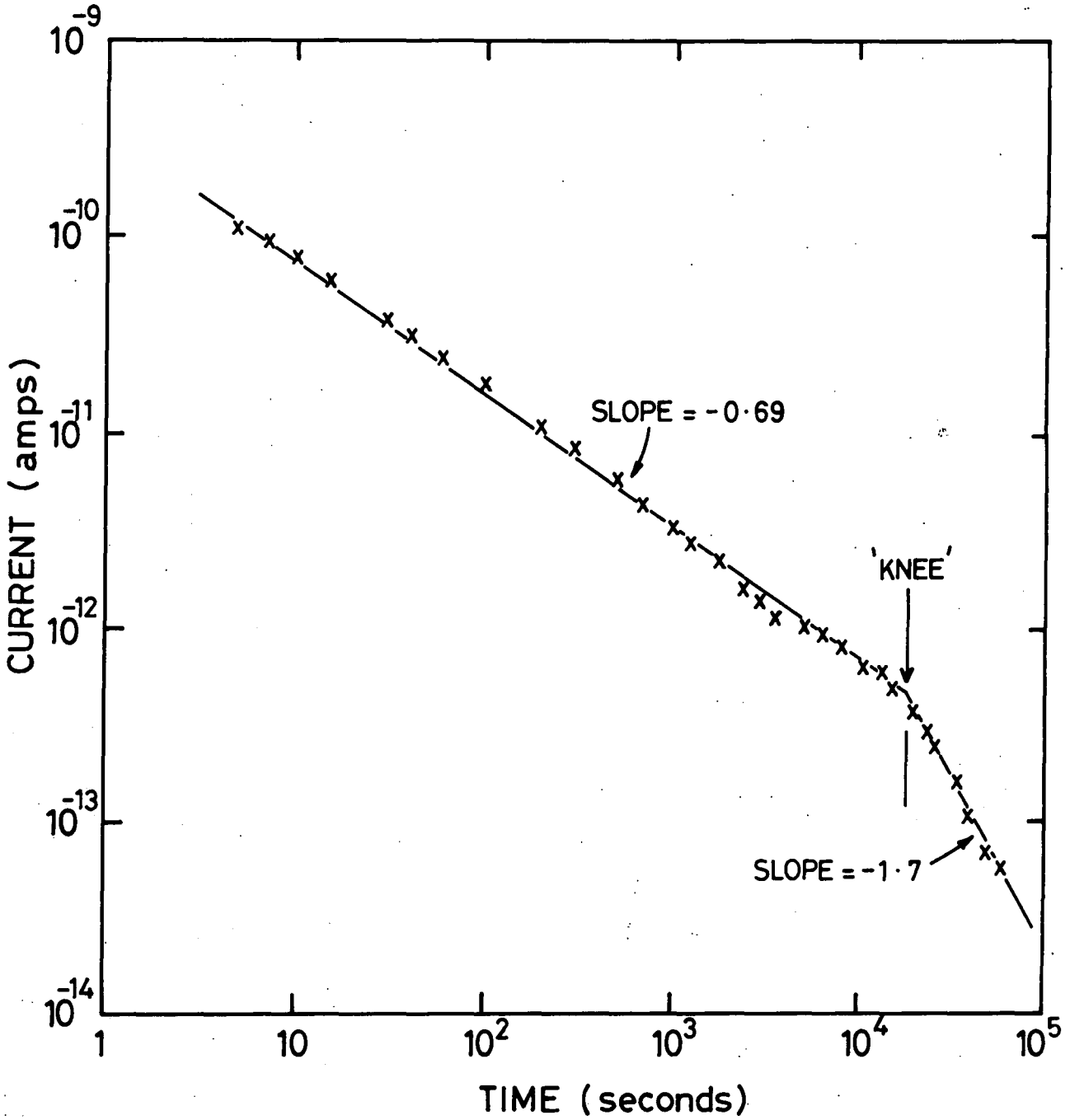

FIG. 8·8 DISCHARGE CHARACTERISTICS FOR HPSN, (Si_3N_4 / 5% MgO) ; 20°C

8.2.2. D.C.Measurements at High Temperatures

Figure 8.9 shows the variation of conductivity with inverse temperature for several 59% weight gain RBSN samples. A variation of conductivity as $1/T^{\frac{1}{4}}$ was not found suggesting that variable range hopping does not occur, at least at these temperatures.

8.2.3 A.C. Measurements

Values of ε' and ε'' for the 59.3% and 64.5% weight gain samples in the frequency range 3 Hz to 100 kHz between 20°C and 900°C are shown in Figures 8.10 and 8.11 (59.3%) and Figures 8.12 and 8.13 (64.5%). ε' is $\sim$ 10 for the 59.3% nitride and $\sim$ 8.5 for the 64.5% one. This difference is probably explained by the higher level of porosity in the 64.5% sample (see Table 2.2) as the value of ε' can be related to porosity by a relation similar to (5.14) where the ε'_p, the fractional permittivity is related exponentially to P, the porosity. On this model the ε' of the 59.3% RBSN would be expected to be greater than the 64.5% material. These figures are in reasonable agreement with those given in Table 1.1.

ε'' for both 59.3% and 64.5% samples show peaks in loss at low frequency and high temperature. This is consistent with the Jonscher two-stage relaxation approach in which the first stage is expected to be complete more quickly at higher temperatures. Figure 8.14 shows this situation graphically, as the 'relaxation' derived from room temperature current discharge is plotted with the high temperature frequency domain points. From ε' and ε'' for the 59.3% and 64.5% samples, tanδ's of 0.005 and 0.0013 at 100°C and 10 kHz respectively have been calculated. The lower value for the higher weight gain sample is expected as the proportion of unreacted silicon remaining in this sample is lower than in the other.

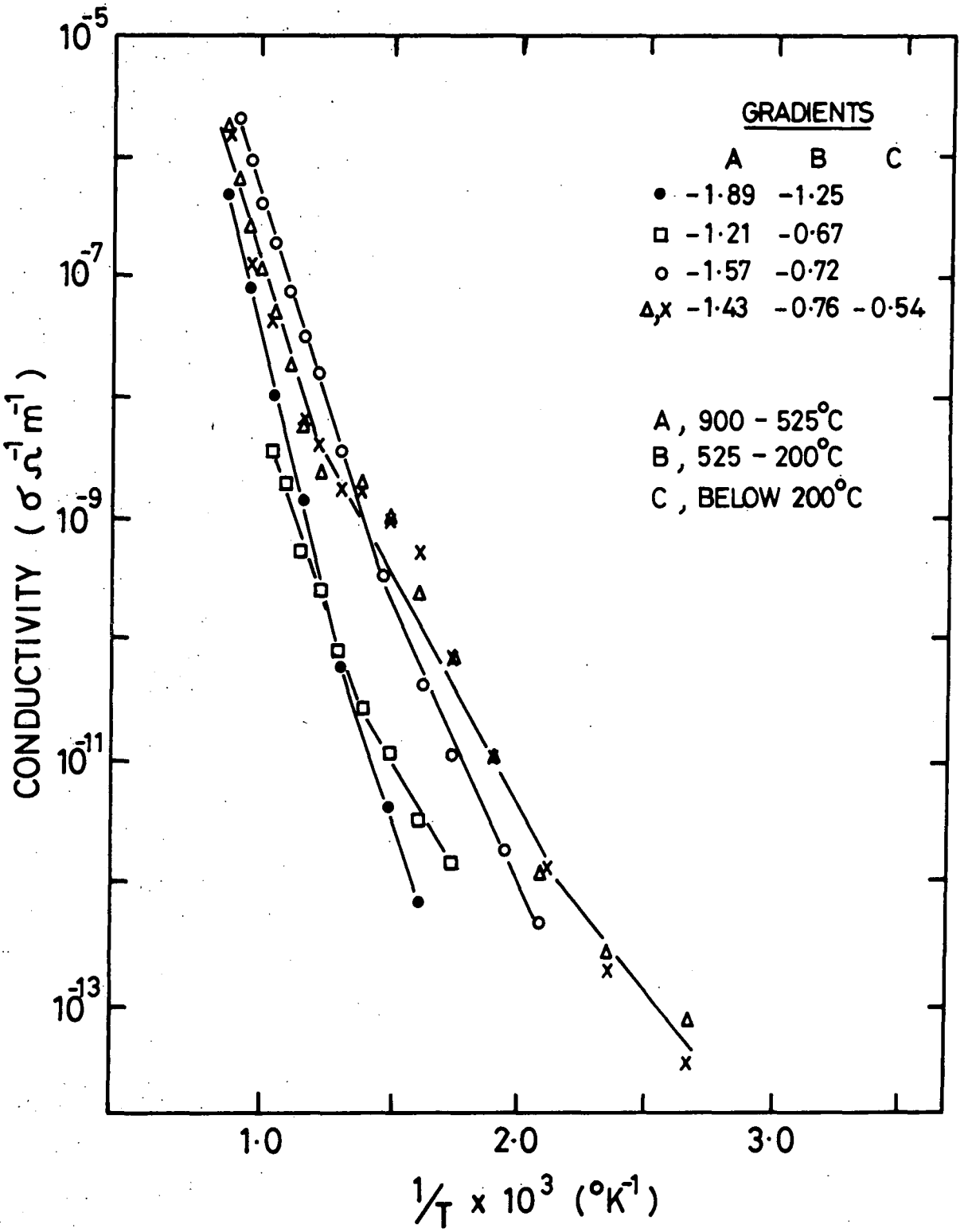

FIG. 8·9 TEMPERATURE DEPENDENCE OF CONDUCTIVITY FOR 59·3 % WEIGHT GAIN RBSN (SYMBOLS CORRESPOND TO DIFFERENT SAMPLES OF NOMINALLY IDENTICAL COMPOSITION)

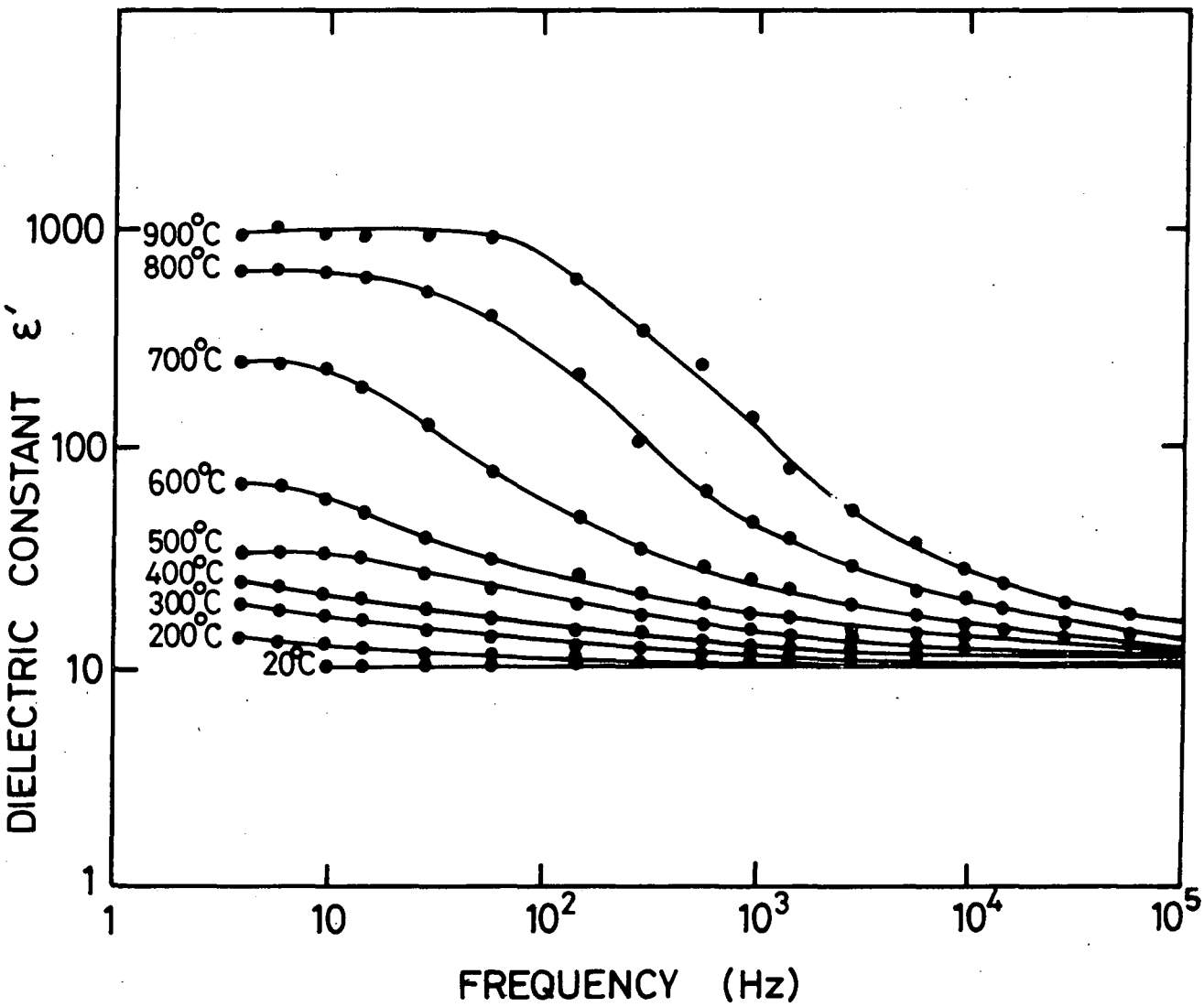

FIG. 8·10 VARIATION OF ε' WITH FREQUENCY AND TEMPERATURE ; 59·3 % WEIGHT GAIN RBSN

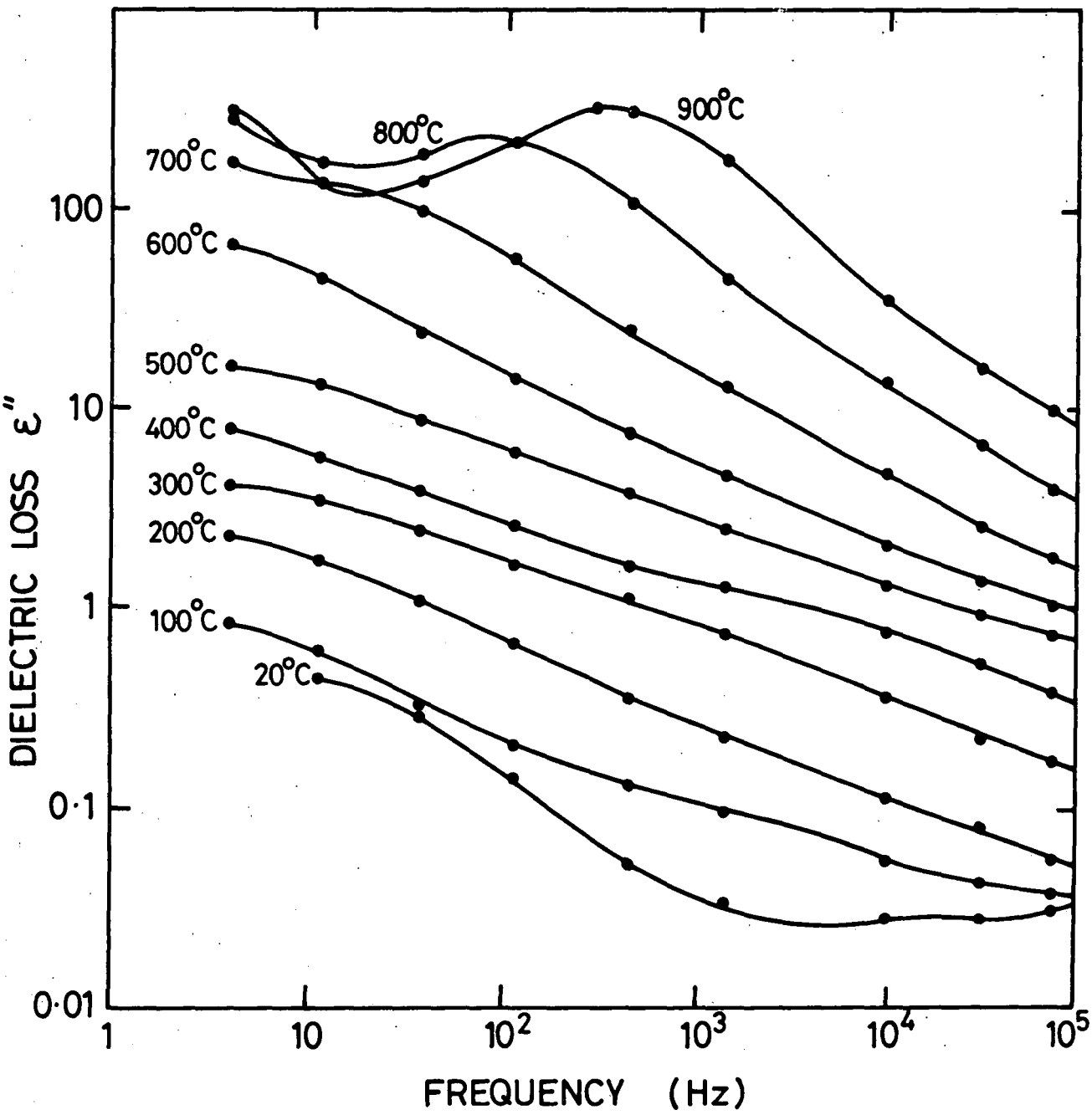

FIG. 8·11 VARIATION OF ε'' WITH FREQUENCY AND TEMPERATURE ; 59·3 % WEIGHT GAIN RBSN

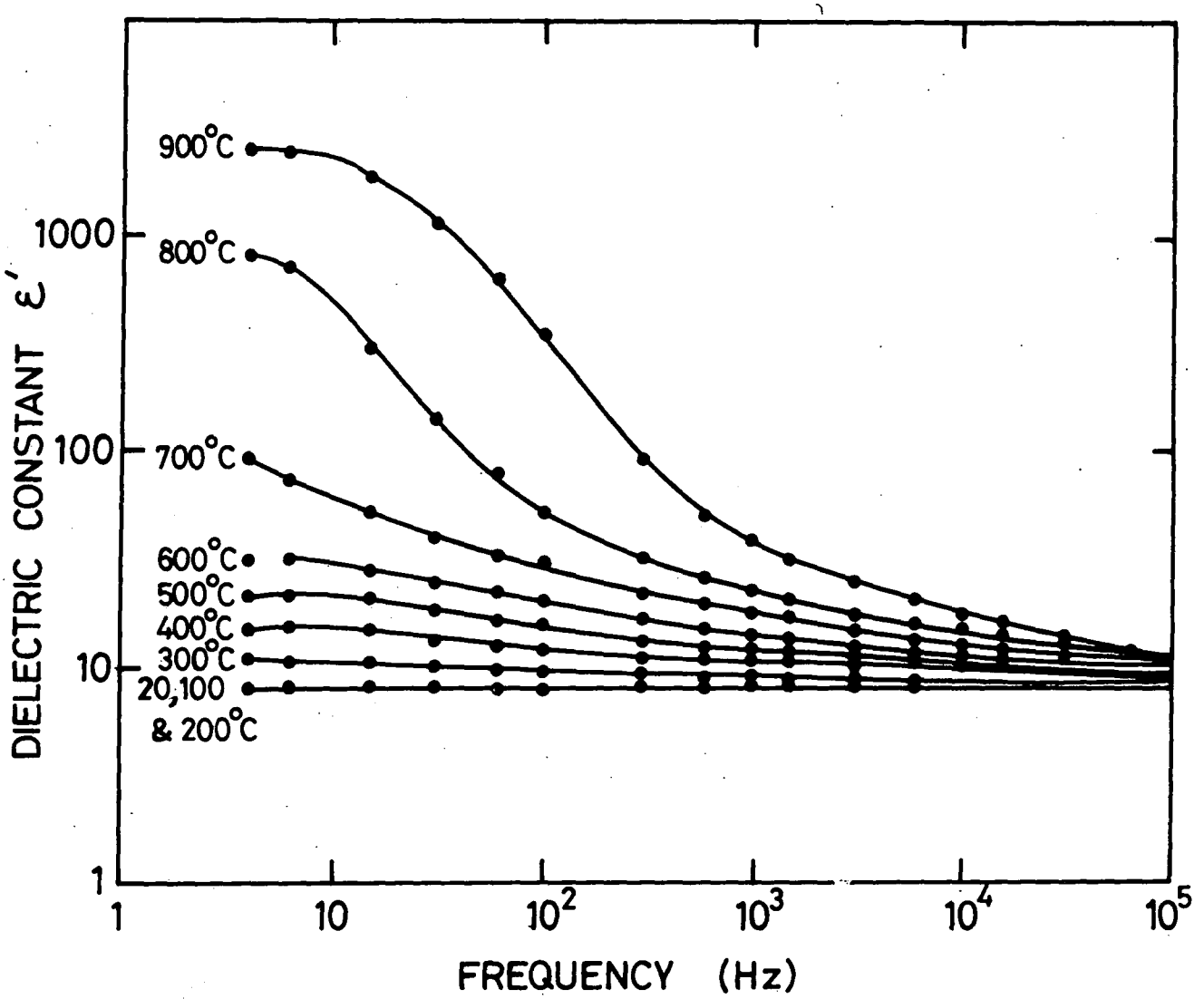

FIG. 8·12 VARIATION OF ε' WITH FREQUENCY AND TEMPERATURE ; 64·5 % WEIGHT GAIN RBSN

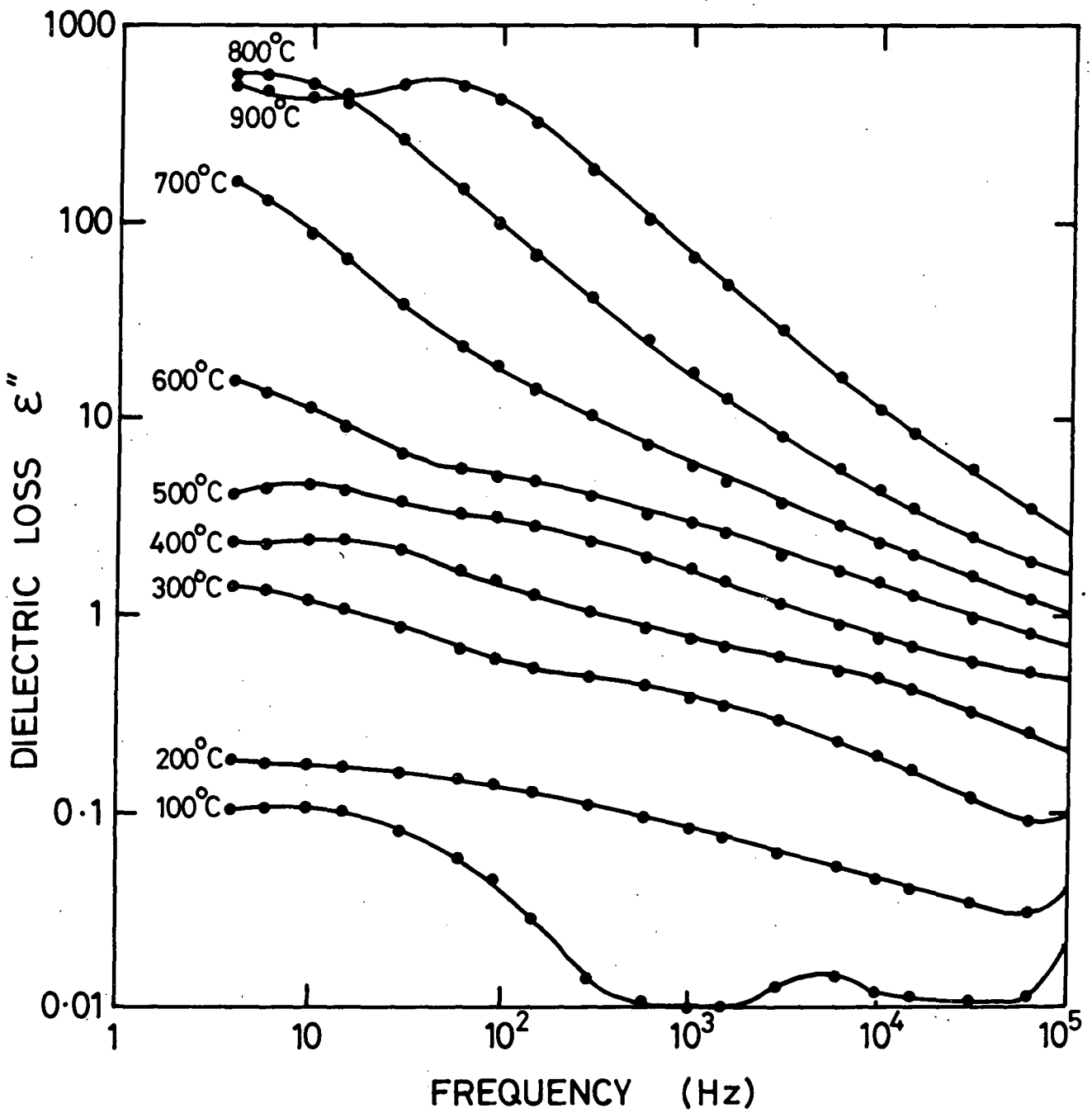

FIG. 8·13 VARIATION OF ε″ WITH FREQUENCY AND TEMPERATURE ; 64·5 % WEIGHT GAIN RBSN

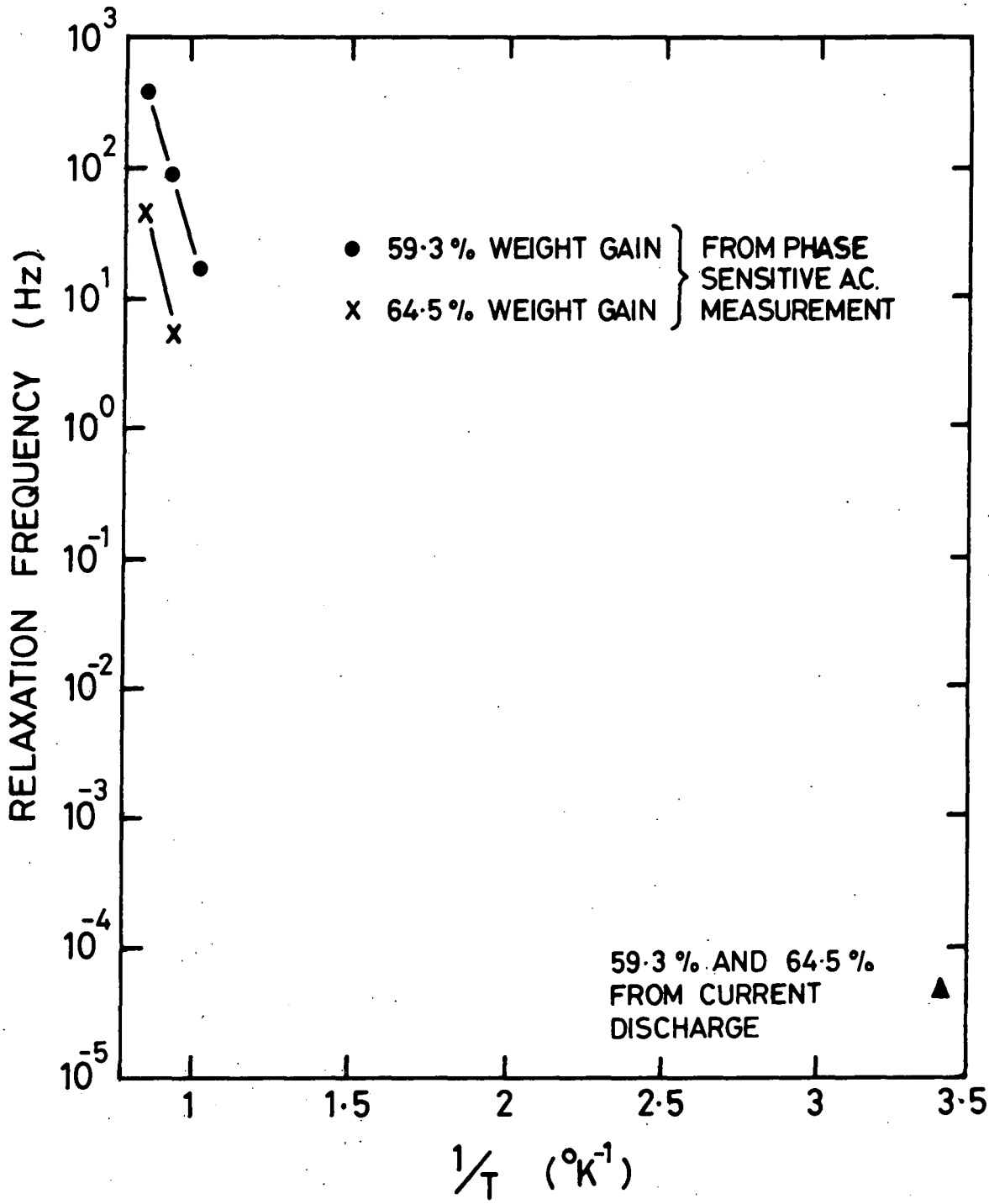

FIG. 8·14 RELAXATION FREQUENCY vs $1/T$ FOR 59·3% AND 64·5 % WEIGHT GAIN RBSN

8.3 DISCUSSION

The previous section shows how the a.c. data is in reasonable agreement with 'The Universal Law'. This approach makes no attempt to explain the causes of the conductivity or the carriers involved.

Table 8.1 summarises the behaviour of d.c. and a.c. conductivity which might be expected on a hopping model. Consideration of Figure 8.9 shows either two or three regions with different slopes ; it is however difficult to place these on the schematic diagram (Figure 7.4) of temperature dependence. Turning now to a.c. conductivity, Figures 8.15 and 8.16 show Re(σ) against frequency for the 59.3% and 64.5% nitrides respectively. The slopes of the curves vary from 0.85 to 0.49 which gives values for s in $\sigma(\omega) \alpha \omega^s$ in reasonable agreement with those predicted, although the behaviour begins to break down at high temperature and low frequency (the onset of Jonscher's second stage relaxation) and the frequency dependence is much reduced. Now consider d.c. and a.c. conduction behaviour together. Figur s 8.17 and 8.18 combine the a.c. and d.c. behaviour of 59.3% (8.17) and 64.5% (8.18) materials.

Referring to Table 8.1 and noting that $\sigma \alpha T^{-\frac{1}{4}}$ was not observed during d.c. measurements (section 8.2.2), the a.c.conductivity has two regions, one essentially temperature independent, and the other, at higher temperatures strongly dependent upon temperature. It should also be noted that at the highest temperatures (approaching 900°C) and low frequency the temperature dependence of a.c. conductivity falls away. It is suggested then that the conduction mechanism falls into regions as follows :-

(i) from room temperature (and possibly below) to about 400°C conduction is by nearest neighbour hopping in midgap defect bands,

(ii) from 400°C to about 750°C conduction is by hopping in the localized levels in the band edges, and

(iii) above 750°C conduction is by carrier transport in the extended stages just above and below the band edges.

8.4 FURTHER WORK

The measurement of d.c. conductivity should be extended below 20°C (i.e. reducing kT) in an attempt to observe $\sigma \alpha T^{\frac{1}{4}}$ conduction behaviour and ther by confirm the mechanisms suggested above.

It is also necessary to obtain intermediate points on Figure 8.14, either by performing step discharge experiments at elevated temperatures, or by lowering the frequency capability of an a.c. measurement technique.

TABLE 8.1: Summary of electronic hopping model

Conduction Type / Region	D.C. Conduction	A.C. Conduction		Comments
Carriers in the extended stages (sections 7.3(a) and 7.6 (a)).	$\sigma \alpha \exp \frac{(-E_A - E_F)}{kT}$	no frequency dependence		
Carriers in localized states in the band tails (sections 7.3(b) and 7.6(b)).	$\sigma \alpha \exp\left(\frac{E_A - E_F + W_1}{kT}\right)$	$\sigma(\omega) \alpha \omega^s$ temperature dependence as for d.c. conduction at the band edge.		band tail hopping
Carriers in defect band in the energy gap (sections 7.3(c) and 7.6(c)).	$\sigma \alpha \exp\left(\frac{-W_2}{kT}\right)$ kT > defect bandwidth	$\sigma(\omega) \alpha \omega^s$ $0.4<s<1.0$	T if kT > defect bandwidth	nearest neighbour neighbour hopping
	$\sigma \alpha T^{-\frac{1}{4}}$ kT < defect bandwidth		αT if kT< defect bandwidth	Variable range hopping

From Mott and Davis (7.1)

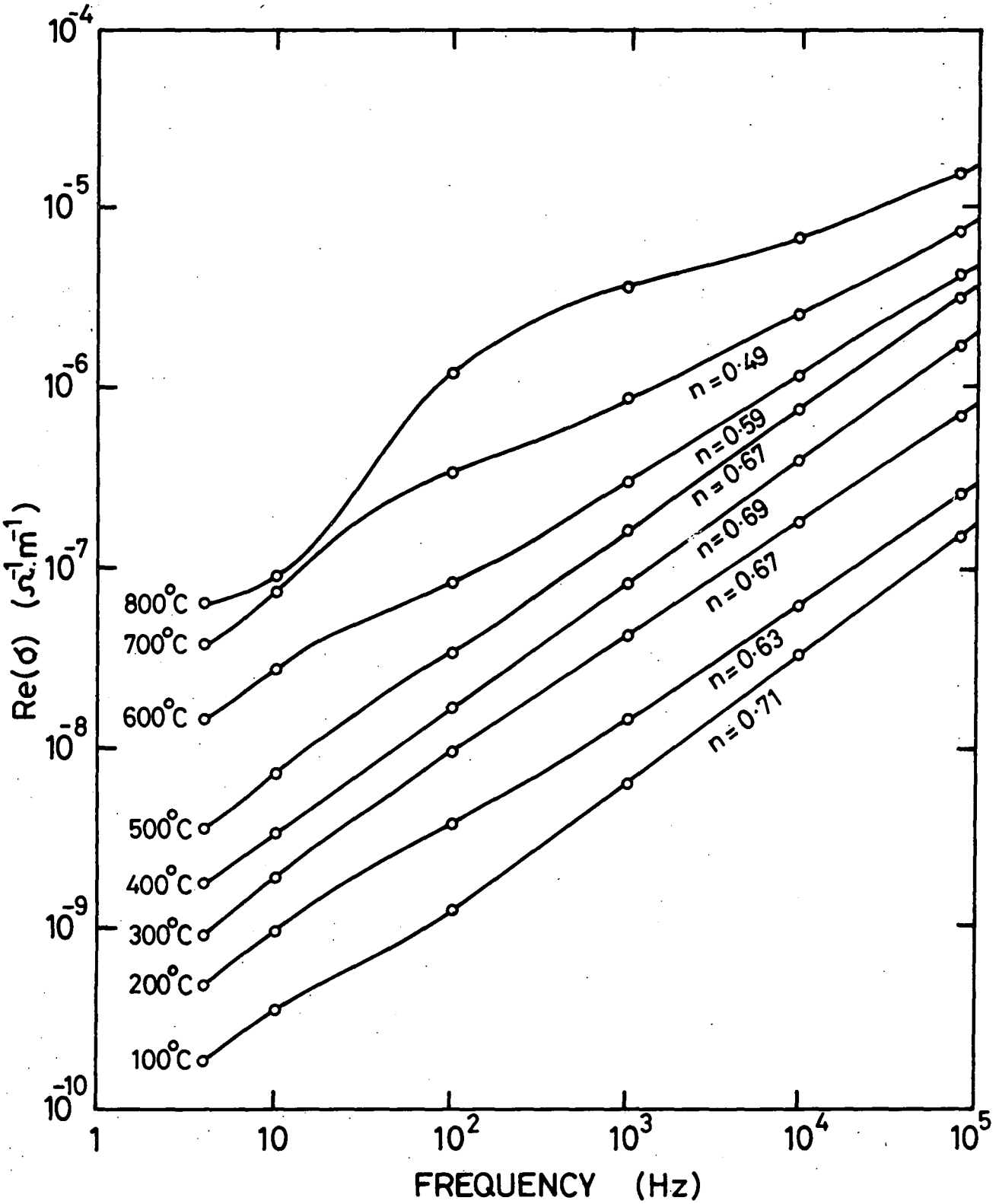

FIG. 8·15 VARIATION OF REAL CONDUCTIVITY WITH FREQUENCY AND TEMPERATURE ; 59·3 % WEIGHT GAIN RBSN

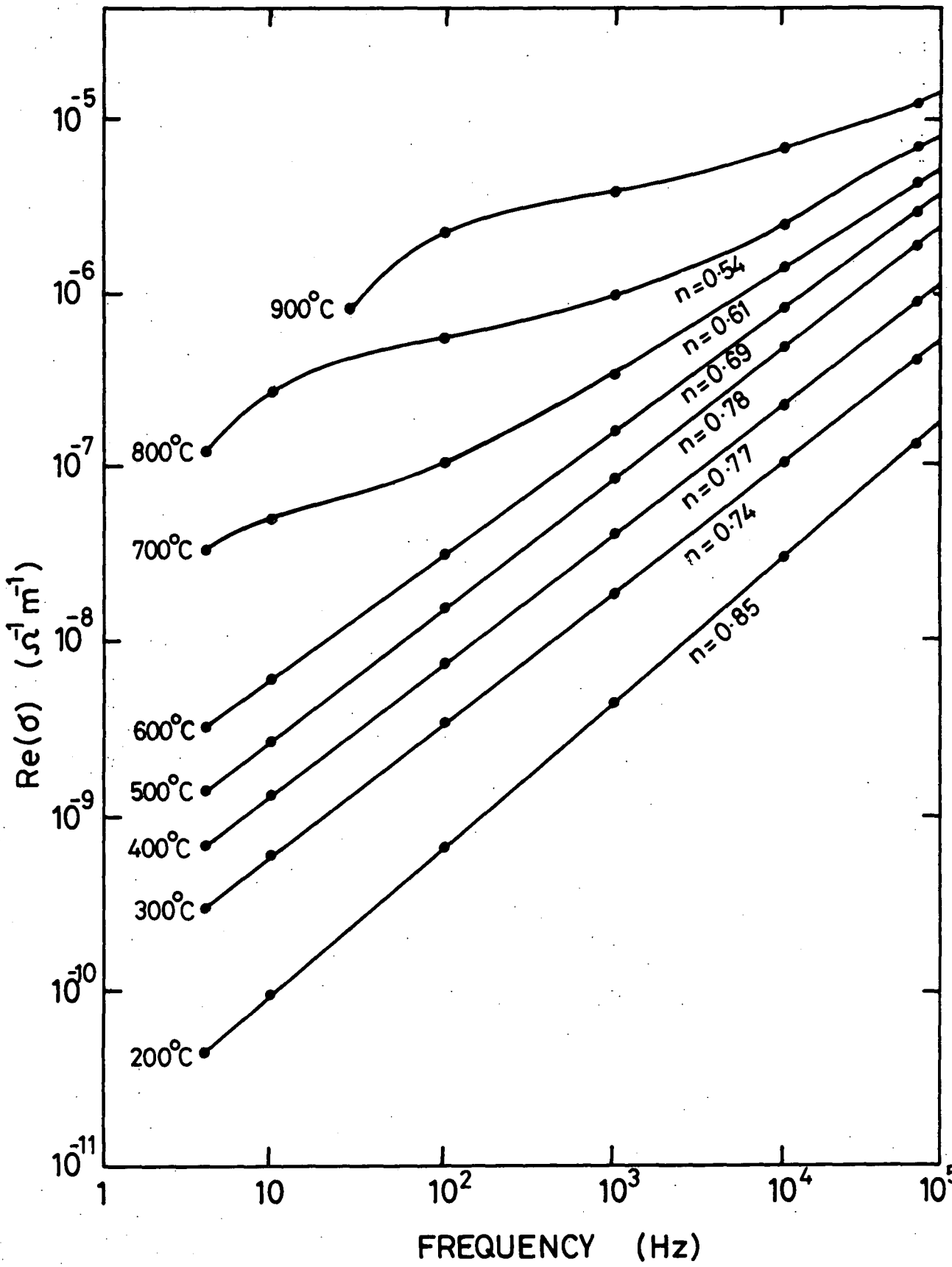

FIG. 8·16 VARIATION OF REAL CONDUCTIVITY WITH FREQUENCY AND TEMPERATURE ; 64·5 % WEIGHT GAIN RBSN

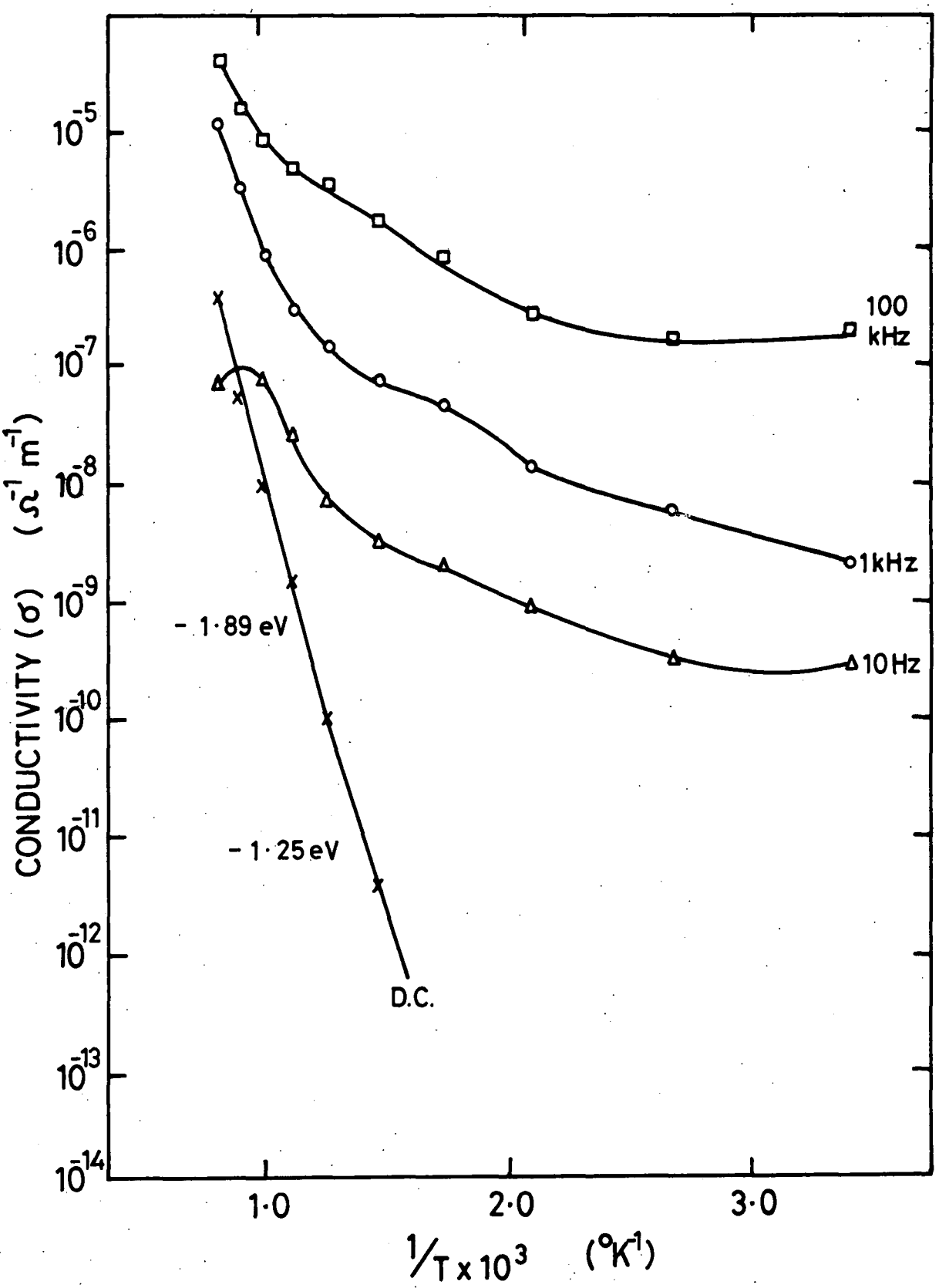

FIG. 8·17 TEMPERATURE DEPENDENCE OF σ_{DC} AND σ_{AC}; 59·3% WEIGHT GAIN RBSN

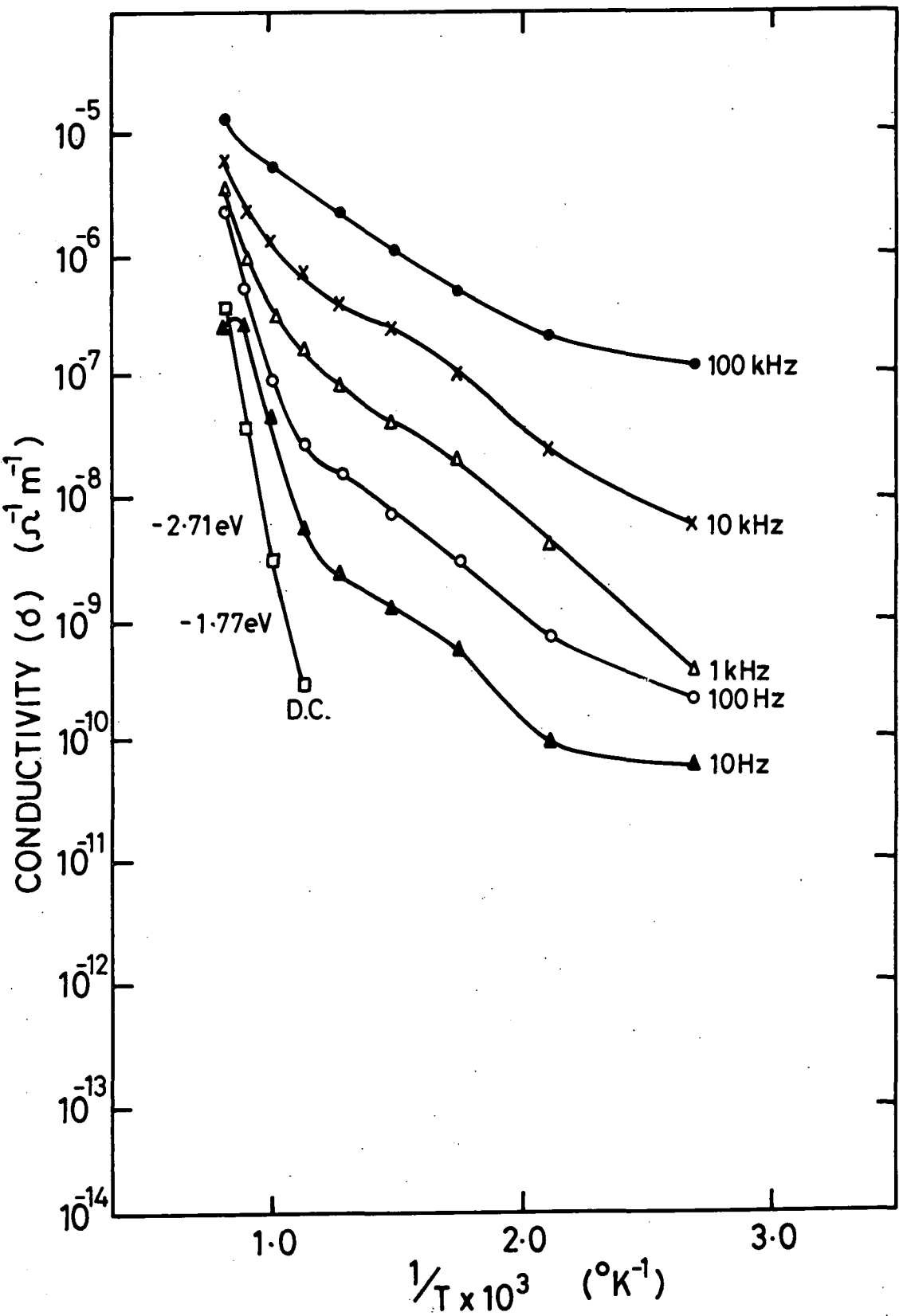

FIG. 8·18 TEMPERATURE DEPENDENCE OF σ_{DC} AND σ_{AC} ; 64·5 % WEIGHT GAIN RBSN

APPENDIX 1

ESR : INTEGRATION OF DERIVATIVE DATA

The computer program used for line shape analysis are given below. Thanks are due to UNITED GLASS plc for the provision of computer facilities. The language used is FORTRAN.

The program integrates a function by Simpson's Rule, and then evaluates the first four moments about an arbitrary point, and then about the mean of the integrated data. From these the coefficients of Skewness and Kurtosis are calculated. The algorithms are given below.

(a) Integration. Simpson's rule, together with Newtons $^3/_8$ rule or a combination of the two are used:-

(Z_j are integral values, y_j function values)

$$Z_j = Z_{j-2} + \frac{h}{3}(y_{j-2} + 4y_{j-1} + y_j) \quad \text{Simpsons rule} \qquad (1)$$

$$Z_j = Z_{j-3} + \frac{3}{8}h(y_{j-3} + 3y_{j-2} + 3y_{j-1} + y_j) \quad \text{Newtons } ^3/_8 \text{ Rule} \qquad (2)$$

$$Z_j = Z_{j-5} + \frac{h}{3}(y_{j-5} + 3.875y_{j-4} + 2.625y_{j-3} + 2.625y_{j-2} + 3.875y_{j-1} + y_j)$$

combination of (1) and (2).

(b) Skew & Kurtosis

$$\text{Arithmetic mean } \bar{x} = \left(\sum_{i=1}^{nn} x_i f_i\right) \sum_{i=1}^{nn} f_i$$

where x_i are magnetic field values and f_i absorption intensity values

Moments about zero

$$M_1' = \bar{x}$$

$$M_j' = \sum_{i=1}^{nn} f_i x_i^j \sum_{i=1}^{nn} ri \quad (j = 1).$$

Moments about mean

$$M_1 = 0$$

$$M_2 = M_2' - (M_1')^2$$

$$M_3 = M_3' - 3M_1' M_2' + 2 (M_1')^3$$

$$M_4 = M_4' - 4M_1' M_3' + 6 (M_1')^2 M_2' - 3 (M_1')^4$$

then Kurtosis $= M_4/M_2^2$

and Skewness $= M_4/M_2^{3/2}$

```
      SHAPAN 1:
C     A PROGRAM TO INTEGRATE ESR DERIVATIVE LINESHAPES
C     AND CALCULATE SKEWNESS & KURTOSIS OF THE
C     INTEGRATED DATA
C
C     SOME OF THE CODING HERE IS SPECIFIC TO EITHER
C     MOTOROLA MDOS FORTRAN OR THE UG plc EXORCISER
C     SYSTEM AND THUS THE PROGRAM IS NOT COMPLETELY
C     PORTABLE.  THE LINES INVOLVED ARE MARKED  **
C
C
C
C     THE MAIN DATA ARRAYS ARE SET UP AS COMMON VARIABLES,
C     THE COMMON STATEMENT APPEARS IN THE TWO ASSOCIATED
C     SUBROUTINES.  THE DUMMY (100) ARRAY IS REQUIRED BY
C     THE EXORCISER PLOTTING ROUTINES; OTHER SYSTEMS
C     MAY HAVE THEIR OWN COMMON REQUIREMENTS.
C     ----------------------START OF CODE ----------------
C
C
**    CALL DEBUG
**    CALL APULIB
      COMMON DUMMY (100), RDATA(300, 6), NVALS, LOOPVL, MINT
**    DIMENSION IFILE 1(7), IFILE2(7), PMOM(4)
C
C     ASK USER FOR DATA & RESULTS FILENAMES.
C
**    PRINT 1000
```

```
* 1000      FORMAT ('DATA FILE NAME')
*           READ 1020, (IFILE1(I), I = 1, 7)
*           PRINT 1010
* 1010      FORMAT ('RESULTS FILE NAME')
*           READ 1020, ( FILE2(I), I= 1,7)
* 1020      FORMAT (7A2)

          BY A NUMBER OF DATA PAIRS (XAXIS, INTENSITY)
          SPECIFIED BY THE FIRST ENTRY IN THE SET UP LINE

*         CALL OPENF (1, IFILE1, 1)
*         CALL OPENF (2, IFILE2, 3)
          READ (1,1030) NVALS, XLENTH, XOFF, STNMR, FINNMR, FREQ.
 1030     FORMAT ( )
          DO 90 I = 1, NVALS
   90     READ (1, 1030) RDATA (I, 1), RDATA (I,2)

          FOR COMPARISON OF DATA OBTAINED WITH DIFFERING
          FREQUENCIES, ALL DATA IS
          NORMALIZED TO APPEAR AS IF THE OPERATING FREQUENCY
          WAS 9.3 GHz.  FIELD VALES ARE PUT IN RDATA (I,3)

          HSTART  =  STNMR / .425776 E -02
          HEND    =  FINNMR / .4255776 E -02
          HCAL    =  (HEND - MSTART) / XLENTH
          FRENOR  =  9.3 / FREQ
          DO 100 I = 1, NVALS
 100      RDATA (I,3) = ((RDATA (I, 1) -XOFF)*HCAL+HSTART)/FRENOR
```

```
C       CALCULATE FIELD INTERVAL FOR INTEGRATION
C       PURPOSES
C
        HINT = RDATA (2,3) - RDATA(1,3)
C
C       ASSUME THAT DATA ARE SYMETRICAL AND CALCULATE
C       AN INTEGER ON THIS BASIS TO GIVE WINGS TO THE DATA
C       OF EQUAL LENGTH
C
        ESRMIN = Q
        ESRMAX = O
        DO 1OO I = 1, NVALS
        if (RDATA(I,2). LT. ESRMAX) GO TO 12O
        ESRMAX = RDATA (I,2)
        MAXMRK = I
  12O   IF (RDATA(I,2. GT. ESRMIN) GOT TO 11O
        ESRMIN = RDATA (I,2)
        MINMRK = I
  11O   CONTINUE
        LOOPVL = MAXMRK + MINMRK
C       ASSUME HORIZONTAL BASE LINE TO ABSORPTION LINE
C       AND CALCULATE & SHIFT DERIVATIVE BASE LINE TO MEAN OF
C       DATA
C
        SMDATA = O
        DO 14O I = 1, LOOPVL
  14O   SMDATA = SMDATA + RDATA (I,2)
        SMDATA = SMDATA/LOOPVL
```

```
      DO 150 I = 1, LOOPVL
  150 RDATA(I, 5) = RDATA (I,2) - SMDATA
C
C     INTEGRATION.  DATA PASSED TO SUBROUTINE SIMP.  INTEGRATED
C     RESULT IS RETURNED IN RDATA (I,6)
C
      CALL SIMP
C
C     NORMALISE INTEGRATED DATA SO THAT VALUES RANGE
C     FROM 0.0 - 1.0
      DO 152 I = 1, 100PVL
  152 IF (RDATA (I, 6). GT. RSTMAX) RSTMAX = RDATA(I,6)
      DO 154 I = 1, LOOPVL
  154 RDATA (I,4) = RDATA (I,6)/RSTMAX.
C
C     CALCULATE FIRST 4 MOMENTS & SKEW & KURTOSIS OF INTGRATED DATA USING
C     SUBROUTINE MOMEN
C
      CALL MOMEN(SKEW, CURT, PMOM)
C
C     WRITE ALL COLS 1-4 OF RDATA TO DISK FILE FOR STORAGE
C
      WRITE(2,1045) LOOPVL, XLENTH, XOFF, NMRST, NMREND, FREQ.
      WRITE(2,1050)((RDATA(I,J), J=1, 4) I=1, LOOPVL), (PMOM(I)I=1,4)
      WRITE(2,1055) SKEW, CURT, MSTART, MEND, MCAL, PRENSOR, MCAL
 1045 FORMAT (I4, F5.2, F5.2, F7.4, F7.4, F6.4)
 1050 FORMAT (4 E13.7)
 1055 FORMAT (E13.7, E13.7, F9.3, F9.3, F7.3, E12.6 E12.6)
C
C     THE INTEGRTATED DATA IS NOW AVAILABLE, NORMALISED TO ALLOW
```

```
C       EASY PLOTTING,IN THE RESULTS FILE
C
        STOP
        END

SUBROUTINE SIMP
C
C       A SUBROUTINE TO INTEGRATE A CONTINUOUSLY VARIABLE
C       FUNCTION.  MORE THAN 6 VALUES MUST BE PRESENT,
C       IN RDATA (I,5).  INTEGRATED VALUES ARE RETURNED
C       IN RDATA (I,6).  HINT FROM THE CALLING PROGRAM IS THE
C       DATA INTERVAL
C
C       * * * * * *  START OF CODE * * * * * * *
C
C
        SUBROUTINE SIMP
        COMMON DUMMY (100), RDATA (300,6) NVALS LOOPVL, HINT.
        HT = 0.3333333 * HINT
C
C       ASSUME THAT MORE THAN 6 VALUES ARE AVAILABLE &
C       PREPARE INTEGRATION LOOP.
C
        SUM1 = MT * (RDATA(1,5) +RDATA(2,5) + RDATA(3,5))
        AUX1 = SUM1 + HT* (RDATA(3,5) + 4*RDATA(4,5) + RDATA (5,5))
        AUX2 = HT * (RDATA(1,5) + 3.875 * (RDATA(2,5) + RDATA(5,5))
        ++ 2.625 * (RDATA(3,5) + RDATA(4,5)) + RDATA (6,5))
        SUM2 = AUX2 - HT * (RDATA(2,5) + 4 * RDATA(3,5) + RDATA (4,5))
        RDATA (1,6) = 0.0
        RDATA (2.6) = SUM2 - HT * (RDATA (2,5) + 4 * (3,5) + RDATA(4,5))
```

```
      RDATA (3,6) = SUM1
      RDATA (4,6) = SUM2
C
C     INTEGRATION LOOP
C
      DO 4 I = 7, LOOPVL, 2
      SUM1 = AUX1
      SUM2 = AUX2
      AUX1 = SUM1 + HT * (RDATA(I-2,5) + 4 * RDATA (I-1,5) + RDATA (I,5))
      RDATA (I-2,6) = SUM1
      IF (I - LOOPVL) 3, 6, 6
    3 AUX2 = SUM2 + HT * (RDATA (I-1,5) + 4 * RDATA (I,5 + RDATA (I+1,5))
    4 RDATA (I-1,6) = SUM2
      RDATA (LOOPVL-1,6) = AUX1
      RDATA (LOOPVL,6) = AUX2
      RETURN
    6 RDATA (LOOPVL-1,6) = SUM2
      RDATA (LOOPVL,6) = AUX1
      RETURN

  SUBROUTINE MOMEN
C
C     A SUBROUTINE TO CALCULATE THE FIRST FOUR MOMENTS OF
C     INTEGRATED ESR DATA, ALONG WITH THE COEFFICIENTS OF
C     SKEW AND KURTOSIS.  ALL THE VALUES ARE RETURNED TO
C     THE CALLING PROGRAM
C
      SUBROUTINE MOMEN(SKEW, CURT, PMOM)
      COMMON DUMMY (100) RDATA(500,6) NVALS, LOOPVL
```

```
      DIMENSION ZROMOM(4), PMOM(4)
C
C     CALCULATE FIRST FOUR MOMENTS ABOUT AN ARBITRARY POINT,
C     IN THIS CASE ZERO
C
      SMDATA = 0
      DO 100 I = 1, LOOPVL
  100 SMDATA = SMDATA + RDATA (I,4)
      ZROMOM = 0.
      DO 110 I = 1,LOOPVL
  110 ZROMOM(1) = ZROMOM(1) + RDATA (I,4) * RDATA(I,1)
      ZROMOM(1) = ZROMOM(1) / SMDATA
      DO 120 J = 2, 4
      ZROMOM(J) = 0.
      DO 130 I = 1, LOOPVL
  130 ZROMOM (J) = ZROMOM(J) + RDATA (I,4) * RDATA(I,1) ** J
  120 ZROMOM (J) = ZROMOM(J) / SMDATA
C
C     NOW CALCULATE MOMENTS ABOUT MEAN
C
      PMOM (1) = 0
      PMOM (2) = ZROMOM(2) - ZROMOM (1) ** 2
      PMOM (3) = ZROMOM(3) - 3 * ZROMOM(L) * ZROMOM(2) + 2 * ZROMOM(1) ** 3
      STPMOM = ZROMOM(4) - 4 * ZROMOM(1) * ZROMOM(3)
      PMOM(4) = STPMOM + 6 * ZROMOM(2) * ZROMOM(1) **2 - 3 * ZROMOM(1) ** 4
C
C     CALCULATE SKEW AND KURTOSIS
C
```

```
RMOM = PMOM(2)

SKEW = PMOM(3) / POWER (RMOM, 1.5)

CURT = PMOM(4) / PMOM (2) ** 1

RETURN

END.
```

APPENDIX II

Electron Spin Resonance Linewidths of Co^{2+} in Magnesium Oxide

While the low temperature electron spin resonance measurements on silicon nitride were being undertaken some time was also devoted to studying the Co/MgO system. This work, which was undertaken jointly with M.D.Hossain, L.J.C.Bluck and J.S.Thorp, arose as part of an investigation of the e.s.r. and dielectric properties of a range of doped MgO single crystals being carried out by other members of the group. From the e.s.r. point of view the Co^{2+} ion is difficult to examine because the e.s.r. spectrum is only observable at temperatures below about 10 K. Consequently the e.s.r. cryogenic facilities and techniques developed for the silicon nitride exa-ination were adapted and used for part of the MgO programme. This Appendix reproduces the paper which was published in the Journal of Materials Science, 15 (1980), 903.

JOURNAL OF MATERIALS SCIENCE 15 (1980) 903–908

Electron spin resonance linewidths of Co^{2+} in magnesium oxide

J. S. THORP, M. D. HOSSAIN, L. J. C. BLUCK*, T. G. BUSHELL
Department of Applied Physics and Electronics, University of Durham, UK

Electron spin resonance linewidths of Co^{2+} in single-crystal MgO at 9 GHz were examined experimentally and theoretically for a range of Co^{2+} concentration from 310 to 9900 ppm. In contrast to the behaviour expected from dipolar broadening, the experimental peak-to-peak linewidth for the octed hyperfine lines were about twelve to fifty times less than the calculated dipolar linewidths according to temperature and concentrations. The peak-to-peak linewidths as determined experimentally increase from 0.8 mT at 310 ppm Co^{2+} to 4.0 mT at 9900 ppm Co^{2+} at a polar angle $\theta_H = 0°$ and at 20 K. Peak-to-peak linewidths independent of polar angle but strongly dependent on temperature and slightly dependent on concentrations were observed. The ratio of moments $M_4^{1/4}/M_2^{1/2}$ derived from the experimental data lay between 1.35 to 1.44 and the lineshapes were markedly Lorentzian in the range of temperature measured. The data suggest that Co^{2+} entered the lattice substitutionally, occupying magnesium sites, that the linewidths were determined, after exchange energy, over the whole concentration range examined and that the exchange energy whose values lay between 6 and 77 GHz, varied linearly with concentration.

1. Introduction

The electron spin resonance (esr) linewidth results of Fe^{3+} and Cr^{3+} in magnesium oxide showing exchange interactions have recently been reported [1, 2]. As part of further studies on different ions, a similar investigation has been made of the cobalt-doped magnesia (Co^{2+}/MgO) in an attempt to provide specimens of known structural characteristics on which electrical conductivity and dielectric loss measurements might subsequently be made. The esr spectra of Co^{2+}/MgO was first observed by Low in 1958 [3] and then by Fry and Llewellyn in 1962 [4], where the characteristic parameters of the spin-Hamiltonian were calculated for cubic crystalline field. There is, however, little detailed information available either on the question of the sites actually occupied by the dopant atoms or on the nature of the interactions between the latter. Information of this nature has been obtained in the literature [1, 2], by making a comparison between observed esr linewidths and those predicted from dipolar broadening. It was decided to adopt a similar approach with Co^{2+}/MgO. The divalent ion of cobalt has electronic configuration of $3d^7(^4F_{9/2})$. In the MgO lattice the ^4F level splits into three, and these are further split by spin orbit interaction [3] and the lowest level is a Kramers doublet. Since the only natural isotope of cobalt is ^{59}Co, which has a nuclear spin $I = 7/2$, considerable hyperfine interaction is expected. This paper presents the results of the linewidth comparison made for the hyperfine transitions in the ground doublet of Co^{2+}.

2. Experimental techniques

The doped single crystals on which measurements were made were obtained from W. & C. Spicer Ltd (Cheltenham), having been grown by electrofusion using pure powdered cobalt oxide and pure powdered magnesia as starting materials. The cobalt concentrations in the specimens examined ranged from 310 to 9900 ppm, these have been

* Present address: Clarendon Laboratory, Parks Road, Oxford, UK.

0022–2461/80/040903–06$02.60/0

determined by optical spectrographic analysis (Johnson-Matthey Ltd) to an accuracy of about 2%. The crystalline quality was good and neither optical examination nor X-ray back-reflection photographs, used to orient the specimens, revealed any evidence of macroscopic cracking, flaws, strain or mosaic formation. This led us to assume that the samples were of good crystalline quality. The crystals were coloured varying from very light pink at 310 ppm Co to deep pink at 9900 ppm Co.

The esr measurements were made both using a conventional 9 GHz spectrometer [2] and a X-band commercial Varian spectrometer. Since the spectrum of Co^{2+}/MgO is only visible below about 65 K, the spectrometers were equipped with helium cryostats having temperature control devices. Spectra were recorded in the range 4.2 to 65 K, by sweeping the magnetic field slowly through a known range. The magnetic field calibrations were obtained using a proton resonance magnetometer system in which the probe could be located exactly in the position normally occupied by the specimen.

3. Experimental results

Initial measurements were made to establish the form of the spectrum in each specimen at various temperatures. An example of this is shown in Fig. 1, which refers to a specimen containing 310 ppm Co examined at temperatures between 4.2 and 65 K. The spectrum, which is isotropic, shows a total of eight hyperfine line with g value about 4.278 and with hyperfine constant about $A = 98.0 \times 10^{-4}\ cm^{-1}$. The values at which the transitions occurred when compared with the values expected from the energy level diagram [5]. There was close agreement and on this basis, and in view of the similarity between Fig. 1 and the features of the liquid helium temperature spectra reported for the 1 and 3 cm regions, respectively, in [3] and [6], it was felt justifiable to attribute the spectrum to Co^{2+} in the octahedral sites. A conspicuous difference in the intensity and the hyperfine line energy separation A was observed between the low and high magnetic field sides. Even at high gain the crystals showed only the lines due to Co^{2+} and a weak line due to iron, which suggests that these crystals are of higher degree of perfection than the corresponding Cr^{3+}/MgO sample [2]. This is possibly due to the fact that since the Co^{2+} ion is doubly charged, a direct substitution for Mg^{2+} is possible in the MgO lattice without the need for charge compensating vacancies.

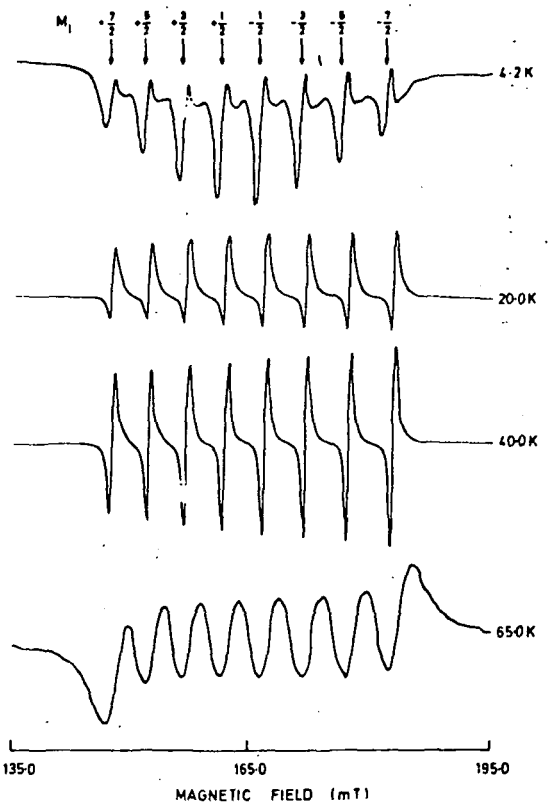

Figure 1 Variation of lineshape with temperature. Co^{2+}/MgO (310 ppm) 9.515 GHz, $\theta_H = 0°$.

The linewidth determinations were made at $\theta_H = 0°$. The linewidths of the eight hyperfine lines were equal to each other and were independent of polar angle θ_H, but strongly dependent on temperature (Fig. 2). There is some difficulty

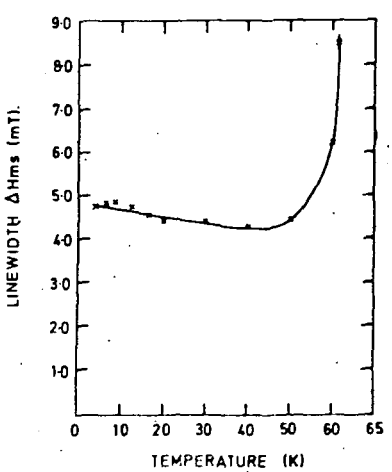

Figure 2 The temperature dependence of the linewidth for Co^{2+}/MgO (8200 ppm), 9.515 GHz, $\theta_H = 0°$.

in ascertaining the linewidth at high temperatures and, above 50 K, the points marked on Fig. 2 have been derived from the separation of points of inflection on the derivative plots. The linewidths were also slightly dependent on concentration but not by as much as the (concentration)$^{1/2}$ behaviour expected from dipolar theory. Increases in resonance linewidth for higher dopant concentrations have been reported by Fry and Llewellyn [4] in the endor experiments. There was no change in either the resonance field or the hyperfine constant A with polar angle at temperatures in the range measured. The peak-to-peak linewidth, defined as the width between points of maximum slope, ΔHms, was obtained directly from the derivative plots. As the temperature decreased from 65 K the linewidth first decreased to a minimum at about 40 K and then increased from 20 K down to 4.2 K. For all the specimens, the linewidths ΔHms at 4.2 K were less than the linewidths at 60 K. For the low concentration specimen (310 ppm Co) at temperatures of 20, 4.2 and 60 K, the linewidths ΔHms were 0.8, 1.7 and 2.4 mT, respectively, while for the high concentration specimen (9900 ppm Co) the values of ΔHms for the corresponding temperatures were 4, 4.9 and 4.9 mT, respectively.

4. Dipolar broadening

It will be assumed in this calculation that the main contribution to homogeneous line broadening is dipole–dipole interaction between Co^{2+} ions. The second moment $\langle\Delta\omega^2\rangle$ of the linewidth caused by dipolar interaction between identical atoms in the magnesium oxide lattice has been derived in the literature [1]. For Co^{2+}, $S = \frac{3}{2}$ and $g = 4.278$ [3] and so the atomic part of the second moment is $6.2644 \times 10^{-24} n$ $(\text{rad sec}^{-1})^2$ cm^6, which leads to the final equation for second moment

$$\langle\Delta\omega^2\rangle = 6.2644 \times 10^{21} n \times [15.9184 - 5.175 Y^*_{4,0}(\theta_H, \phi_H) - 6.218 Y^*_{4,4}(\theta_H, \phi_H)], \quad (1)$$

where the symbols have their usual meanings as described in [1]. Using the transformation equation and considering $\phi_H = 0°$, the peak-to-peak derivative linewidths ΔHms can be evaluated and compared with experimental values. The general curves for the variation of linewidth with polar angle are given in Fig. 3, which also shows the experimental values of linewidth. The predicted concentration dependence of linewidth at $\theta_H = 0°$ (obtained from Fig. 3) is shown in Fig. 4, which also gives the experimental points.

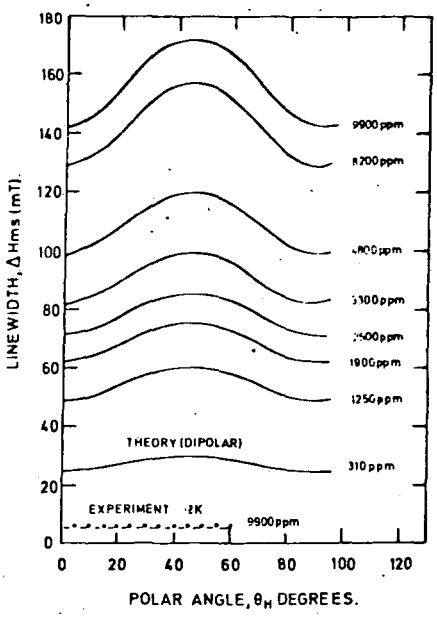

Figure 3 Comparison of predicted and observed variation of linewidth with polar angle.

5. Discussion

Two salient features emerge from initial comparison between the experimental results for the as-grown crystals and dipolar theory. Firstly, the predicted linewidths are about fifty times larger than the observed linewidths; secondly, the linewidth appears to be independent of polar angle in contrast to the maximum linewidth at 45° expected for dipolar broadening. The former discrepancy was similar to that encountered with both Fe^{3+}/MgO [1] and Cr^{3+}/MgO [2]. These both showed linewidths of about 100 times less than the predicted dipolar widths, an effect attributed to exchange narrowing; the independence of width on polar angle has also been observed in Cr^{3+}/MgO. In Co^{2+}/MgO, the measured linewidth varied from between twelve and fifty times less than predicted by dipolar broadening theory (Table I). This large numerical disparity in Co^{2+}/MgO suggested that there was a strong narrowing mechanism such as had previously been found in both Fe^{3+}/MgO and Cr^{3+}/MgO.

To substantiate the possibility of exchange narrowing within the range of measured concentrations and temperature, additional evidence based on lineshape analysis has been obtained and

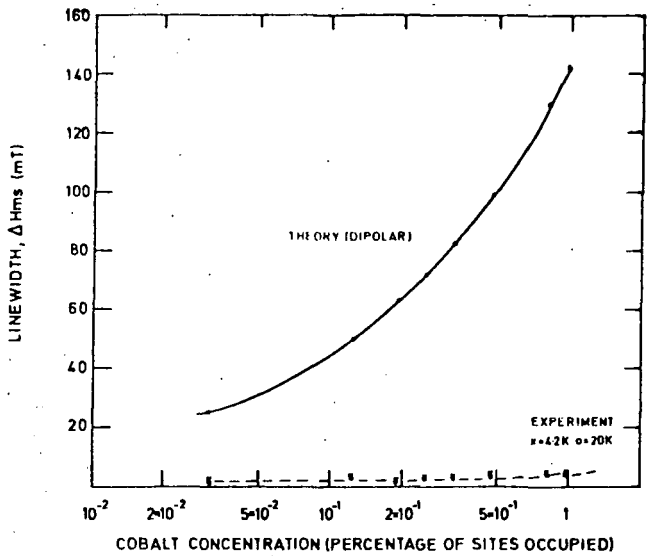

Figure 4 Comparison of predicted and observed variation of linewidth with concentration; $\theta_H = 0°$, 9.51 GHz.

these data are also given in Table I. To obtain the data it was considered that in all cases an undistorted lineshape could be obtained from the leading (or trailing) half of the first (or last) line of the octet; this, when integrated, gave one side of the absorption line. It was also assumed that the line was symmetrical about the mid point. The ratio $M_4^{1/4}/M_2^{1/2}$ (where M_2 and M_4 are, respectively, the second and fourth moments) was then derived and the results are tabulated in column 5 of Table I. The values of the ratio are similar to the figures quoted for Fe^{3+}/MgO [1] and Cr^{3+}/MgO [2]. This suggests that at temperatures between 60 and 4.2 K exchange narrowing is important, even at the lowest cobalt concentration (310 ppm).

The lineshape factor is defined as the ratio of the peak-to-peak derivative linewidth, ΔHms, to the width of half-height, $\Delta H_{1/2}$, of the absorption curve. The values of this factor for Lorentzian and Gaussian lines are, respectively, 0.577 and 0.846

TABLE I Lineshape data for a range of cobalt concentrations at temperatures of 4.2, 20 and 60 K; 9.515 GHz, $\theta_H = 0°$

(1) Cobalt concentration (ppm)	(2) ΔHms (dipolar) $\theta_H = 45°$ (mT)	(3) Temperature (K)	(4) ΔHms (obs) (mT)	(5) $M_4^{1/4}/M_2^{1/2}$	(6) ΔHms (obs) / $\Delta H_{1/2}$ (obs)
310	30.1	4.2	1.7	1.44	0.57
		20	0.8	1.39	0.57
		60	2.4	1.396	0.61
1250	60.1	4.2	2.9	1.358	0.58
		20	2.1	1.41	0.55
2500	86.7	4.2	2.9	1.365	0.48
		20	2.1	1.41	0.64
3300	99.7	4.2	2.9	1.39	0.47
		20	2.0	1.39	0.51
4800	120.1	4.2	3.6	1.36	0.50
		20	2.4	1.38	0.57
		60	3.9	1.37	0.55
8200	157.1	4.2	4.7	1.37	0.69
		20	4.4	1.43	0.65
		60	6.3	1.41	0.58
9900	172.6	4.2	4.9	1.35	0.63
		20	4.0	1.37	0.54
		60	4.9	1.39	0.67

TABLE II Evaluation of exchange energy and Weiss constant, for various concentrations of cobalt, 4.2 K

Sample concentration (ppm)	Exchange energy (GHz)	Weiss constant θ (K)
310	6.11	0.88
1250	14.67	2.10
2500	25.48	3.66
3300	33.00	4.75
4800	40.76	5.87
8200	7374	10.61
9900	77.60	11.17

[7]. Exchange narrowing would make the line adopt a Lorentzian shape. To confirm this, the widths at half-height, $\Delta H_{1/2}$, have been calculated from the observed integrated lineshapes and the ratio of $\Delta Hms/\Delta H_{1/2}$ derived; the values are tabulated in column 6 of Table I and show that the lineshapes are more Lorentzian than Gaussian in the range of concentration and temperature used.

The assumption, on the above basis, of an exchange-narrowed model enables evaluation of the exchange energy J to be made by adopting the method used previously [2]. The values of J for the different specimens at 4.2 K have been tabulated in column 2 of Table II. Further, a plot of J against concentration gives a straight line as shown in Fig. 5. If this line is extrapolated to 50% of the available sites occupied by Co^{2+}, i.e. to the point corresponding to CoO, an exchange energy of 32×10^{11} Hz is obtained. This may be compared with the value for CoO of 1.43×10^{11} Hz obtained from the temperature dependence of susceptibility [8] and also with the reported value of $J = 6.298 \times 10^{11}$ Hz as measured from the intensity of pair spectra in Co^{2+}/MgO [9].

We have also calculated the values of Weiss constant θ, from the Weiss molecular field equation

$$3k\theta = 2JzS(S+1) \qquad (2)$$

where z is the number of nearest neighbours and k is the Boltzmann constant; in the MgO lattice $z = 6$.

Even though the actual spin of Co^{2+} is $\frac{3}{2}$, we observed only the octet of hyperfine lines due to the interaction between an effective spin of $\frac{1}{2}$ and the nuclear spin $I = \frac{7}{2}$. Thus taking $S = \frac{1}{2}$, the values of θ have been evaluated from Equation 2 and tabulated in column 3 of Table II. Similar effective spin value considerations have been reported in the literature [9, 10]. A plot of θ against concentration also gives a straight line (Fig. 5). If this line is extrapolated to the point representing pure CoO, a value of Weiss constant $\theta = 550$ K is obtained. This is comparable to the literature value CoO of 330 K [11] and thus supports the validity of assuming $S = \frac{1}{2}$.

The differences in both the intensity and hyperfine energy separation A in the octet spectrum of Co^{2+}/MgO are the same at all temperatures. These effects may be due to cross-relaxation between cobalt ions, an interaction which also is temperature independent. Cross-relaxation would be expected to affect the population distribution in the components of the octet and hence their relative intensities. Cross-relaxation between cobalt ion in MgO has been reported by Pryce [5] for specimens containing less than 230 ppm Co and so cross-relaxation would be very likely at the higher doping levels used in the present work. The increase of linewidth, ΔHms, in the range of temperature 20 to 4.2 K may be due to unresolved hyperfine interaction with the ^{25}Mg nuclide while the increase in linewidth above 40 K can be attributed to relaxation broadening.

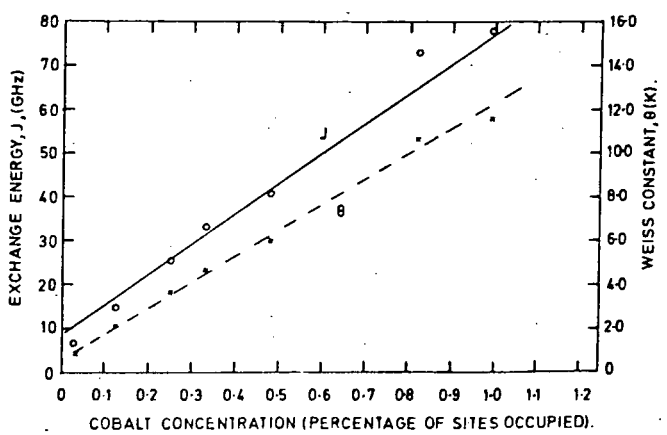

Figure 5 The variation of J and θ with cobalt concentration, 4.2 K.

Acknowledgements

It is a pleasure to record our thanks to C. Savage and T. C. Harcourt for their assistance in specimen preparation. We wish to thank the University of Rajshahi, Bangladesh, for the award of a research scholarship to M.D.H. and the Science Research Council for a postgraduate studentship to T.G.B.

References

1. J. S. THORP, R. A. VASQUEZ, C. ADOCK and W. HUTTON, *J. Mater. Sci.* 11 (1976) 89.
2. J. S. THORP, M. D. HOSSAIN and L. J. C. BLUCK, *ibid.* 14 (1979) 2853.
3. W. LOW, *Phys. Rev.* 109 (1958) 256.
4. D. J. I. FRY and P. M. LLEWELLYN, *Proc. Roy. Soc. A* 266 (1962) 84.
5. M. H. L. PRYCE, *Proc. Roy. Soc. London* A283 (1965) 433.
6. J. C. M. HENNING and J. H. DEN BOEF, *Phys. Rev.* B14 (1976) 26.
7. C. P. POOLE, "Electron spin resonance" (Wiley, New York, 1967) p. 775.
8. P. W. ANDERSON, *Solid State Phys.* 14 (1963) 99.
9. S. GESCHWIND, "Electron paramagnetic resonance" (Plenum Press, New York, 1972).
10. E. B. TUCKER, *Phys. Rev.* 143 (1966) 264.
11. "C.R.C. Handbook", 57th Edn. (1977–78) edited by R. C. Weast (C.R.C. Press, Cleveland, Ohio, 1978) p. E. 120.

Received 26 July and accepted 20 September 1979.